This is to certify that the
dissertation entitled

THERMOELECTRIC MODULE CONTACT FABRICATION AND ANALYSIS AT ELEVATED TEMPERATURES BY HIGH TEMPERATURE VOLTAGE PROFILING SYSTEM (HTVPS)

presented by

MUHAMMAD FARHAN

has been accepted towards fulfillment
of the requirements for the

Doctoral degree in Electrical Engineering

Major Professor's Signature

8-24-09

Date

THERMOELECTRIC MODULE CONTACT FABRICATION AND ANALYSIS AT ELEVATED TEMPERATURES BY HIGH TEMPERATURE VOLTAGE PROFILING SYSTEM (HTVPS)

By

MUHAMMAD FARHAN

A DISSERTATION

Submitted to
Michigan State University
In partial fulfillment of requirements
For the degree of

DOCTOR OF PHILOSOPHY

Electrical Engineering

2009

ABSTRACT

THERMOELECTRIC MODULE CONTACT FABRICATION AND ANALYSIS AT ELEVATED TEMPERATURES BY HIGH TEMPERATURE VOLTAGE PROFILING SYSTEM (HTVPS)

By

Muhammad Farhan

High temperature bulk thermoelectric (TE) materials $Ag_{1-x}Pb_mSbTe_{2+m}$ and $Ag(Pb_{1-x}Sn_x)_mSbTe_{2+m}$ (also known as LAST and LASTT) developed at Michigan State University have exhibited a figure of merit, ZT, of 1.7 at 700 K. Thermoelectric power generation devices based on these materials are being developed at the Electronic Material, Pulse Laser Deposition and Transport Characterization laboratory. For optimal performance, low resistance high temperature electrical contacts are required.

In this research work a new high temperature voltage profiling system has been designed and fabricated to investigate the temperature dependence of the hot side contact resistance. The system can measure contact resistance and electrical conductivity of a sample from room temperature to 800 K. The system was used to characterize bonds of tin-tellurium, braze and solder to hot pressed LAST, cast LAST and LASTT type thermoelectric materials.

The second research effort focuses on spring loaded TE modules and their output parameters (open circuit voltage and short circuit current) from 300- 800 K. This has helped to explore a practical TE generator configuration. Also InGa based liquid contacts were investigated to circumvent coefficient of thermal expansion (CTE) mismatch

problems with hot side metal electrodes. The results are in good agreement with the expected output based on module modeling efforts.

The high temperature voltage profiling system has been utilized to evaluate a variety of potential electrode materials including brass, copper, nickel and stainless steel. During this investigation we developed SnTe based bonds which proved to be our optimum solution in terms of low contact resistance, high power output and sustainable operational endurance.

ACKNOWLEDGEMENTS

I am thankful to Almighty Allah for giving me the courage to accomplish this task. I am deeply grateful to my advisor Dr. Tim Hogan for all the guidance and patience without which it all would not be possible. My gratitude for my fellow lab mates specially Ajmal Khan for his cooperation during research and course work, Nuraddin Matchanov for closely collaborating on experiments, Jarrod Short for introducing me to thermoelectrics and Jonathan D'Angelo for useful inputs and allowing me to use his equipment.

I am thankful to my mother for her untiring efforts, my brother for his constant persuasion and sisters for all the care.

Finally, financial support from Higher Education Commission Pakistan, National Science Foundation for nanowire research, Office of Naval Research and SERDP for thermoelectric research is gratefully acknowledged.

TABLE OF CONTENTS

LIST OF TABLES

LIST OF FIGURES

Chapter 1: Introduction to Thermoelectric Research

Chalcogenide based thermoelectric materials $Ag_{1-x}Pb_mSbTe_{2+m}$ and $Ag(Pb_{1-x}Sn_x)_mSbTe_{2+m}$ (also known as LAST and LASTT) developed at Michigan State University have exhibited promising thermoelectric properties for power generation applications [1]. Thermoelectric generators consisting of this material are expected to operate at hot side temperature of ~ 900 K and cold side temperature of ~300 K. This thermoelectric research is a collaborative effort between the Electrical and Computer Engineering, Material Science and Engineering, and Mechanical Engineering departments at Michigan State University and the Chemistry department at Northwestern University. For this project a goal of Material Characterization and Pulsed Laser Deposition Lab at Michigan State University Electrical and Computer Engineering Department is to study these new materials through characterization and develop them into thermoelectric generators. Material characterization involves transport measurements which include electrical conductivity, thermal conductivity, thermopower, and ZT measurements. A thermoelectric generator consists of an array of unicouples each having one n-type leg of $Ag_{1-x}Pb_mSbTe_{2+m}$ (LAST) and one p-type leg of $Ag(Pb_{1-x}Sn_x)_mSbTe_{2+m}$ (LASTT) electrically interconnected with electrode. These electrode-thermoelectric material contacts need to be low resistance for higher efficiency and power output. Typical acceptable total contact resistance values are less than 10% of the total thermoelectric legs resistance. The purpose of this thesis is to investigate

methods of bonding and high temperature contact behavior of thermoelectric material to metal electrodes. The electrodes on hot side are typically more difficult to fabricate as they must operate at temperatures where common solders are molten and the issue of differing coefficient of thermal expansions (CTE) between the thermoelectric material and the electrode material becomes critical. As part of this effort various diffusion bonding processes have been investigated to develop low resistance bonds. These low resistance bonds need to be stable at high temperature which brings in the issue of elemental diffusion from the metal electrode. To circumvent this problem, diffusion barriers have been studied on the electrode and on the thermoelectric materials. Liquid contacts consisting of InGa were used to avoid coefficient of thermal expansion mismatch challenge between thermoelectric material and metal electrode. Spring loaded modules were tested under ambient conditions and inert environment for short circuit current measurements. To investigate thermoelectric contact behavior at high temperature a new high temperature voltage profiling system has been designed and fabricated. In this system a voltage probe pin scans across the metal electrode-thermoelectric leg contact. Data obtained from this measurement is used to determine the sample resistance at various temperatures, to monitor the sample uniformity, to see if any cracks in the sample exist, and to measure the contact resistance as a function of temperature.

This dissertation is divided into four chapters. The first chapter describes fundamental thermoelectric phenomenon with discussion of LAST and LASTT material properties along with a review of the literature related to contact resistance studies. The second chapter includes diffusion bonding results and diffusion barrier coatings on metal electrodes. The third chapter discusses liquid contacts and spring loaded modules output

short circuit current measured under ambient conditions and inert environments. In the fourth chapter the design of a voltage profiling system is given along with experimental results of high temperature contact resistance measurements. Due to funding constraints, my research focus has changed. My initial research efforts in this group were towards nanowire synthesis for sensor applications. As part of that effort, GeO_2, ZnO and InSb nanowires were synthesized by vapor-liquid-solid (VLS) mechanism. Moreover ZnO and GeO_2 nanowires were grown through direct heating on hot plate under ambient conditions. These results are mentioned in appendix A of this dissertation.

1.1 Thermoelectric Materials

Thermoelectric (TE) generators convert heat energy into electrical energy when a thermal gradient is maintained across the device. The process is reversible such that thermoelectric coolers (also known as Peltier coolers) operate by supplying electrical energy to the thermoelectric module resulting in a temperature gradient being established across the module. These devices are rugged and have no moving parts which make them ideally suitable for harsh environments and unmanned places. The focus of this research is on TE generators, and this chapter begins with descriptions of the governing thermoelectric effects of the Seebeck effect, Peltier effect, and the Thomson effect.

1.2 Seebeck Effect

If the two materials are joined at two junctions such that a closed loop electrical circuit is formed there will be a current in the close loop given that there is a temperature difference between the two junctions. Thomas Johann Seebeck originally observed this phenomenon when a compass needle placed close to such a loop moved when junctions were maintained at different temperatures. The current resulted in a magnetic field which moved the compass needle. He also observed that magnitude of deflection depended upon the amount of heat provided at the junction and type of material used. Typical voltages from the Seebeck effect range from a few microvolts per Kelvin for metals to several hundred microvolts per Kelvin in semiconductors, and into the millivolts per Kelvin for insulators. The Seebeck coefficient is the voltage developed for a one Kelvin temperature difference maintained between the ends of the conductors. Seebeck coefficient is given as:

$$\alpha = \frac{dV}{dT} \text{ (V/K)} \qquad (1)$$

and by integration, the voltage can be found as:

$$V = \int_{T_1}^{T_2} \alpha . dT \text{ (V)} \qquad (2)$$

1.3 Peltier Effect

The Peltier effect was discovered by Jean Peltier in 1834 and states that heat is liberated or absorbed when electric current passes through the interface between two different conductors. It is a reversible effect, such that if the direction of the current is reversed, the direction of the heat exchange at the boundaries of material will also change. The Peltier effect is based on the fact that heat current accompanies electric current in homogenous conductors. The Peltier coefficient Π_{AB} is related to individual Peltier coefficients as:

$$\prod_{AB} = \prod_{A} - \prod_{B} \qquad (3)$$

The Peltier coefficient is related to absorption or liberation of heat through [2]:

$$\frac{dQ}{dT} = \prod_{AB} i \qquad (4)$$

where

$$i = \frac{dq}{dt} \qquad (5)$$

Here q ($q = -1.602 \times 10^{-19}$ C for an electron) is the charge. Above equation can be integrated to give:

$$\Delta Q = \prod_{AB} \Delta q \qquad (6)$$

This is related to the Seebeck coefficient as:

$$\prod_{AB} = T\alpha_{AB} \text{ (V)} \qquad (7)$$

1.4 Thompson effect

The Thompson effect was discovered by William Thompson (Lord Kelvin) in 1854 and states that heat is liberated when an electrical current is passed through a homogenous conductor which is subjected to a temperature gradient. The heat is absorbed or emitted based on type of material, direction of the current flow relative to temperature gradient and thermopower of the conductor [3].

The Thompson coefficient (β) and Seebeck coefficient (α) are related as:

$$\beta = \frac{d\alpha}{dT}.T \text{ (V/K)} \qquad (8)$$

or

$$\alpha = \int_0^T \frac{\beta(T')}{T'}.dT' \text{ (V/K)} \qquad (9)$$

Thompson coefficient can be related to the Thompson heat and Thompson current as:

$$T_Q = \frac{dQ}{dT} = -\beta I \Delta T \text{ (W)} \qquad (10)$$

For materials like Zn and Cu, the higher temperature end of the conductor is at a higher potential, so heat will be liberated if current moves from hotter end to the colder end. It is known as positive Thompson effect. For materials like Ni, Fe and Co, the colder end will

be at higher potential, so heat will be absorbed when current moves from hotter end to colder end, known as negative Thompson effect.

1.5 Figure of Merit (ZT)

Thermoelectric materials are characterized by a dimension less figure of merit ZT.

$$ZT = \frac{\alpha^2 \sigma}{\kappa} T \qquad (11)$$

Here α is the absolute Seebeck coefficient, σ is electrical conductivity and κ is thermal conductivity. It indicates that a good thermoelectric material will have high electrical conductivity and low thermal conductivity. Thermal conductivity of a material is its ability to conduct heat. Both phonons and charge carriers participate in heat conduction in metals and semiconductors.

$$\kappa_{total} = \kappa_{electrical} + \kappa_{lattice}$$

Materials like metals which are good electrical conductors are also good thermal conductors and materials like quartz which have low thermal conductivity also have low electrical conductivity whereas; thermoelectric materials need to have low thermal conductivity and high electrical conductivity. At low temperature there is very little vibration of lattice and thermal conduction is through charge carriers and at higher temperature lattice vibration dominates and much of the heat conduction is through phonons. In between these extremes both charge carriers and phonons participate in thermal conductivity. The relationship between electrical and thermal conductivity can be given by the Wiedemann Franz Law:

$$\frac{\kappa}{\sigma} = LT \qquad (W\Omega K^{-1}) \qquad (12)$$

Here L is proportionality constant and is known as Lorenz number.

For metals:

$$L = \frac{\kappa}{\sigma T} = \frac{\pi^2}{3}(\frac{k_B}{e})^2 = 2.44 \text{x } 10^{-8} \quad (W\Omega K^{-2}) \qquad (13)$$

This value of Lorenz number is applicable for temperatures above the Debye θ_D value.

This law indicates that charge carriers are involved in both electrical and thermal conduction. For LAST material with a typical room temperature value of electrical conductivity of 1850 S/cm [1], thermal conductivity of 2.3 W/m-K [1] and the value of the Lorenz number of 2.28 x 10^{-8} $W\Omega K^{-2}$ [4] gives the value of $\kappa_{lattice}$= 1.27 $W\Omega K^{-2}$.

We can easily now calculate the value of $\kappa_{electronic}$=1.03 $W\Omega K^{-2}$.

1.6 Thermoelectric Applications

Fossil fuel has been the energy work horse for more than a century, however, this resource will deplete one day, forcing humans to look for alternate energy resources. Thermoelectric generators and coolers typically are small in size and have no moving parts and are more reliable because of their rugged solid state construction. Their silent operation makes them ideally suited for military applications like submarine power generators where silence is paramount for undetected submarine operation. In areas like space exploration where human intervention is not possible on unmanned missions and

there is no oxygen available, radioactive isotope thermoelectric generators (RTG) are used. TE generators are also eco-friendly unlike hydrocarbon where exhaust gases are harmful to the environment. Thermoelectric coolers have been commercially manufactured to serve as heat pumps. They can enhance cooling of the CPU in computers for overclocking. Thermoelectric coolers can be cascaded for applications requiring larger temperature gradients for example a six stage cooling device capable of achieving below 170 K has been manufactured [3]. These devices can provide distributed cooling and heating. Another potential application area is automotive industry. About 65% of fuel energy is lost as waste heat in a typical diesel vehicle [5]. If waste heat recovery can be utilized to meet the accessory load requirement of over the road vehicles, more fuel energy can be used for propulsion. A typical alternator on a diesel vehicle can consume 10 kW of fuel chemical energy to produce 1 kW of output. If the alternator is replaced by an integrated TE radiator, overall vehicle efficiency can improve by 3.3 % [5]. However this task has a number of challenges that must be considered in design which include additional weight of TE modules, increased complexity in power management design, engine backpressure concern and aerodynamic drag increase. Application of thermoelectrics within the medical field have included TE based cooler box (Thermoelectric Cooling America Corporation, TECA) to carry intravenous solutions. Other applications include cold plates for tissue freezing, cooling tank for beverages, Peltier stirring cold plates, liquid chiller, cooling of infrared detectors, air conditioning for small enclosures, thermal blankets for treating hypothermia, and thermoelectrically driven wrist watches.

1.7 Lead-Antimony-Silver-Tellurium (LAST) TE Material

Different TE materials are suitable at different temperatures i.e. their ZT values peak in a certain temperature range and no single TE material can be used for entire temperature range. Traditional materials used near room temperature include Bi_2Te_3, Sb_2Te_3 and Bi_2Se_3 are used up to temperature of 400 °C [6]. These alloys have ZT better than unity. From 400 °C to 600 °C range, historically PbTe based materials are best suited and above this range SiGe has commonly been the best material. In the last decade new materials such as skutterudites, calathrates, and half-husler alloys have been reported along with nanostructured variations of traditional materials [6]. Goldsmid and Nolas have discussed various new materials and have indicated their preference of higher power factor over lower thermal conductivity for TE materials [6]. High power factor can be obtained by higher effective mass or higher mobility. As for lattice thermal conductivity, it can be reduced by preferential scattering by grain boundaries. Scattering from the grain boundary can reduce thermal conductivity even if grain size is larger than phonon mean free path [6]. Larger grain size may not affect carrier mobility unless career free path becomes comparable to grain size. Bhindari [7] has discussed various methods to reduce TE material thermal conductivity that include introduction of point defects in alloys (alloy disorder), resonant scattering, scattering by charge carriers and scattering by grain boundaries. Most of these efforts relate to limiting the phonon mean free path [7].

For LAST material, low thermal conductivity is believed to be due to the structural and compositional inhomogeneity at the nanoscopic level [8], which is responsible for interface phonon scattering by nanostructures of Ag/Sb. The size of these

nanostructures was found to be ~ 5-20 nm [9]. Another possible reason for low thermal conductivity of LAST material is microcracks in bulk material [10]. Androulakis *et al* [9] attributed LAST low thermal conductivity to Pb/Sn regions which reside in the surrounding Pb matrix without disturbing its electronic structure. Quarez *et al* studied LAST material and found that material has resonant states near Fermi level and Ag/Sb microstructures in Pb/Te matrix may be responsible for higher thermopower in LAST [11]. Earlier it was proposed that $AgSbTe_2$ – PbTe is a solid solution [12], however Quarez *et al* showed this is not the case and there are nanostructure periodic domains [11]. There is large anisotropy in carrier effective mass for such systems [1]. For p-type material $Ag(Pb_{1-y}Sn_y)_mSbTe_{2+m}$, the TE parameters can be controlled by adjusting Pb/Sn ratio and by tuning the Ag/Sb nanostructures. Increasing Sn increases the electrical conductivity and thermopower has been found to vary linearly with Sn concentration reaching approximately 280 (μV/K) at 680 K [9]. For cast samples the electrical conductivity decreases with increasing temperature and at about 650 K is 22%-28% of room temperature electrical conductivity [9]. The magnitude of the thermopower appreciably increases in the 330 K to 550 K range which is attributed to an increase in the effective mass with increasing temperature [9]. Lattice thermal conductivity values for LASTT were found to be ~ 0.70 W/m-K at room temperature and ~ 0.43 W/m-K at 640 K [9]. This indicates that there is significant change in lattice dynamics at higher temperature and it deviates from Debye-Peierls law of $\kappa_{lattice} \sim 1/T$ [9]. The highest ZT

achieved for a p-type material was ~1.45 for $Ag_{0.5}Pb_6Sn_2Sb_{0.2}Te_{10}$ composition at 627 K [9]. Bothe LAST and LASTT materials have NaCl structure (*Fm3m* symmetry) [1].

To increase strength and sample homogeneity, powder processing and hot pressing have been investigated. Some of the initial hot pressed samples showed bloating after annealing. Both p-type and n-type ingots release CO_2 at annealing and p-type sample release Te or Te_2 on annealing under vacuum at high temperature [13]. It is assumed that carbon enters the system during powder processing or from graphite dye in the hot press system [13]. Hot pressed samples also show increasing electrical conductivity with increasing temperature. Kosuga *et al* [14] also reported an increase in electrical conductivity with increasing temperature for hot pressed materials as did Zhou *et al* [15] for spark plasma sintering.

1.7.1 Lead-antimony-silver-tellurium (LAST) Mechanical Properties

During thermoelectric materials applications thermo-mechanical stresses are generated from thermal gradient across the TE material, thermal expansion mismatch between TE legs-hot side electrode, mechanical vibrations and thermal cycling. These stresses can create micro and macro-cracks resulting in material failure. For better understanding and to avoid mechanical failure under thermo-mechanical stresses LAST material mechanical properties that include hardness, Young's Modulus, Weibull modulus and bending strength were investigated in [13] and [16].

1.7.1.1 Hardness

Hardness (**H**) of a material is its resistance to shape change when a force is applied. It has been used as a tool to characterize material mechanical properties as a function of alloy compositional changes [13]. Vickers indentation technique is often used to determine hardness where material's ability to resist plastic deformation from a standard source (load) is measured in Pascals. Hardness is also associated with machinability and wear of materials e.g. wear in ceramics is related to hardness by K_C/H where K_C is the fracture toughness. Hardness is also related to compressive fracture strength ~ **H**/3 [13]. Wang *et al* found that material machinability is correlated to both Young's Modulus and hardness [17]. Since for thermoelectric generator fabrication LAST material will require machining of legs from ingots, hardness is an important material property to be considered. The mean values of hardness (H) for cast type LAST ($Ag_aPb_bSb_cTe_d$) with mole fraction ranges $0.006 < a < 0.043$, $0.417 < b < 0.480$, $0.011 < c < 0.050$, $0.496 < d < 0.517$ were found to be 0.548 to 0.922 GPa [6]. For comparison, PbTe hardness falls in the range of 0.339 to 0.451 GPa and Zinc antimonide has the highest hardness value of 2.24 GPa.

1.7.1.2 Young's Modulus

Young's Modulus (E) is the measure of stiffness of a material and is defined as the ratio of uniaxial stress to uniaxial strain:

$$E = \sigma/\varepsilon$$

Here σ is the stress on the material when it is subjected to strain ε and E is young's modulus. Since thermoelectric generators are subjected to thermo-mechanical stresses during operation ($\sigma = E\,\varepsilon$), Young's Modulus is an important parameter to characterize material response. For cast type LAST material Young's Modulus was measured using microindentation (indentation loads of 2.94 N and 0.49 N) and nanoindentation. Measured values ranged from 24.6 GPa to 71.2 GPa [13] for different specimens. Kosuga *et al* [14] measured Young's Modulus for hot pressed LAST material and values ranged between 27.6 and 54.2 GPa. For comparison, Young's Modulus value for PbTe is 58 GPa and SiGe has highest value of 137-145 GPa [16].

1.7.1.3 Weibull Analysis and bending strength

For brittle materials Weibull modulus is a measure of the distribution of flaws in the material which is used to obtain information about the scatter in strength expected from a set of specimen [13]. Bending strength (or fracture strength) represents upper limit of normal stress at which fracture or plastic deformation of material takes place. The Weibull relationship for fracture strength distribution is given as:

$$\ln\ln(1/(1-P_f)) = m\ln(\sigma/\sigma_o) = m\ln\sigma - m\ln\sigma_o$$

Here m is Weibull modulus, σ_o is a scaling factor and P_f is probability of failure.

Weibull modulus for LAST material was found to be 3.16 which is a small number that corresponds to extensive scatter in fracture strength whereas desirable modulus range is 10-30. The bending strength for a cast type LASTT material was measured to be 15.3 MPa and for hot pressed LAST material its value was determined to be 51.6 MPa [16].

For comparison, the bending strength for Bi_2Te_3 ranges from 8 to 166 MPa. No bending strength data could be found for PbTe material.

1.8 Calculation for thermoelectric generator out put and efficiency with and without contact resistance

Min and Rowe have described the effect of contact resistance in comparison to ideal module calculations [3] for a thermoelectric generator. For an ideal module power output P is given by

$$P = \frac{(2\alpha dT)^2}{4R} \tag{14}$$

Here dT is the temperature difference between hot side and cold side of module, α is Seebeck coefficient and R is the total resistance of the module given by

$$R = 2\rho\frac{L}{A} \tag{15}$$

Here L is the length, A is the area of thermoelement and ρ is electrical resistivity.

Replacing R in equation will give

$$P = \frac{AdT\alpha^2}{2L\rho} \tag{16}$$

To account for thermal and electrical contact resistances:

$$P_r = \frac{P}{(1+n/L)(1+2rw)^2} \tag{17}$$

here

$$(1+2rw) = \Delta T / dT \tag{18}$$

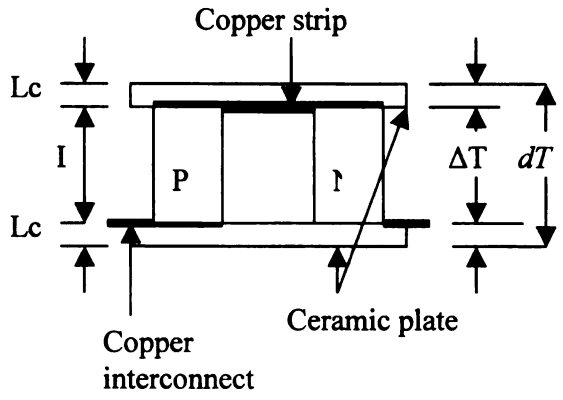

Figure 1-1. Thermoelectric unicouple.

Here ΔT is the temperature difference when two alumina plates are attached to top and bottom of the module and $r = \lambda/\lambda c$ where λ is thermal conductivity of thermoelements and λc is thermal conductivity of contacting layers. Also $w = Lc/L$ where Lc is the thickness of contacting layer as shown in Figure 1-1. In equation (17) term n/L is taken from the expression:

$$R_a = 2\rho\frac{L}{A}\left(1+\frac{n}{L}\right) \tag{19}$$

Here $R_a = R + R_c$ and $R_c = 4\rho_c/A$ and $n = 2\rho_c/\rho$ where R_c is electrical contact resistance and ρ_c is contact resistivity. The efficiency of an ideal thermoelectric generator is given by

$$\eta = \left(\frac{T_h - T_c}{T_h}\right)\left[2 - \frac{1}{2}\left(\frac{T_h - T_c}{T_h}\right) + \frac{4}{ZT_h}\right]^{-1} \tag{20}$$

Efficiency of a realistic thermoelectric generator including thermal and electrical contact resistance is given by:

$$\eta=\left(\frac{T_h-T_c}{T_h}\right)\left\{(1+2rw)^2\left[2-\frac{1}{2}\left(\frac{T_h-T_c}{T_h}\right)+\left(\frac{4}{ZT_h}\right)\left(\frac{1+\frac{n}{L}}{1+2rw}\right)\right]\right\}^{-1} \tag{21}$$

Here Z is thermoelectric figure of merit and T_h and T_c are hot side and cold side temperatures respectively.

Cobble [3] has given a description of thermoelectric efficiency with and without including contact resistance. The efficiency of a thermoelectric generator without contact resistance is given by

$$\eta = P/Q \tag{22}$$

Where electrical power out put is

$$P=I^2R_o \tag{23}$$

And heat input is given by

$$Q=K\Delta T+\alpha TI-\frac{1}{2}I^2R \tag{24}$$

Following relationships are used for above equations:

$$I=V/R_t \tag{25}$$

Where V is open circuit voltage and R_t is total resistance given by

$$R_t = R+R_o \tag{26}$$

If λ is thermal conductivity then total thermal conductance is

$$K=\lambda_n\gamma_n+\lambda_p\gamma_p \tag{27}$$

here

$$\gamma_i = A_i / L_i \quad , i = n, p \tag{28}$$

If we define

$$\Delta T = T_h - T_c \tag{29}$$

and

$$\alpha = \left|\alpha_n\right| + \left|\alpha_p\right| \tag{30}$$

$$R = \rho_n / \gamma_n + \rho_p / \gamma_p \tag{31}$$

$$V = \alpha \Delta T \tag{32}$$

$$\mu = R_o / R \tag{33}$$

We define Carnot efficiency as

$$\eta_c = \Delta T / T_h \tag{34}$$

The expression (22) can be written as

$$\eta_t = \frac{\mu \eta_c}{\left[KR(\mu+1)^2 / \alpha^2 T_h + (\mu+1) - \eta_c / 2 \right]} \tag{35}$$

In above expression

$$KR = \lambda_n \rho_n + \lambda_n \rho_p \Psi + \lambda_p \rho_n / \Psi + \lambda_p \rho_p = KR(\Psi) \tag{36}$$

where $$\Psi = \gamma_n / \gamma_p \tag{37}$$

Thus $$\eta_t = \eta_t(\mu, \Psi) \tag{38}$$

Thermoelectric figure of merit is given by

$$Z = \alpha^2 / KR = Z(\Psi) \tag{39}$$

Efficiency is then given by

$$\eta_t = \frac{\mu\eta_c}{\left[(\mu+1)^2/ZT_h + (\mu+1) - \eta_c/2\right]} \tag{40}$$

For thermoelectric efficiency with contact resistance included the input heat in expression (24) is now given by

$$Q = K\Delta T + \alpha T_h I - \frac{1}{2}I^2R - I^2R_{ch} \tag{41}$$

With total resistance R_t given by

$$R_t = R + R_o + R_c \tag{42}$$

and

$$R_c = R_{ch} + R_{cc} = R_{ch1} + R_{ch2} + R_{cc1} + R_{cc2} \tag{43}$$

Let us define

$$\delta = \delta_c = R_c/R \quad \text{and} \quad \delta_{\text{ch}} = R_{ch}/R \tag{44}$$

Efficiency is now given as

$$\eta_t = \frac{\mu\eta_c}{\left[KR\left(\mu+1+\delta^2\right)/\alpha^2T_h + (\mu+1+\delta) - \varphi_c\eta_c/2\right]} \tag{45}$$

We can write above expression in terms of figure of merit Z

$$\eta_t = \frac{\mu\eta_c}{\left[(\mu+1+\delta)^2/ZT_h + (\mu+1+\delta) - \varphi_c\eta_c/2\right]} \tag{46}$$

Conclusions

LAST and LASTT are promising thermoelectric materials with high ZT and good thermoelectric properties. The properties of LAST and LASTT materials have been investigated and prototype modules have been assembled for contact studies and power output characterization.

Chapter 2: Thermoelectric Module Bonding and Diffusion Barriers

Introduction

Electrical contact resistance causes a drop in thermoelectric module efficiency and overall increase in module resistance [18] so it is desirable to have low contact resistance. Typically the contact resistance should be less than the 10% of the resistance of the thermoelectric materials making up the module. The selection of a suitable hot side contact material depends on various factors which include high thermal and electrical conductivity and coefficient of thermal expansion (CTE) matching with the thermoelectric material. Yamashita *et al* [19] studied the effect of different electrodes (Cu, Ag, Zn, Ni, Pt, Au, Mo, Al) work function on the effective Seebeck coefficient of bismuth telluride compounds and found that it had negligible effect. They also found that both n-type and p-type legs display similar (linear) behavior for all electrode types; indicating ohmic contacts being formed in all cases. Another important consideration is the diffusion coefficients of the electrode elements into the thermoelectric material which is governed by Fick's laws and depends upon flux concentration gradients. Some materials like Cu quickly diffuse in bismuth telluride and deleteriously alter the thermoelectric properties of Bi_2Te_3. To avoid this, diffusion barriers are commonly used and have been investigated as part of this research effort for LAST and LASTT materials. Thermoelectric bonds should be able to survive thermal cycling and remain stable at high temperatures. In this lab we have experimented with diffusion bonding, soldering, liquid

contact with InGa and spring loaded modules. Here I will discuss solder and diffusion bonding results.

2.1 Diffusion Bonding

Diffusion bonding is used to bond metals with metals, alloys and ceramics. The diffusion mechanism involved in this bonding takes place along grain boundaries and through vacant lattice sites and can be described by:

$$D=D_0 e^{(-E/kT)}$$

Here D_0 is diffusion coefficient and it represents the amount of solute migrating across a unit cube of solvent in unit time with unit concentration gradient [20]. E is the activation energy required to move atoms from one site to another. This expression shows that diffusion is temperature dependent process. During diffusion bonding mating surfaces are pressed together and heated to bond surfaces through interdiffusion of atoms across this interface. Pressure and heat during bonding helps to eliminate voids at the surfaces which are filled by diffusion. These voids may also contain surface oxides, which are purged during the process. This process is carried out in an inert or reducing atmosphere to help avoid oxidation. The interface bond can be mechanically strong or weak depending upon the materials used. The applied temperature is usually $0.75Tm$ where Tm is the melting point of lower melting point material being bonded [21]. However, the bonding temperature at the same time should be high enough to enable dissolution of surface oxide films.

In some cases solder bonding is used instead of diffusion bonding when an appropriate solder can be found. Some diffusion bonding processes also involve a

transient liquid phase [21]. Often this interlayer is needed to bond dissimilar metals or alloys. At high enough temperature this intermediate layer becomes molten. A liquid also posses surface energy and tend to draw up into droplet shapes where its surface energy is higher than its volume energy. Surface of liquid acts as elastic skin and is in the state of tension where under isothermal conditions surface energy is equal to surface tension. The liquid will wet the surface if all three surface tension forces are in equilibrium. These surface tension forces are between the liquid droplet and solid substrate, liquid droplet and the atmosphere and the substrate and the atmosphere [22]. When an intermediate layer of filler or solder material is used, it will form intermetallic phases after heating and this part of the bond will have different mechanical strength, often less than the original material. In bimetallic systems, formation of intermetallic compounds can be accompanied by an increased porosity that takes place due to different rate of diffusion of species and the layer thickness is less than 100μm [22]. Good wetting of the surface enhances the formation of filler between layers and results in good bond. For diffusion bonding the mating surfaces should be smooth to minimize the size of interface voids. Moreover, if oxides can not be purged in a reducing atmosphere during bonding then plastic flow of asperities should be strong enough to scrub away the surface to remove oxides by mechanical dispersion [21]. Grain boundary diffusion can also play an important role in diffusion bonding such that an increased number of grain boundaries enhance atomic diffusion across the interface [23]. More than one mechanism are involved in diffusion bonding [22] that include creep of the surface asperities, plastic yielding of surface asperities, volume and surface diffusion and as mentioned above, grain boundary diffusion at the bond interface. The four main process variables are

temperature, pressure, time and surface condition as creep and diffusion are temperature and time dependent. Plastic deformity depends upon temperature, pressure and the materials being bonded. Surface asperities' height and frequency determines the initial surface contact and influence the bonding rate [22]. In our experiments an interlayer is used that melts and fills the voids, wets and disrupts thin oxide films on mating surfaces for a better bond.

2.2 Diffusion Furnace

Bonding experiments are carried out in a three zone diffusion system [23] designed and assembled by Jonathan D Angelo. The three zone furnace has a 12 inch long center zone with 6 inch zones one on each side through which an 8' long quartz tube extends. Approximately 2' of tube extends out each end of the furnace to allow for cooling of the tube before the O-ring seals on the ends of the tube. Quartz tube has an inside diameter of over 5" to accommodate larger module assembly. The bonding range for LAST based materials is ~ 700 °C. Furnace consists of 8 feet long quartz tube. Quartz tube end caps provide a vacuum seal and the chamber is evacuated using a dry pump to less than 10 mTorr vacuum. The 9" isoflange end caps can be easily removed and angle brackets are provided to hold them in place for back filling with Ar gas. The vacuum pump and pressure gauge are attached to the vacuum port end-cap and a valve is used to isolate the furnace from the vacuum pump. Three PID controllers are used to control the temperature of the three zones. The controller can be set to ramp and soak time as desired by user and typical ramp time is 4 hrs followed by soak time of 4 hrs. To maintain

isothermal region and further isolate the center zone circular disks of stainless steel are inserted in the quartz tube as heat shield.

2.3 Room Temperature Scanning Probe system

For room temperature scanning of thermoelectric material's electrical conductivity and contact resistance of unicouples a room temperature scanning probe system

(RTSP) is used as shown in Figure 2-1 below. This system gives voltage vs. position slope (*dV/dx*) of TE specimen under test. The slope is then used to calculate electrical conductivity using the following equation:

$$\sigma = \frac{1}{\frac{dV}{dx}} \frac{1}{Area} S/cm \qquad (1)$$

System consists of one Keithly 2004 current source and Keithly 2002 nanovoltmeter. Current is sourced through the sample at approximately 33 Hz with 50% duty cycle square wave function. Voltage is measured by a probe scanning along the sample surface. The current is flipped approximately 20 times at each measurement point. This is done to avoid any Seebeck voltage development in the sample. It also cancels out voltage offset in measurement wires developed due to voltage gradient. The system has three axis (X, Y, Z) of motion to adjust the sample and then scan the measuring pin across the sample.

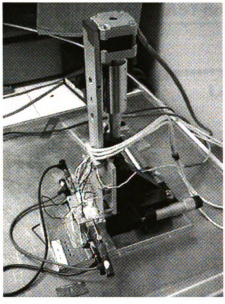

Figure 2-1. Room temperature scanning probe system.

2.4 LAST to LAST bonding

To circumvent the issue of CTE mismatch, it is ideal to use a hot side electrode with same coefficient of thermal expansion (CTE) as the thermoelectric (TE) element. This makes LAST a suitable candidate as hot side electrode. However, LAST has inherently low thermal and electrical conductivity compared to metals like Cu, Ag or Fe. It is possible to heavily dope LAST to increase thermal and electrical conductivity but then it might change the coefficient of thermal expansion of material. To check this hypothesis two pieces of thermoelectric material were bonded using an interface paste consisting of Sb powder + LAST powder mixed in ethylene glycol. Bonding was carried out at 700 ^{o}C with a 2 hr soak time.

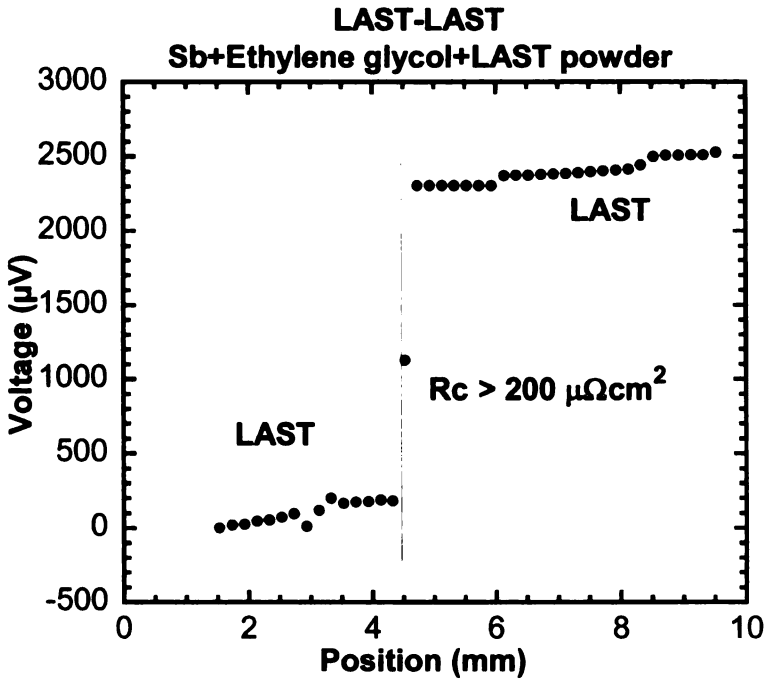

Figure 2-2. LAST to LAST bonding.

Figure 2-2 above shows an n-type to n-type LAST material bonding experiment. Room temperature scan indicates a high resistance bond. Mechanically it was weak bond and broke off easily.

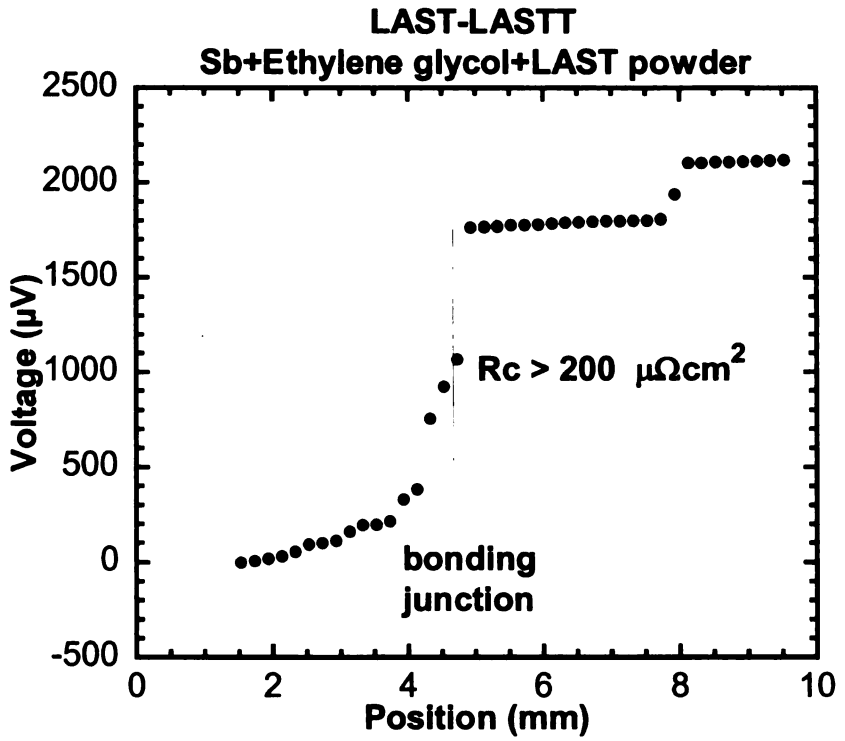

Figure 2-3. LAST-LASTT bond.

Figure 2-3 above shows a p-type to n-type cast materials bond at ~ 700 °C. Antimony (Sb) and LAST powder mixed in ethylene glycol were used as intermediate bonding material and bonding time was 2 hrs. It appears that Sb and LAST did not melt and diffuse during diffusion bonding process. Very high contact resistance at junction makes this unsuitable for any application.

Figure 2-4 below shows two p-type cast samples bonded at ~ 700 °C in the same run as above. In case of p-type samples a mixture of ethylene glycol and LAST powder reacts with thermoelectric material during bonding process and allows interdiffusion to make a successful bond. The small kink at the junction may be due to interdiffusion of extra antimony (Sb) into joining materials. It can be seen that slope is different at either

side junction indicating different electrical conductivities. It may be due to antimony diffusion to different batch materials (ETP 47 and ETP 51).

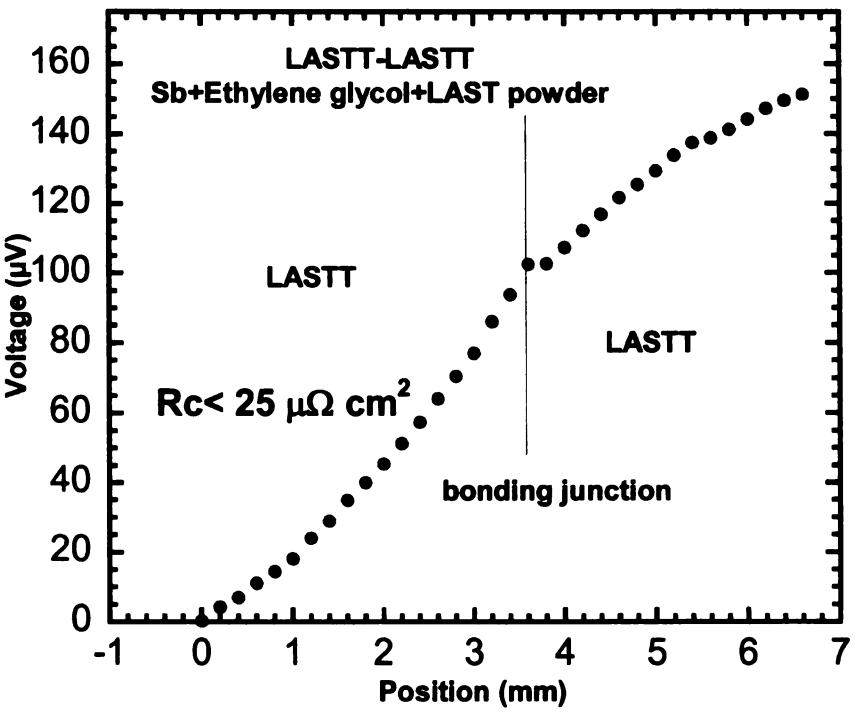

Figure 2-4. LASTT to LASTT bond using Sb and LAST powder.

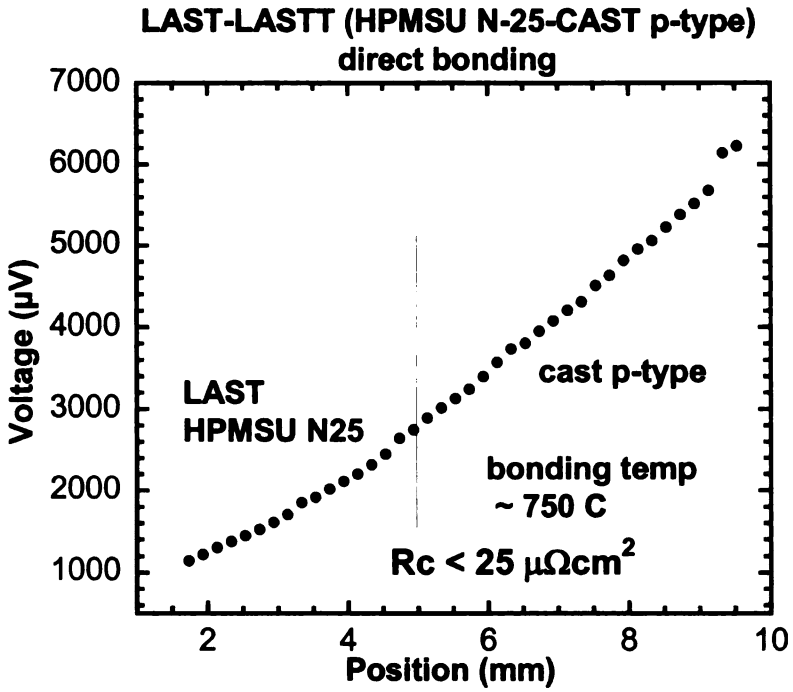

Figure 2-5. LAST-LASTT direct bonding.

Figure 2-5 above shows direct bonding between n-type hot pressed samples with a cast p-type sample with bonding temperature ~ 700 °C for 2 hrs where a low resistance bond is obtained as evident by a negligible jump in voltage across the interface. Although this is a n-type to p-type junction, no interlayer formation is observed and one ohmic interface is measured. The same module was tested in the high temperature voltage profiling system where scan taken at 700 K again show low contact resistance as seen in Figure 2-6.

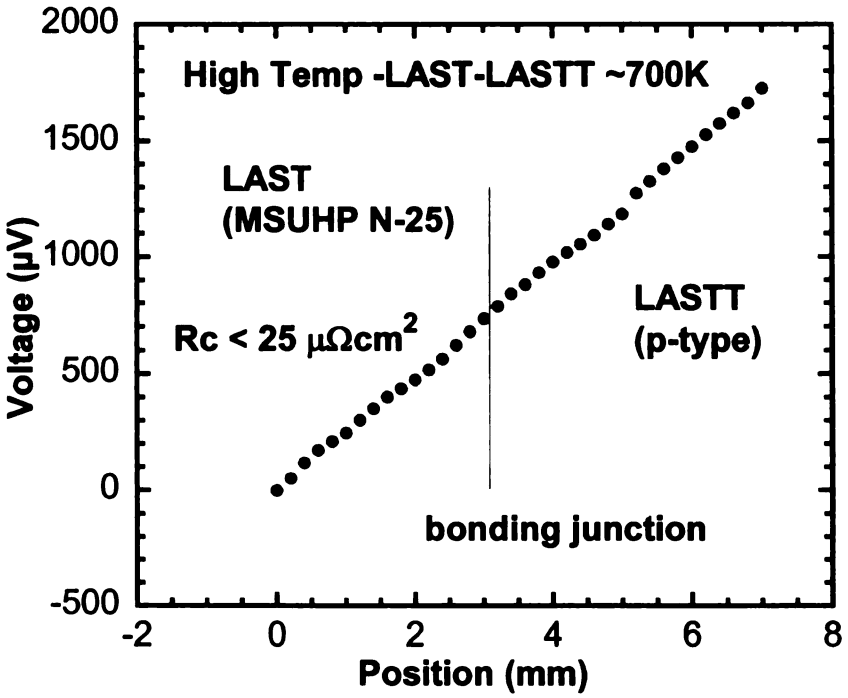

Figure 2-6. High temperature scan for LAST to LASTT bonding.

A number of bonding experiments were carried out to directly diffusion bond two p-type samples together without any interlayer however efforts proved to be unsuccessful and the bonds were often too fragile and broke off easily.

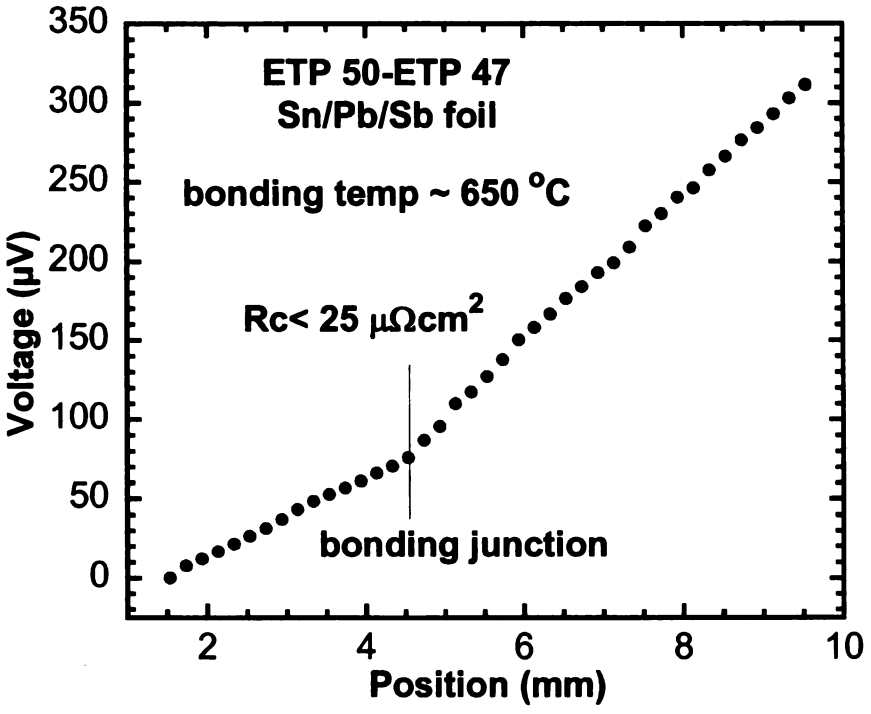

Figure 2-7. Room temperature voltage scan of the LASTT to LASTT bond using a solder foil at the interface.

For the next experiment a solder foil was used as an interface bonding material consisting of Sn/Pb/Sb solder foil 0.006 mm thick (Goodfellow) placed between two cast p-type samples and bonded at ~ 650 °C. A low resistance bond was achieved as seen in Figure 2-7. A similar experiment was carried out using a Sn/Pb/Sb foil but this time bonding temperature was 750 °C. As we can see from the room temperature scan in Figure 2-8 a low resistance bond is obtained and there is no kink at the junction which is slightly different from previous plot.

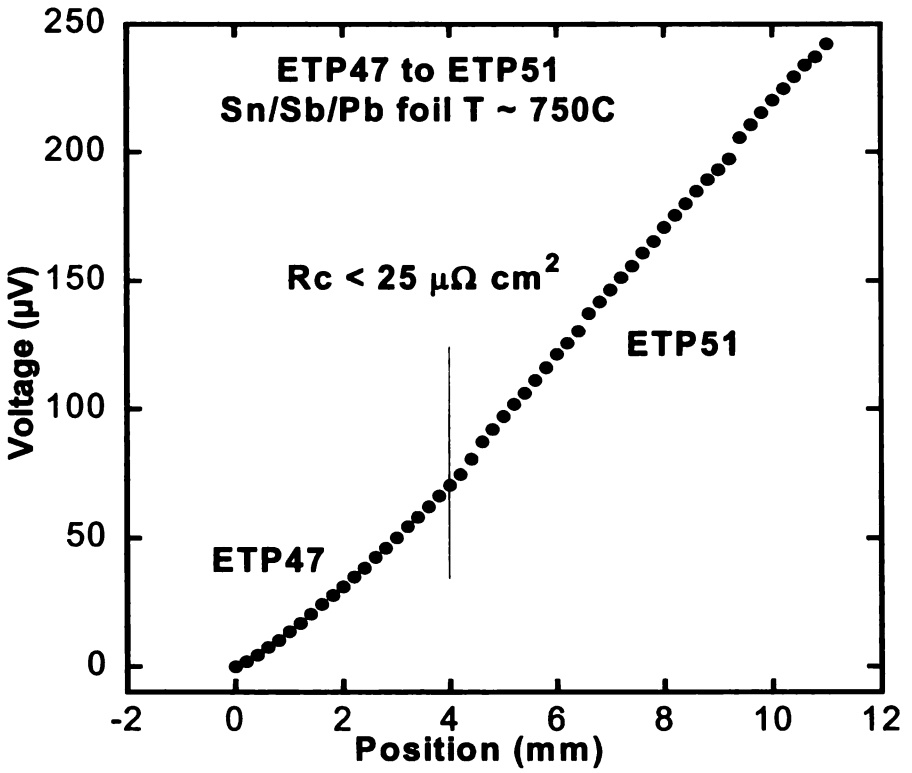

Figure 2-8. ETP 47 bonded to ETP 51 using a Sn/Sb/Pb solder foil.

Figure 2-9 shows a bond between two p-type cast samples at ~ 650 °C. A low melting point Cerromatrix solder ($Bi_{48}Pb_{28.5}Sn_{14.5}Sb_{9.0}$) was used between the samples as an interface bonding layer. The initial process was carried out on a hotplate under ambient conditions to wet the sample mating surfaces. Sample was then placed inside diffusion furnace and bonded at 650 °C and 800 Torr pressure. The solder was expected to reflow under the high temperature conditions and completely wet the mating surfaces but room temperature scan indicates that it is a high resistance bond. However, inspection of the interface under an optical microscope revealed significant number of voids and gaps at

the interface suggesting poor wetting and/or oxides at the interface. From above experiments it appears that solder foil is a better choice as intermediate bonding material.

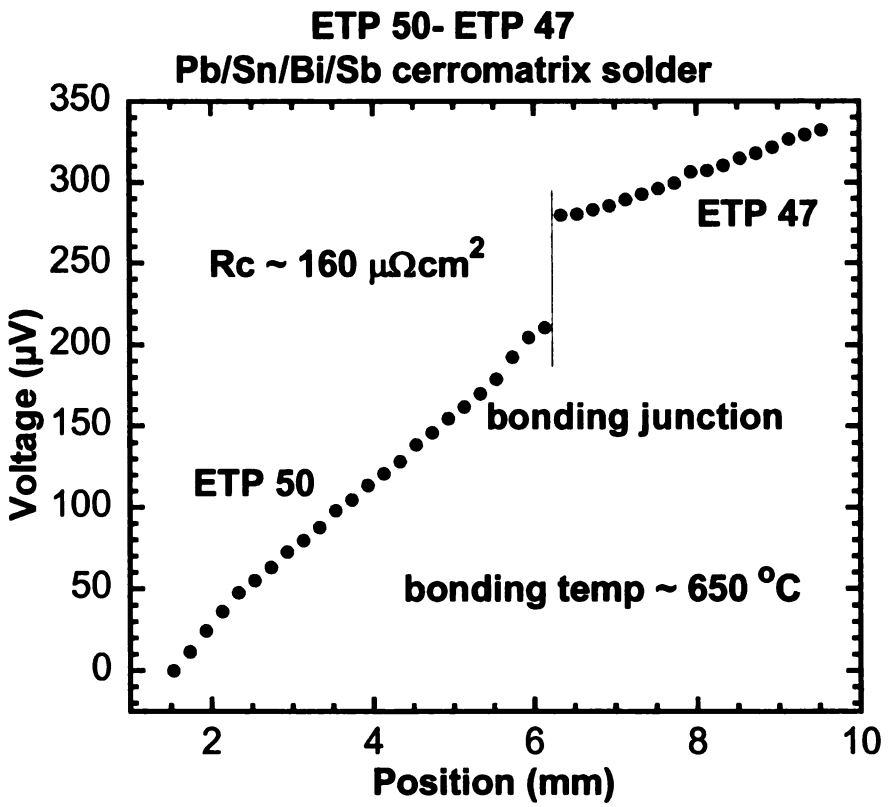

Figure 2-9. LASTT to LASTT bond using solder.

LASTT bonding with hot pressed material using SnTe powder also showed low contact resistance junctions. For this powdered Sn50% by weight was added to Te50% by weight and mixed for about 15 minutes by shaking in a glass container. The mixture was then layered between LASTT and an n-type hot pressed LAST leg. Bonding was carried out at ~ 750 °C for about 30 minutes. As shown in room temperature scan in Figure 2-10 it is low resistance junction. Since hot pressed samples have very low room temperature electrical conductivity (< 100 S/cm) as compared to cast p-type samples which have

conductivity in the range of 1800 S/cm, the hot pressed sample has a relatively steep slope on the voltage vs. position plot of Figure 2-10.

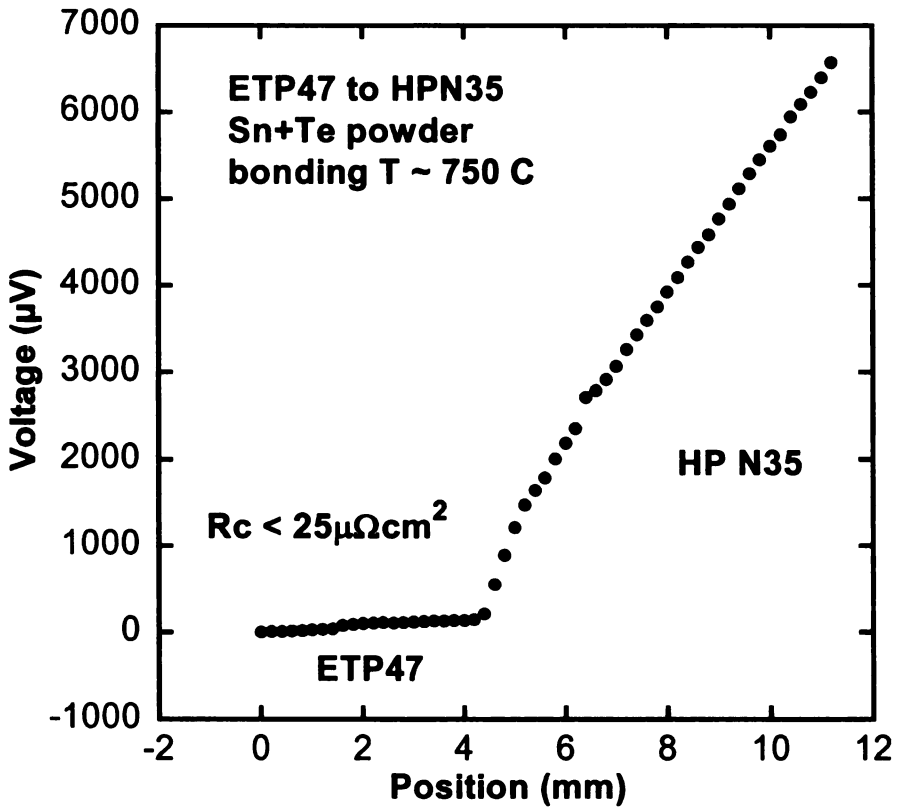

Figure 2-10. ETP 47 bonded to HPMSU 35 using SnTe powder.

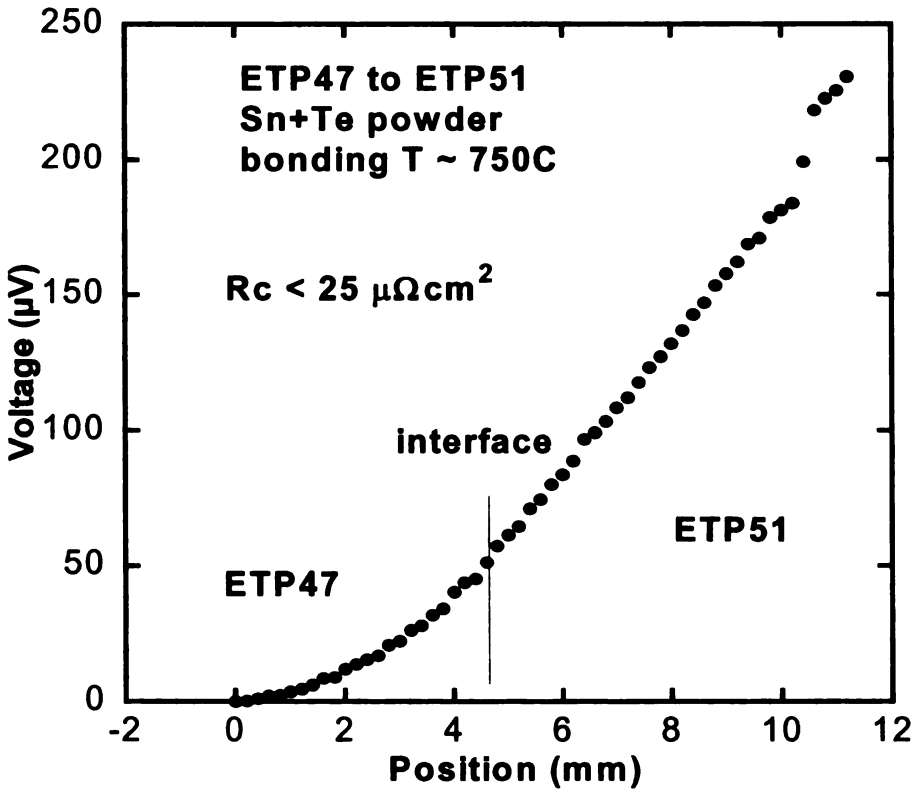

Figure 2-11. ETP 47 bonded to ETP 51 using SnTe powder.

Sn and Te powder mixture was also tried for LASTT to LASTT bonding and it produced low resistance bonds as shown in the Figure 2-11 above. The results for LAST to LAST and LASTT bonding are summarized in Table 2-1 below.

Table 2-1. LAST to LAST bonding summary.

TE Material	Bonding material	T (°C)	comments
Cast LAST Cast LAST	Sb+ ethylene glycol + LAST powder	700	High resistance bond
Hot pressed n-type Cast LASTT	Direct bonding	700	Low resistance bond
Cast LAST Cast LASTT	Sb+ ethylene glycol +LAST powder	700	High resistance bond
Cast LASTT Cast LASTT	Sb+ ethylene glycol +LAST powder	700	Low resistance bond
Cast LASTT Cast LASTT	Pb/Sn/Sb foil	650	Low resistance bond
Cast LASTT Cast LASTT	Cerromatrix Solder	650	High resistance bond
Hot pressed n-type Cast LASTT	Sn+Te powder	750	Low resistance bond
Cast LASTT Cast LASTT	Sn+Te powder	750	Low resistance bond

2.5 Room temperature scan of stainless steel bonded unicouples

Initial experiments in the bonding furnace included direct bonding of stainless steel 316 with cast LAST thermoelectric 5mm x 5mm x 7mm legs without any intermediate bonding material. Six unicouples were scanned for room temperature contact resistance. Unicouples were bonded by Jonathan D'Angelo and analysis was carried out in collaboration with Jarrod Short in this lab.

Figure 2-12. Six unicouples tested for room temperature contact resistance. (a) Low resistance p-type bond (b) N-type sample cracked (c) High resistance bond for both types of legs. (d) Low resistance bond for n-type. (e) P-type sample cracked (f) High resistance bond for both legs.

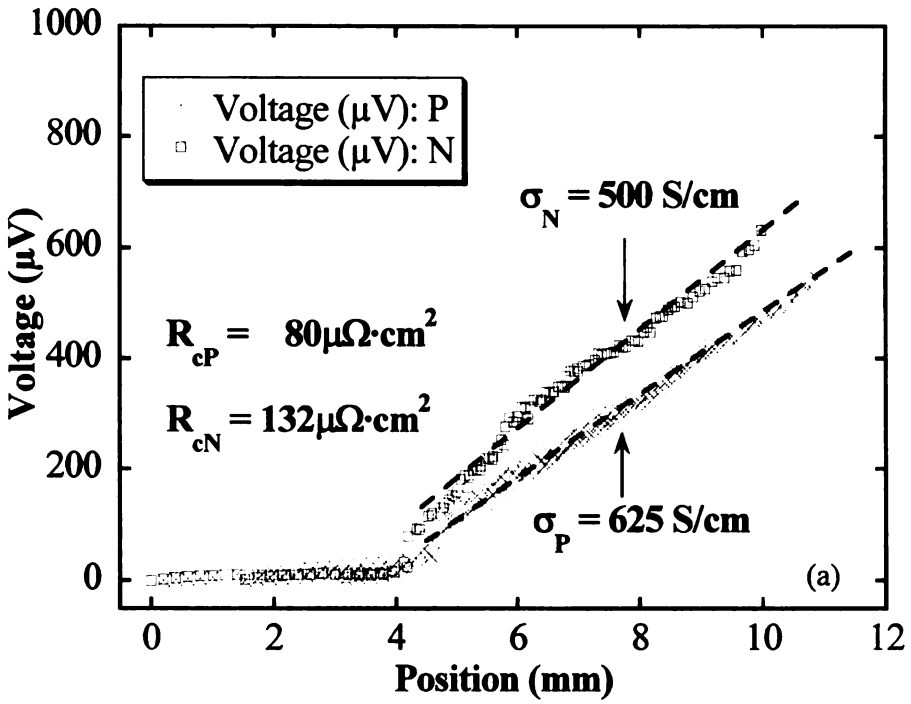
Voltage (μV): P
Voltage (μV): N
σ_N = 500 S/cm
R_cP = 80μΩ·cm²
R_cN = 132μΩ·cm²
σ_P = 625 S/cm
(a)
Voltage (μV)
Position (mm)

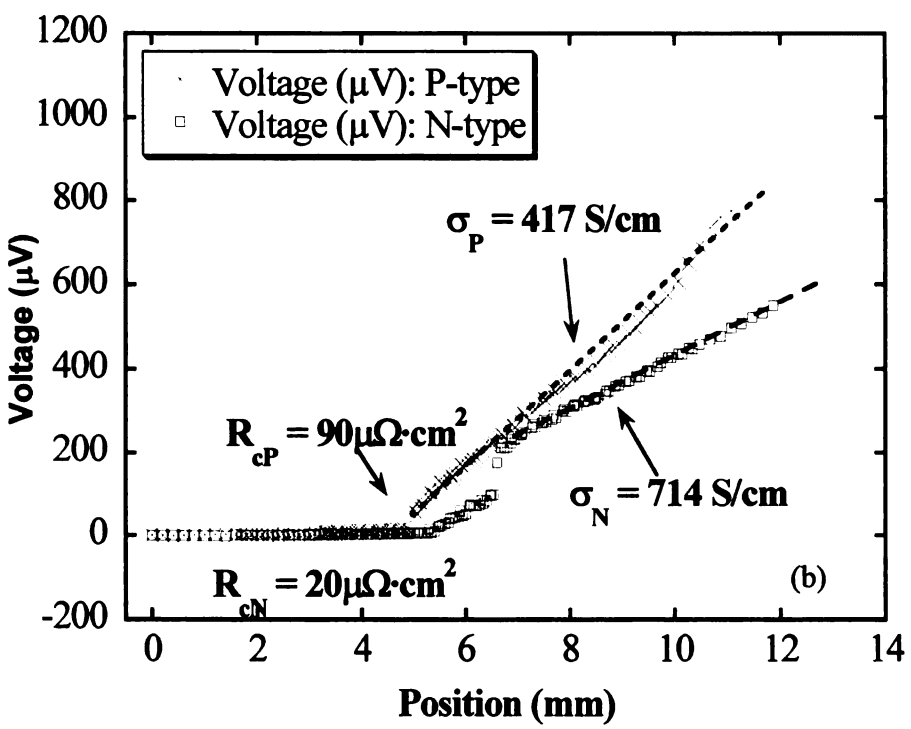
Voltage (μV): P-type
Voltage (μV): N-type
σ_P = 417 S/cm
R_cP = 90μΩ·cm²
σ_N = 714 S/cm
R_cN = 20μΩ·cm²
(b)
Voltage (μV)
Position (mm)

Figure 2-12. Continued.

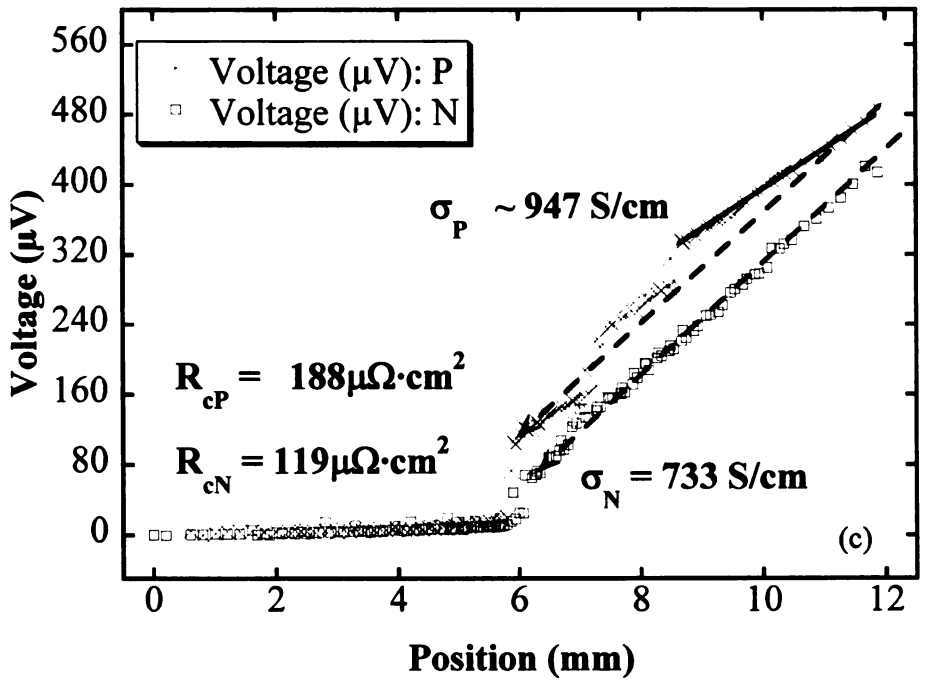

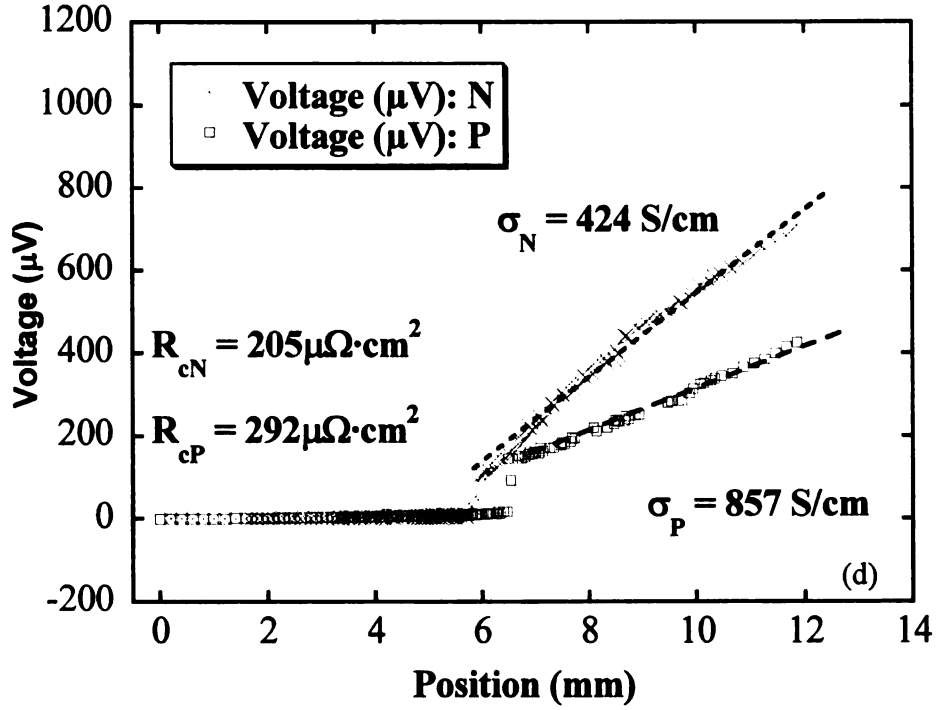

Figure 2-12. Continued.

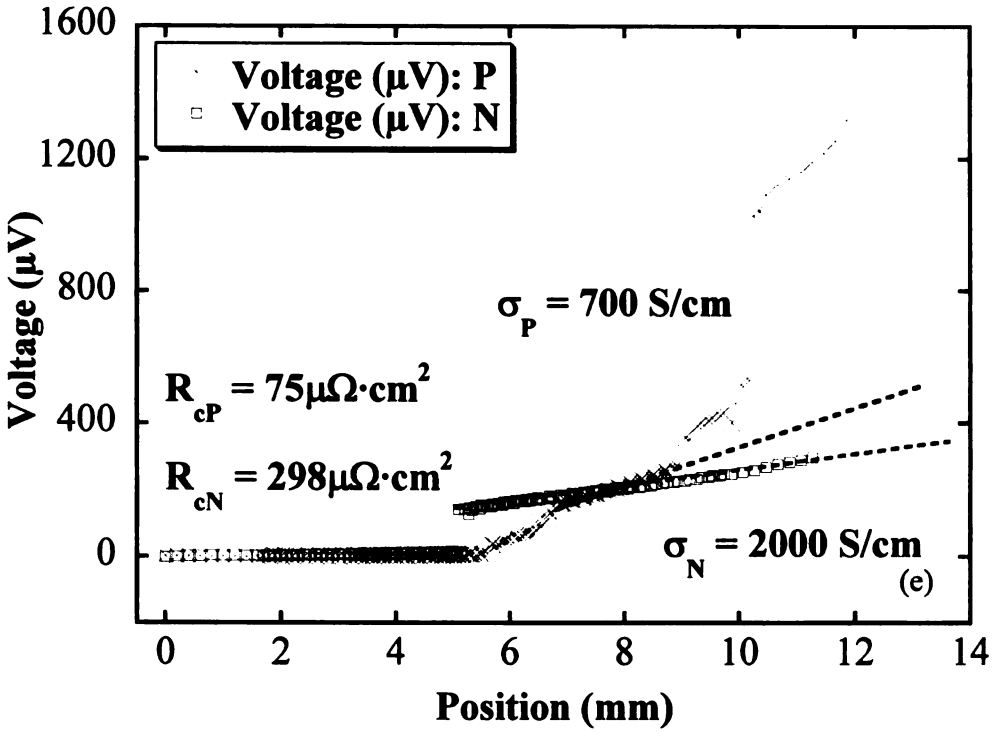

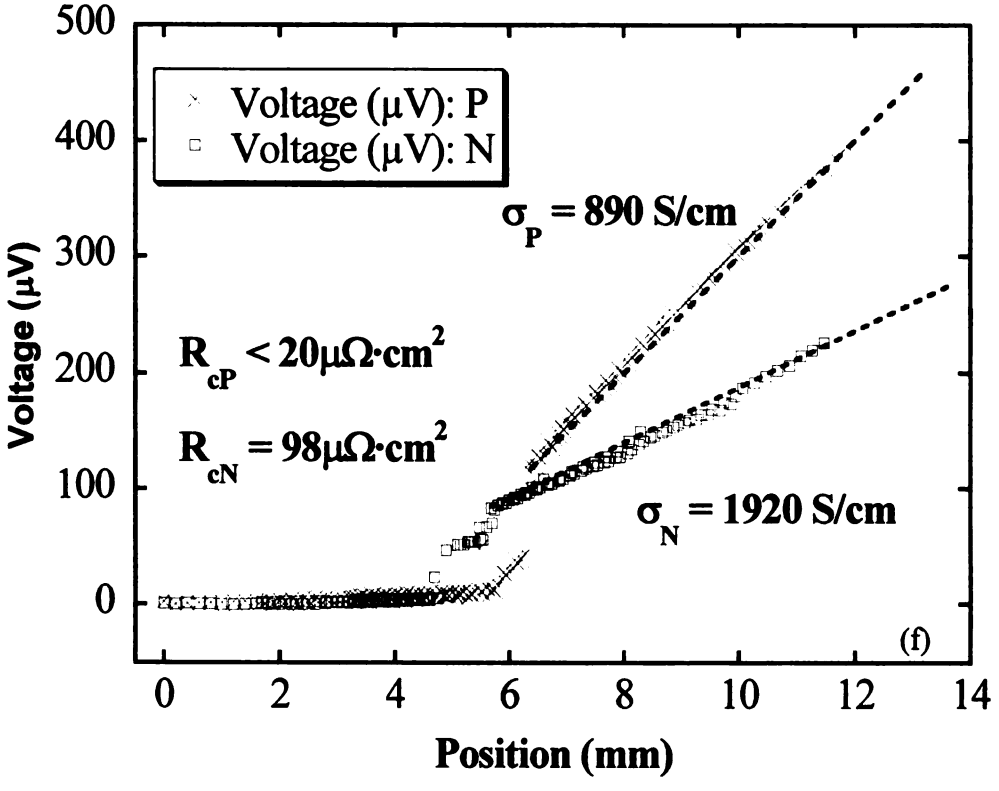

Table 2-2 below summarizes the results for room temperature scanning of direct bonding to stainless steel 316 to LAST material.

Table 2-2. Unicouple contact resistance values.

Unicouple #	σ_N (S/cm)	σ_P (S/cm)	R_n (mΩ)	R_p (mΩ)	R_{cn} ($\mu\Omega\cdot cm^2$)	R_{cp} ($\mu\Omega\cdot cm^2$)	Cracks?	R_t (mΩ)
1	500	625	6.3	5.1	130	80	No	22
2	714	417	4.4	7.6	< 20	90	N	19
3	733	947	4.3	3.3	120	200	P	11
4	424	857	7.5	3.7	200	300	No	23
5	2000	700	1.6	4.5	300	80	P	8
6	1920	890	1.7	3.6	100	< 20	Both	6.6

It can be seen that there is no clear pattern for n-type or p-type contact resistance, either one can be high in a given unicouple making it a high resistance module. Two out of six modules have less than 10 (mΩ) total resistance. Four out of six modules have cracks after bonding as shown by a sharp increase in the voltage scan. These cracks may have occurred during cutting of the legs, or during the bonding process. However in high temperature contact resistance scans, direct stainless steel bonded modules have shown higher resistance at the junction as shown in Figure 2-13.

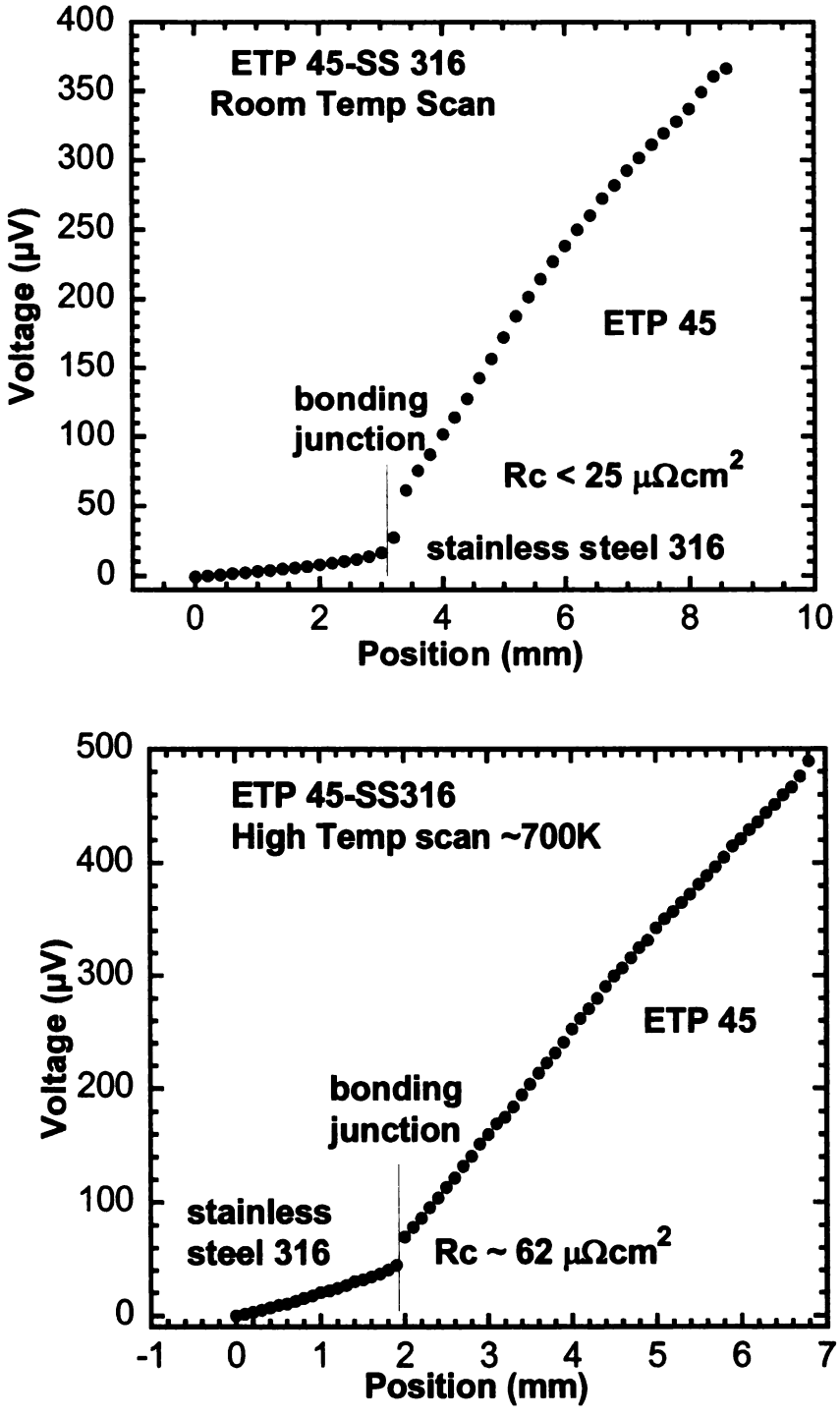

Figure 2-13. Room temperature and 700 K scan indicating increased contact resistance.

2.6 Soldered vs. silver paste contacts

As mentioned in previous section room temperature scanning of thermoelectric legs provides important information about contact resistance and material integrity. Contacts for these measurements were made to the samples using a soldering iron. The rapid heating of the sample in the vicinity of the soldering iron was a suspected cause of cracking. To test this hypothesis six legs were first solder contacted and measured. These were compared with six legs from same batch (ETP 38) which were contacted using silver paste. Since silver paste is applied at room temperature no thermal shock to the sample occurs. Figure 2-14 below shows scan from six legs using soldering iron at ~ 477 K. Four out of six samples showed cracks.

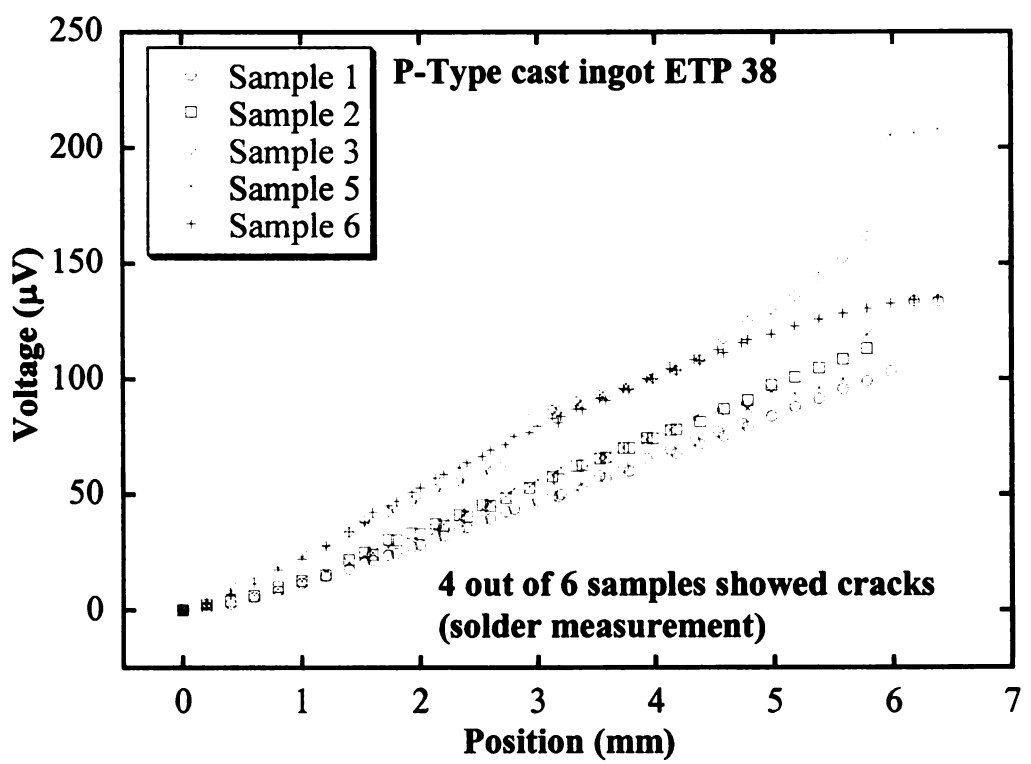

Figure 2-14. Soldered contact thermoelectric (ETP 38) legs.

Figure 2-15 shows six samples contacted using silver paste. It can be seen that only one out six samples showed cracks as compared to four out of six for soldered contact samples.

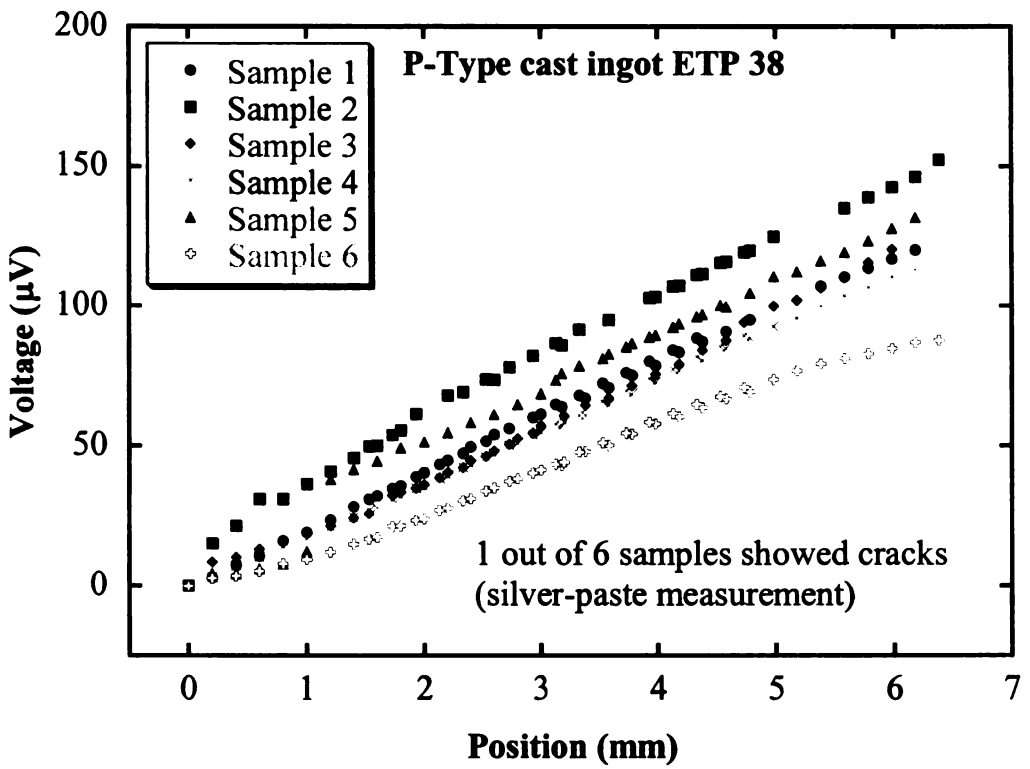

Figure 2-15. Silver paste contact measurements for six samples.

Although silver paste shows better results for room temperature scanning contacts, soldered contact are preferred for unicouple cold side junctions because of its superior mechanical strength and low contact resistance as compared to silver paste. To circumvent thermal shock due to the soldering iron we investigated the use of a hot plate and a slower heating rate. The cold side electrode (Cu or Ni) was then first coated with solder and placed on top of hot plate. The TE leg was then placed on top of the soldered electrode and the hot plate was switched on. The hot plate was heated slowly by

gradually increasing the set point. Using this process a hot pressed sample was bonded to Ni and Cu electrodes as shown in Figure 2-16 and Figure 2-17 respectively.

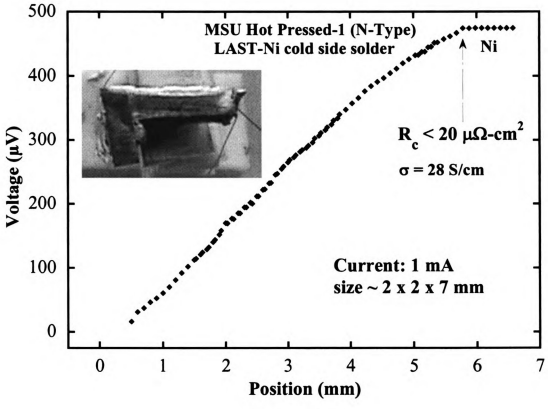

Figure 2-16. Hot pressed sample bonded to Ni electrode using solder.

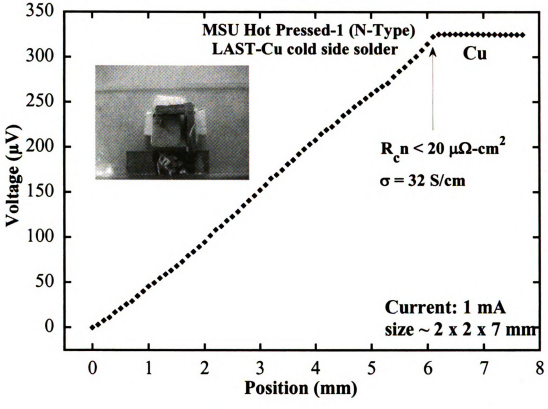

Figure 2-17. Hot pressed sample bonded to Cu electrode using solder.

Three samples from ETP 38 cast p-type were solder contacted for room temperature scanning using hotplate and showed no cracks as shown in Figure 2-18 below.

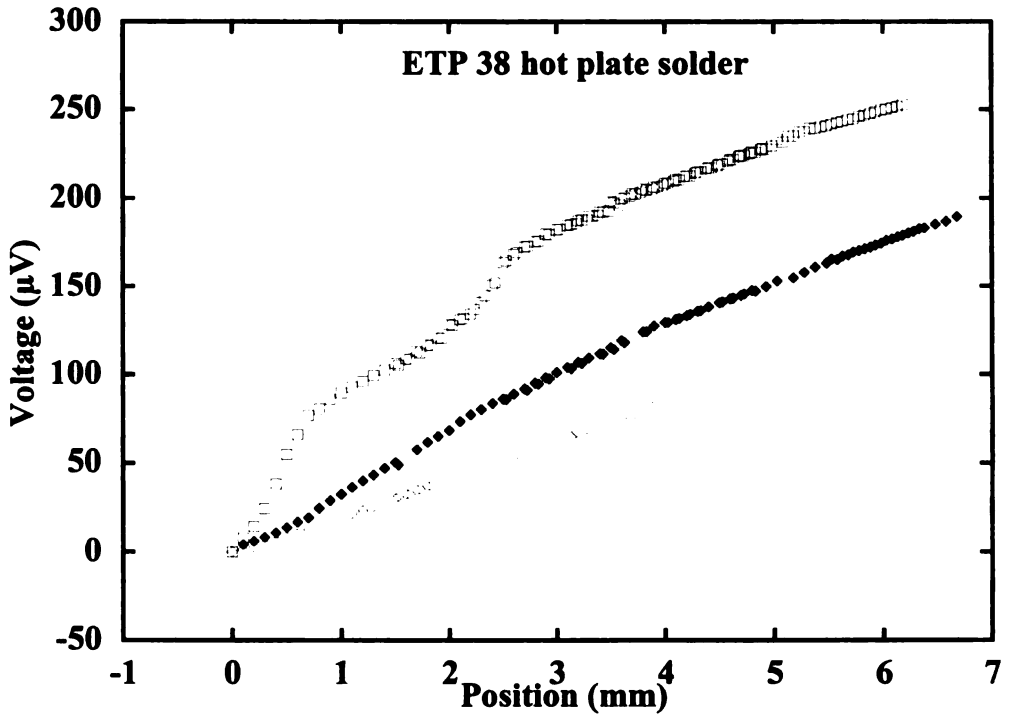

Figure 2-18. ETP 53 samples solder contacted on hot plate.

2.7 Diffusion barriers in thermoelectric – previous efforts

As mentioned above it is desirable to have low contact resistance between the thermoelement and electrode. The hot side contact should be able to withstand thermal cycling thus electrodes with thermal expansion near that of the thermoelectric materials are desired. It is well known that element like Cu, Ni and Cr can degrade properties of bulk TE materials, especially telluride based thermoelements [24]. Kendall *et al* studied PbTe diffusion bonding to AIS 300 stainless steel [25]. They found the mechanical failure due to thermal expansion mismatch can be eliminated however they also discovered elements like Cr in stainless steel can diffuse into the material and deteriorate the thermoelectric properties. A thin diffusion barrier of Fe, Mo or W can help to prevent

this diffusion. Weinstein *et al* [26] used braze tin telluride between PbTe and Fe electrode. A good bond was obtained by diffusion and subsequent solidification of the tin telluride braze. It behaved well up to elevated temperatures of 600 °C. However, the braze joint failed after thermal cycling in which joint was first raised to 600 °C and then brought back to 100 °C [26]. The failure occurred at the tin-telluride-iron interface and was due to the formation of a brittle layer. The n-type PbTe was easily bonded to Fe ingot by diffusion bonding at 858 °C, which is 15 °C lower than the eutectic temperature of Fe and PbTe. Kendall *et al* [25] found that by adding a small amount of antimony the brittle layer at tin-tellurium-iron interface would not form and the joint could sustain thermal cycling. It was also found that if ferrous metal has trace amount of carbon, manganese and silicon as is the case with commercial ingots, it would generate cracks in PbTe bulk material even if the braze was good with no brittle layer. These cracks were mainly due to CTE mismatch of PbTe (21×10^{-6} in/in/°C) and iron ingot (14×10^{-6} in/in/°C). When Fe ingot was replaced by stainless steel, the problem of CTE mismatch was removed. However, it was revealed that doping agents in PbTe were eroded in the braze region when stainless steel electrode was used. The reason could be the chromium in stainless steel diffusing through molten tin-telluride and passing into bulk PbTe and then reacting with free tellurium in p-type material. This would result in increased electrical resistance [25]. Nickel also dissolves in tin telluride and reacts with PbTe. This forms a eutectic mixture and lowers the working temperature of module. The rate of diffusion is higher at the hot side and this diffusion also occurs even if braze material is not used and electrode and bulk material is bonded through diffusion bonding process. As a solution to these problems, thin 0.002 inch thick foils of iron, molybdenum and tungsten were deposited

on stainless steel electrode through diffusion bonding. Unicouple were fabricated and tested for 750 hrs and 36 thermal cycles with no degradation observed [25]. It was found that presence or absence of tin telluride braze layer had no effect on degradation of performance of thermoelectric device. Other alloys having similar range of CTE like constantan, brass, silicon bronze, aluminum bronze or beryllium copper can also be used as hot side electrodes. Although this literature shows satisfactory results but in practice PbTe thermoelectric module have been assembled with spring loaded configuration especially for space applications. Probably diffusion bond with PbTe has not been successful in long term operation.

As described above the purpose of the diffusion barrier is to prevent diffusion of contaminations from the hot side electrode into the thermoelement and at the same time prevent reaction between electrode and thermoelement. The need is to provide a barrier layer which is thin enough not to interfere as CTE mismatch between thermoelement and electrode (which are generally both chosen to have similar CTE) and at the same time thick enough to prevent diffusion of contaminants. Refractory materials are suitable as barrier layers however; these materials have very low coefficient of thermal expansion e.g. [W (4.5), Mo (4.8), Ta (6.3), Ni (7.3)] μm/m-K at 25 °C. Therefore the barrier should be thin enough that forces arising from barrier thermal properties are negligible as compared to the thermal forces exerted by larger masses of electrode and thermoelement. Krebs [27] found that even if the barrier material has larger tensile strength, but it is thin enough, it will not have deleterious effect on thermoelement and a refractory element (W, Mo, Ta) diffusion barrier of about 0.05 to 0.5 mils thickness can be used with electrode of 10 to 40 mils thickness having CTE of 18 x 10^{-6}/°C. An alternate way to address this

problem is to use an intermediate layer of a low resistance semiconductor which will allow diffusion of contaminants into the intermediate layer but will not be able to cross into the thermoelement. Contaminants will form a solid solution at the intermediate layer until the barrier layer saturates. Such barrier layer has life of about five years [27]. This was tested under accelerated condition. The barrier layer has to be thick enough to absorb contaminants and thin enough that it does not start acting as separate thermoelement with uncontrollable properties. Suitable thickness of such barriers is found to be about 10 to 20 mils [27]. Formation of such polycrystalline thermoelement barrier of same material as main thermoelement can be obtained by sputtering or vapor deposition. Probable cause of slow diffusion of contaminants into poly crystalline segment may be due to increased number of grains and therefore impurities have to take a longer path along the grain boundaries. Another way to improve the performance of TE device is to use both above mentioned permeable and impermeable layers. Impermeable layers can be of tungsten, tungsten carbide, molybdenum and silicon carbide [27]. The permeable barrier can consist of materials like bismuth-telluride, lead-telluride, (lead telluride-germanium telluride), lead-tin-telluride and alloys of (lead telluride-lead selenide) [27]. However, microcrystalline structure of permeable layer needs to be different than the bulk thermoelement. Kerbes used Ni as the bonding material between lead-telluride and stainless steel. A 0.05 to 0.15 mils thick layer of Ni was deposited on a stainless steel electrode and annealed in a reducing atmosphere for about 10 minutes at about 800 °C. This allowed the diffusion of Ni into stainless steel. Ni was then coated with tungsten layer of 0.1 to 0.5 mils thick and then another layer of nickel was deposited. Bonding was

carried out in an inert atmosphere. This formed a eutectic alloy of nickel-lead-telluride. A reasonable thickness of such an alloy is 0.1 to 0.10 mils.

2.7.1 Brass diffusion barrier coatings

The following diffusion barrier and bonding experiments were carried out in collaboration with Dr. Nuraddin Matchanov in this lab. Some materials like Mn/Pd despite having high CTE can not be used because it undergoes transformation at higher temperature (300- 350 °C) that includes volume change and high electrical resistivity [28]. Since LAST material is very close in stoichiometry to PbTe, diffusion barriers mentioned in literature can also be tested. Yellow brass with 33% zinc has CTE of ~18.9 x 10^{-6} in/in/C which is very close to LAST. Following coatings were tested on 2 mm x 5 mm x 12 mm brass pieces.

Table 2-3. Brass coatings with diffusion bonding.

Electrode coatings	**Thermoelectric material**	**Bonding material**	**T(°C)**	**comments**
Ni plated brass with Ti/Zr/Ni coating	LASTT	Pb/Sn/Sb foil	650	High resistance bond and Zn diffusion was observed around sample
Ni plated brass	LASTT	Pb/Sn/Sb foil	700	No bond
Ni plated brass	LAST	Pb50/Sn50 solder	700	Bonded but brass reacted with LAST
Brass coated with Mo. Substrate cold when coated	LAST	Pb/Sn/Sn	700	Mechanically good bond but Zn appeared on LAST. Mo film peeled off.
Brass coated with TiN	LAST	Direct bonding	700	Zn appeared on LAST
Brass coated with Ti/TiN/Ti in PLD system	LASTT	Direct bonding	650	No bond
Brass coated with Ti/TiN/Ti/Sb	LAST	Direct bonding	650	Zn appeared on LAST
Ni plated brass coated with TiN in PLD system	LAST	Direct bonding	700	No bond
Brass coated with Mo	LAST and LASTT	SnTe	720	No bond
Ni coated brass	Hot pressed LAST	SnTe	610	Good bond. Cu and Zn diffusion observed

Figure 2-19 below shows a bond between p-type cast sample and 2mm x5mm x12mm brass sample. As mentioned above brass was chosen as hot side electrode because it has a close CTE (18.9×10^{-6} cm/cm/°C) match with LASTT.

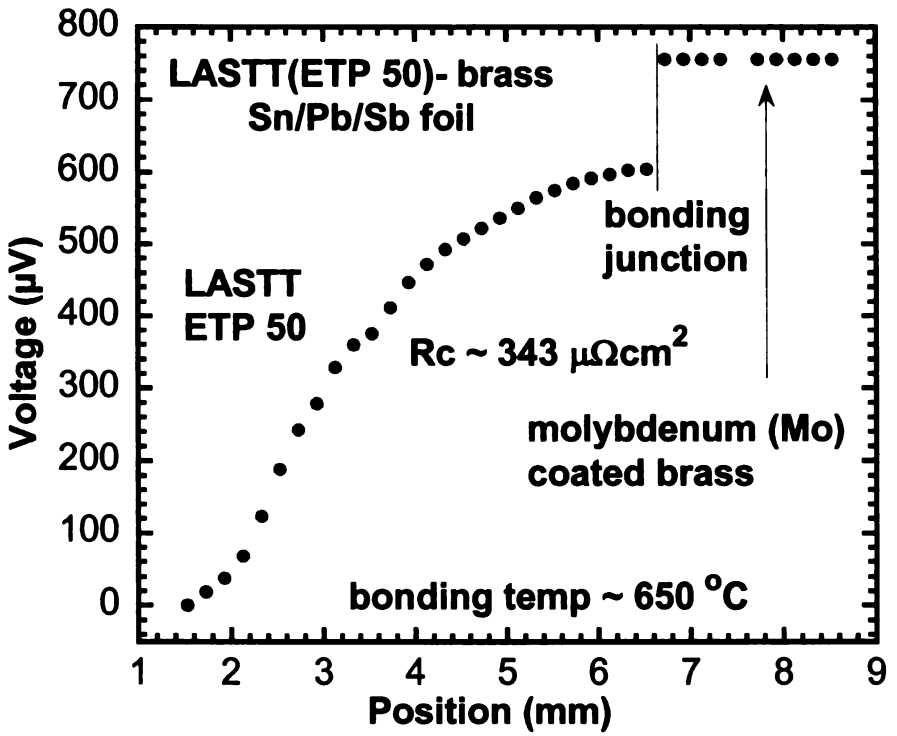

Figure 2-19. LASTT to brass bonding.

In this particular run Sn60/Pb39/Sb1 solder foil was used as intermediate bonding material and the bonding was done at 650 °C for 2 hrs in a flowing Ar/H_2 gas under 800 Torr. It is a high resistance bond and has non linear slope at the junction as shown in the plot. Similar coatings of Ti/TiN have not been able to stop Zn diffusion from brass to LAST material. Following is the EDS result (Figure 2-20) for brass/Ti/TiN/Ti/LAST bonding carried out at 720 °C for 4 hrs under Ar/H_2. EDS was carried out 4mm from the junction towards the sample. It can be clearly seen that Zn has diffused through coating on electrode into the thermoelement leg.

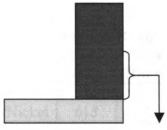

Element	Weight %	Atomic %
C K	3.98	25.12
Zn K	31.56	36.60
Te L	64.46	38.29
Total	100	

Figure 2-20. EDS results for Zn diffusion from brass to LAST.

2.7.2 Diffusion bonding with coatings for Ni, Cu and steel

In addition to brass other electrodes with different coatings as listed below were also tried for diffusion bonding:

Table 2-4. Diffusion bonding with coatings for Ni, SS316 and Cu.

Thermoelectric Material	Contact Material	Bonding Temp (°C)	Bonding Time (Hours)	Results
LAST(Hot pressed)	SnTe+PbTe/Nickel	615	4	Successful Bond
LAST(Hot pressed)	SnTe/Nickel	615	4	Successful Bond
LAST(Hot pressed)	PB616/SS316	615	4	Good bond, but Cu and Ag diffusion was observed
LAST(Hot pressed)	Pb616/Ni	610	4	Bonded but high contact resistance
LAST(Hot pressed)	PB616/FeMnC	610	4	Mechanically weak bond, Cu and Ag diffusion was observed
LAST(Hot pressed)	SnTe/SS316 layer (2.85 mm)/Copper	610	4	Good bond, high contact resistance
LAST(Hot pressed)	SS316(347)(~ 0.5-1 mm)/Ni coated brass	720	4	Good bond, high contact resistance (oxide layer between SS and Ni)
LAST(Hot pressed)	SS316(347) piece(~ 0.5-1 mm)/Ni coated Cu	720	4	Good bond, high contact resistance (oxide layer between SS and Ni)
LAST(Hot pressed)	FeMnC piece(~ 0.5-1 mm)/Ni coated brass	720	4	No bond
LAST(Hot pressed)	FeMnC piece(~ 0.5-1 mm)/Ni coated Cu	720	2	No Bond
LAST and LASTT	Mn/Si/Mn/Si/FeMnC	750	4	Good bond, high contact resistance
LAST and LASTT	Mn/FeMnC	720	6	Good bond, high contact resistance
LAST and LASTT	Mn/Si/Mn/Si/SS316	750	4	Good bond, high contact resistance
LAST and LASTT	Mn deposited/SS316	720	6	N-leg not bonded
LAST and LASTT	Mn deposited/Ni	720	6	N leg melted
LAST and LASTT	In solder/FeMnC	810	4	Mechanically weak bond
LAST and LASTT	In solder/SS316	810	5	No Bond (single Stage unicouple run)

Table 2-4. Continued.

Thermoelectric Material	Contact Material	Bonding Temp (°C)	Bonding Time (Hours)	Results
LAST and LASTT	In solder/Mn/SS316	700	5	No Bond (single stage unicouple run)
LAST and LASTT	FeMnC	800	1	No bond
LAST and LASTT	SnTe powder/FeMnC	800	1	Mechanically good bond
LAST and LASTT	SnTe powder/SS316	800	1	No bond (single Stage unicouple run)
LAST and LASTT	Mo(~0.9 mm)/Mo (~0.9 mm)/Cu	720	2	Samples melted
LAST and LASTT	Mo/SnTe powder/Mo/Cu	650	16	low contact resistance bond, Cu diffusion was observed
LAST and LASTT	Mo(~1.4 mm)/PbSn solder/Mo (~1.4 mm)/Cu	650	16	Bonds well and low contact resistance, Cu diffusion was observed
LAST and LASTT	Mo/In solder/Mo/Cu	650	16	Bonds well and low contact resistance, Cu diffusion was observed
LAST and LASTT	Mo(~1.4mm)/Mo (~1.4 mm)/Cu	680	2	Bonds well but high contact resistance
LAST and LASTT	Mn(~200nm)/In/316 Stainless Steel	750	4	Bonds well, but high contact resistance
LAST and LASTT	Mo(~900nm)/In/316 Stainless Steel	760	4	Bonds well, but high contact resistance
LAST and LASTT	Mo/Sb/316 Stainless Steel	770	4	Good bond, high contact resistance (single stage unicouple run)
LAST and LASTT	Mn/Sb/316 Stainless Steel	810	4	Good bond, high contact resistance (single stage unicouple run)

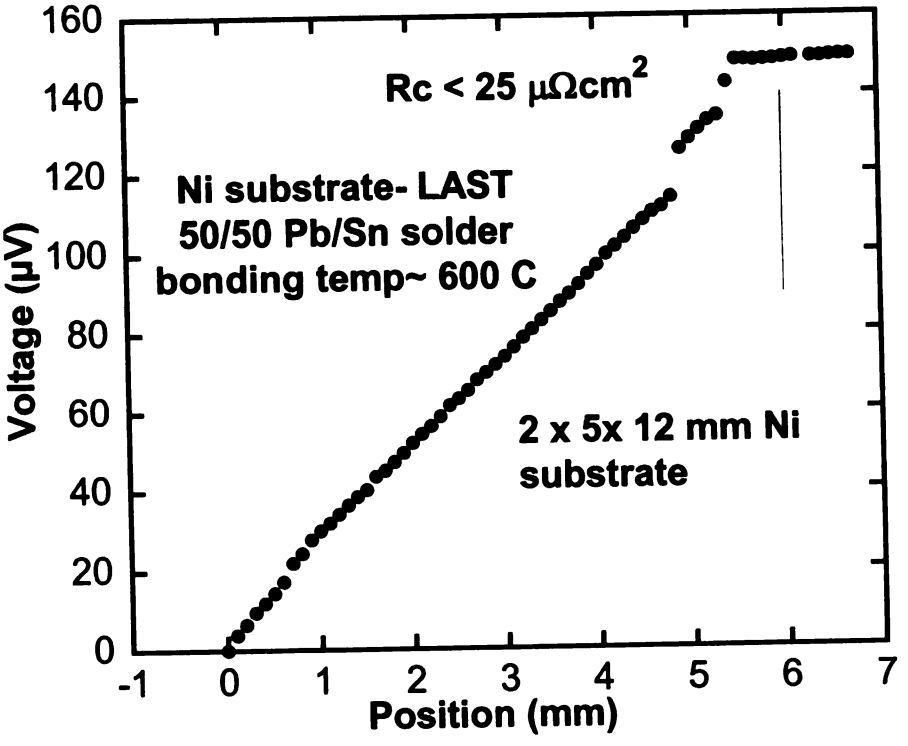

Figure 2-21. LAST bonded to Ni electrode.

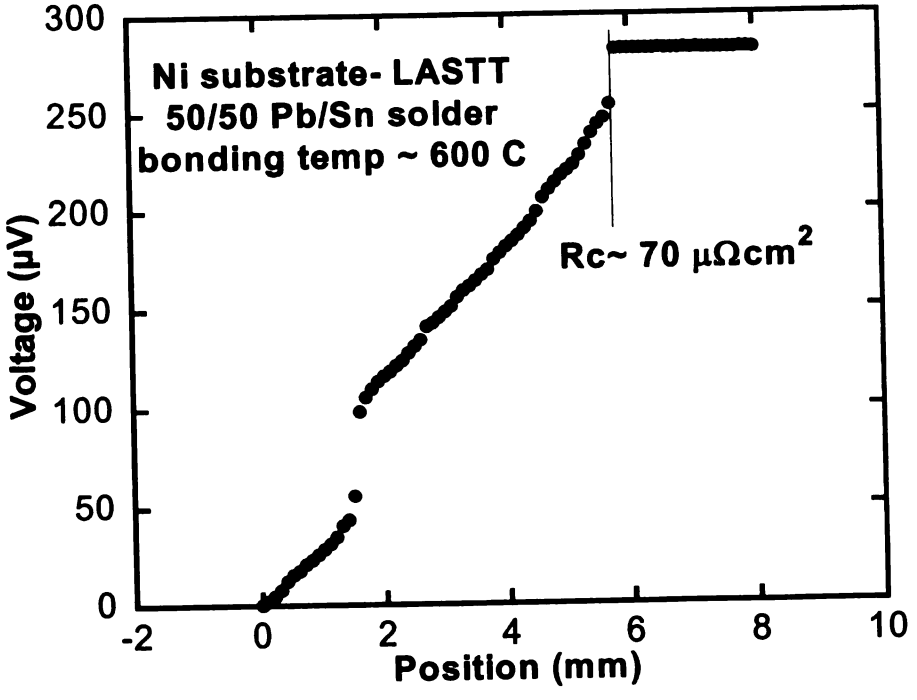

Figure 2-22. LASTT bonded to Ni electrode.

Figure2-21 and Figure 2-22 show voltage scans of bonded 2mm x 5mm x 12 mm Ni electrodes as the hot side contact. These were done using a low temperature bond of 50/50 Pb/Sn solder. Bothe n-type and p-type legs were bonded in the same run. Nickel is not a suitable electrode material for LAST as it reacts at high temperature (~ 700 C) and CTE mismatch (Ni ~ 13 $x10^{-6}$/K at 20 C and LAST ~ $21x10^{-6}$/K) may lead to thermal stresses inducing cracks during operation.

2.8 Diffusion bonding with Sn and Te powder

The most promising bonding experiments in terms of low contact resistance were carried out using Sn + Te powder (Sn70%Te30%) cold pressed coins (2000 psi) in oxygen free environment of glove box. Diffusion bonding was carried out in Ar+5%H environment at 820 Torr with ramping time of 4 hr, soaking time of 0.5 hr , heating rate of 2.7 °C/min and cooling time of 0.83 °C/min. Samples were pressed under spring pressure of 6.3 Kg/cm^2 during bonding. Electrode coatings and 4-probe unicouple resistance are given below.

Table 2-5. SnTe based diffusion bonding.

Electrode	p-type leg	Bonding T(^{0}C)	4-probe Unicouple Resistance (mΩ)	TE legs resistance (mΩ)	Contact resistance (mΩ)
Ni	ETN 153 ETP 55	615	3.5	2.78	0.71
Ni	ETN 153 ETP 55	615	3.89	2.78	1.10
Ni	ETN 153 ETP 55	615	4	2.78	1.21
Ni coated Cu	ETN 153 ETP 55	615	4.3	2.78	1.52
SS 316	ETN 153 ETP 55	615	4.3	2.78	1.22
SS316	ETN 159 ETP55	650	5	3.46	1.24
SS 316	ETN 159 ETP52	650	5.14	3.46	1.38
Cu coated with SS316	ETN 159 ETP55	650	5.5	3.46	1.94
Cu coated with SS316	ETN 157 ETP55	650	5.6	4.26	1.24
iron	ETN 153 ETP55	615	5.82	2.78	3
SS 316	ETN 157 ETP52	650	5.9	4.26	1.3
SS316	ETN 157 ETP55	650	6	4.26	1.4
Ni	ETN 157 ETP52	650	6.49	4.26	2.22
Ni coated brass	HPMSU 46, ETP52	615	35.7	29.16	6.0

For Table 2-5 resistance values of thermoelectric legs are given in Table 2-6 below. Leg size is 5mm x 5mm x 7mm.

Table 2-6. TE legs resistance values.

TE material	**σ (S/cm)**	**Resistance (mΩ)**
ETP 55	2400	1.16
ETP 52	2400	1.16
ETN 153	1726	1.62
ETN 157	900	3.1
ETN 159	1200	2.3
HP 94	100	28

For Table 2-5 resistance values for hot side electrodes are given in Table 2-7 below:

Table 2-7. Hot side electrode resistance values.

Electrode	**resistance (μΩ)**
Ni	80
Cu	20
Ni plated Cu	50
SS 316	350
SS 316 plated Cu	100
Iron (Fe)	50
Brass	60

LAST and LASTT based unicouples bonded using compacted Sn+Te powder discs were checked with room temperature scans for contact resistance and SEM images for junction analysis. As it can be seen from following SEM image (Figure 2-23) that

there are no cracks at the junction for austenitic steel (carpenter steel 19-2) with LASTT (ETP 52) and no intermediate layer was observed in the SEM images after bonding.

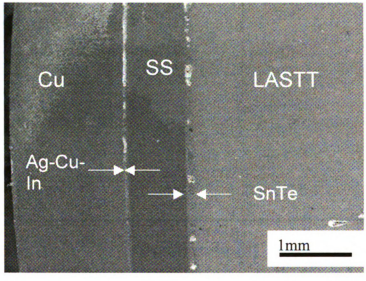

Figure 2-23. Carpenter steel 19-2 bonded to ETP 52 using SnTe.

The room temperature scan in Figure 2-24 shows that it is a low resistance contact at the junction of carpenter steel and ETP 52 as there is no abrupt voltage jump. We also do not observe any crack in the thermoelectric material.

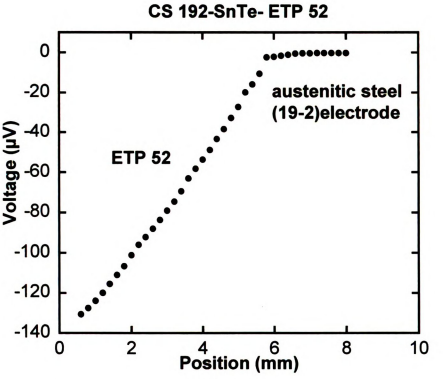

Figure 2-24. Room temperature scan for carpenter steel bonded to ETP52.

SEM image in Figure 2-25 shows a crack free interface with no intermediate layer between cast LAST and austenitic steel using Sn+Te compacted coin.

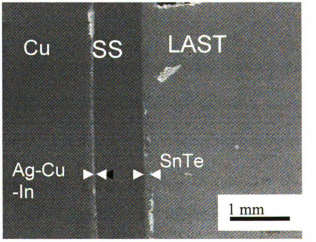

Figure 2-25. SEM image for austenitic steel and HPMSU 41.

The room temperature scan for carpenter steel bonded to hot pressed sample in Figure 2-26 shows a low resistance bond at the junction but the slope is non linear which might be due to diffusion of Sn into the hot pressed material.

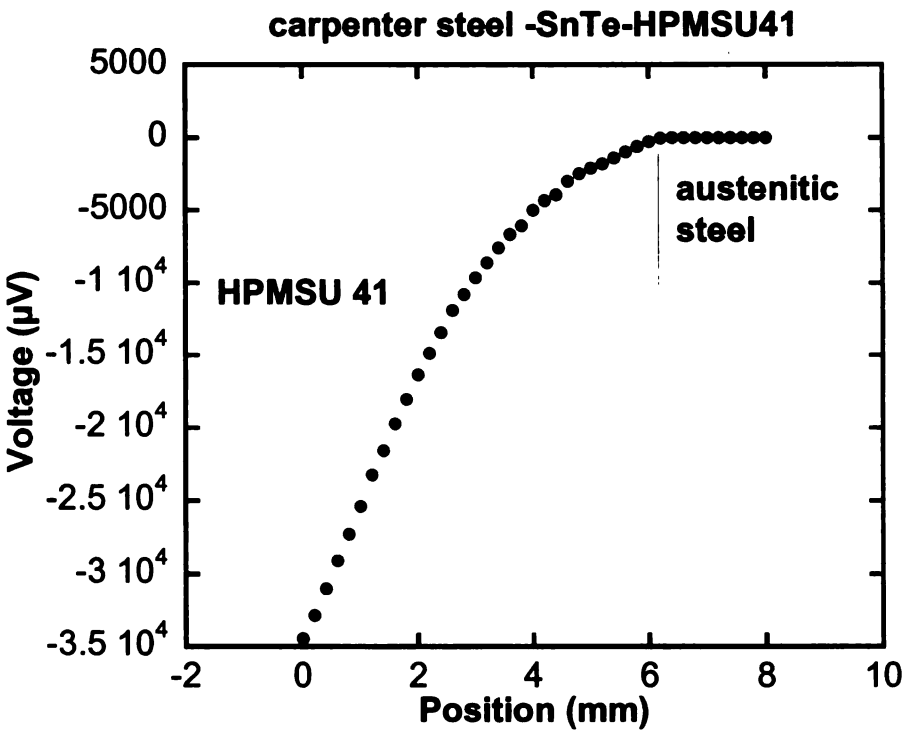

Figure 2-26. Carpenter steel bonded to HPMSU 41.

LAST and LASTT based unicouples bonded using compacted Sn+Te powder discs were tested by Nuraddin Matchanov for short circuit current in module testing system and consistently produced > 8 A currents which is reported elsewhere [29].

2.9 Electrical contact resistance measurement

In a typical thermoelectric module we want hot side contacts to be ohmic in nature or a schottky barrier height of zero. For ohmic contacts resistance is independent

of voltage. This implies that work function of metal should be close to or larger than the electron affinity plus bandgap of p-type semiconductor and the metal work function should be less than or equal to the electron affinity of an n-type semiconductor.

For our measurement purposes, we use curve fitting for the slope of the voltage vs position plot. In a typical experimental setup, current is sourced through the thermoelectric sample and voltage is measured using Keithley nanovoltmeters. Current is flipped approximately 20 times for each measurement to avoid Peltier effects. The following formula is then used to measure the contact resistance.

$$R_c = \frac{V_2 - V_1}{I} \times Area$$

Here V_2 and V_1 are the voltages at the junction of metal-semiconductor.

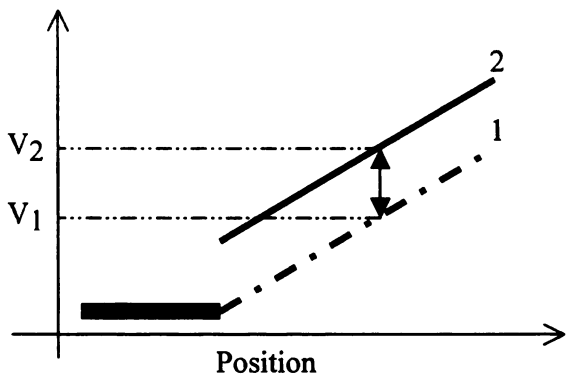

Figure 2-27. Calculation of contact resistance from voltage vs position plot.

The Figure 2-27 above shows how to take values of V_1 and V_2 from the voltage vs. position plot. The dark line is the actual voltage slope and dotted line is the slope if there had been no contact resistance. The area is the cross sectional area of thermoelectric leg

in contact with the metal electrode. Care has to be taken as to which point to select as the end of electrode and start of slope because that will cause variation in the $V_2 - V_1$.

A special case would be if the slope is not linear at the end rather shows a curve as indicated in Figure 2-28 below. In this case the part of the slope which is linear should be considered for measuring voltage difference because if V_2-V_1 is directly measured from two nearest data points separating electrode and thermoelement (in Figure 2-28 this value is shown to be 135 μV), that will result in erroneous value of contact resistance. However, if the slope is curve fitted, the voltage difference is 200 μV which corresponds to more accurate contact resistance value.

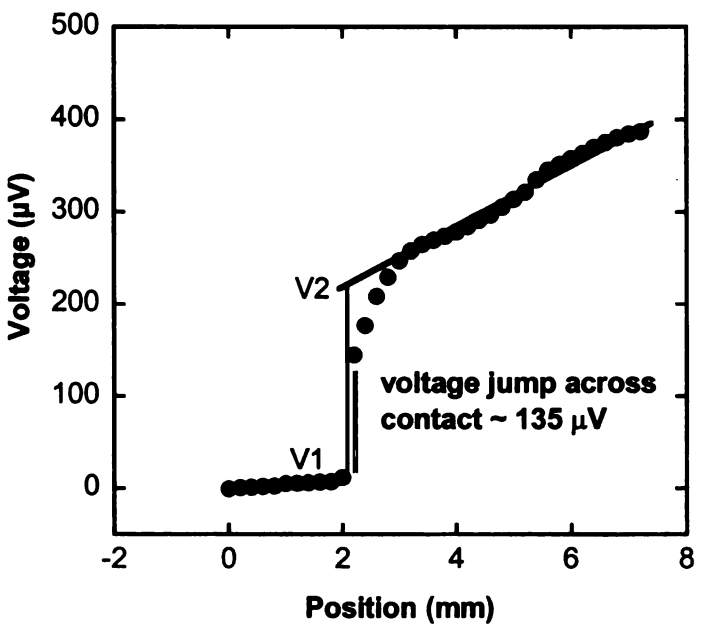

Figure 2-28. Curve fit for contact resistance measurement.

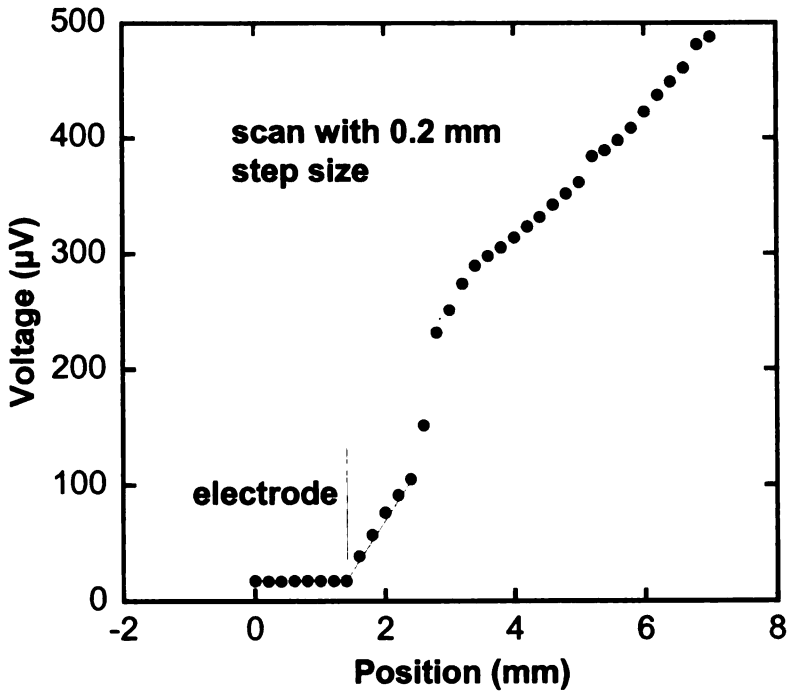

Figure 2-29. Scan with 0.2 mm step size.

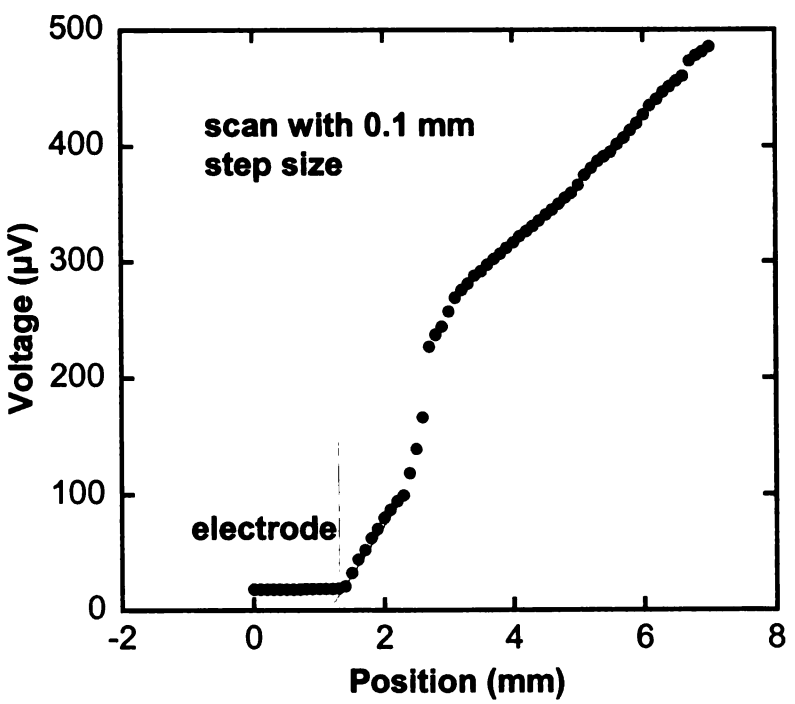

Figure 2-30. Scan with 0.1 mm step size.

Another aspect to consider is the step size of scanning pin. That directly corresponds to sensitivity of measurement: smaller the step size, more accurate will be the value of measured resistance. Figure 2-29 shows a metal electrode-thermoelement scan with step size of 0.2 mm and Figure 2-30 shows same sample with 0.1 mm step size.

We can see that in both cases curve fit gives negligible contact resistance. However, when two plots are superimposed as shown in Figure 2-31, the step size makes a difference in measurement for high resistance area (shown by the circle). The 0.1 mm scan gives a voltage difference of 58 μV and 0.2 mm scan shows ~ 80 μV difference.

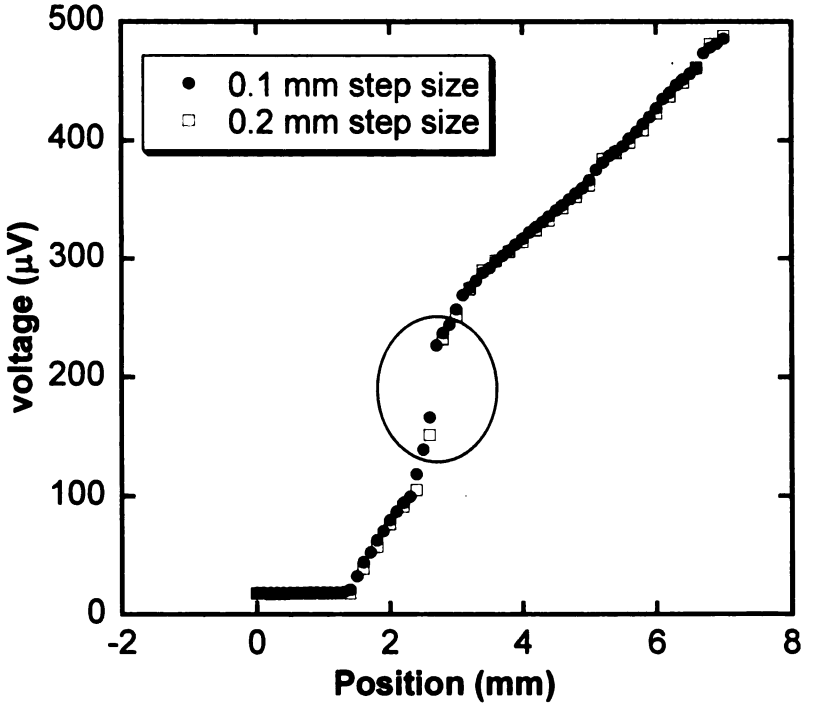

Figure 2-31. Superimposed scans of 0.1 and 0.2 mm step size.

The sensitivity of the system is also dictated by the radius of scanning pin. For example in our high temperature voltage scanning system we can use scanning pogo pin with a tip radius of 0.53 mm (manufactured by Otsby Pylon), that means any voltage gap across the

contact less than 0.53 mm can not be detected. However, system also has the provision to use 0.08 mm tip radius pogo pin to improve sensitivity.

Conclusions

A number of bonding and diffusion barrier coating experiments were carried out. Stainless steel (SS316) has been promising but due to slight mismatch in CTE, causes microcracks in LAST sample after bonding. Another emerging option is LASTT as hot side electrode but that will need heavy doping to make it more thermally and electrically conductive. Brass has a close CTE match but the zinc tends to diffuses into the LAST material to form ZnTe, even when diffusion barriers of Ni, Mo, Ti and TiZrN were used. Low contact resistance in the range of 4 to 7 (mΩ) have been obtained using cold pressed SnTe coins based diffusion bonding and have proven to be a better option for LAST diffusion bonded unicouples.

Chapter 3: InGa and Spring Loaded Modules

Introduction

Due to coefficient of thermal expansion (CTE) mismatch problems it was decided to use InGa as liquid contact between the LAST material and metal electrodes. Dumke *et al* found that the surface of InGa eutectic is enriched with indium and they experimentally evaluated that with bulk Ga concentration of 83.5 % the surface concentration of Ga was less than 6% [30]. Gallium is highly reactive metal and dissolves most metals at high temperature however Ni and Au moderately react at high temperature with gallium [31] and therefore have been tried in our experiments. We used 75.5 Ga/24.5 In alloy by Goodfellow with melting point of 15.7 °C. This eutectic has high electrical conductivity (3.4×10^4 S/cm) [32], wets most surfaces, makes a low contact resistance interface with variety of materials [33] and is known to flow after a surface stress of 0.5N/m is applied [34]. Molten InGa surfaces in air primarily consist of oxides of Ga [35] which is an n-type semiconductor. In ambient air it has an adsorbed film of water as it has high surface energy (630 dynes/cm) [32]. The room temperature electrical properties of InGa are stable in time after the initial surface oxide is formed.

3.1 InGa Module Fabrication

Module legs consisted of n-type $AgPb_mSbTe_{m+2}$ (LAST) and p-type $Ag(Pb_{1-y}Sn_y)_mSbTe_{2+m}$ (LASTT) which were cut to 5 mmx5mmx7 mm and polished to remove oxides. Two 2mm x 5mm x12mm Cu pieces were used as cold side contacts and were mounted on an AlN piece using double sided carbon tape. Care was taken to prevent

short circuit at cold side by removing the double sided tape between Cu pieces. Low temperature Ceromatrix solder was used to mount both TE legs on the Cu pieces. InGa liquid was then applied on the top surface of each leg. Different metal electrodes were investigated. First a 2mm x5mm x12 mm copper piece was nickel plated. It was lightly polished with 1200 grit sand paper to produce a shiny surface. Residues left on surface from the Ni plating solution were found to cause poor wetting of InGa on the electrode surface. After acetone cleaning InGa is applied using a wooden applicator and the electrode is placed on top of already mounted TE legs. A thick binding solution of QS/B4 by Fortafix is prepared and applied around the legs such that it also engulfs the electrode sides thus holding it in place and providing necessary mechanical support. Two types of measurements were carried out, one in ambient air and other under Ar atmosphere inside the Long Term Module Testing System (LTMTS) [36]. For ambient air short circuit current measurements a thick short wire was used to short two legs of the unicouple. Initial measurements were carried out inside the LTMTS. A 2mm x5mm x12 mm Ni electrode was used. Nickel has lower electrical and thermal conductivity than Cu but previous experience showed that LAST readily reacts with Cu at high temperature and that Cu has tendency to oxidize. Two unicouples consisting of LASTT (ETP 53) and LAST (ETN 224) were prepared. InGa was used as liquid contact between Ni electrodes and TE legs. QS/B4 was used to hold the electrodes in place on top of legs. Four-probe resistance for the unicouple module was 14 (mΩ). Temperature was then ramped up to 600 °C and the maximum short circuit current was measured as 6.4 (A) for T_h= 600 °C and T_c= 30 °C. Output short circuit current then started decreasing indicating that InGa

reacted with LAST material which could be seen upon sample removal. Figure 3-1 shows the power output for this module. After thermal cycling the 4-probe resistance was 45 (mΩ). The measuring wires for LTMTS system were about one meter long and had 14 (mΩ) resistance whereas matched load resistance per unicouple is typically < 10 (mΩ). The measurement configuration was then changed by measuring the sample in air and using a short thick Cu wire which greatly increased the measured short circuit current.

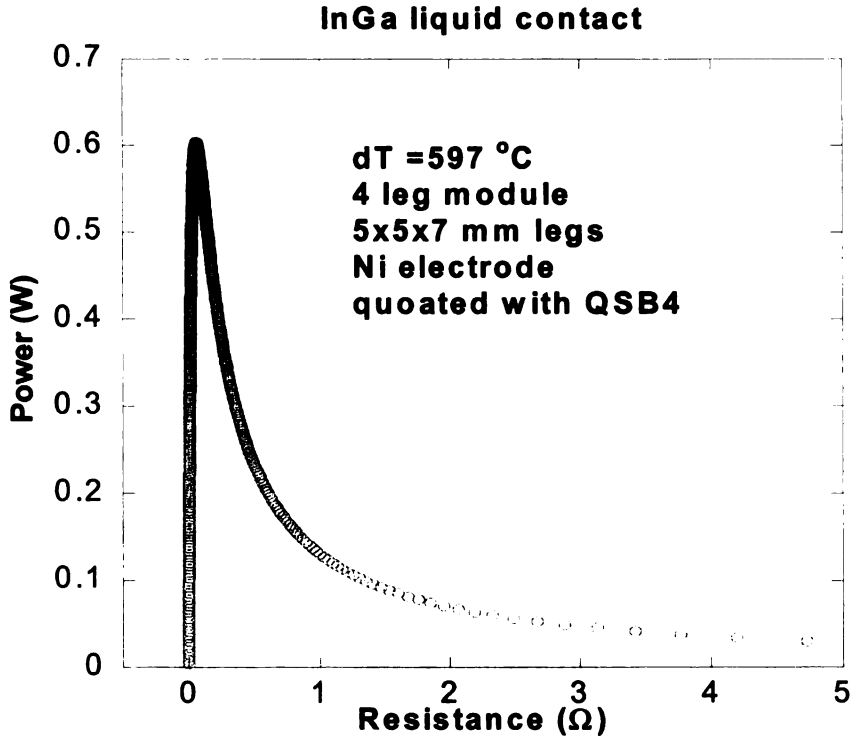

Figure 3-1. Ni electrode based InGa liquid contact.

Different geometrical configurations for the electrodes were investigated primarily to increase the contact surface area. One such configuration is shown in Figure 3-2, where 12 mm long TE legs were used such that 5mm was inside the electrode and 7

mm outside. The 5mm leg portion inside the electrode would give five times the contact surface area compared to that of a regular 7mm leg surface.

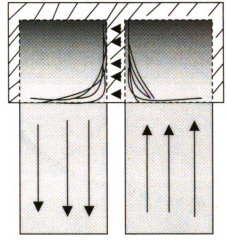

Figure 3-2. Stainless Steel 316 electrode for 12mm TE legs.

A single unicouple module was assembled with 5mm x5mm x12mm legs of LASTT (ETP 53) and LAST (ETN 221) and InGa was used as liquid contact. A recess was machined in the electrode to enclose a part (5mm) of 12 mm leg with InGa as shown in Figure 3-2. The module was run inside the LTMTS and the maximum current reached was 4.0 (A) for ΔT of 560 ^{o}C. Figure 3-3 shows the power output for this module. After thermal cycling module resistance was 45(mΩ). The output current was steady for a longer duration than with Ni electrode however; current started decreasing after one hr due to InGa reaction with stainless steel. This is because TE legs with InGa permanently bonded with stainless steel electrode and without InGa the TE legs remained separate from SS 316 electrode up to 600 ^{o}C.

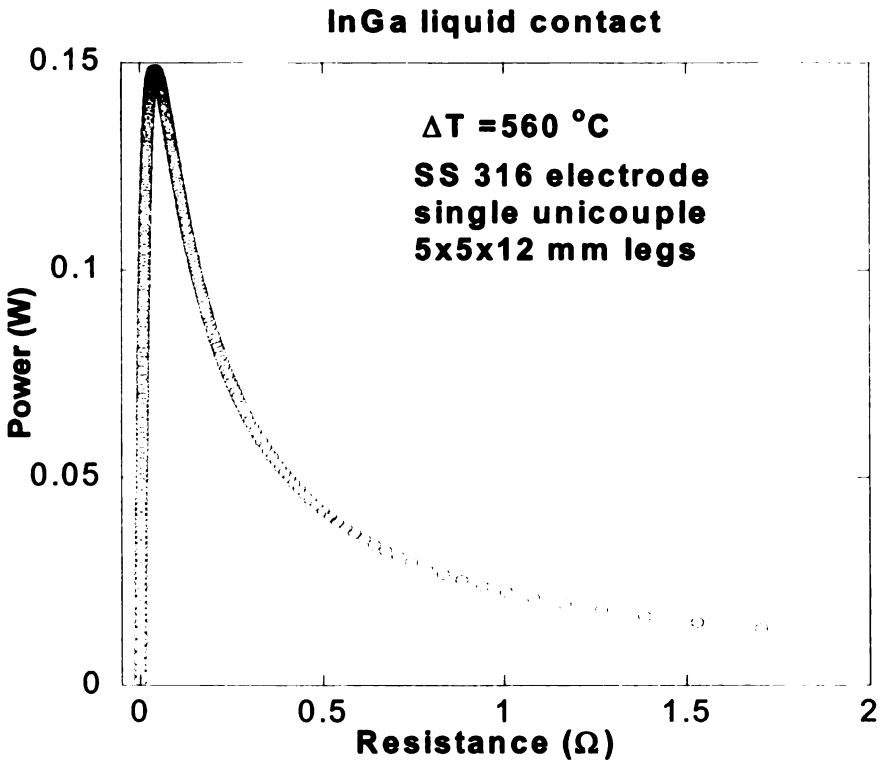

Figure 3-3. Output for 12mm long TE legs.

A similar module was prepared with 12mm long TE legs and InGa liquid contact. It was measured in open air with a smaller measurement wire (R < 1mΩ). Starting 4-probe resistance was R ~ 7.5 (mΩ). The short circuit current plot is shown in Figure 3-4. The maximum current reached was 6.47 (A) at 684 °C and current stayed at this level for about four hrs which is longer than with Cu or Ni electrode. After thermal cycling module 4-probe resistance increased to R ~ 30 (mΩ).

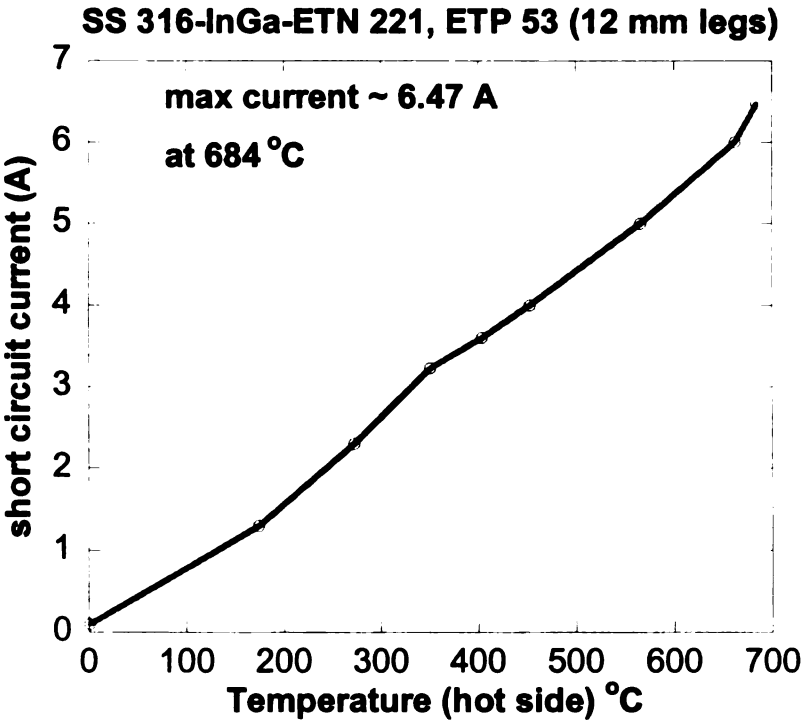

Figure 3-4. Stainless steel 316 electrode with 12 mm TE legs.

For metal electrodes copper has the second highest electrical (59.6 x 10^8 S/cm) and thermal (400 W/m-K) conductivity after silver. Copper also has a relatively large coefficient of thermal expansion; 18 (ppm/°C), which is also of interest since LAST and LASTT have coefficients of thermal expansion greater than 20 (ppm/°C). Previous experiments proved that copper readily reacts with LAST material and oxidizes thus increasing the contact resistance. Nickel plating of the copper electrodes was used and it was found to significantly improve the stability of the contacts; however InGa moderately reacts with Ni. InGa was used as liquid contact and QS/B4 was used to minimize sublimation and to mechanically hold the Cu electrode in place. Four probe resistance for the unicouple module was 5.5 (mΩ). Short circuit current was measured with module inside the LTMTS under argon and the maximum value of the current was5.23 (A).

Current was measured by first shorting the current wires in series with the module and using hand held current clamp meter (EXTECH 380942).The output current plot is shown in Figure 3-5 below [indicated by (x) line].

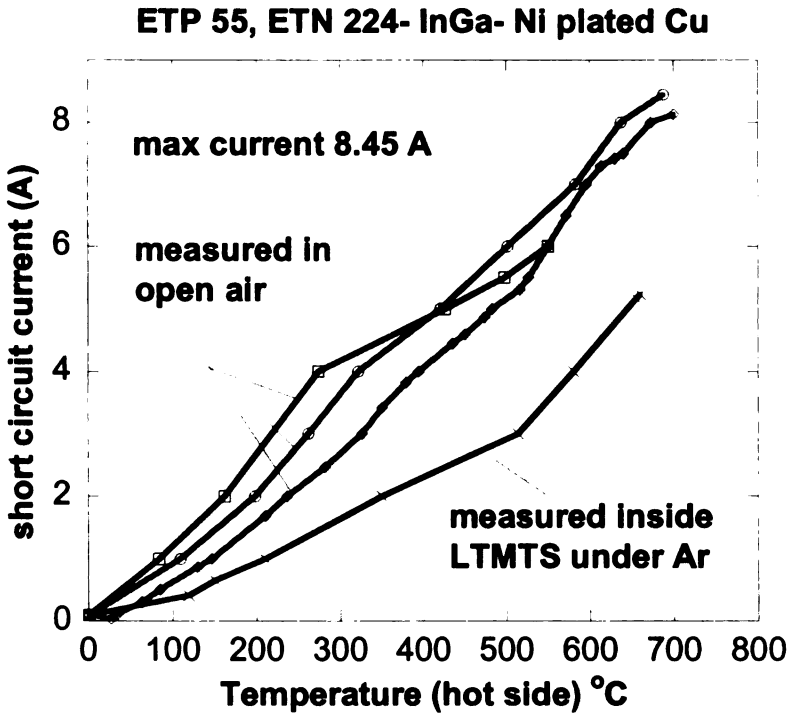

Figure 3-5. Module first measured under Ar, then three cycles with different electrodes measured in open air.

The current started decreasing as InGa reacted with LAST material. Module was cooled down, taken out and the QS/B4 was removed by using a screw driver to replace with new electrode. After removal of the electrode, the surfaces of the thermoelectric legs were polished, cleaned and new InGa was applied. Second time module was tested using a short thick Cu wire with a resistance ~ 800μΩ in open air. Starting 4-probe resistance for module was ~ 7.5 (mΩ). Current reached 8.13 (A) for hot side temperature of 700 °C

[indicated by (◊) line in Figure 3-5]. However, cold side temperature also increased to 120 °C at this point which effectively created a ΔT of 580 °C. To see if the results could be repeated the module was cooled down, QS/B4 removed, and a new electrode was put in place with new QS/B4 coating. Legs were polished for clean surface. This time short circuit current reached only 6.0 (A) at hot side temperature of 550 °C [indicated by (□) line in Figure 3-5]. The module was cooled down and the QS/B4 was removed for inspection. It was revealed that electrode was not properly put in place and only a fraction of total electrode area was covering TE leg surfaces thus not providing full contact. New electrode was replaced, legs were polished clean, and new QS/B4 coating was applied with InGa as liquid contact. Module was tested third time in open air and current reached 8.45 (A) at 688 °C [indicated by (o) line in Figure 3-5]. This module proved that LAST is a robust material capable of surviving rough handling, multiple thermal cycling and still can maintain its TE properties.

3.1.1 Coatings on TE legs

Several experiments were done to find suitable diffusion barriers to prevent an InGa reaction with the LAST material at high temperatures. P-type LASTT (ETP 55) and n-type LAST (ETN 224) materials were used to make legs of 5mm x5mm x7 mm size which were then polished and sputtered with Au (100 nm), Ni plated to few micron thickness and again Au sputtered (100 nm). Sputtering was carried out at room temperature. The reason for first Au coat was that Ni plating did not hold on to LAST surface well. However this pre-coating did not serve the purpose and during InGa application of module fabrication it was observed that Ni film was still peeling off along

with Au film thus exposing LAST material surface. Probably due to room temperature sputtering Au films did not bond to LAST surface. Short circuit current (I_{SC}) reached to 9.00 (A) at hot side temperature of 662 °C as shown in Figure 3-6 below. For this module we first time observed 8.62 (A) for hot side temperature of 600 °C which is the proposed operating temperature for LAST based modules. Coatings did not help and current started decreasing at high temperature.

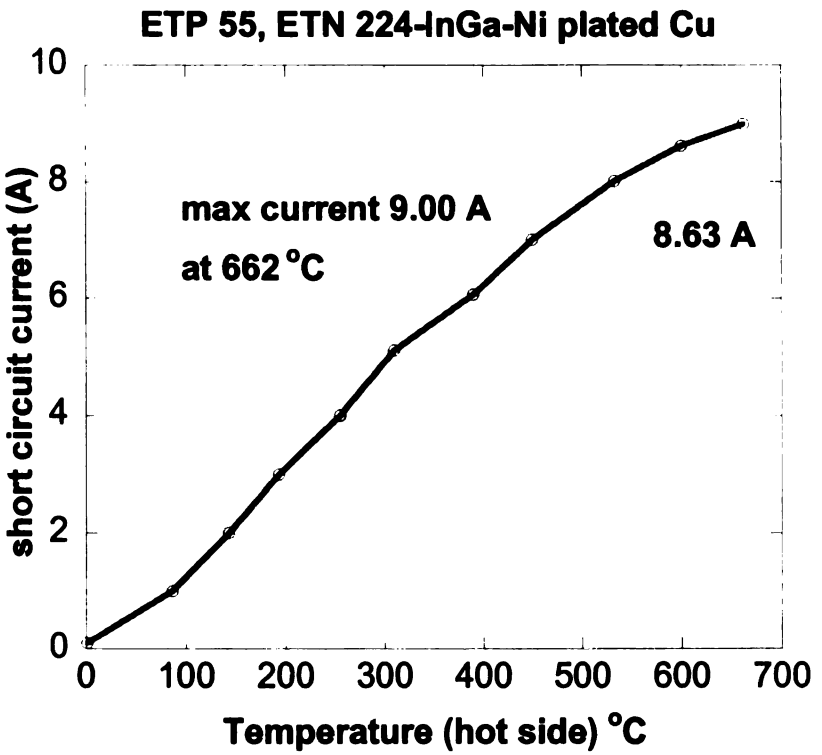

Figure 3-6. Au and Ni coated TE legs based unicouple output.

Next module was tested with a sputtered Mo coating on TE legs. Mo was sputtered with substrate temperature ~ 150 °C and coating thickness was < one micron. The coating did not stick well to the surface and could be brushed off with thumb

pressure only. Moreover, there was black soot like contamination on target holder inside the PVD system that might have altered the Mo coating properties. Same module was tested twice in open air to check the results. Each time current reached 7.5 (A) as shown in Figure 3-7 below. The Mo coating was not able to prevent InGa reaction with LAST material and the current started decreasing in both cases.

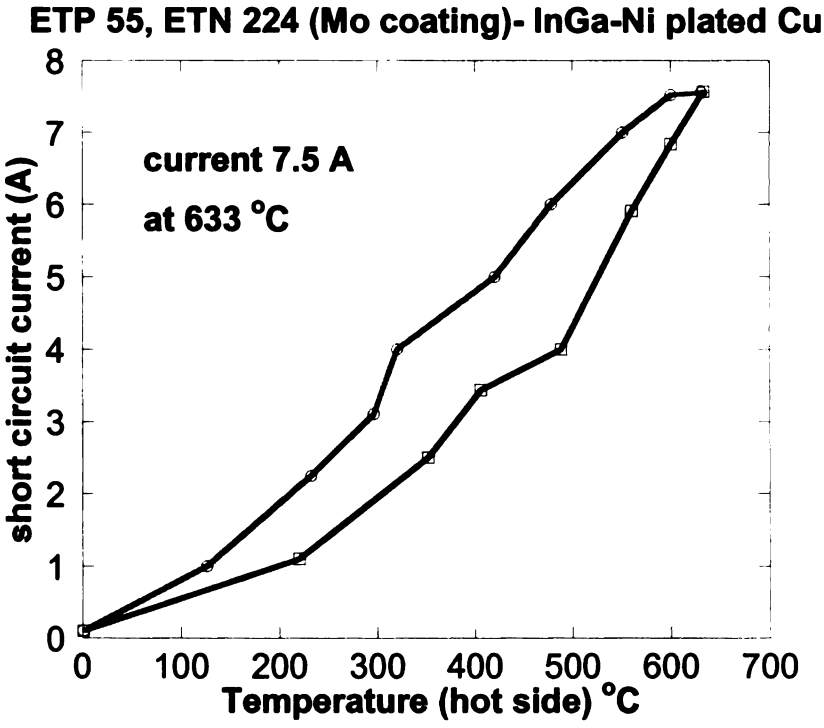

Figure 3-7. Mo coated TE legs based module tested twice in open air.

3.1.2 SS-Ni-Au coating

In next experiment same legs were first coated with stainless steel using pen plating system and stainless steel solution, then Ni plated and again Au sputtered (150 nm). The idea was that stainless steel might help to hold the Ni plating on the LAST surface. A coating of QS/B4 was put around the TE legs and InGa was used as liquid

contact. The resulting module was tested in open air and a measured short circuit current of 2.5 (A) at 341 °C hot side temperature was obtained. After the run the module was cut open to remove QS/B4 with electrode and the thin film of stainless steel-Ni was still intact but appeared dull, easily peeled off and perhaps did not allow direct contact of InGa with LAST material.

3.1.3 Mo-Au coating

In this experiment TE legs (ETP 55 and ETN 224) were coated on the ends with Mo by sputtering at a substrate temperature of 150 °C and then Au sputtered (150 nm) at room temperature. The module was QS/B4 coated and InGa was used as a liquid contact. The Au coating was investigated here as a possible method for reducing the interface resistance between LAST and Ni plated Cu. The short circuit current reached 7.12 (A) for 660 °C hot side temperature as shown in Figure 3-8 and then started decreasing right away. It was the third experiment in which a Mo coating did not help prevent an InGa reaction with LAST material.

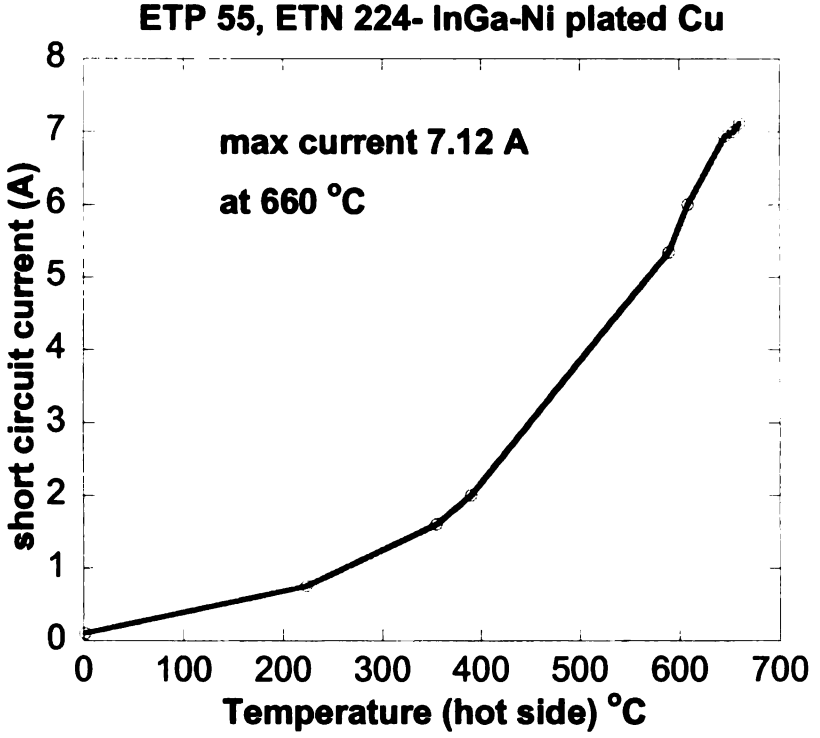

Figure 3-8. Mo-Au sputtered TE legs module.

3.1.4 Mo-Ni coating

In this Mo coating experiment a module was tested inside the LTMTS under an inert environment (Ar) of one atmosphere to see if the degradation rate could be slowed (assuming oxidation at the interface as the cause). For this unicouple module LASTT (ETP 55), LAST (ETN 224) TE legs were polished, Mo sputtered and Ni plated using pen plating system. Before exposing the module to a large temperature gradient, the room temperature four-probe resistance was measured to be ~ 4.5 (mΩ). As mentioned above measuring wires of the LTMTS were cut short to reduce wire resistance to ~ 4 (mΩ). The same module was then tested again in open air with short Cu wire (R < 1 mΩ). Module output is shown below in Figure 3-9. For open air measurement starting 4-probe

resistance was R ~ 6.7 (mΩ). It can be seen that the open air measurement still performed better due to low resistance measurement wires. This shows that open air oxidation of interface is less deleterious for module out put than higher series resistance of measuring wires.

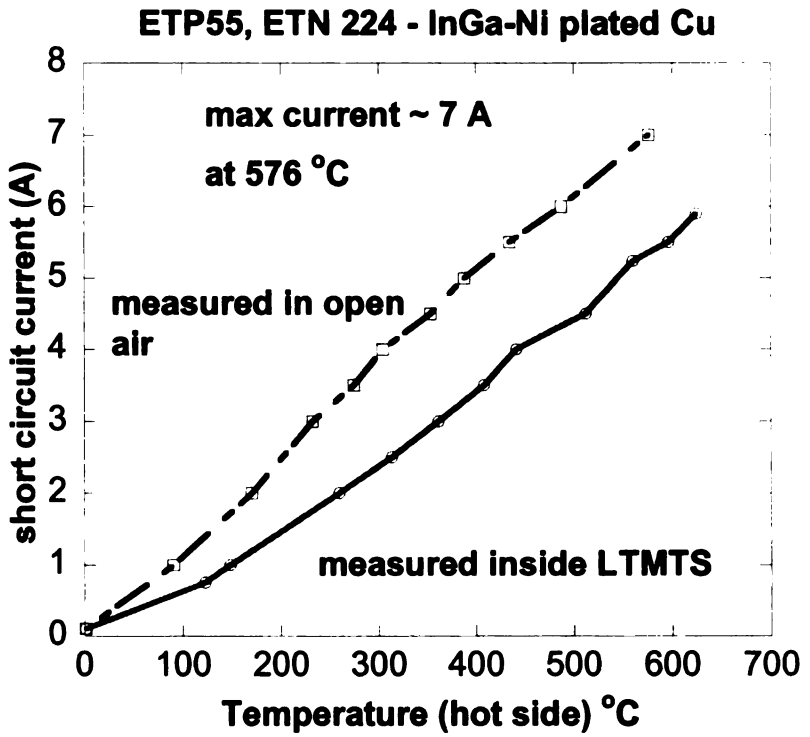

Figure 3-9. Mo-Ni plated TE legs measured under Ar and ambient air.

In previous experiments various coatings were investigated on the TE legs but they were not successful in stopping the reaction between InGa and LAST rather most of them increased resistance at the interface. An InGa layer between the TE legs and the metal electrode without any coating on LAST surface was investigated. The same module used in the previous experiment was cooled down, the QS/B4 removed, TE leg surfaces polished to remove any contaminants from previous experiments, and prepared again

using a new Ni plated Cu electrode and coated with InGa. Module was taken high in temperature and maximum short circuit current of 10.5 (A) was observed at 672 °C hot side temperature. It was for the first time that any LAST based module crossed 9.0 (A) within hot side temperature of 600 °C as shown in Figure 3-10 below. The short circuit current then began decreasing, so the module was cooled down and the QS/B4 removed. InGa could still be seen on the n-type leg, however the p-type leg permanently bonded to the electrode. For the hot side temperature of 672 °C the cold side was 113 °C, thus the effective ΔT was 559 °C and the maximum short circuit current obtained was 10.5 A.

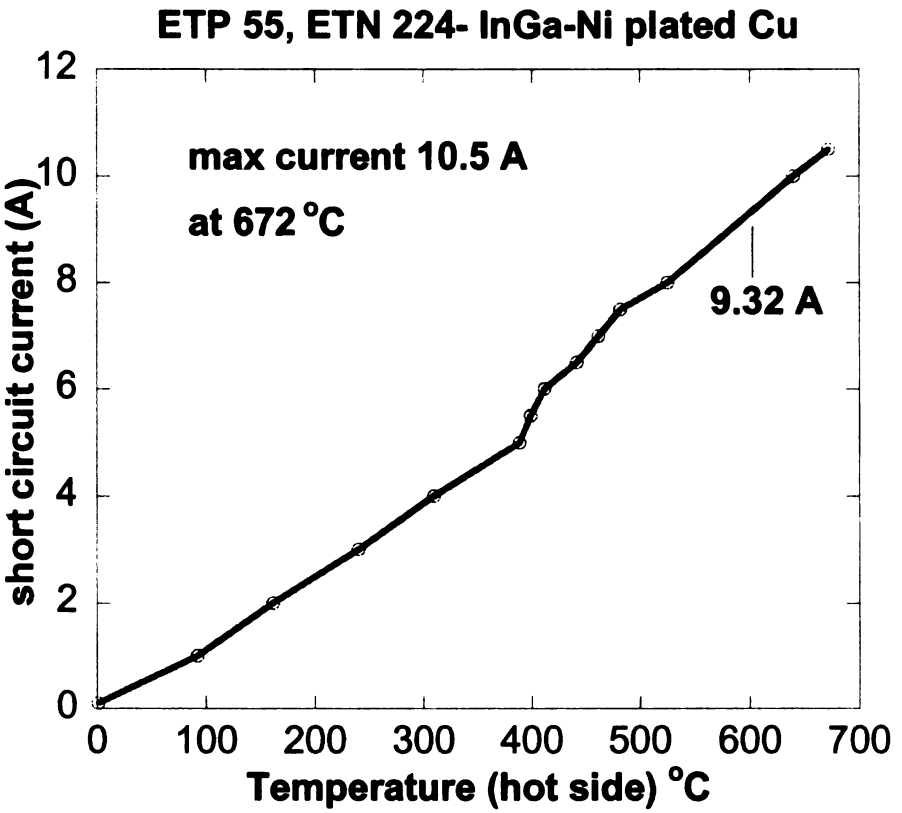

Figure 3-10. Module prepared without any coating on TE legs.

Table 3-1. Summary results for InGa based modules.

Electrode	Material & coatings	Air/Ar	Th (°C)	Tc (°C)	I_{sc} (A)	Comments
Ni	ETP53 ETN 224	Ar	600	30	6.4	4 leg module
Stainless Steel 316	ETP 53 ETN 221	Ar	600	40	4.0	12 mm legs
Stainless Steel 316	ETP 53 ETN 221	Air	684	62	6.47	12 mm legs (second run)
Ni plated Cu	ETP 55 ETN 224	Ar	660	74	5.23	7 mm legs first run
Ni plated Cu	ETP 55 ETN 224	Air	700	120	8.13	7 mm legs Second run
Ni plated Cu	ETP 55 ETN 224	Air	550	34	6.0	7 mm legs Third run
Ni plated Cu	ETP 55 ETN 224	Air	688	107	8.45	7 mm legs Fourth run
Ni plated Cu	Au-Ni-Au ETP 55 ETN 224	Air	662	103	9.0	7 mm legs coatings did not work
Ni plated Cu	Mo on ETP 55 ETN 224	Air	633	83	7.57	7 mm legs 2 runs
Ni plated Cu	SS-Ni-Au ETP 55 ETN 224	Air	341	28	2.5	7mm legs Dull colored SS film
Ni plated Cu	Mo-Au ETP 55 ETN 224	Air	660	91	7.12	7mm legs
Ni plated Cu	Mo-Ni ETP 55 ETN 224	Ar	624	61	5.90	7 mm legs First run
Ni plated Cu	Mo-Ni ETP 55 ETN 224	Air	576	57	7.00	7 mm legs second run
Ni plated Cu	ETP 55 ETN 224	Air	672	113	10.5	7 mm legs

3.2 Spring Loaded Modules

The history of spring loaded modules is at least fifty years old [37]. Space launched radio isotope generators (RTGs) used SNAP series thermoelectric converters. These generators used PbTe and SiGe based modules and all PbTe based modules were spring loaded [3]. Although we were not able to find much published data for spring pressure used, Fritts [37] recommended 100 psi spring pressure.

3.2.1 Surface asperities and contact resistance

When two solid surfaces are pressed against each other, they make contact only at certain spots because no matter how flat the surfaces are; there will be surface micro roughness. Due to this roughness there will be micro peaks, valleys and geometrical shapes which will come in contact. Thus the actual contact area is much smaller than the nominal surface contact area. The asperities of the contact spots undergo elastic and/or plastic deformation depending upon the surface hardness, applied pressure and temperature [38]. As the actual contact between surfaces is limited to these spot, electrical current lines become increasingly distorted and bundle together to pass through these spots as shown in Figure 3-11 below.

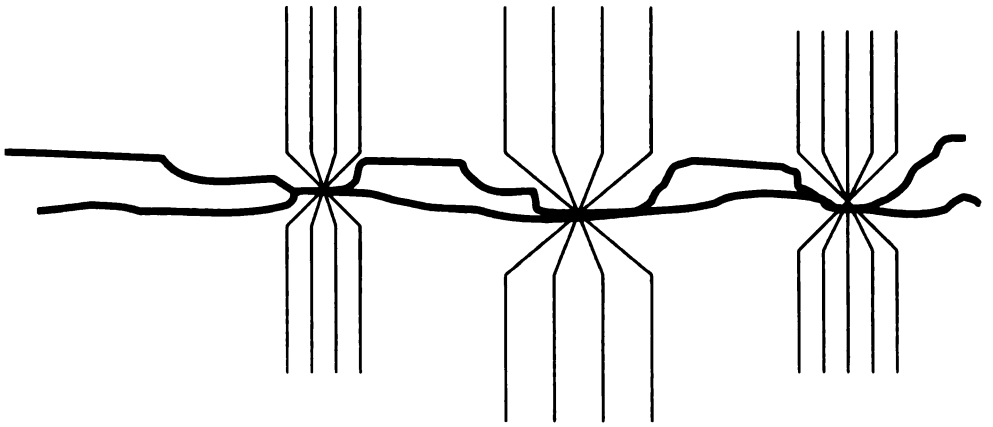

Figure 3-11. Bulk electrical interface with current lines passing through asperities (points of contacts between surfaces).

Due to these spots (called a-spots) actual volume of contact reduces and gives rise to constriction resistance as current is constricted through these a-spots. The other factor causing the increase in interface resistance is insulating film (usually oxide films) on the material surface. The combination of these two resistances is called contact resistance. For circular a-spots the equipotential surfaces in the contact members consist of ellipsoids:

$$\frac{z^2}{\mu^2} + \frac{r^2}{a^2+\mu^2} = 1 \qquad (2.1)$$

Where μ is the vertical axis of the vertical ellipsoidal surface and (r and z) are cylindrical coordinates. The resistance between these equipotential surfaces is then:

$$R = \rho / 2\pi \int_0^{\mu} d\mu / (a^2 + \mu^2) = (\rho / 2\pi a) \tan^{-1} (\mu / a) \qquad (2.2)$$

Here μ represents resistivity of conductor. If spreading resistance R_s is defined as constriction resistance for very large μ then:

$$R_S = \rho/4a \tag{2.3}$$

The total constriction resistance is then:

$$R_C = \rho/2a \tag{2.4}$$

If two surfaces consist of dissimilar metals then

$$R_C = (\rho_1 + \rho_2)/ 4a \tag{2.5}$$

Spreading resistance for elliptical a-spots with semi axis a and b is given by:

$$Rs(a,b) = \rho / 2\pi \int_0^\infty d\mu / \{(a^2 + \mu^2)(b^2 + \mu^2)\}^{1/2} \tag{2.6}$$

Spreading resistance for square a-spots with side length 2L is given by:

$$R_S = 0.434\rho /L \tag{2.7}$$

In practice, a-spots are considered circular for all practical purposes. In real contacts surfaces mate where there are clusters of a-spots and their combined effects give the contact resistance:

$$Rc = \rho (1/2na + 1/2\alpha) \tag{2.8}$$

Here n is the number of a-spots, a is the mean radius of a-spots and α is radius of cluster. When the surfaces are firmly pressed against each other, a-spots (asperities) go through plastic deformation and these deformed asperities have slightly larger contact area. If one of the two mating surface material is softer than the other then load **F** applied to the contact and contact area Ac are related by:

$$\mathbf{F} = Ac\mathbf{H} \tag{2.9}$$

Here **H** is the hardness of softer material. This expression reveals the true area of mechanical contact is independent of area of nominal contact for two surfaces. In other words it is independent of dimensions of contacting bodies and only depends upon applied force (load) and hardness of the materials. If insulating films on surface are not present then contact resistance in terms of above expression can be given as:

$$R = \{\rho^2 \eta \pi H / 4F\}^{1/2} \tag{2.10}$$

Where η is an empirical coefficient and for a clean surface its value is unity. It is a simple expression saying that with increased applied force contact resistance will decrease. This can be explained as the force is increased, there is plastic deformation of a-spots and they become more flatten and actual contact area is increased. As a-spots flatten the constriction of electrical lines of force also eases and they have larger cross section available to pass through between the two surfaces. Moreover, as the load is increased, depending upon the surface hardness, more spots will come into contact thus increasing the actual contact area.

When a-spot makes contact with opposite surface there is angle between the spot and opposite surface depending upon the shape of asperity as shown in Figure 3-12 below

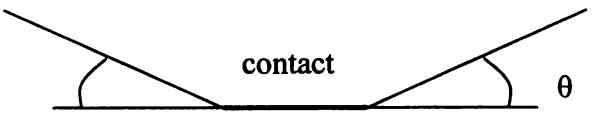

Figure 3-12. A-spot making an angle with opposite surface due to conical asperity.

In this case the spreading resistance is given as:

$$R = (\rho / 4a)\tan\{(\pi + 2\theta)/4\} \qquad (2.11)$$

3.2.2 Effect of Surface Film

Film coating on a conductor may change its properties. If there is inter-diffusion across the films of opposite surfaces, the contact resistance will normally increase due to an inter-metallic compound formation under pressure. For insulating oxide films or thin weakly conducting films, conduction will only take place once the film is ruptured under force to enable metal to metal contact. A change in the surface hardness due to the presence of a metal film may also change its contact resistance. Usually surfaces are electroplated with nickel to stop inter-diffusion between mating surfaces. If the electroplated material is such that the surface hardness is reduced as compared to original surface, then the contact resistance will decrease. It is also possible that an electroplated film has higher conductivity than the original surface. Coatings also help to stop oxidation thus improving contact resistance. However, if the film is porous it may not be able to perform this protective role under long term operation. The contact resistance depends upon the relative resistance of the deposited film to that of the substrate and the radius of a-spots. As shown in the Figure 3-13 if the film resistance is higher, electric lines of force will be constricted and contact resistance will be higher. In this case the film resistance overshadows constriction resistance. If the deposited film resistance is lower than the substrate, then the electric lines of force will spread more in the film and the underlying metal and electric contact resistance will be low.

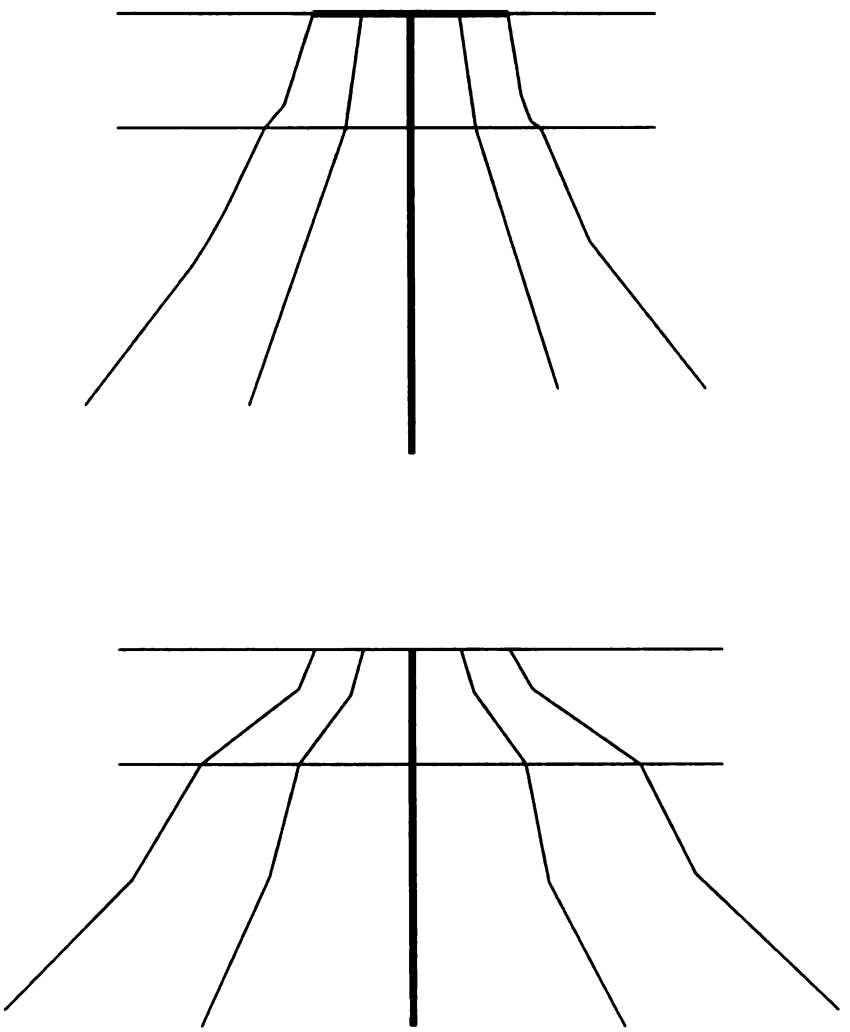

Figure 3-13. Electric lines of force in (a) high resistance film (b) low resistance film.

3.3 Room Temperature Spring Loaded module parameters

To study room temperature spring loaded parameters a new apparatus was designed as shown in Figure 3-14 below. The apparatus was designed such that it could fit in room temperature scanning system that allowed contact resistance and electrical conductivity measurements. Two types of springs were used in these experiments: compression springs and die springs, both purchased from Mcmaster Carr Inc.

Compression springs are soft and have force range of 10-15 lbs for 1"-1.5" length whereas; die springs are hard and have a range of up to 30 lbs force for same length. With multiple experiments it was found that surface roughness had more impact than spring load for a low resistance module. A better-polished surface with less spring force would give low contact resistance.

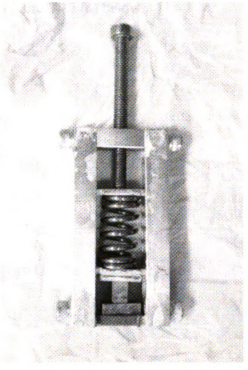

Figure 3-14. Spring loaded design for RT scan.

Initial experiments with cast ingot p-type material showed high contact resistance. The first few polishing attempts did not produce a good result as it was not possible to hold 5mm x5mm x 7mm samples by hand and get flat surface during polishing. The sample would inevitably tilt and there would be unparallel surface mating between the electrode and the TE leg, leaving large gaps. To solve this problem, a two leg stainless

steel sample holder was designed as shown in Figure 3-15 (a) and (b) below. Legs were firmly secured to avoid any movement during polishing which also helped to remove any size difference between n-type and p-type legs as both were polished in the same run. A sequential polishing procedure was used that included a first polishing step with 800 grit sand paper, a second polishing step with 1200 grit san paper and third step of using a 0.3 micron liquid alumina solution on felt cloth. All three steps were carried out on a Leco 2000 polisher as shown in Figure 3-15 (c) below.

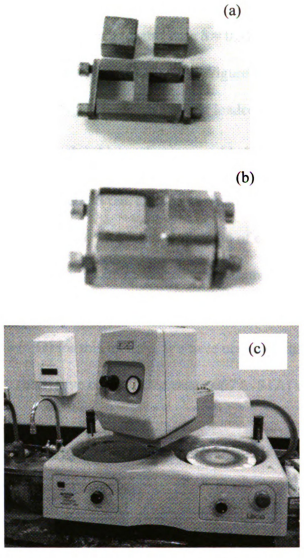

Figure 3-15. (a) Sample holder for polishing (b) TE legs secured inside holder (c) Leco 2000 Polisher with felt cloth on right side plate.

The best p-type result after polishing is shown in Figure 3-16. The contact resistance is 187 $\mu\Omega$ cm^2 which is very high as compared to our goal of less than ~25 $\mu\Omega cm^2$. This contact resistance goal is based upon 10% of total thermoelectric leg resistance. For a p-type leg with electrical conductivity of 1400 S/cm, the total leg

resistance for a 5mm x5mm x 7mm leg is ~ 2 (mΩ). If we define δ as the ratio of contact resistance to total leg resistance, then for this case δ = 0.374. However it can be noted that 4-probe resistance for a single leg is 2.7 (mΩ). Figure 3-17 below shows the result for LAST (ETN 224) cast n-type TE leg with spring loaded contacts. Here again contact resistance is 615 $\mu\Omega cm^2$ which is higher than acceptable limit of 10% of leg resistance.

For electrical conductivity of 800 S/cm, total leg resistance for 5mm x 5mm x 7mm LAST (ETN 224) leg is 3.5 (mΩ). For this leg, the ratio of contact resistance to leg resistance δ = 0.70 and the four-probe resistance for the same leg is 7.1 (mΩ). So if we combine the individual 4-probe resistance of both n-type and p-type leg, we will get a total resistance of 9.8 (mΩ) for this module. We have observed that modules with total 4-probe resistance < 10 (mΩ) give output in the range of 7 to 8 (A) short circuit current.

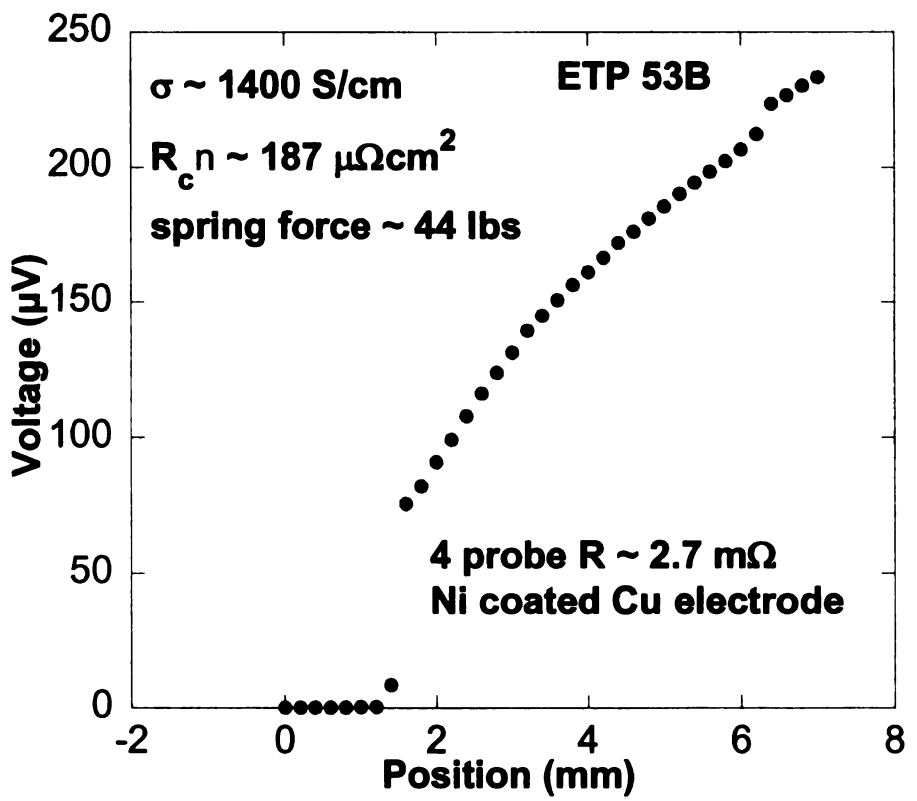

Figure 3-16. Spring loaded ETP53 with Ni plated Cu electrode.

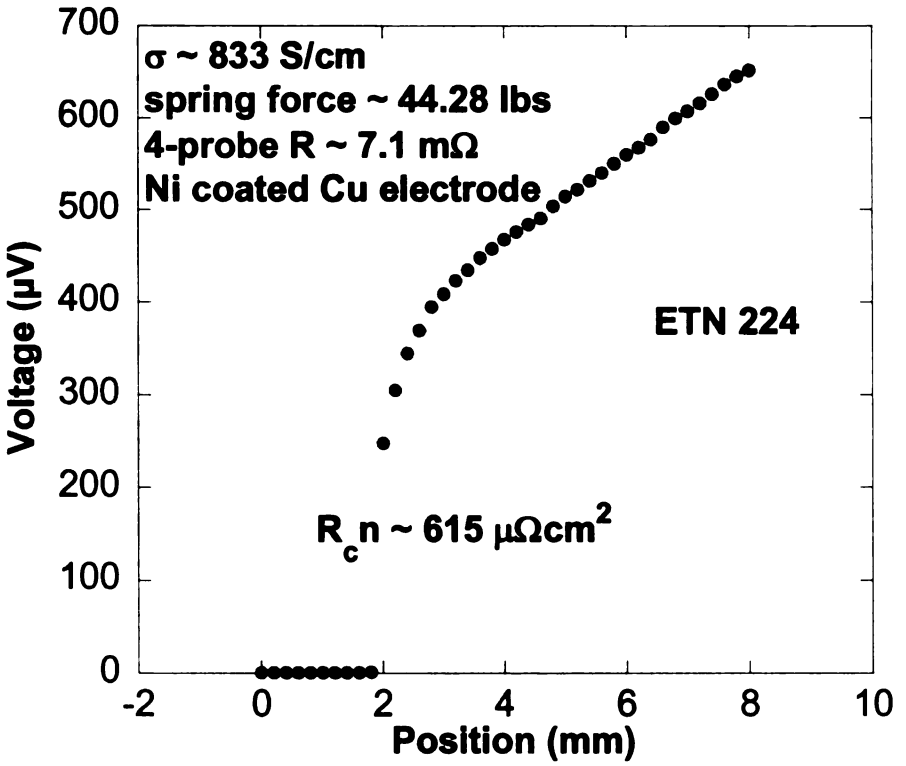

Figure 3-17. Spring loaded ETN 224 with Ni plated Cu electrode.

As described in literature [37], initial module resistance for spring loaded modules is very high as compared to diffusion bonded modules. This is because surface oxide films on TE legs and the electrode initially prevent good electrical contact. However, when the module is heated close to 400 °C range, these oxides dissipate to produce direct mating between the surfaces, giving good electrical contact. Figure 3-18 below shows a plot for spring loaded hot pressed n-type LAST (MSUHP 94). Its contact resistance of 250 $\mu\Omega cm^2$ is much lower than that of a cast ingot which had a contact resistance of 615 $\mu\Omega cm^2$, whereas, the electrical conductivity of hot pressed leg is ~ 100 S/cm and that of the cast TE n-type leg is ~ 800 S/cm. The ratio of contact resistance to leg resistance is δ = 0.036. We speculate that this improved contact resistance may be because of the

smaller grain size of the hot pressed (5-50 micron) as compared to the ~ 700 micron grain size of the cast material.

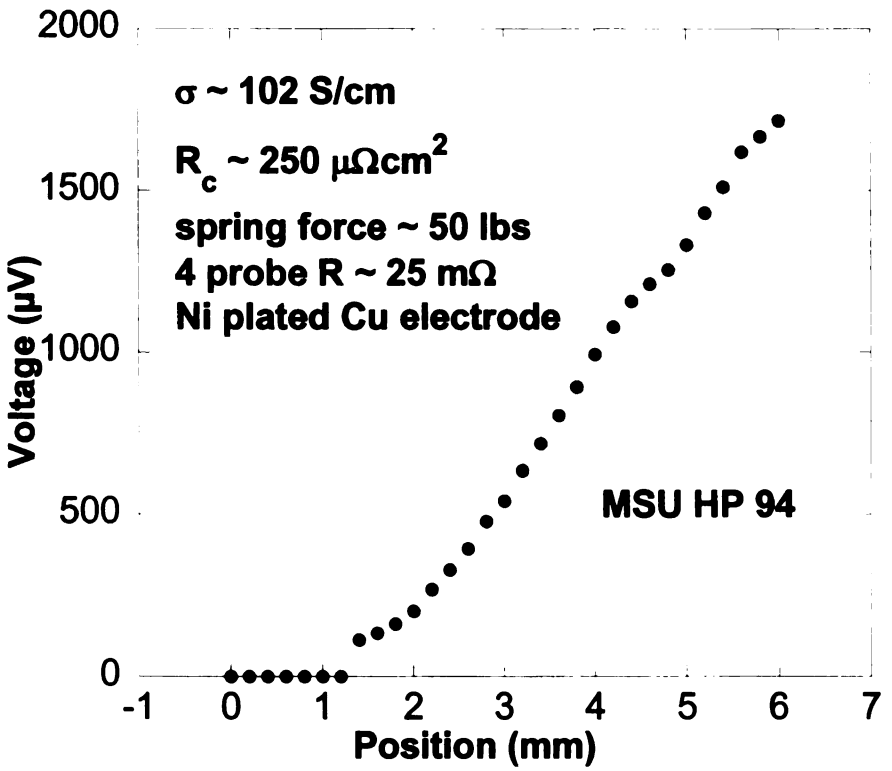

Figure 3-18. Spring loaded hot pressed sample with Ni plated Cu electrode.

3.4 Spring Loaded High Temperature Short Circuit Current Measurements

After several room temperature scans, a high temperature unicouple output measurement apparatus was designed as shown in Figure 3-19 below. It uses two springs and can accommodate a locally made Nichrome (Ni80/Cr20) wire-based heater which is assembled by first winding Nichrome wire on a square piece of alumina, then sandwiching it between another two alumina plates. The three pieces are held together by Fortafix QS/B4 high temperature binder. These heaters have a short life and after a few runs they either fail electrically or alumina plates crack under stress at high temperature.

The first design did not have the four supporting pillars with the middle plate and had difficulty in maintaining balance on the unicouple electrode. The bottom plate is made of Cu for good thermal conductivity which helps keep the cold side temperature down.

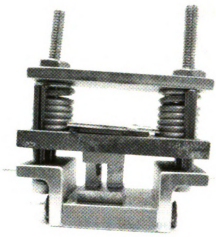

Figure 3-19. High temperature spring loaded unicouple measurement system.

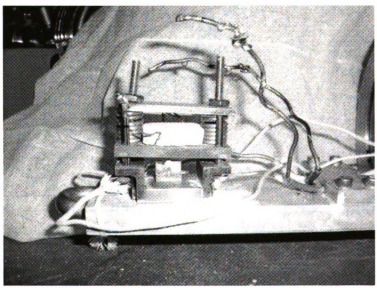

Figure 3-20. Spring loaded apparatus on module testing system (LTMTS).

As mentioned before, due to the high resistance of the measurement wires of the LTMTS, a thick, short wire was used with individual unicouples during short circuit current measurement. If this wire was only soldered to the cold side electrode, it would fall off at high temperature making measurements impossible. To overcome this problem, the soldered joint on the cold side was also coated with QS/B4 for mechanical support. However, this permanent short circuit wire does not allow an open circuit voltage measurement during operation. The first spring-loaded holder did not allow good contact between the electrode and TE legs. The first module tested with this holder was measured under ambient conditions and consisted of LAST (ETN 221), LASTT (ETP 55) and Ni plated Cu electrode. The output is shown in Figure 3-21.

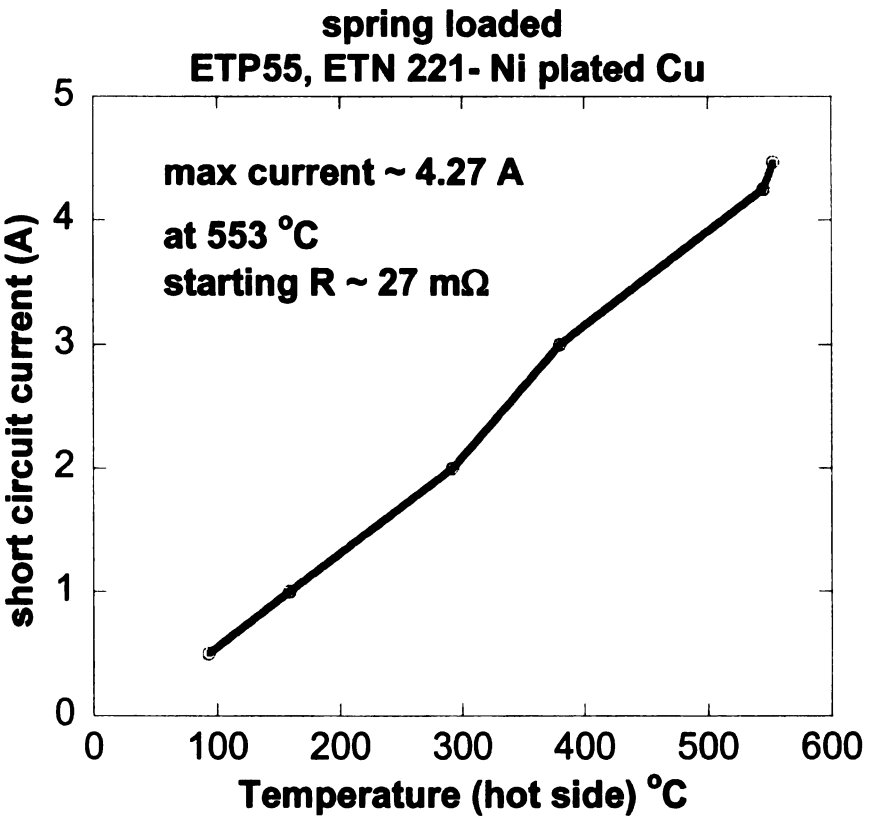

Figure 3-21. First spring loaded module with Ni plated Cu electrode.

For this first module starting four probe resistance was R~ 27 (mΩ), maximum current obtained was 4.27 (A) at 553 °C with corresponding cold side temperature of 55 °C, whereas; expected (simulated) value of short circuit current at this temperature using an iterative technique is 11.1 (A). At 553 °C the heater failed and it was not possible to make any further measurements. The second module tested used an improved design for the module holder that included four pillars passing through the middle plate. This helped to align and keep the two plates parallel thus applying uniform pressure on the hot-side electrode under load. The second module consisted of LASTT (ETP 55) and LAST (ETN 184) with Ni plated Cu electrode and its short circuit current reached 5.82 (A) for cold side temperature of 43 °C as shown in Figure 3-22 below. For these values, the expected short circuit current calculated using iterative technique is 10.69 (A).

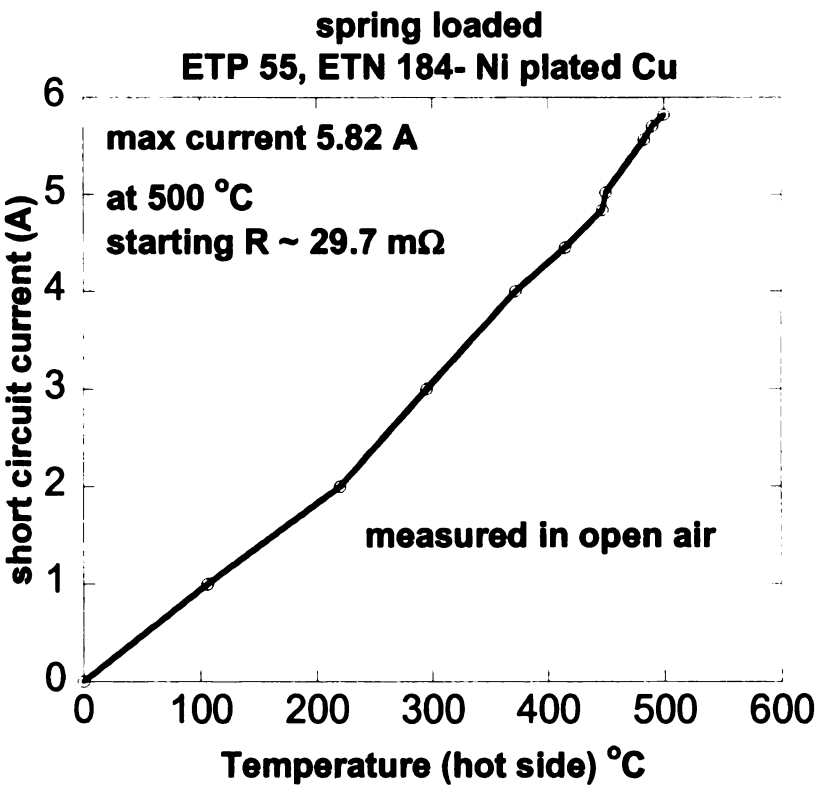

Figure 3-22. Second spring loaded module measured in open air.

The starting resistance of this module was R ~ 30 (mΩ), but when the module was measured after the thermal cycle, resistance dropped to 17 (mΩ) while still under spring load. Probably, the materials expanded during run and developed more a-spots, yielding better conductivity. The springs were further compressed to increase the load and the 4-probe module resistance dropped to 13.7 (mΩ) indicating that even after thermal cycle under ambient condition, pressing the load can break oxide films and increase the true contact area between TE material and electrode. The module was again checked for resistance the next day and the value did not change. This suggested that modules can survive room temperature oxidation.

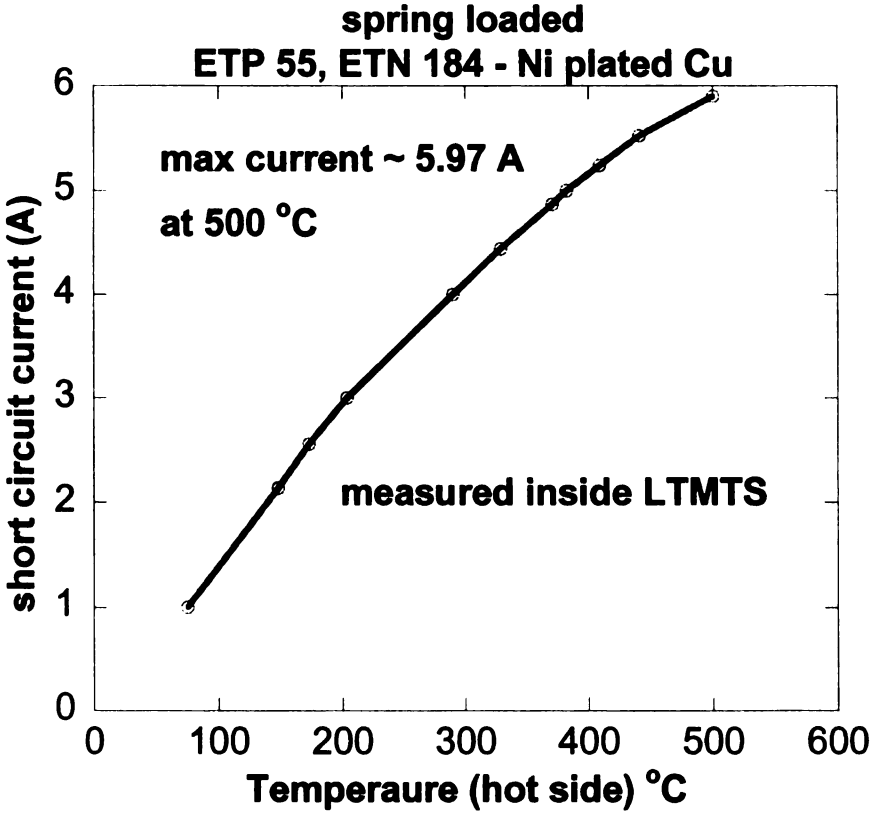

Figure 3-23. First module measured inside LTMTS under Ar.

The second spring loaded module was again measured inside the LTMTS under Ar with a new Ni plated Cu electrode. The open circuit voltage reached 190 mV with short circuit current of 5.67 (A) as shown in Figure 3-23. However, module could not sustain the output current and it started decreasing. The module was cooled down and taken out of measurement system. After cooling, the 4-probe resistance was 20 (mΩ). When the module was removed from the spring loaded structure, resistance increased to 86 (mΩ), confirming the idea that even with high resistance surfaces, spring loading can improve the contact area. No sign of Cu diffusion was observed visually.

3.4.1 New heater location

In previous modules the heater was not placed directly on the module, but rather the middle of the Cu plate contacted the module and the heater was placed on top of the Cu plate. Because of this indirect heating of the module, heat losses were high.

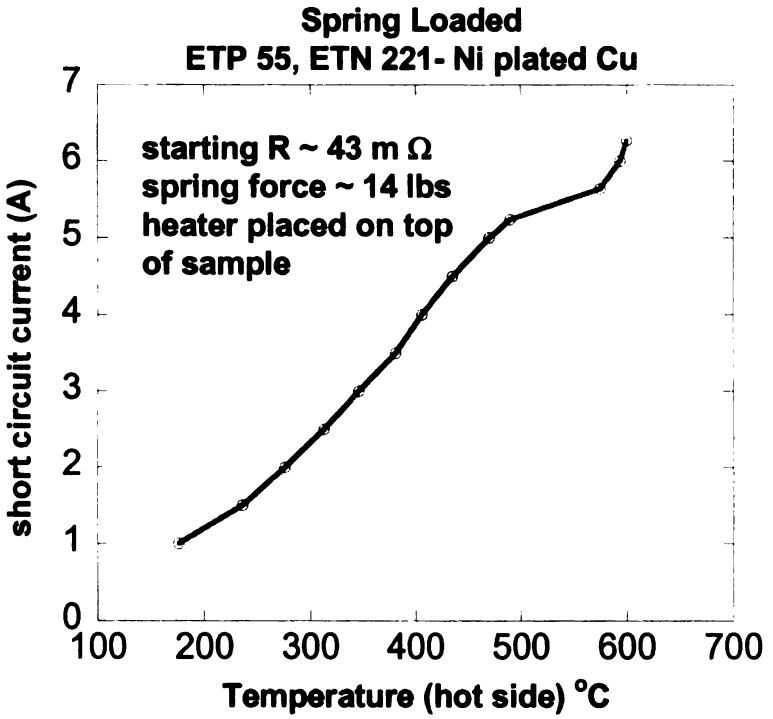

Figure 3-24. Spring loaded module with heater directly on unicouple.

A third module was prepared with LASTT (ETP 55), LAST (ETN 221) and Ni plated Cu. The heater was placed directly on top of the unicouple for better heat transfer. The output is shown in Figure 3-24 above. Maximum short circuit current obtained was 5.24 (A) at 490 °C. However, since now the heater was much closer, the cold side temperature also rapidly increased to 71 °C. The current started decreasing after the module reached 490 °C. Expected short circuit current using an iterative technique for these values of hot side and cold side temperature is 10.43 (A).

A fourth module was prepared with LASTT (ETP 55) and LAST (ETN 164). The n-type leg (ETN 164) had good temperature dependent electrical conductivity values as shown in Figure 3-25 below.

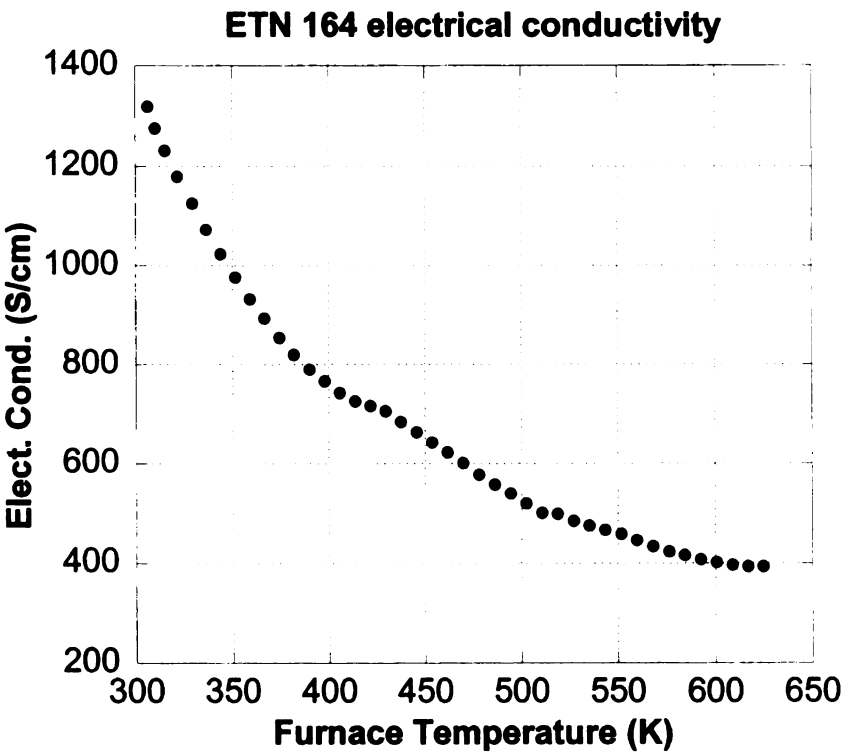

Figure 3-25. Temperature dependent electrical conductivity for ETN 164.

As mentioned before, to measure open air short circuit current, the short circuit Cu wire was coated after soldering with QS/B4 so that at higher temperature the solder would not melt on the cold side and hold the wire for measurement. The module was coated with QS/B4 to avoid sublimation during operation. The module was spring loaded and heater was placed immediately on top of the unicouple. This module was measured in open air and short circuit current reached 10.0 (A) for a hot side temperature of 589 °C and corresponding cold side temperature of 91 °C as shown in Figure 3-26 below. Expected short circuit current for these values of temperatures using iterative technique is 10.72 (A), however, current started decreasing immediately.

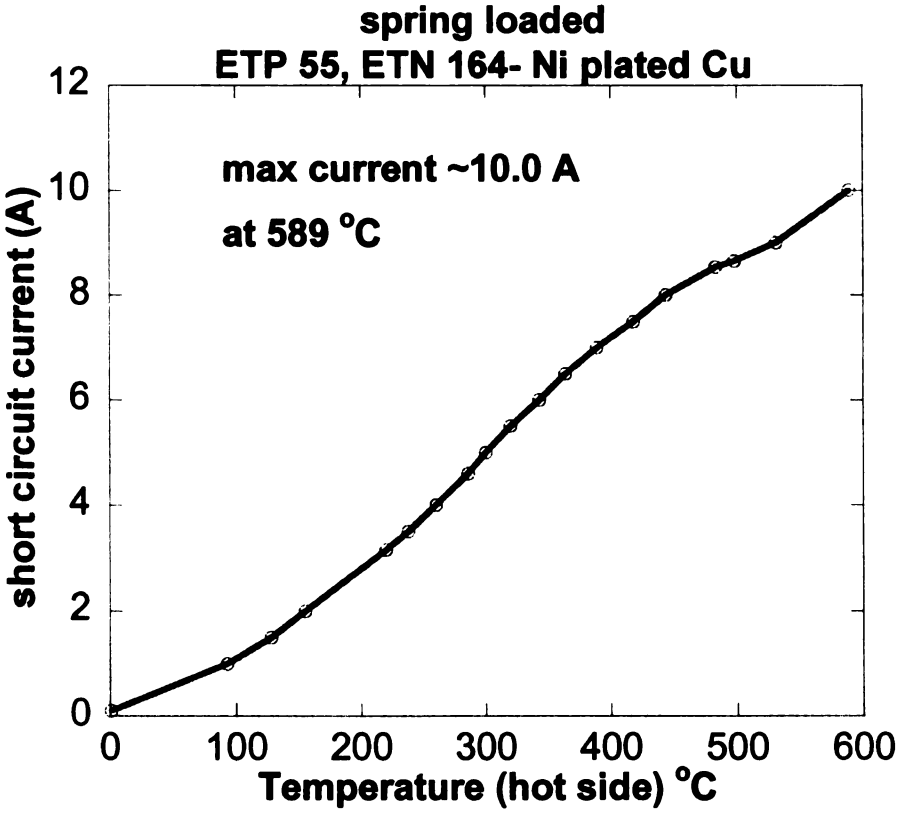

Figure 3-26. Spring loaded module with highest recorded current.

3.4.2 Spring Loaded Hot Pressed Module

Next a spring loaded module was prepared with a hot pressed n-type material (MSUHP 94) which had room temperature electrical conductivity of ~ 100 (S/cm). High temperature measurements for electrical conductivity and thermopower are not available at the moment. However, based on previous hot pressed sample data of electrical conductivity and thermopower we assumed that module output would be low. The heater was placed immediately on top of the unicouple and the module was measured in open air. The output values for short circuit current are shown in Figure 3-27 below.

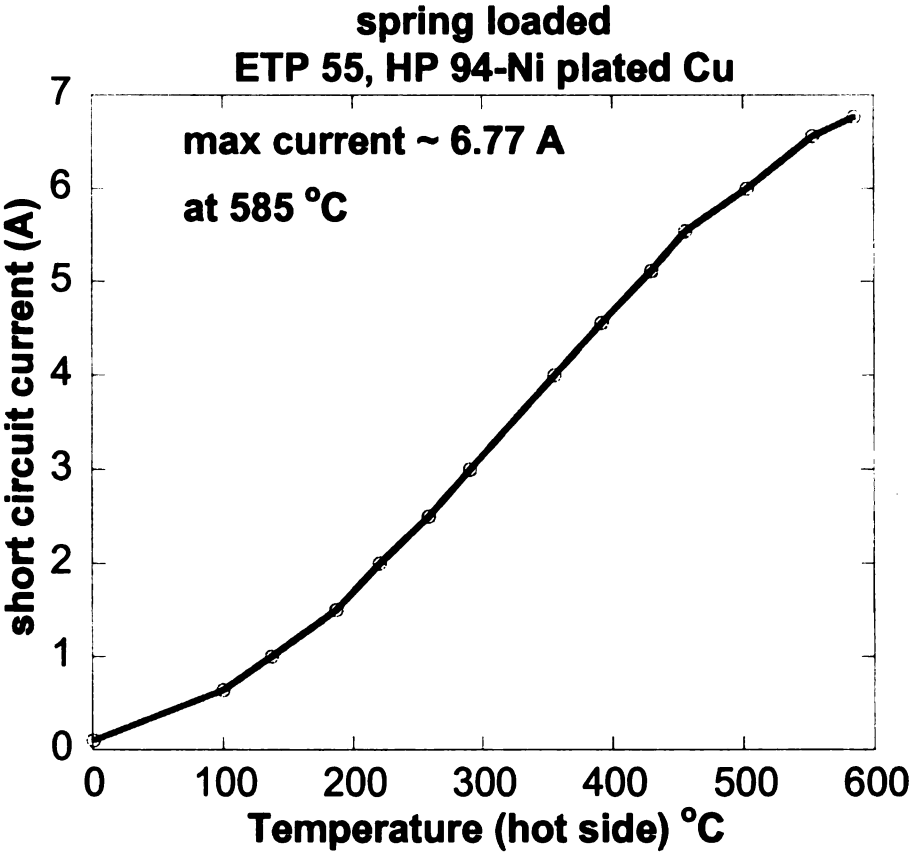

Figure 3-27. Spring loaded module with MSUHP94.

As shown above, the short circuit current reached 6.77 (A) for a cold side temperature of 83 °C. This is the highest short circuit current observed for any hot pressed module in our lab, however, current started decreasing immediately at this temperature.

3.4.3 Spring Loaded Ni Electrode Module

Previous modules used Ni plated Cu for better electrical conductivity but Cu is notorious for its high reactivity and a thin Ni coating cannot stop Cu diffusion through TE material at high temperature. A thick Ni electrode of 5mm x 5mm x 12mm (R ~ 33.5 μΩ) was used as a hot side electrode for next experiment. This module was spring loaded and coated with QS/B4 to avoid sublimation during heating and it reached an output short circuit current value of 8.00 (A) for a hot side temperature of 515 °C and cold side temperature of 62 °C as shown in Figure 3-28 below.

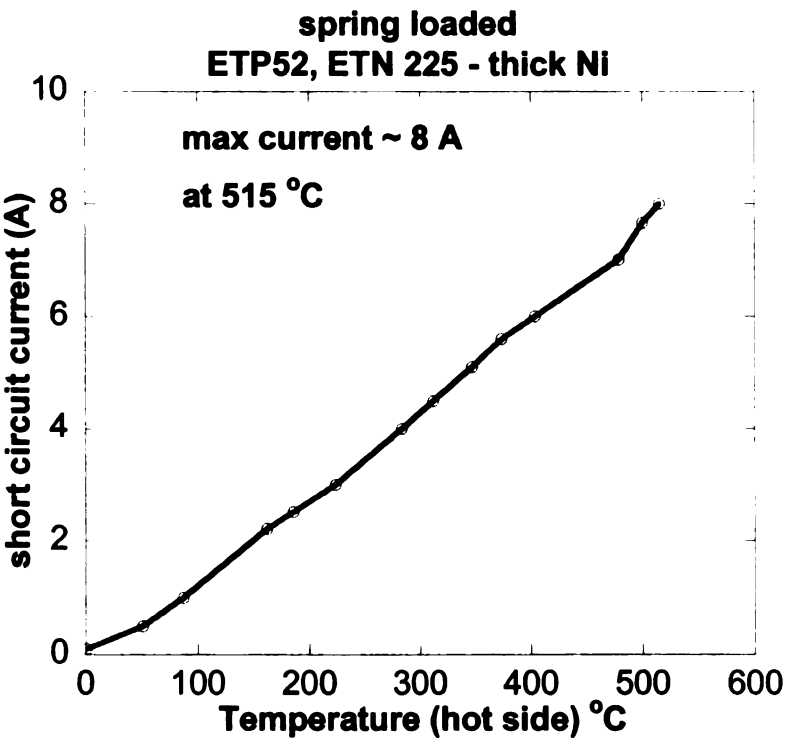

Figure 3-28. Spring loaded module with Ni electrode.

The expected value of short circuit current using iterative technique for these values of hot side and cold side temperature is 10.71 (A), however; current started decreasing after this temperature.

A second module was prepared with ETN 225, ETP 52 II, thick Ni electrode and measured inside the module testing system (LTMTS) under Ar. This module reached 6.13 (A) for hot side temperature of 600 °C and cold side temperature of 57 °C as shown in Figure 3-29 below. The low current can be attributed to the high resistance of measurement wires of the module testing system. The current started decreasing at 600 °C and this module was brought down to room temperature.

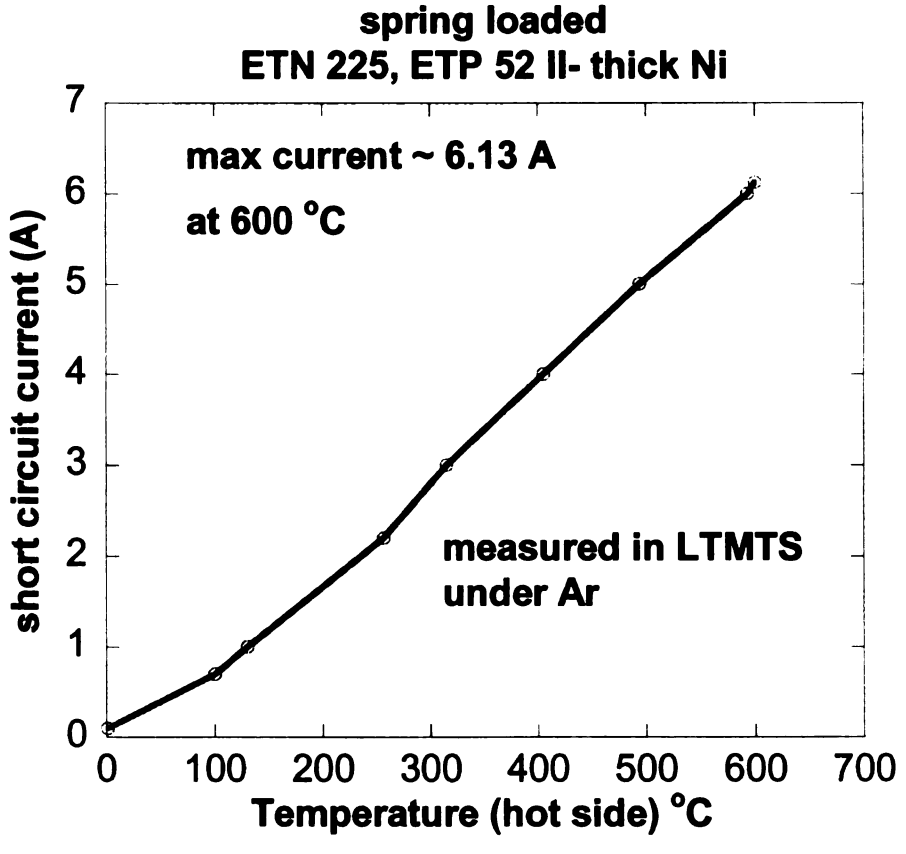

Figure 3-29. Spring loaded Ni electrode based module measured under Ar.

3.4.4 Spring Loaded Silver (Ag) Electrode Module

Silver (Ag) has the lowest electrical resistivity (15.87 nΩ-m) and highest thermal conductivity (429 W/m-K). Modules based on Ag electrode are supposed to perform better than Ni based modules due to these properties. However Ag reacts with sulfur (S) in air and turns into tarnish brown color silver-sulfide (Ag_2S) and reacts with tellurium in TE material to form silver-telluride (Ag_2Te) which is an n-type semiconductor. The next module was prepared with silver electrode using LAST (ETN 225) and LASTT (ETP 52II). This module was measured in open air and its short circuit current reached 8.00 (A) for a hot side temperature of 507 °C and a cold side temperature of 78 °C as shown in Figure 3-30 below. The expected short circuit current using iterative technique for these temperatures is 10.40 (A). The current started decreasing at 507 °C and the module was cooled down to room temperature.

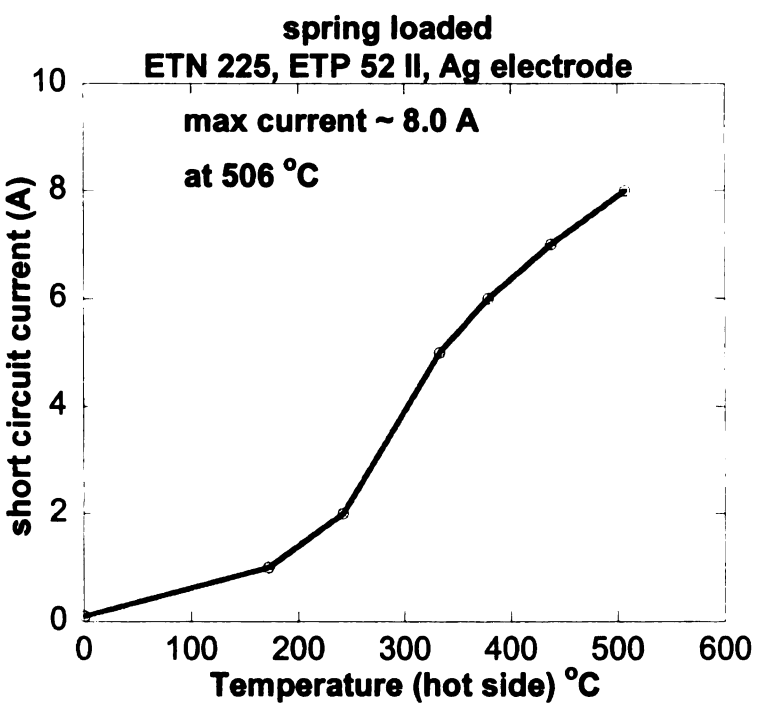

Figure 3-30. Spring loaded Ag electrode module.

3.4.5 Spring Loaded Module with tungsten (W) coated samples

In all previous spring loaded experiments current could not be sustained at its peak value. EDS has shown that Te comes off at the TE leg surface and reacts with the electrode. Kortier [39] has successfully used tungsten (W) with PbTe thermoelectric legs as hot side electrode since tungsten is non reactive to Te. However, tungsten makes a stable bond with oxygen at higher temperatures which is difficult to remove. Moreover tungsten has a very low co-efficient of thermal expansion (CTE) ~ (4.5×10^{-6} in/K) which makes it unsuitable for diffusion bonding with LAST (with CTE of 22×10^{-6} in/K). However, since spring loaded modules are supposed to have no permanent bond between TE legs and electrode, tungsten can still work. For this experiment, LAST and LASTT legs were coated with tungsten (~10 nm) then Ti (~ 200 nm) and Au film inside the physical vapor deposition (PVD) system through e-beam evaporation of target material. Ti film was coated as it is more resistant to oxidation than tungsten and Au film was deposited to increase surface conductivity. A spring loaded module was prepared using these coated TE legs (ETN 225 and ETP 52) and thick Ni electrode and measured inside the module testing system (LTMTS) under Ar. The reason for Ar atmosphere was to provide an oxygen free environment. The module out put is shown in Figure 3-31.

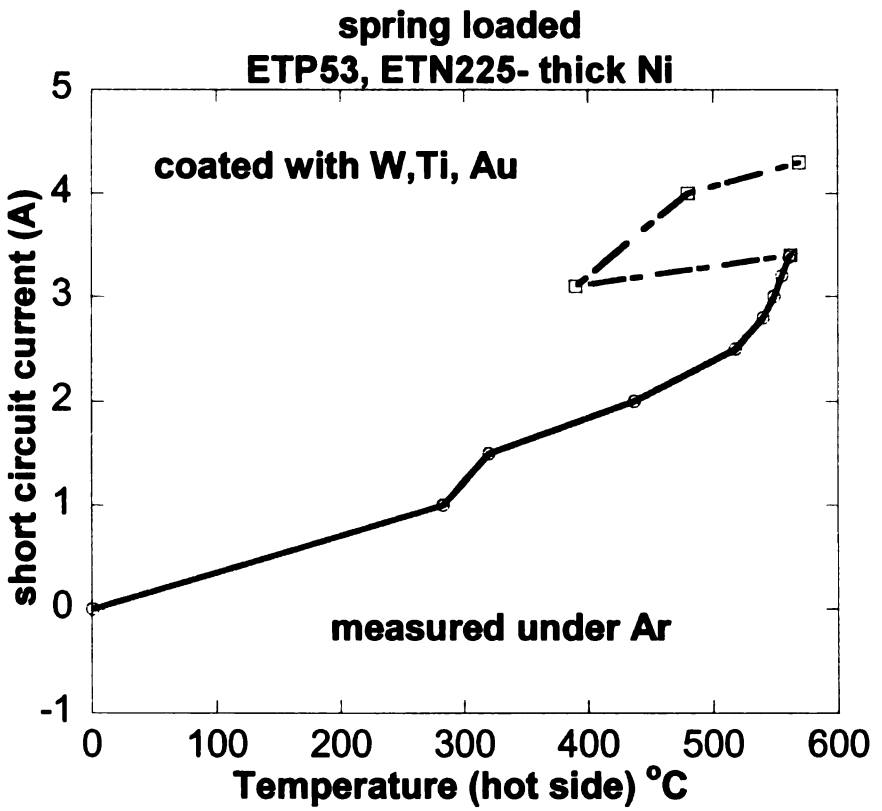

Figure 3-31. Spring loaded tungsten coated module measured under Ar.

It appears that coated film has high resistance as current initially only reached 3.4 (A) at 561 °C. The temperature was decreased and increased again to see thermal cycling effect and current started increasing again and reached 4.3 (A) for about the same hot side temperature. This led to the module being cooled down and opened to inspect the surface. A dark green film could be seen indicating tungsten-titanium-oxide (WTiO). Also, there were cracks on the film and we postulate that from cracks tellurium seeped out and was responsible for late increase in output current. The heater failed during the second cycling and it was not possible to do any further measurements.

The same module was again tested in open air with a new Ni coated Cu electrode and TE leg surfaces were left untouched from previous run to see the post run effect of

coated film. Short circuit output current is shown in Figure 3-32 below. Current could not be sustained at high temperature and module was cooled down.

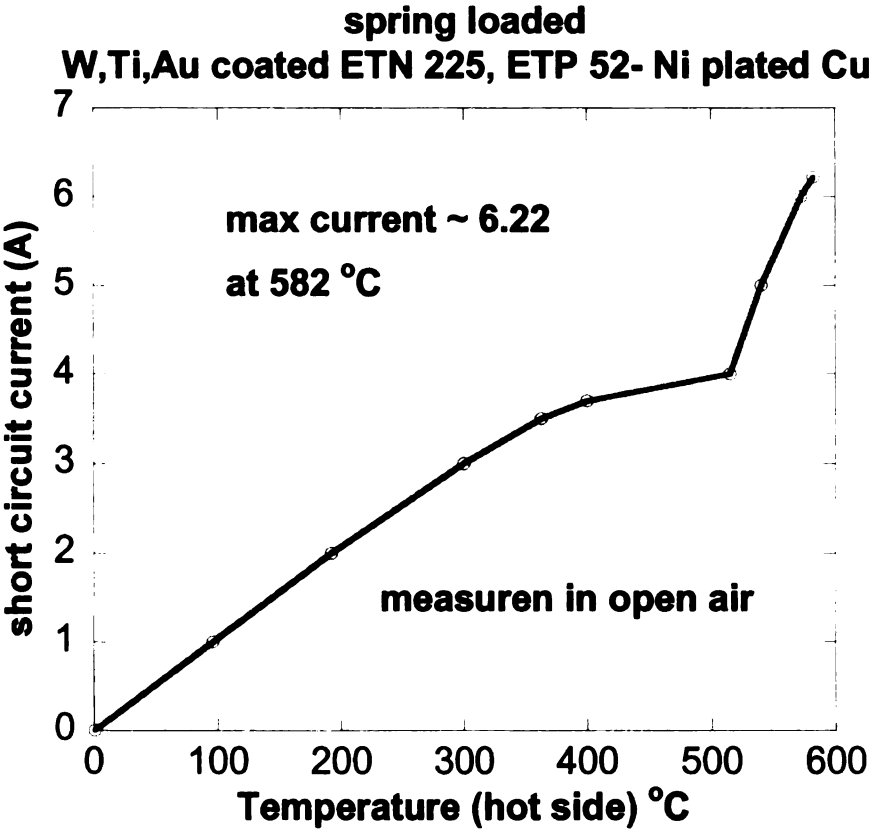

Figure 3-32. Spring loaded module with tungsten coating measured in air.

After this run module was opened to investigate hot side surfaces. There was no indication of Cu diffusion into TE leg, however tungsten coating was black like a thick carbon film and rather a depression could be seen in Ni coated Cu electrode indicating strong oxidation.

3.4.6 Spring Loaded and InGa Based Combined Module

Experiments were carried out to see the combined effects of using InGa under spring load. For this a module was prepared with LAST (ETN 221), LASTT (ETP 55) polished legs, InGa was used as liquid contact and Ni plated Cu was used as hot side electrode. The module was spring loaded and measured under Ar inside the LTMTS. Before high temperature cycling module 4-probe resistance was R ~ 8.5 (mΩ).

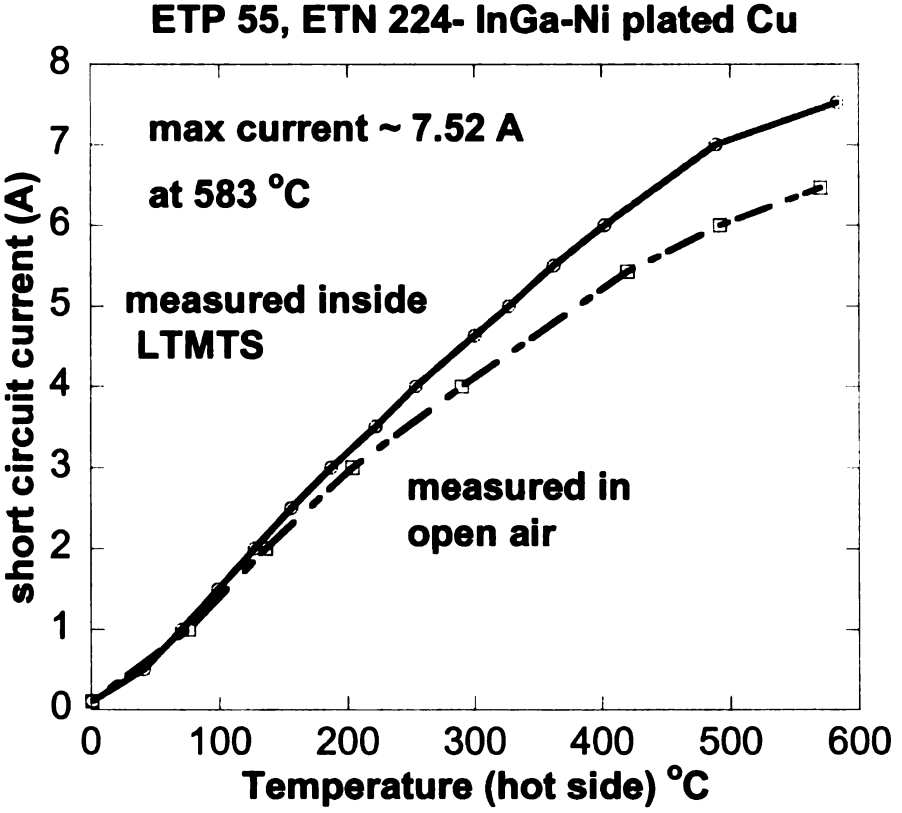

Figure 3-33. Combined spring loaded and InGa liquid contact based module.

As shown in Figure 3-33 above, the short circuit current reached 7.52 (A) for a hot side temperature of 583 °C and a cold side temperature of 33 °C with an open circuit voltage of 212 (mV). The current started decreasing at this temperature and module was cooled

down to room temperature. The same module was then measured in open air with a starting resistance of 12.0 (mΩ). As shown in Figure 32, short circuit current reached 6.47 (A) for a hot side temperature of 570 °C with a cold side temperature of 42 °C. This low output current is probably due to InGa reaction with LAST and LASTT in previous high temperature cycle. A similar experiment was carried out with silver (Ag) electrode combining InGa and spring loaded configuration. Two open air high temperature runs were carried out as shown in Figure 3-34 below. In the first run measurement wire broke at 440 °C and experiment could not be continued. In the second run the output current reached 5.93 (A) at 600 °C with corresponding cold side temperature of 106 °C.

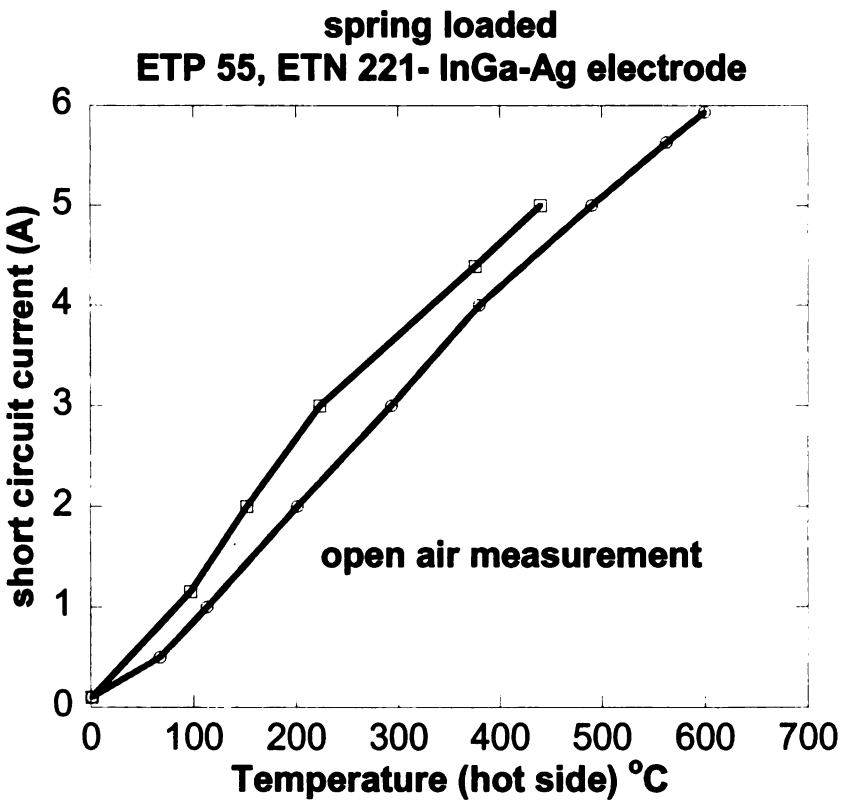

Figure 3-34. Spring loaded InGa based Ag electrode module.

The module was cooled down and after a visual inspection it did not appear that InGa reacted with Ag but a thick layer could be seen on module's surface facing the electrode which probably consisted of high resistance AgTe.

Table 3-2. Summary results for spring loaded modules.

Electrode	**Material & coatings**	**Air/Ar**	**Th (°C)**	**Tc (°C)**	**I_{sc} (A)**	**Comments**
Ni plated Cu	ETP 55 ETN 221	Air	553	55	4.27	First design
Ni plated Cu	ETP 55 ETN 184	Air	500	43	5.82	Improved design First run
Ni plated Cu	ETP 55 ETN 184	Ar	500	31	5.67	second run
Ni plated Cu	ETP 55 ETN 221	Air	490	71	5.24	Heater on unicouple
Ni plated Cu	ETP 55 ETN 224	Air	589	91	10.72	Thick short wire
Ni plated Cu	ETP 55 HP 94	Air	585	83	6.77	Hot pressed n-type
Ni	ETP 52 ETN 225	Air	515	62	8.00	Thick Ni with 33.5 μΩ
Ni	ETP 52 ETN 225	Ar	600	57	6.13	Measured inside LTMTS
Ag	ETP 52 ETN 225	Air	606	78	8.0	Silver electrode
Ni (Thick, 33.5 μΩ)	W-Ti-Au ETP 52 ETN 225	Ar	561	51	3.4	Measured inside LTMTS. First run
Ni plated Cu	W-Ti-Au ETP 52 ETN 225	Air	582	67	6.22	Second run with different electrode
Ni plated Cu	ETP 55 ETN 224	Ar	583	33	7.52	Measured inside LTMTS, 1st run
Ni plated Cu (with InGa)	ETP 55 ETN 224	Air	570	42	6.47	Second run
Ag (with InGa)	ETP 55 ETN 221	Air	600	106	5.93	Silver electrode

Conclusion

A series of experiments were carried out to obtain short circuit current for LAST and LASTT material using InGa liquid contacts and a spring loaded configuration. Both types of module fabrication techniques produced high output currents of 10.5 (A) and 10.0 (A) respectively. Different types of coatings were tested on TE leg surfaces to prevent reaction between LAST, LASTT and InGa at high temperature. In case of spring loaded modules tungsten films were tested but these efforts have not been able to sustain current at their peak value during high temperature operation. The spring loaded design looks more promising since it has been employed in the past for PbTe based module. Future experiments will include using a tungsten electrode to prevent tellurium reactivity with hot side electrode.

Chapter 4: High Temperature thermoelectric contact investigation using Voltage Profiling System (HTVPS)

Introduction

The compound Pb-Sb-Ag-Te (LAST) has shown promising thermoelectric properties for power generation application [1]. TE power generation modules made with this compound operate at ~ 900 K. High electrical conductivity, low thermal conductivity and low contact resistance are important characteristics of thermoelectric modules. At room temperature contact resistance acceptable limit is below 20 $\mu\Omega\cdot cm^2$ for 5 mm x5 mm x 7 mm LAST based TE legs (within 10% of total leg resistance) and various methods are under investigation to achieve this goal [23]. However, contact resistance is a function of temperature as rate of diffusion changes with temperature. Moreover, at high temperature materials undergo thermal stresses which may induce micro cracks in the material resulting in degradation of TE module performance. Electrical conductivity of LAST TE material decreases with increasing temperature while contact resistance tends to increase. To investigate electrical conductivity and contact resistance of thermoelectric modules at high temperatures, a novel voltage profiling system is designed and fabricated. The system is designed to scan across the individual samples for *in situ* monitoring of voltage variations along a sample from which electrical conductivity and contact resistivity can be determined. The motor motion, furnace temperature, and data acquisition are automated with LabVIEW National Instruments software. To confirm the validity of the system NIST reference sample SRM 1461 was measured at room

temperature and ~ 700 K, showing electrical conductivity values of 12585 S/cm and 9505 S/cm which is in good agreement with reference data. Thermoelectric unicouples were then scanned for high temperature contact resistance measurement.

4.1 System Description

The system is designed to measure electrical conductivity and contact resistances within the range of 300K to 800K. The system works on a four-probe measurement principle. A variable magnitude square wave function switching current is supplied at 33 Hz with a 50 % duty cycle. Usually for LAST material samples, a 100 m(A) current is used. Current is sourced through a Keithley 2400 source meter and voltage is measured by Keithley 2002 Multimeter. The unique feature of this system is the use of bellows. A 20DAM series (20DAM10D2U-K) digital linear actuator DC stepper motor by Portescap is used for bellows movement. It has linear travel of 0.0254 mm per step with maximum travel distance of 15 mm. It uses a 12 V power supply and produces a maximum force of 20 N. A Lini Stepper controller along with NI USB-6501 24 line digital I/O is used for motor interface to a PC. A detailed system sketch is shown in Figure 4-1. To create the scanning motion, the bellows is positioned on top of the motor. Bellows movement is transferred through an alumina tube, which is coupled to the bellows by a one-inch stainless steel interface at the bottom. At the top end of this tube is the probe tip which drags across the sample with up-down movement of the bellows. The probe tip design is an important aspect of this apparatus. Initially a tungsten wire wrapped around an alumina tube was used. But it did not effectively make contact with sample in motion that resulted in erroneous data. Our previous experience of using pogo connector pins with a

room temperature scanning probe was a success. The same idea is applied here and a new probe pin holder was designed as shown in Figure 4-2. The collar design firmly holds on top of the alumina tube with the help of a set screw and another two set screws hold the pogo connector in place. The connector is pushed against the sample and tightened with the set screws. The spring inside the connector ensures a good connection with the sample even if the sample surface is not perfectly flat.

The sample holder is a round nickel disc with five holes to accommodate the top edge of the alumina tubes. Wires for current sourcing and voltage measurements are run through four alumina tubes. Alumina is selected as it can withstand high temperatures. At the base an aluminum cage is designed to hold these tubes with provision for addition of a fifth tube. This aluminum cage is fastened to the base plate where bellows are positioned on top of the DC motor. The sample holder and alumina tubes are inserted into a quartz tube to maintain vacuum and sustain a high temperature inside the furnace. A PID controlled ceramic furnace by Omega is used which can go up to ~ 982 °C with RS-232 interface used to automate the furnace. There is also provision for using a local heater inside the quartz tube. The sample is placed so that it touches the heater. This allows visual inspection at high temperature of pogo pin movement across the sample contact. This local heater is custom made with Ni80/Cr20 thin wire with a heater resistance in the range of ~ 15 Ω. A type K thermocouple is used to measure furnace temperature. Since the sample is under vacuum, there is a difference between sample temperature and furnace temperature. For accuracy of data, the sample temperature is also measured using a single ended Pt/PtRh Type-S thermocouple. Silver paste is used to attach the thermocouple and measurement wires to the sample. Initially we used low

temperature silver past for high temperature measurements but this resulted in erroneous measurements. To overcome this problem a 2" x 1" stainless steel rectangle was designed as shown in Figure 4-3. The sample is now pressed under a screw during operation which helps to maintain good contact of the measuring voltage and current wires with the TE sample. Lately we have started using high temperature silver paste by SPI Supplies and wire contacts have performed better than with low temperature silver paste. Omega RTD Pt (100Ω) is used along with two Keithley 2182 Nanovoltmeters for reference and sample temperature measurement. A Keithley 2601 source meter is used to source 10 μA to the RTD. For better noise immunity, twin axial cable and connectors are used. The vacuum system consists of a Varian V70 Turbo pump and a dry scroll-roughing pump. This enables the system to achieve better than milli-Torr range vacuum. All materials have the tendency to outgas under vacuum at high temperature which has caused a problem with measurement as the Au from measuring probe would come off at higher temperature and deposit on the LAST material. Also, the motor would not be able to pull down the probe after upward motion as bellows had to be moved against the vacuum suction power. It was also noticed that backfilling the bonding furnace apparatus in this lab with non reactive gas like Ar improves the results. Now the system is equipped with an Ar gas backfilling option. IEEE-488 GPIB is used to control all equipment through a PC.

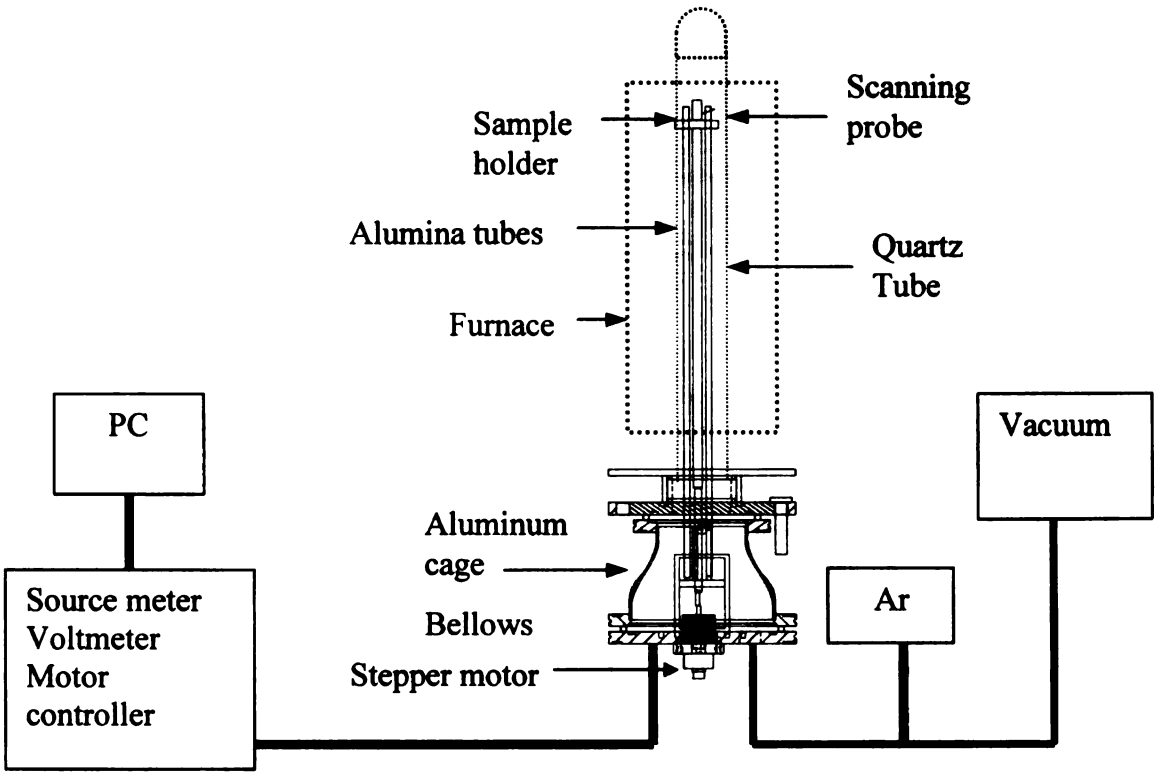

Figure 4-1. High Temperature voltage profiling system.

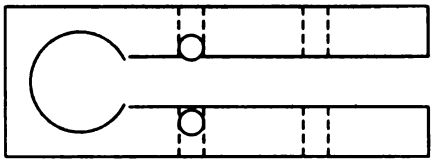

Figure 4-2. Probe pin holder.

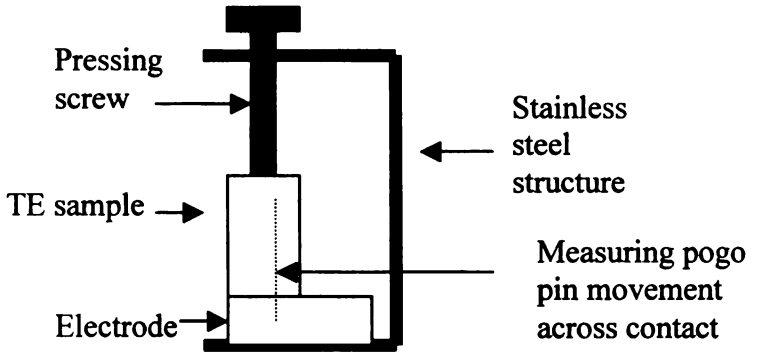

Figure 4-3. New sample holding arrangement.

4.2 System Operation

For all voltage measurements, the current through the sample is rapidly switched from positive to negative values (at a frequency of greater than 30 Hz) to avoid thermal offset voltages [40] which can be a significant source of error. The current is flipped more than 20 times and the magnitude of the readings is averaged for a single measurement. Voltage is scanned along the surface of the sample and plotted against position (X). The electrical conductivity (σ) is then determined by calculating the slope dV/dX along with sample dimensions using following expression:

$$\sigma = \frac{I}{\frac{dV}{dx} \cdot \text{area}} \left(\frac{\text{S}}{\text{cm}}\right) \qquad (4.1)$$

This method is more accurate than typical four-probe measurement as the voltage profile is fitted to many points along the sample instead of just two points. To ascertain the

accuracy and validity of equipment a NIST SRM 1461 sample was cut into 2.9mm x 2.9 mm x 9.7 mm dimensions for electrical conductivity (σ) measurements. The sample was first scanned at 294 K and then at ~700 K. As expected there is a considerable decrease in electrical conductivity at higher temperatures. As shown in Figure 4-4 measured values are 12686 S/cm at room temperature and 8606 S/cm at ~ 700 K, which are in good agreement with reference data.

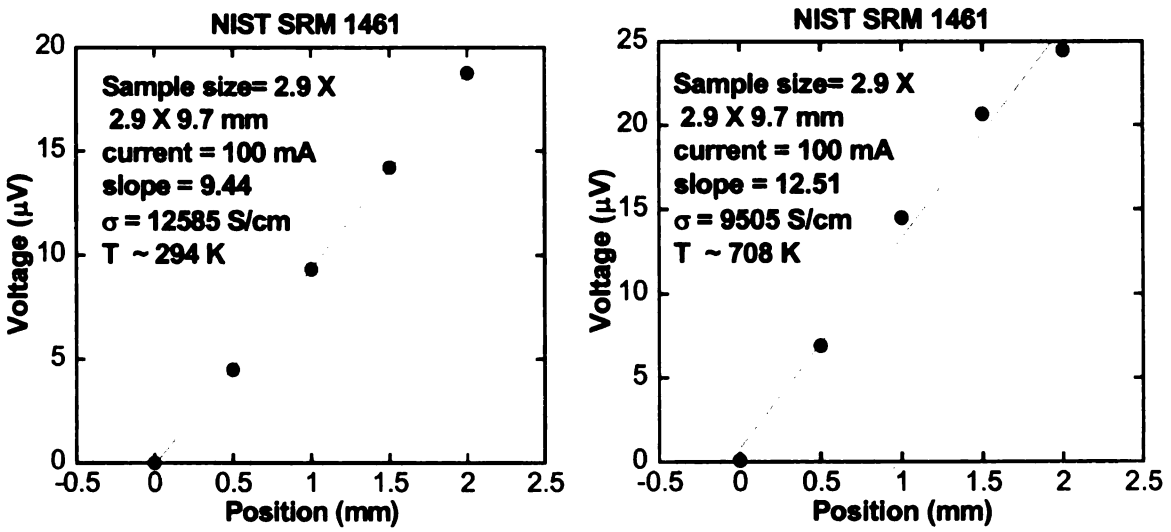

Figure 4-4. NIST SRM 1461 room temperature and high temperature plots.

4.3 High temperature contact investigation

High temperature contact resistance measurements were carried out to determine the viability of different diffusion bonding alloys using the high temperature voltage profiling system (HTVPS) described above. The flow chart in Figure 4-5 shows the different bonding materials investigated for high temperature contact resistance measurement.

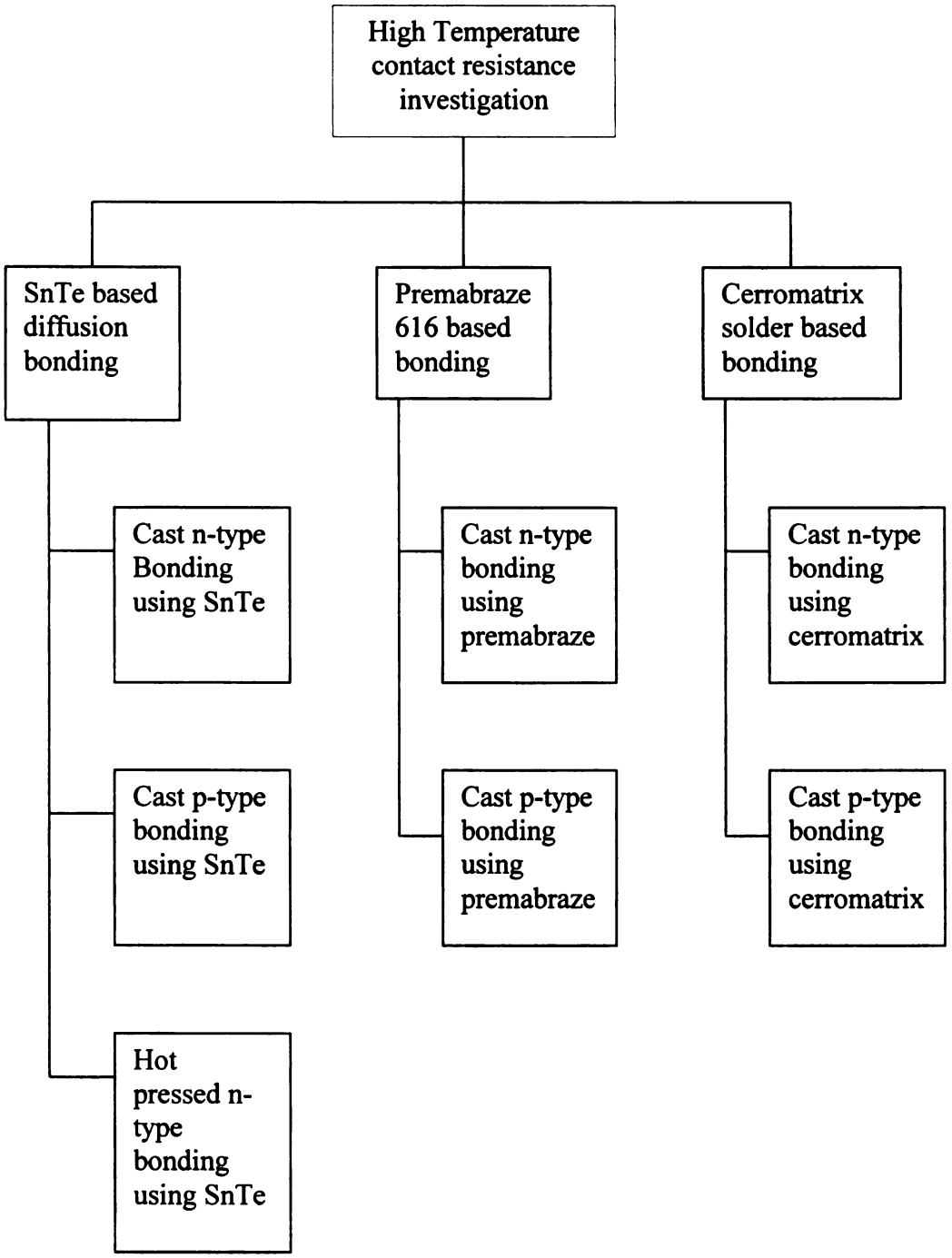

Figure 4-5. Bonds and materials investigated for high temperature contact resistance measurement.

4.3.1 SnTe based modules

SnTe is a p-type semiconductor extensively studied for PbTe and $(AgSbTe_2)_{0.15}(GeTe)_{0.85}$ (commonly known as TAGS85) based TE modules [41]. Seetoo[42] used a stoichiometric Sn and Te powder mixture at the bonding site to generate sufficient heat through an exothermic reaction which is local to the bonding site and does not affect the entire TE leg. We follow Seetoo [42] for our bonding procedures.

Sn and Te powders are added in a ratio of 70:30 respectively, mixed thoroughly and then cold pressed in a dye producing circular discs of ~ 500 microns thick and 6 mm in diameter. The prepared disc is placed between the hot shoe (comprised of either stainless steel 316 or Ni) and LAST material. This arrangement is pressed under load in a custom-made diffusion bonding apparatus and inserted into a three zone furnace operated under Ar. Temperature is raised to 888 K and is allowed a bonding time of ~ 4hrs. The exothermic reaction can be described as:

$$Sn + Te \longrightarrow SnTe + Q \qquad (4.2)$$

Here Q is the heat generated during the process. This reaction is initiated at about 571 K [42]. As mentioned previously LAST material has a linear CTE of 22×10^{-6} (ppm/°C) and a suitable material is needed at the hot side junction to match this property and avoid shear stress on the mating surfaces during high temperature operation. CTE for SnTe is 21.3×10^{-6} (ppm/°C) [40] which is closely matched to that of LAST material. The thermal conductivity of SnTe is ~ 10 W/m-K above 100 K and its electrical conductivity is ~ 2×10^{4} S/cm [43]. LAST unicouples diffusion bonded using cold pressed SnTe were

tested for high temperature contact resistance in high temperature voltage profiling system (HTVPS) and the results are presented in next section.

4.3.1.1 SnTe based cast n-type bonded modules

Carpenter high expansion 19-2 alloy has a nominal composition of (0.55C, 1.0 Mn, 0.20Si, 2Cr, 19Ni, Bal Fe), electrical resistance value of 79 uΩ-cm and is used for hot side electrode because it has a CTE of (20×10^{-6} /°C) which is closely matched to the CTE of LAST material (22×10^{-6} /°C). This helps to avoid shear stresses during heating of unicouple. As can been seen from the following plots it forms a high resistance bond even at room temperature and as the temperature is increased, contact resistance also increases. This is probably the reason that in literature [41] and [42] SnTe is used only for p-type semiconductor TE legs. However, this is not the case in [44] where SnTe was used to bond both n-type and p-type PbTe legs with W and Ta as the hot shoe with satisfactory results. Figure 4-6 below shows the progression with temperature for an n-type cast TE leg ETN 72 bonded to Carpenter Steel 19-2 using cold pressed SnTe. Bonding temperature was 650 °C and bonding was carried out under Ar for 0.5 hr. As the temperature was increased inside the HTVPS, the contact resistance decreased. It can also be observed that the temperature dependent contact resistance is strongly dependent upon the initial room temperature value of contact resistance. In this particular case there is no 'break' between the electrode and TE leg, rather there is a high resistance region at the junction which is probably due to SnTE diffusion into the TE leg during the bonding operation. This high temperature region can probably be attributed to oxygen in cold pressed SnTe as the coin was pressed in open air in this particular case.

Figure 4-6. ETN 72 bonded to Carpenter Steel 19-2 using SnTe (a) Room temperature scan (b) Scan at 100 °C. (c) Scan at 200 °C (d) Scan at 300 °C. (e) Scan at 400 °C (f) Scan at 550 °C.

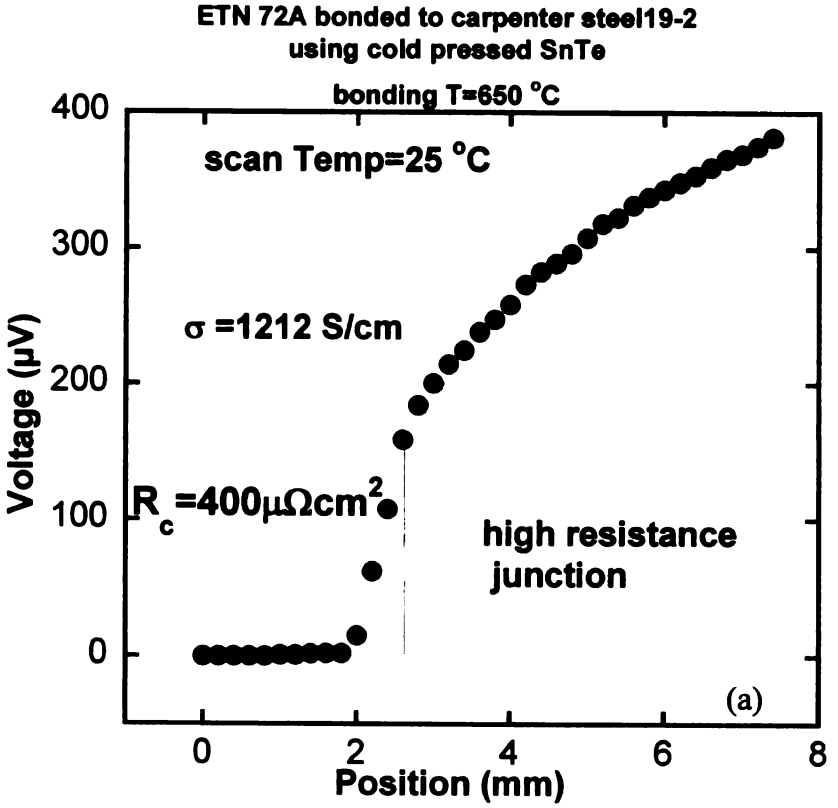
ETN 72A bonded to carpenter steel19-2
using cold pressed SnTe
bonding T=650 °C
scan Temp=25 °C
σ =1212 S/cm
R_c=400μΩcm^2
high resistance
junction
(a)
Voltage (μV)
Position (mm)
0
100
200
300
400
0
2
4
6
8

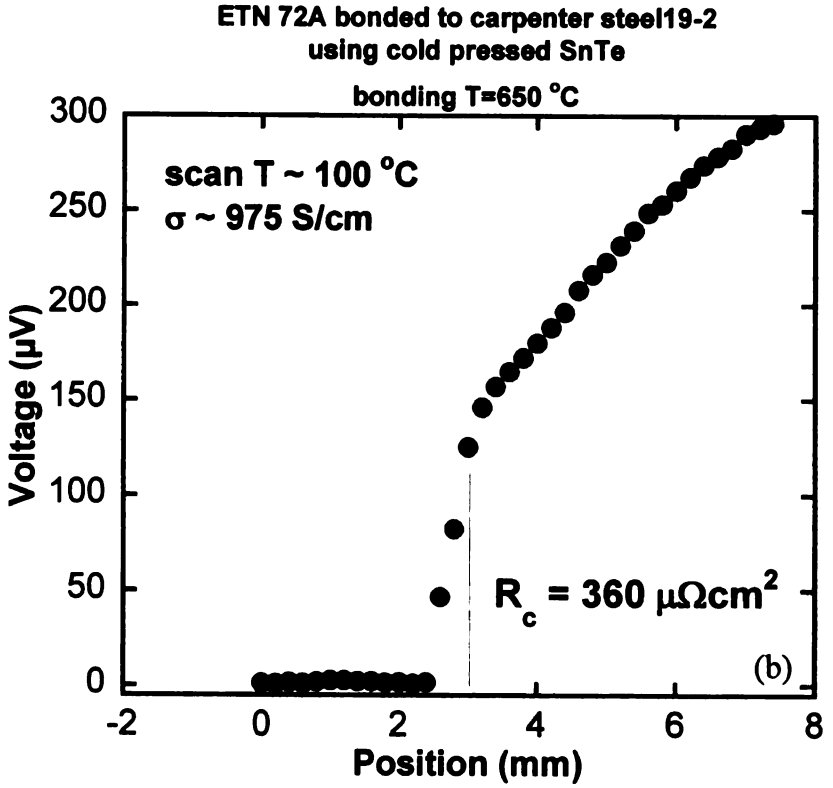
ETN 72A bonded to carpenter steel19-2
using cold pressed SnTe
bonding T=650 °C
scan T ~ 100 °C
σ ~ 975 S/cm
R_c = 360 μΩcm^2
(b)
Voltage (μV)
Position (mm)
0
50
100
150
200
250
300
-2
0
2
4
6
8

Figure 4-6. Continued.

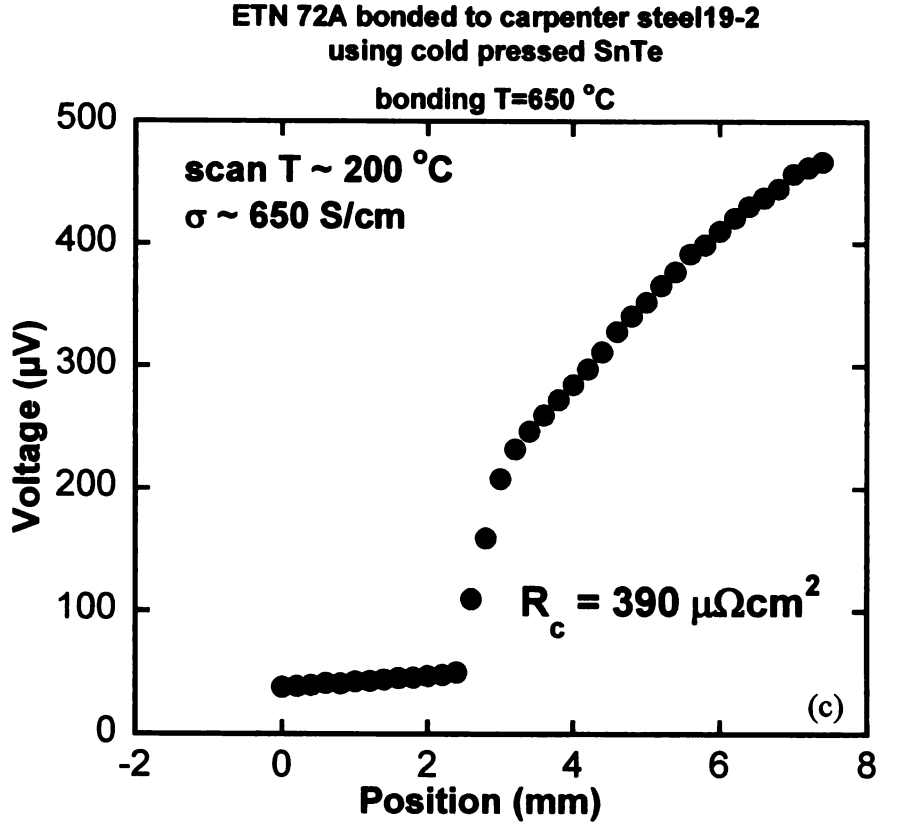

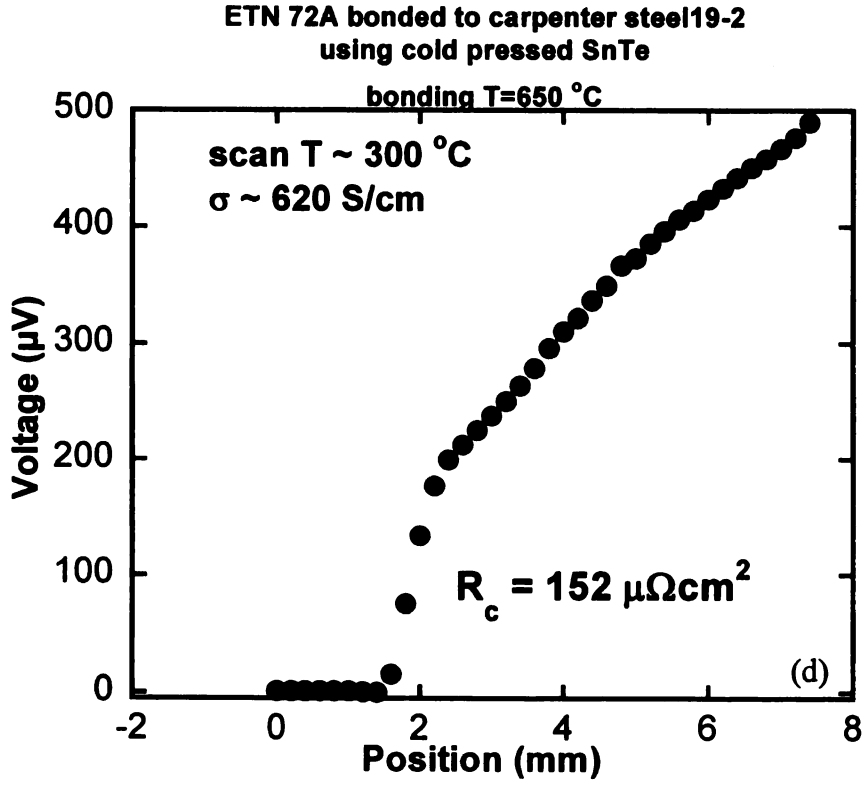

Figure 4-6. Continued.

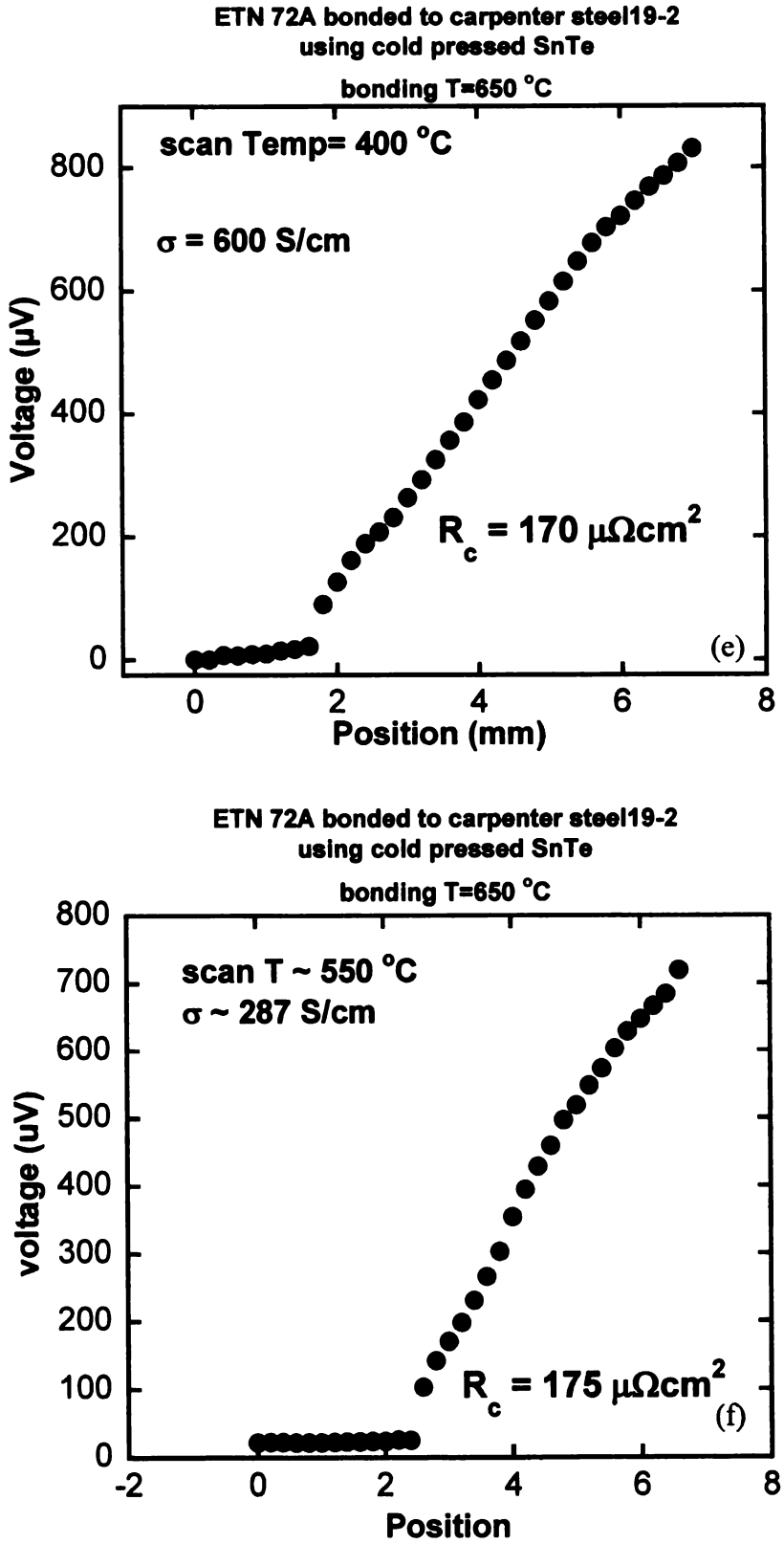

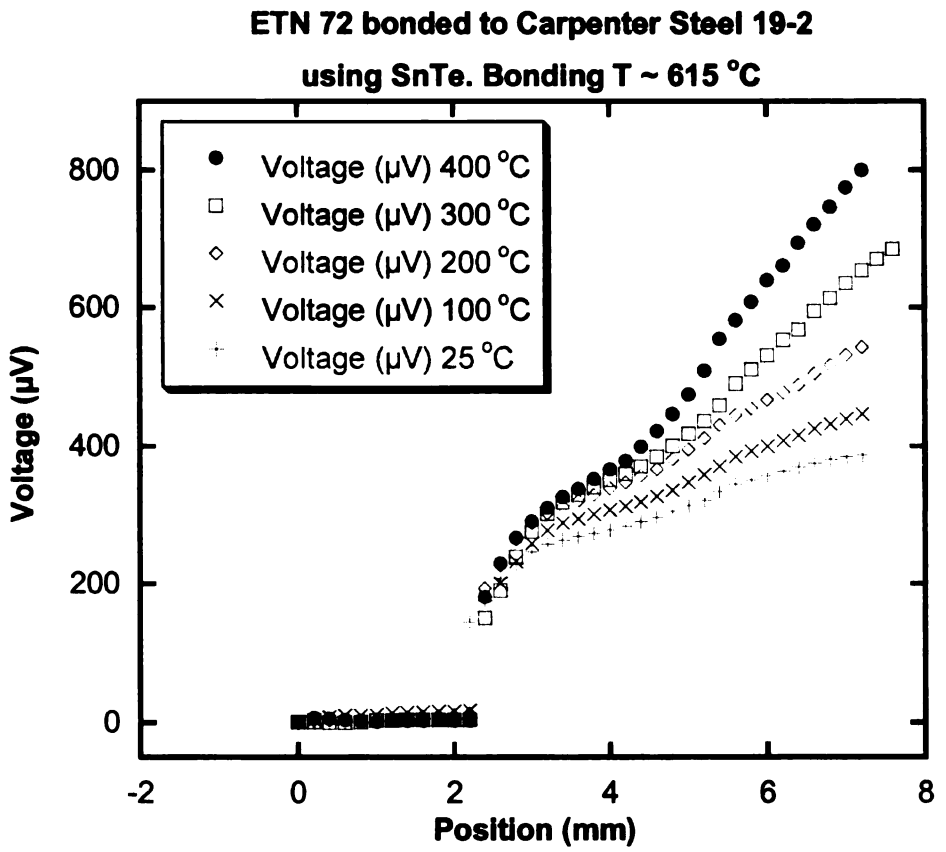

Figure 4-7. ETN 72 bonded to carpenter steel 19-2 using SnTe.

Figure 4-7 above shows a second sample ETN 72 bonded to carpenter steel using SnTe coin. It emphasizes the same point mentioned in previous sample description that as the temperature increases during measurement, electrical conductivity decreases and contact resistance increases. However, since the initial contact resistance is high there is no appreciable change in contact resistance with temperature. Another difference from the previous sample is that there is a clean 'break' between electrode and sample at the junction whereas in the previous sample there was a high resistance region at the junction but not a clean 'break' (or direct voltage jump). This shows that even with the same bonding conditions and material it is difficult to reproduce diffusion bonding results.

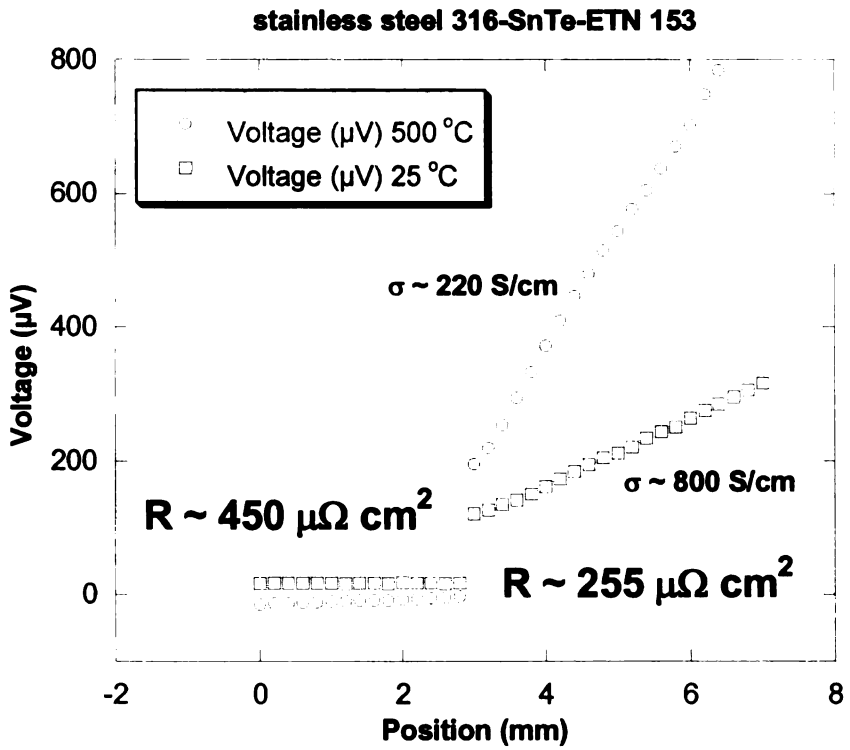

Figure 4-8. Stainless steel 316 bonded to ETN 153 with SnTe.

Figure 4-8 above shows a SnTe based diffusion bond between stainless steel 316 and LAST (ETN 153) with a bonding temperature of 615 °C. A SnTe coin was pressed in open air and probably had more oxygen which resulted in a high resistance bond. This follows a similar trend of decreasing electrical conductivity and increasing contact resistance with increasing temperature. The next logical step is to determine how thermal cycling would affect contact resistance permanently. As shown in following three plots of Figure 4-9 the contact resistance initially increases with temperature as compared to a room temperature scan. As it is cooled to room temperature after thermal cycling, there is a permanent increase in contact resistance. This may be attributed to thermal expansion and contraction with changing temperature. Another interesting observation is that

electrical conductivity has actually increased after thermal annealing. This has been previously observed for hot pressed samples but not for cast material.

Figure 4-9. Stainless steel 316 bonded to ETN 153 using SnTe. (a) Pre anneal room temperature scan (b) Scan at 550 °C indicating increase in contact resistance. (c) After anneal room temperature scan indicating a permanent increase in contact resistance accompanied with increase in electrical conductivity.

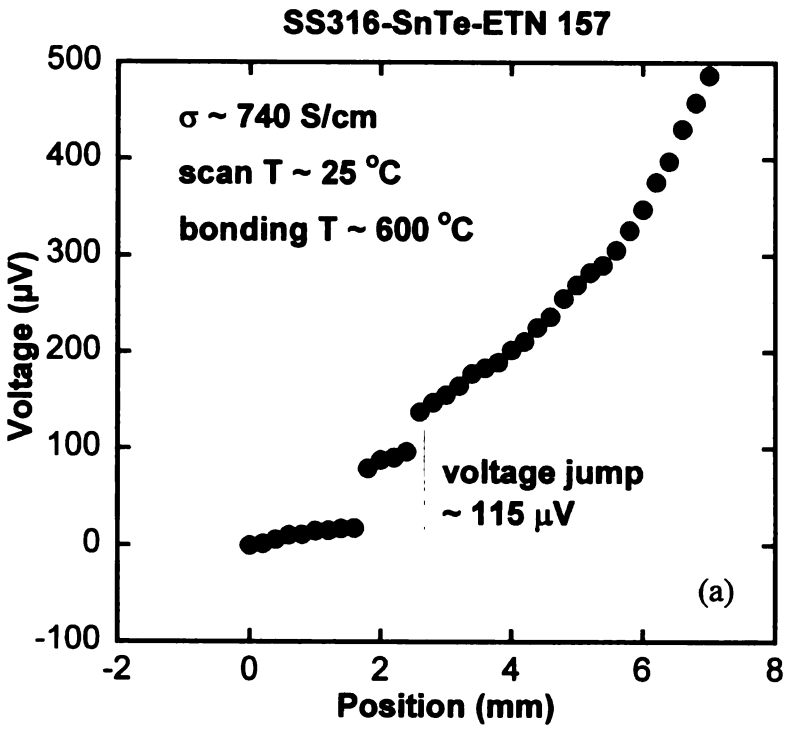
SS316-SnTe-ETN 157
σ ~ 740 S/cm
scan T ~ 25 °C
bonding T ~ 600 °C
voltage jump
~ 115 μV
(a)
Voltage (μV)
Position (mm)
500
400
300
200
100
0
-100
-2
0
2
4
6
8

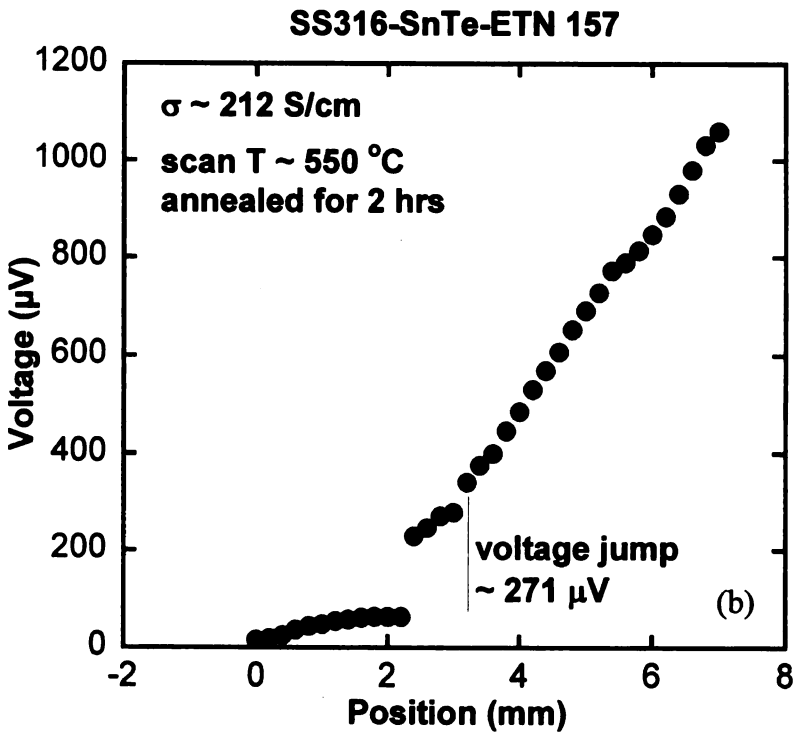
SS316-SnTe-ETN 157
σ ~ 212 S/cm
scan T ~ 550 °C
annealed for 2 hrs
voltage jump
~ 271 μV
(b)
Voltage (μV)
Position (mm)
1200
1000
800
600
400
200
0
-2
0
2
4
6
8

Figure 4-9. Continued.

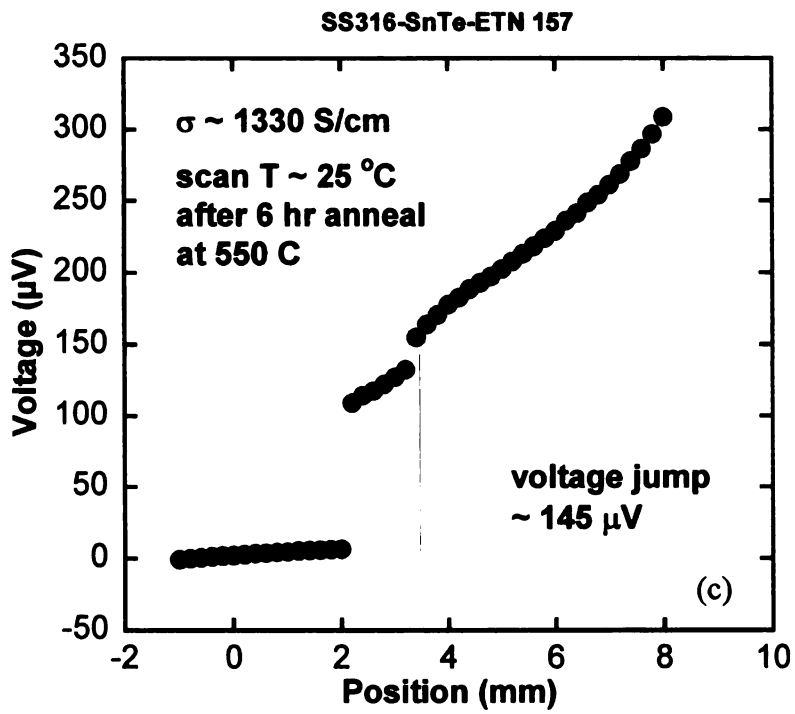

A similar experiment was carried out with LAST (ETN 157) bonded to Ni using SnTe. This time the SnTe coin was prepared inside a glove box oxygen free environment and bonding was carried out at 650 °C. As the following plots in Figure 4-10 show there is increase in contact resistance at high temperature. However, the pre-annealing contact resistance is very low and after one annealing cycle the contact resistance is back to the pre-annealing value thus indicating that module can sustain multiple thermal cycles.

Figure 4-10. ETN 218 bonded to Ni electrode using SnTe.

(a) Pre-anneal room temperature scan (b) 500 °C scan indicating increase in contact resistance. (c) After anneal room temperature scan indicating contact resistance value returned to pre anneal value.

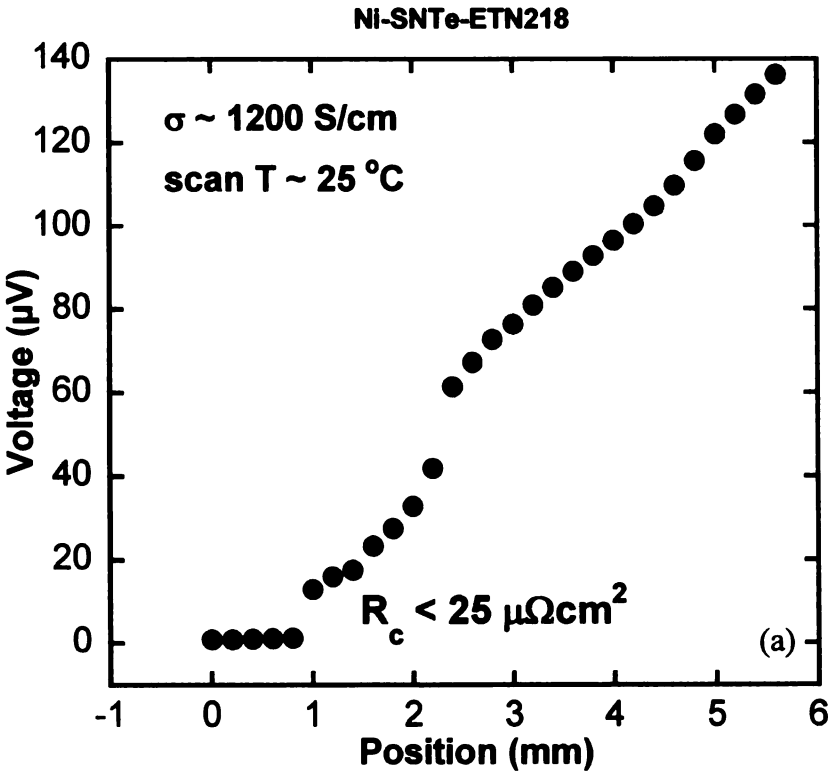
Ni-SNTe-ETN218
σ ~ 1200 S/cm
scan T ~ 25 °C
R_c < 25 μΩcm²
(a)
Voltage (μV)
Position (mm)
140
120
100
80
60
40
20
0
-1
0
1
2
3
4
5
6

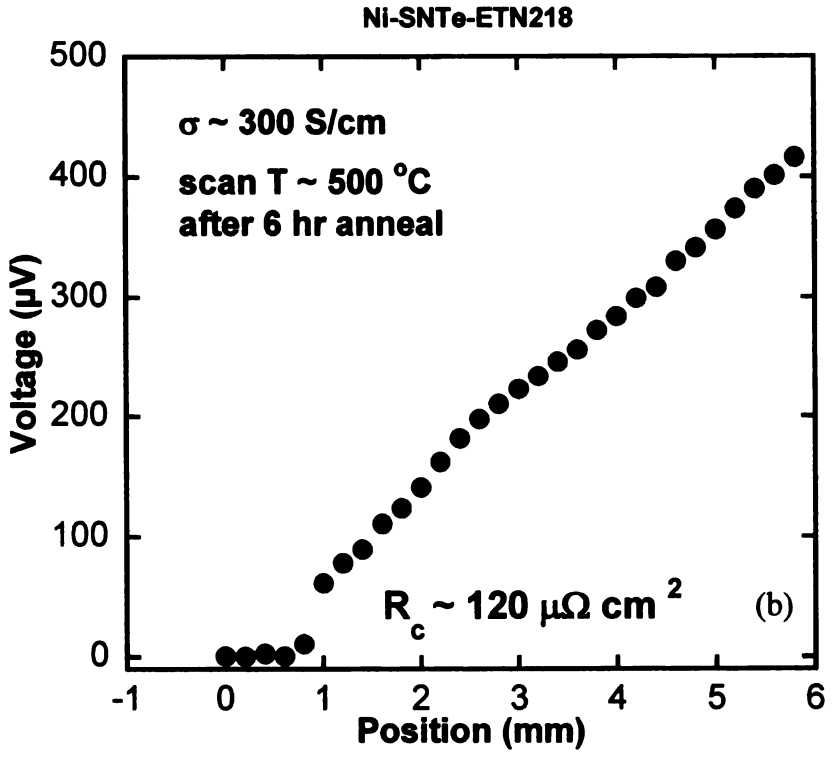
Ni-SNTe-ETN218
σ ~ 300 S/cm
scan T ~ 500 °C
after 6 hr anneal
R_c ~ 120 μΩ cm²
(b)
Voltage (μV)
Position (mm)
500
400
300
200
100
0
-1
0
1
2
3
4
5
6

Figure 4-10. Continued.

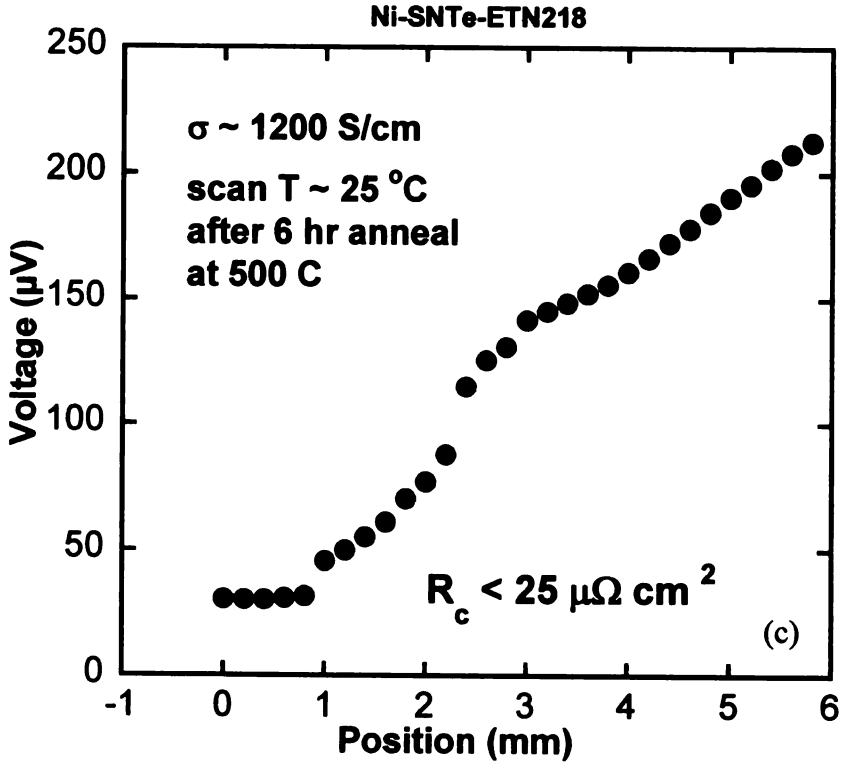

Previous modules were tested for short periods of time. In order to run a module long term testing is required. For this purpose a low contact resistance ETN 153-SnTe-Ni electrode unicouple was tested for five days under Ar at 450 °C. A SnTe coin was prepared in a glove box to avoid oxidation which produced low contact resistance diffusion bond as shown in Figure 4-11. The unicouple had a 4-probe resistance of 4.5 (mΩ). It can be seen that for the first two days there is negligible change in contact resistance and by the fifth day contact resistance has increased to 250 $\mu\Omega cm^2$.

Figure 4-11. ETN 153 bonded to Ni electrode using SnTe coin. Bonding temperature 615 °C. (a) Pre-anneal room temperature scan. (b) 450 °C scan after 12 hrs. (c) 450 °C scan after 48 hrs. (d) 450 °C scan after 5 days indicating increased contact resistance.

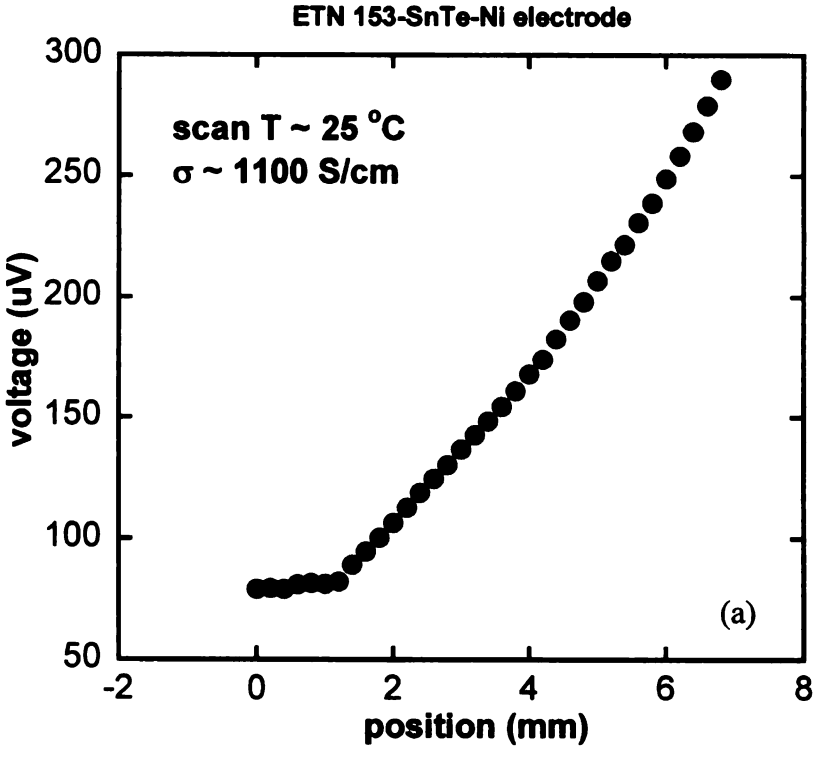
ETN 153-SnTe-Ni electrode
scan T ~ 25 °C
σ ~ 1100 S/cm
voltage (uV)
position (mm)
(a)
300
250
200
150
100
50
-2
0
2
4
6
8

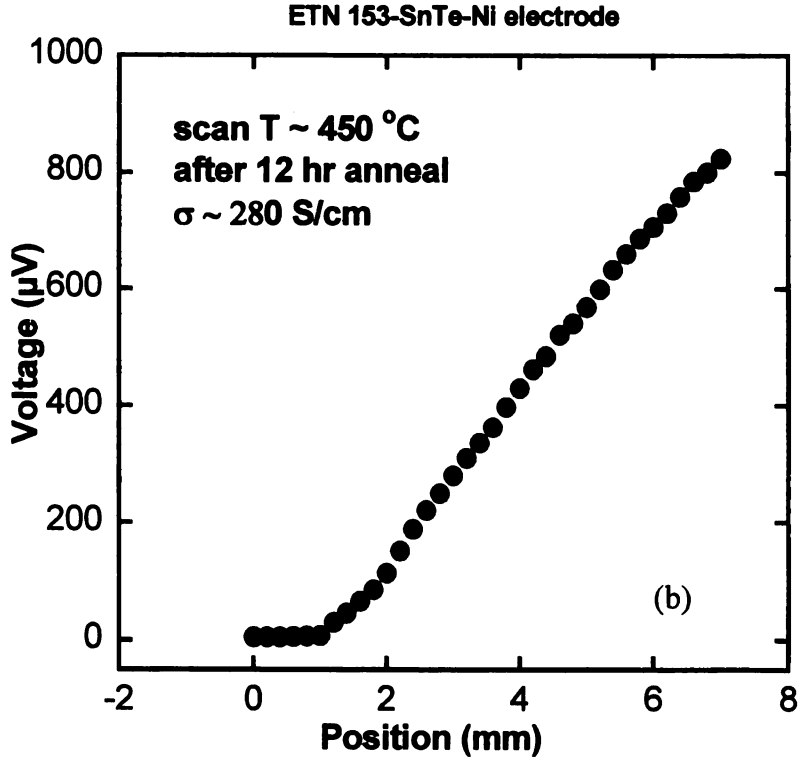
ETN 153-SnTe-Ni electrode
scan T ~ 450 °C
after 12 hr anneal
σ ~ 280 S/cm
Voltage (μV)
Position (mm)
(b)
1000
800
600
400
200
0
-2
0
2
4
6
8

Figure 4-11. Continued.

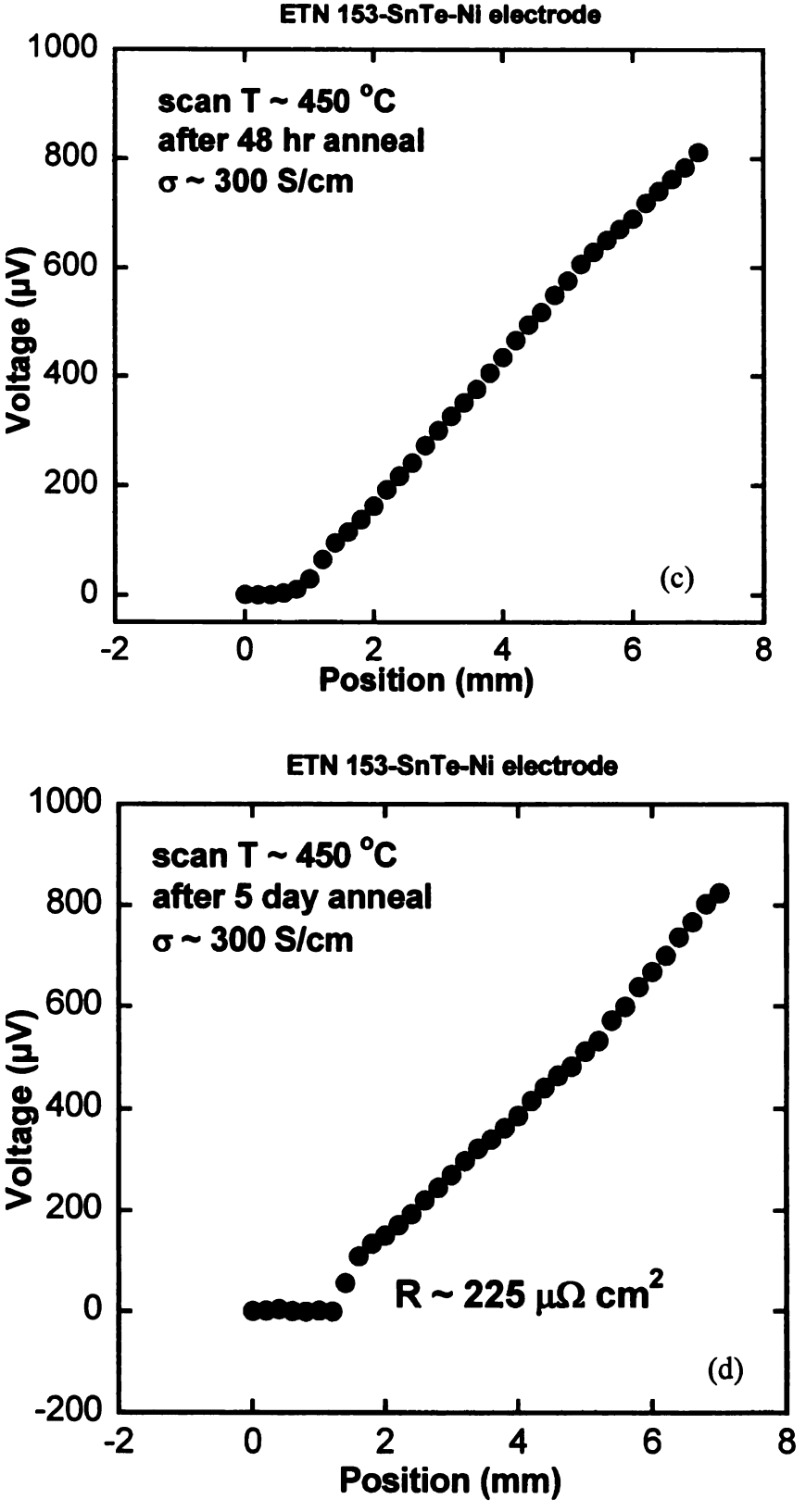

4.3.1.2 SnTe based cast p-type bonded module

SnTe bonding is traditionally used for p-type material in literature [41], [42] since SnTe itself is a p-type semiconductor. In the first sample LASTT (ETP 50) was bonded to carpenter steel 19-2 at 615 °C using cold pressed SnTe coin. This coin was prepared in open air and had excessive oxygen. Room temperature contact resistance was high and it decreased as temperature was increased as shown in Figure 4-12. A major difference between n-type bond and p-type bond using SnTe is that with n-type cast material, if initial room temperature contact resistance was high it would not appreciably change with temperature but for p-type material it still improves with increasing temperature.

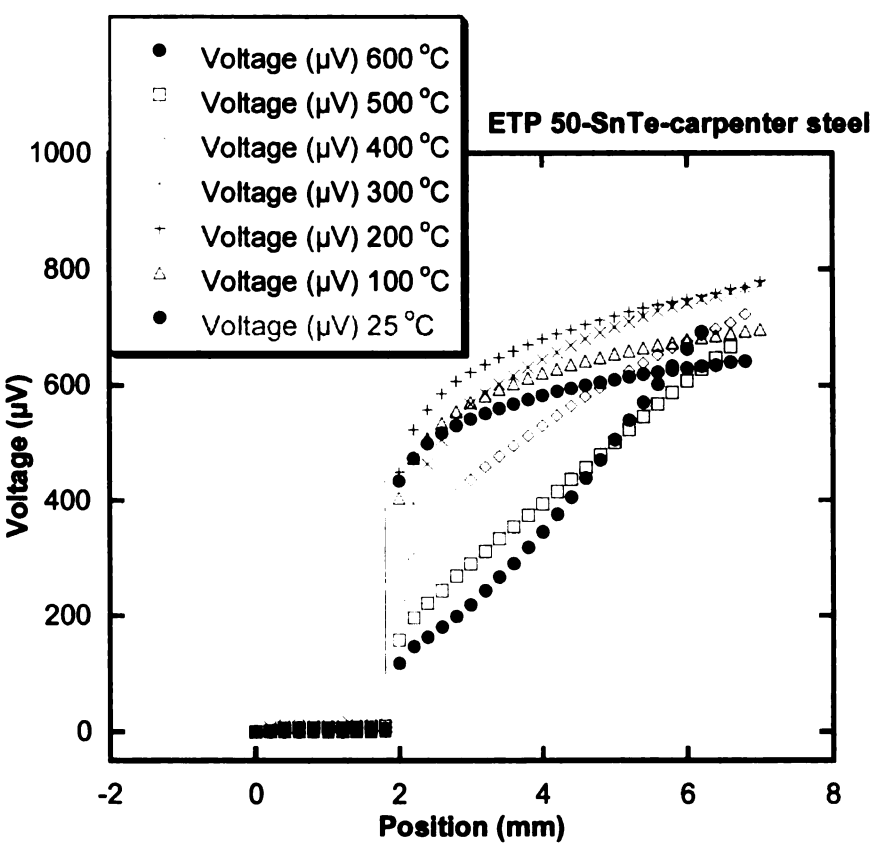

Figure 4-12. ETP 50 bonded to carpenter steel 19-2 using SnTe. As the temperature is increased electrical conductivity and contact resistance decrease.

A similar behavior is observed for ETP 53 bonded to Ni electrode using SnTe cold pressed coin indicating that this phenomenon is electrode material independent as shown in Figure 4-13 below.

Figure 4-13. ETP 53 bonded to Ni using SnTe. (a) Pre-anneal room temperature scan (b) 500 °C scan indicating decrease in contact resistance. (c) After anneal room temperature scan indicating a permanent decrease in contact resistance.

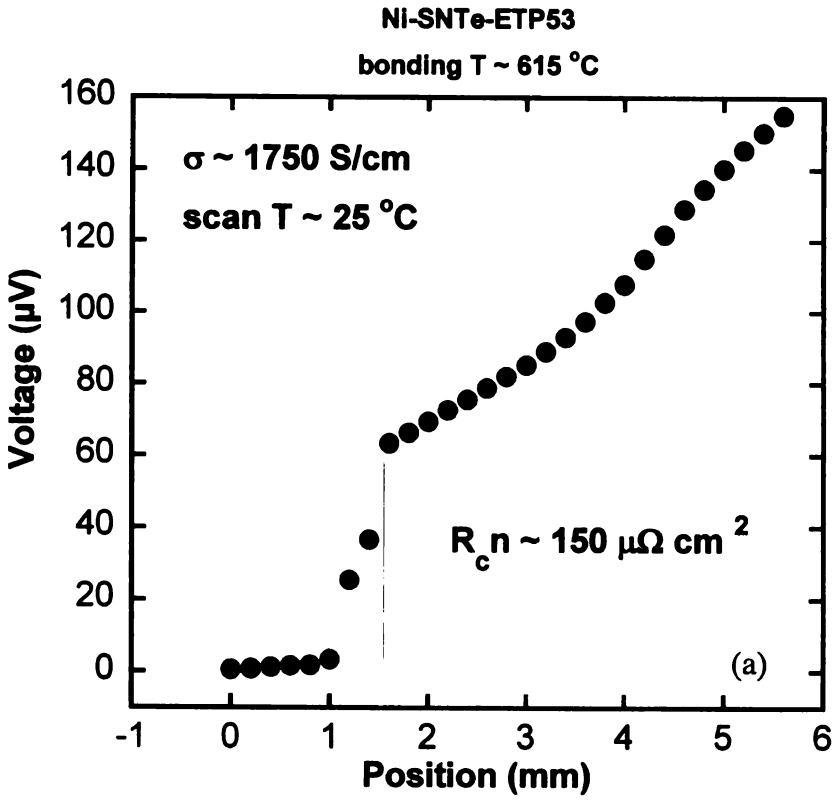
Ni-SNTe-ETP53
bonding T ~ 615 °C
σ ~ 1750 S/cm
scan T ~ 25 °C
$R_c n$ ~ 150 μΩ cm ^{2}
(a)
Voltage (μV)
Position (mm)
160
140
120
100
80
60
40
20
0
-1
0
1
2
3
4
5
6

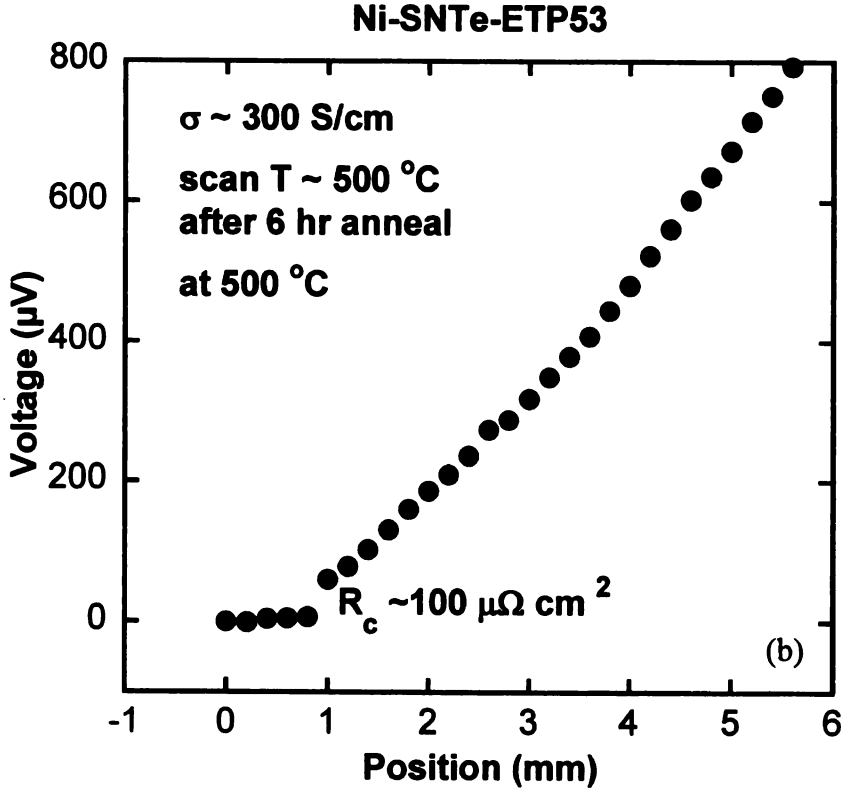
Ni-SNTe-ETP53
σ ~ 300 S/cm
scan T ~ 500 °C
after 6 hr anneal
at 500 °C
R_c ~100 μΩ cm ^{2}
(b)
Voltage (μV)
Position (mm)
800
600
400
200
0
-1
0
1
2
3
4
5
6

Figure 4-13. Continued

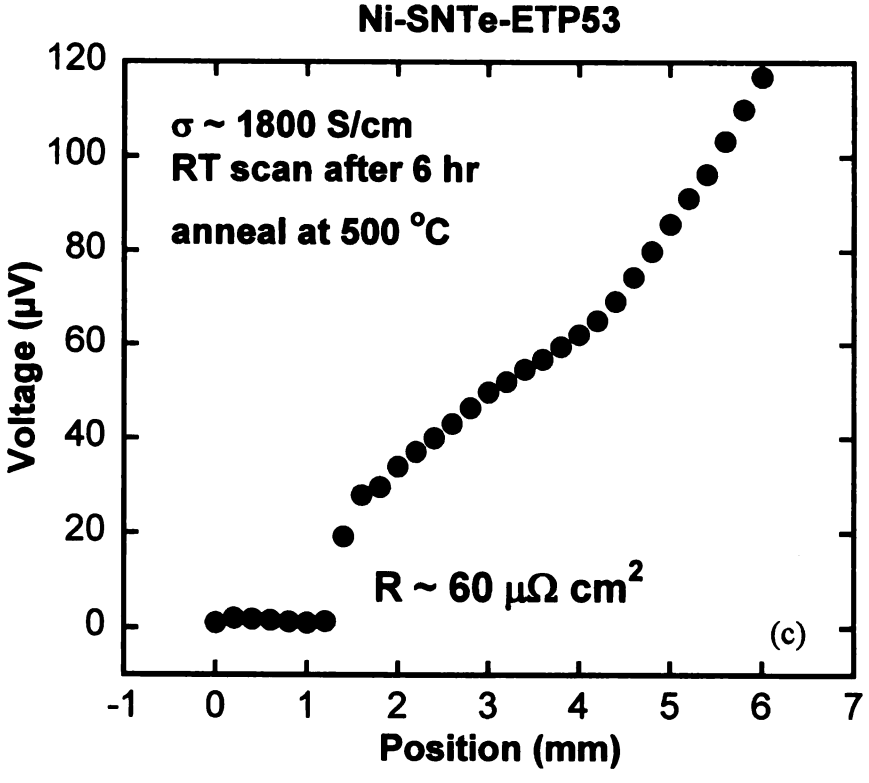

However there were two occasions when SnTe based p-type bond showed different behavior and in these instances the contact resistance increased with increasing temperature. This might have been caused by excess oxygen present during bonding. The effects are shown in Figure 4-14.

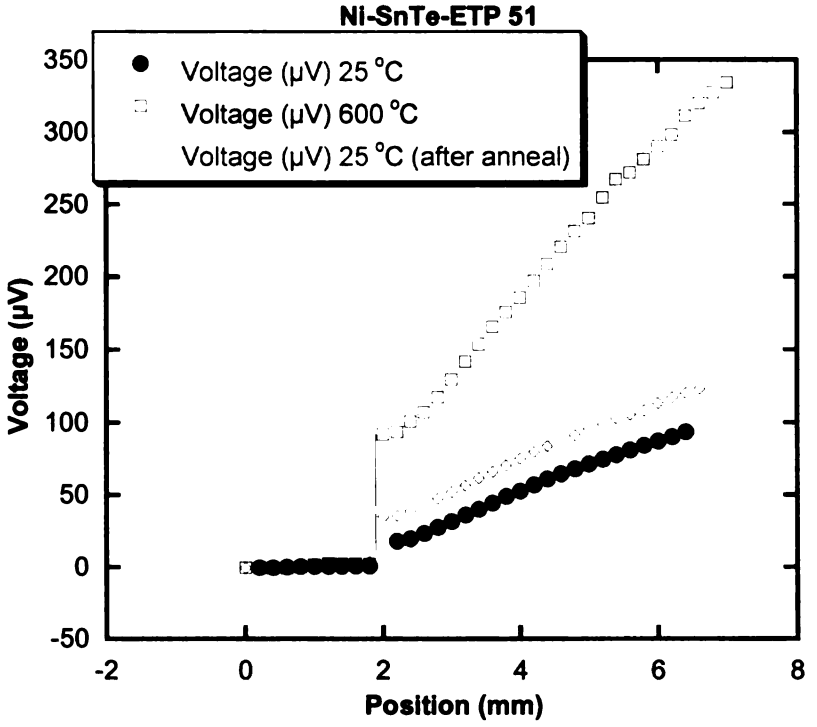

Figure 4-14. ETP 51 bonded to Ni using SnTe coin. Contact resistance increases with temperature with a permanent increase after cooled down to room temperature.

This can be compared with direct diffusion bonding of p-type material to stainless steel 316 as shown in Figure 4-15 below where no SnTe interface layer was used. As with results in Figure 4-14 the contact resistance increases with increasing temperature with a permanent increase in contact resistance after it is cooled down to room temperature.

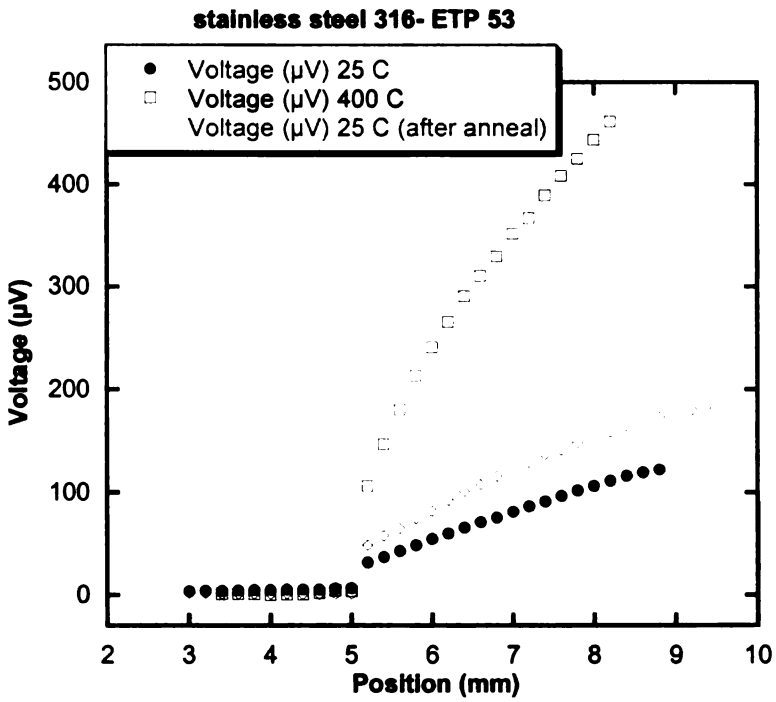

Figure 4-15. ETP 53 directly bonded to stainless steel 316. Contact resistance increases with measurement temperature accompanied with permanent increase after cooling down to room temperature.

A third type of behavior was observed for p-type material diffusion bonded using SnTe in which contact resistance increases with measurement temperature but then comes back to pre-annealed value. This is different from previous behavior where thermal cycling resulted in permanent increase in contact resistance. As shown in Figure 4-16 the module was cycled twice and maintained its room temperature contact resistance value.

Figure 4-16. ETP 52 bonded to carpenter steel using SnTe. (a) Pre-anneal room temperature scan (b) First anneal at 600 °C with increase in contact resistance. (c) Room temperature scan after first anneal. Contact resistance reduced to pre-anneal value (d) Second anneal run at 600 °C. Contact resistance increased. (e) Room temperature scan after second annealing run. Contact resistance reduced to first pre-anneal value.

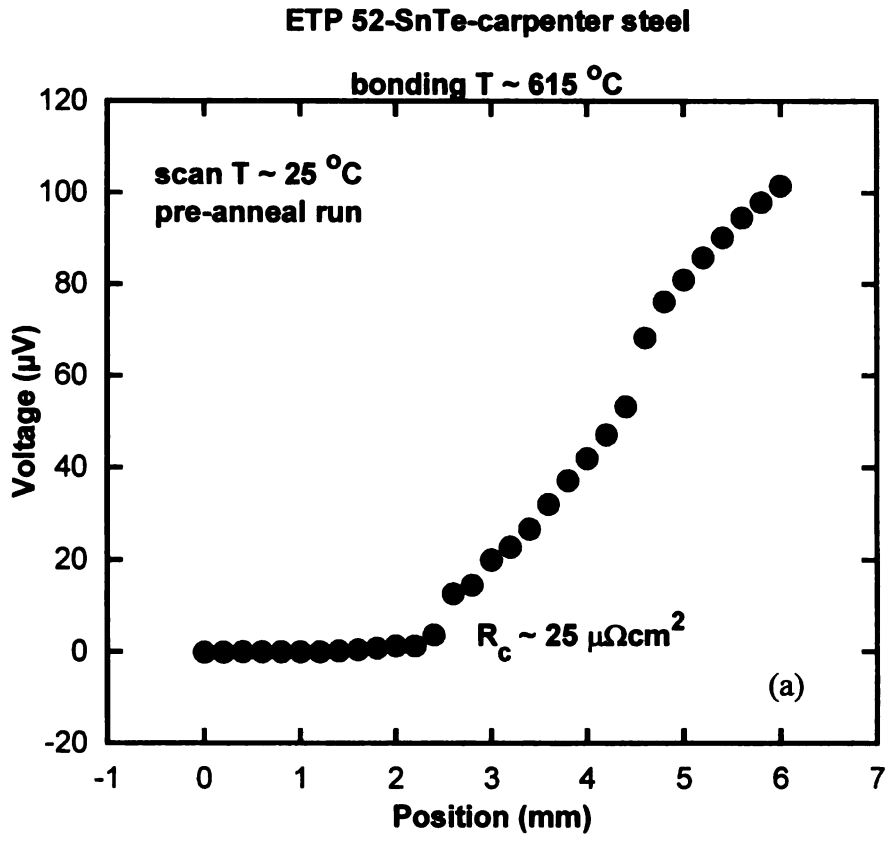
ETP 52-SnTe-carpenter steel
bonding T ~ 615 °C
scan T ~ 25 °C
pre-anneal run
R_c ~ 25 μΩcm^2
(a)
Voltage (μV)
Position (mm)
120
100
80
60
40
20
0
-20
-1
0
1
2
3
4
5
6
7

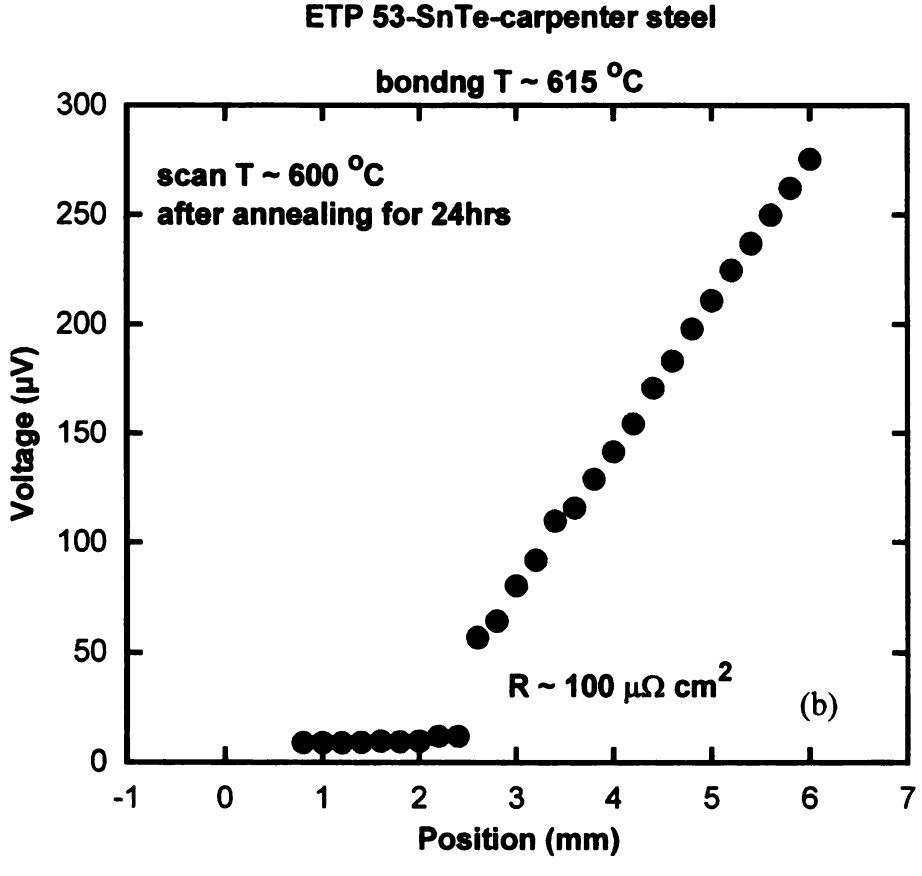
ETP 53-SnTe-carpenter steel
bondng T ~ 615 °C
scan T ~ 600 °C
after annealing for 24hrs
R ~ 100 μΩ cm^2
(b)
Voltage (μV)
Position (mm)
300
250
200
150
100
50
0
-1
0
1
2
3
4
5
6
7

Figure 4-16. Continued.

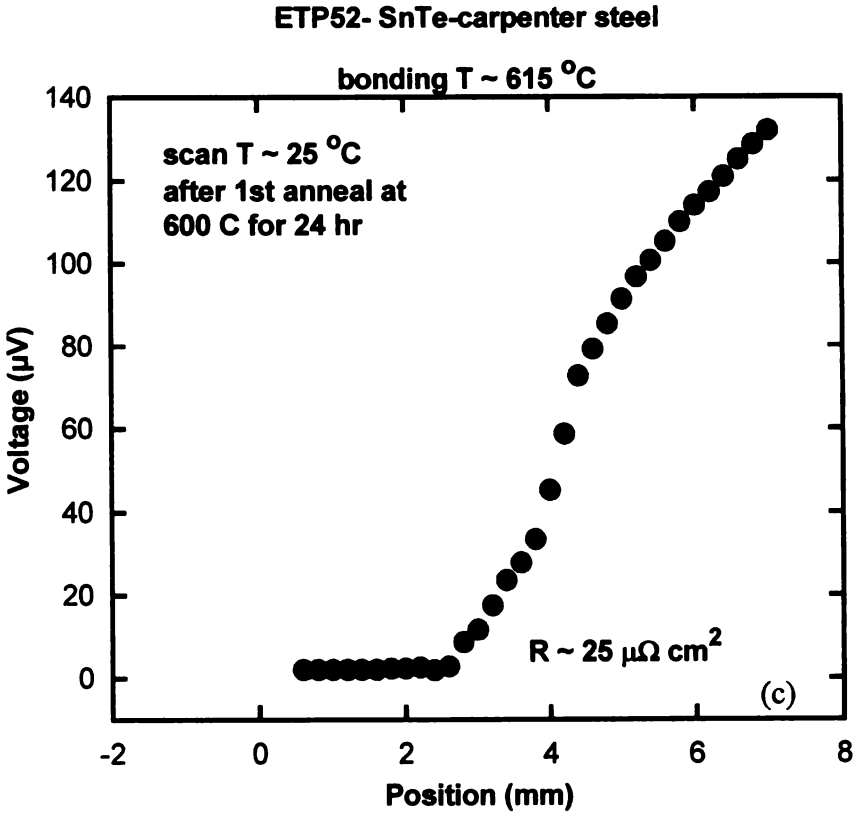

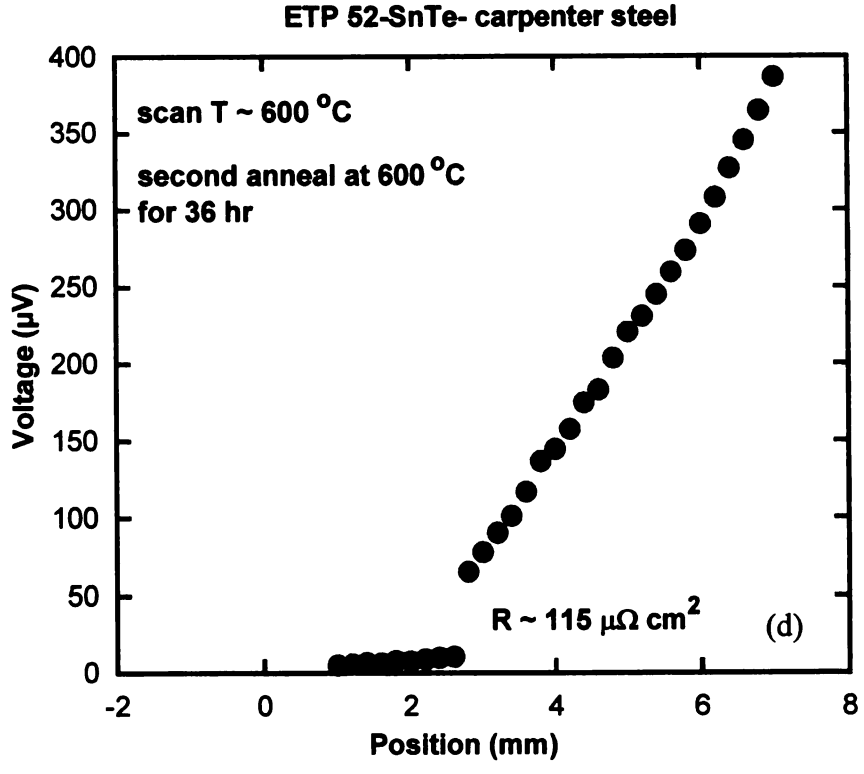

Figure 4-16. Continued.

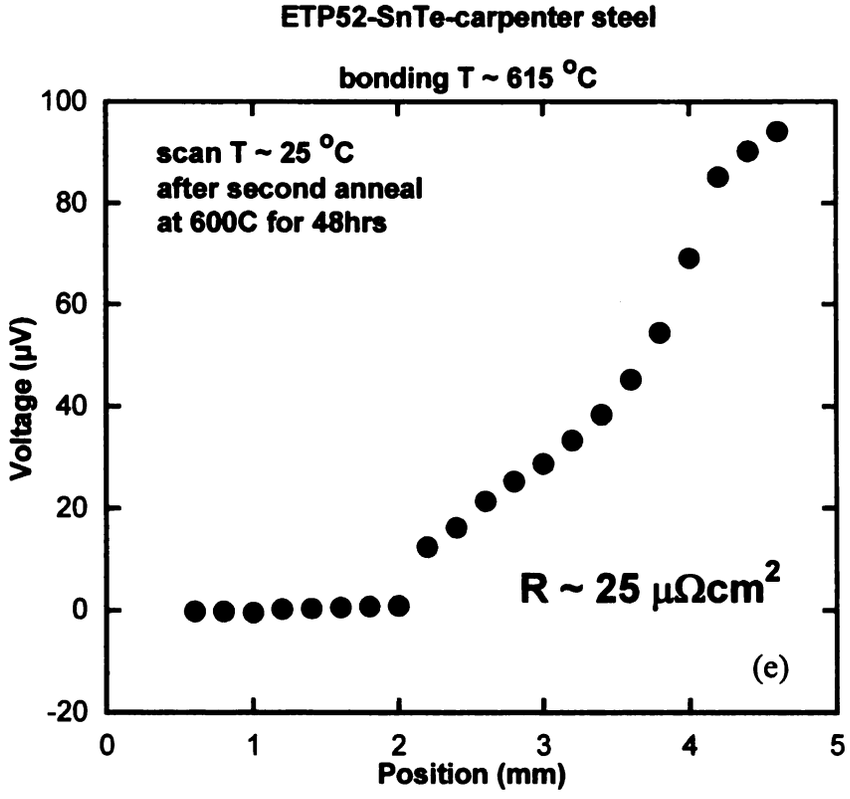

To ascertain the viability of SnTe based diffusion bonding for LASTT material a four day measurement with two high temperature thermal cycles was carried out. In this module stainless steel 316 was bonded to ETP 52 using cold pressed SnTe coin. Stainless steel 316 is used because of its close CTE match (17.5 μm/m/°C) with LAST material. It has relatively low thermal conductivity (21.5 W/m-K) and relatively high electrical resistivity (740 nΩm) in comparison to metals like Ag or Cu. Bonding was carried out at 615 °C. As can be seen from Figure 4-17 below, the contact resistance did not increase during the annealing run and the module successfully survived two thermal cycles.

Figure 4-17. ETP 52 bonded to stainless steel 316 using SnTe. (a) Pre-anneal run with low contact resistance (b) Post anneal room temperature scan indicating no change in contact resistance. (c) Second anneal run at 600 °C for 12 hr (d) Second anneal run at 600 °C for 24 hr. (e) Second anneal run at 600 °C for 48 hrs (f) Second anneal run at 600 °C for 60 hrs indicating no appreciable change in contact resistance.

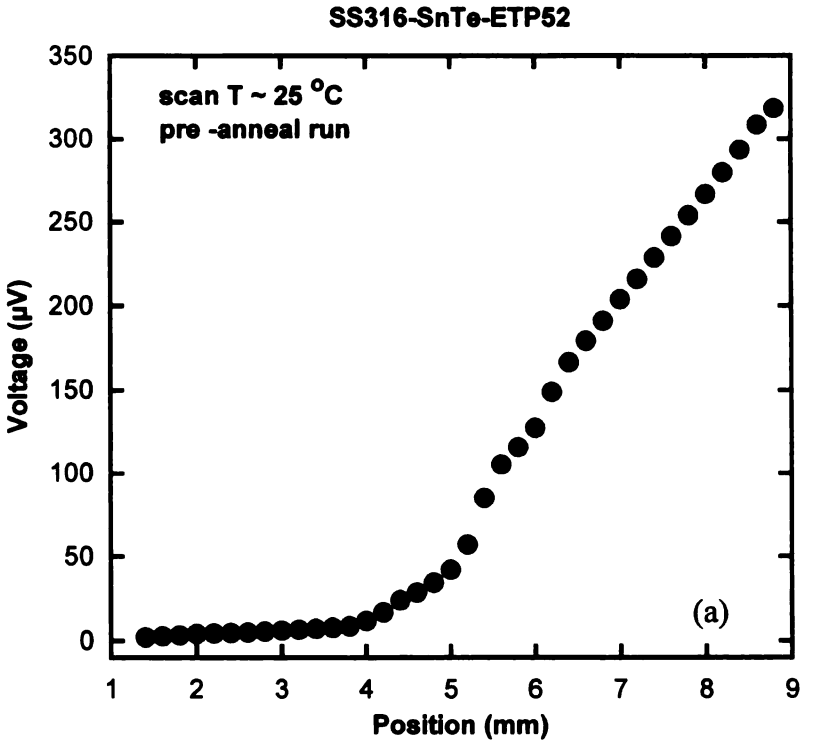
SS316-SnTe-ETP52
scan T ~ 25 °C
pre -anneal run
Voltage (μV)
Position (mm)
(a)

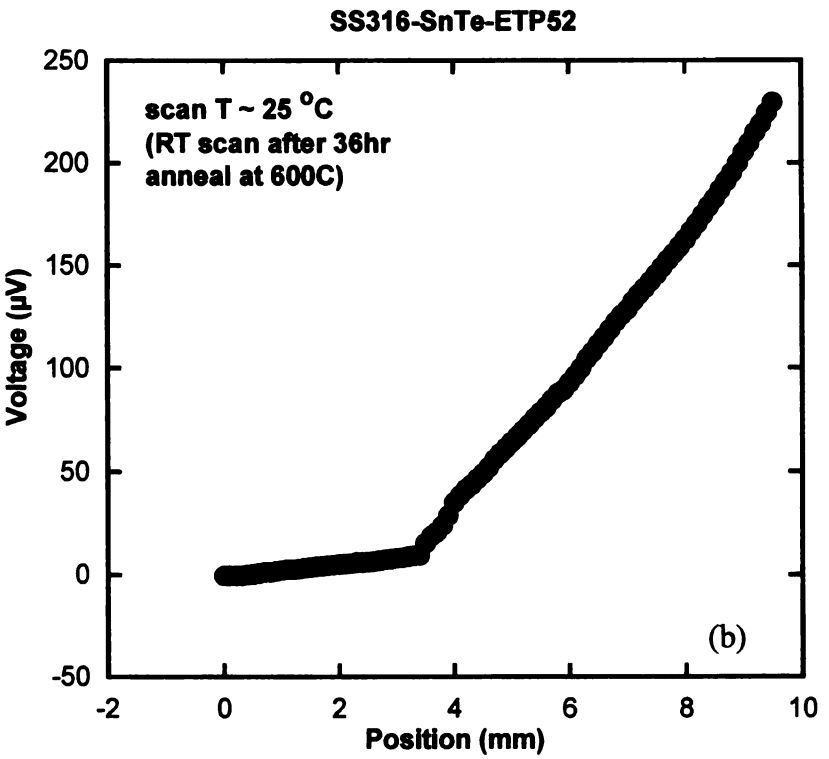
SS316-SnTe-ETP52
scan T ~ 25 °C
(RT scan after 36hr
anneal at 600C)
Voltage (μV)
Position (mm)
(b)

Figure 4-17. Continued.

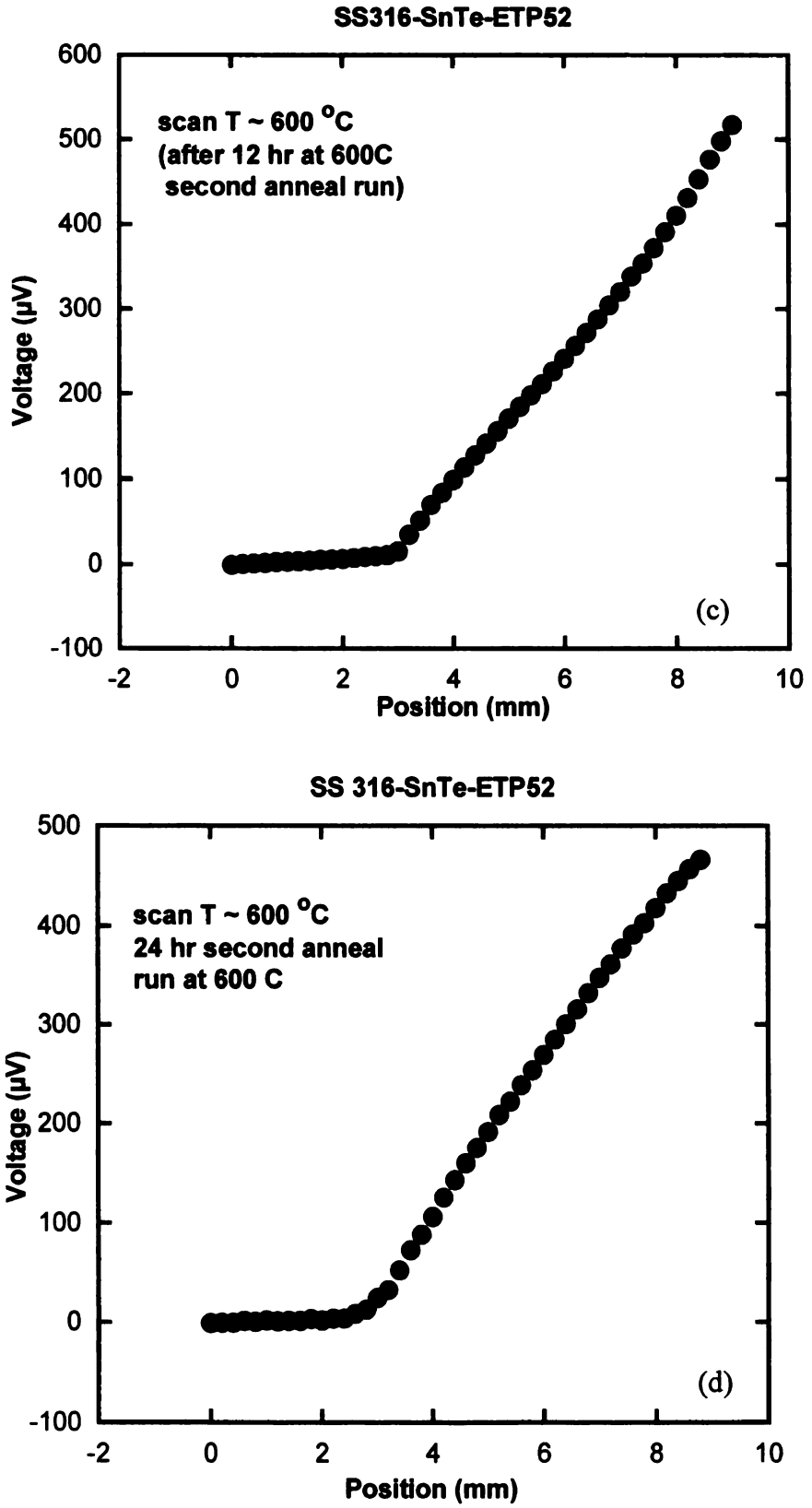

Figure 4-17. Continued.

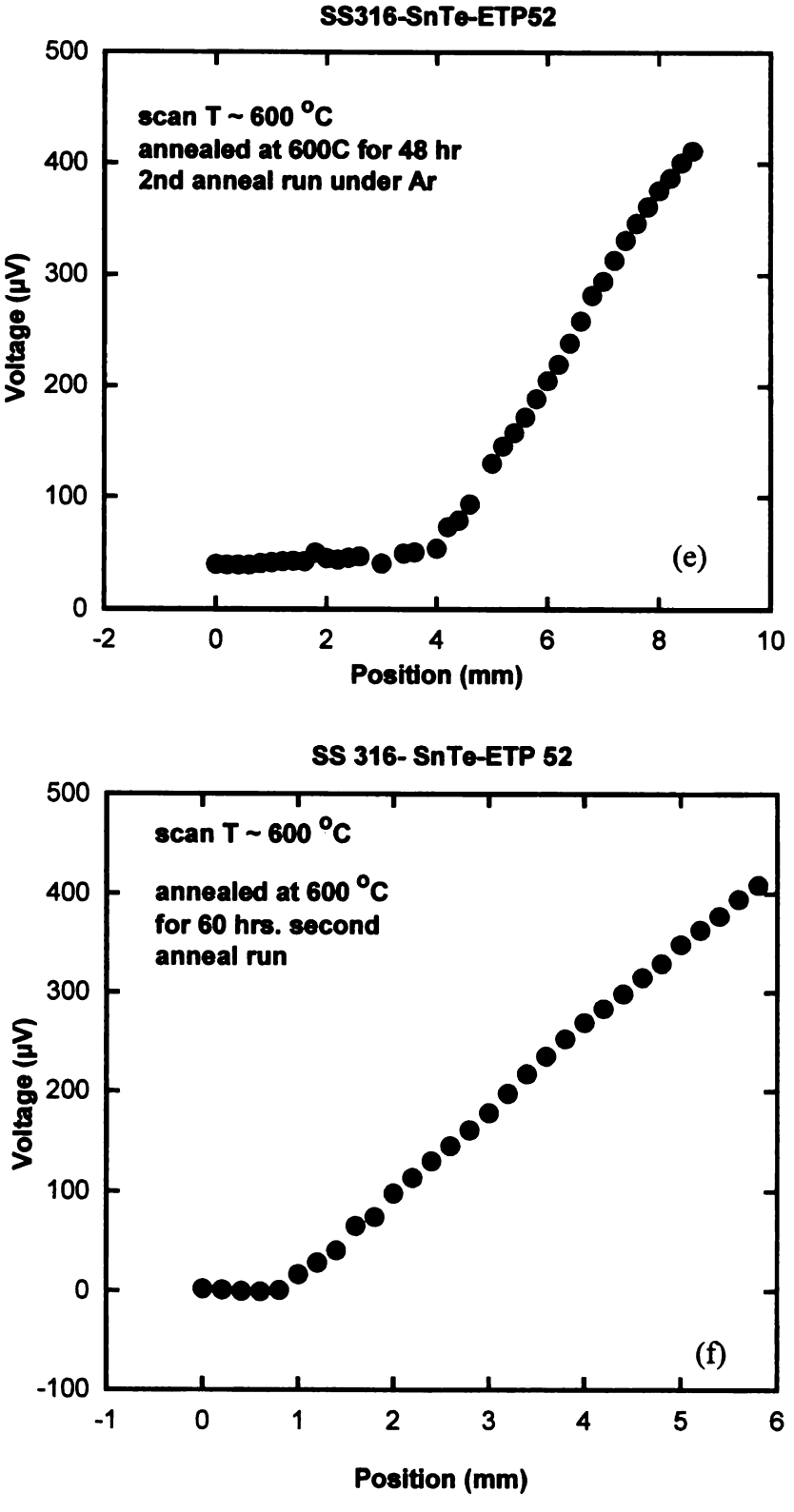

4.3.1.3 SnTe based hot pressed bonded modules

Hot pressed n-type materials was diffusion bonded using SnTe. Hot pressed specimens have higher density (close to 95 % of theoretical density) and show increase in electrical conductivity with increasing temperature. Diffusion bonded samples using SnTe show an improvement in contact resistance with increasing temperature. Figure 4-18 below shows plots for MSUHP 35 bonded to carpenter steel using SnTe cold pressed coin. This behavior is unique to hot pressed samples because for cast p-type diffusion bonded samples we observed decrease in contact resistance but electrical conductivity also decreased with temperature, whereas for hot pressed samples both electrical conductivity and contact resistance improve with temperature.

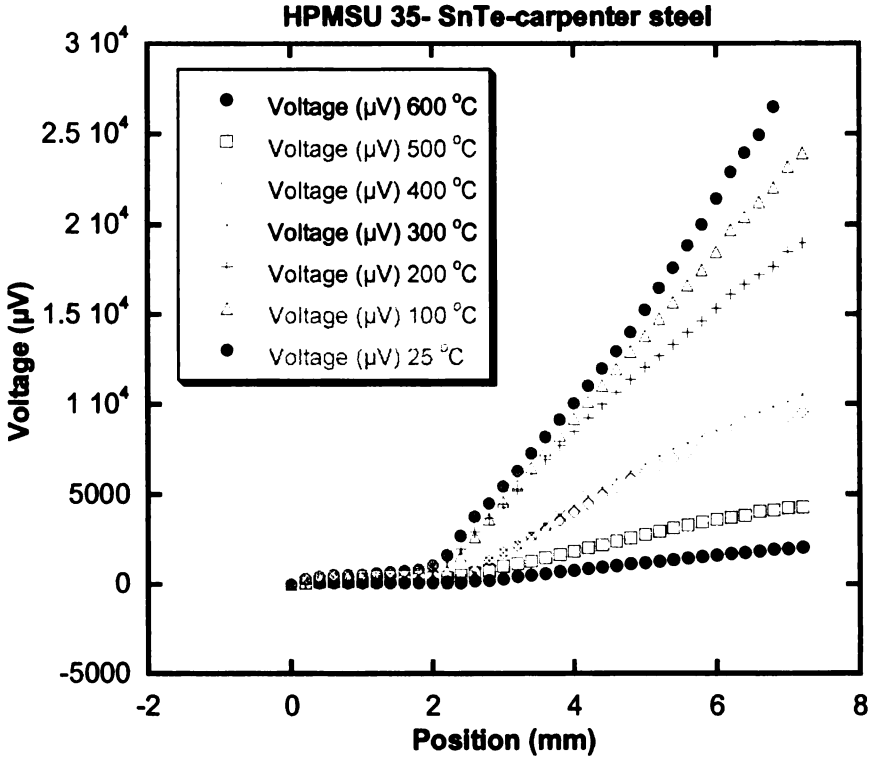

Figure 4-18. MSUHP 35 bonded to carpenter steel using SnTe. Electrical conductivity increases and contact resistance decreases with increasing temperature.

A similar behavior was observed for stainless steel 316 electrode bonded to MSUHP 37. In this case a permanent increase in hot pressed material conductivity is observed after annealing cycle. Module started with a low contact resistance and it did not change during annealing and maintained its value after the annealing cycle of 24 hrs as shown in Figure 4-19 below.

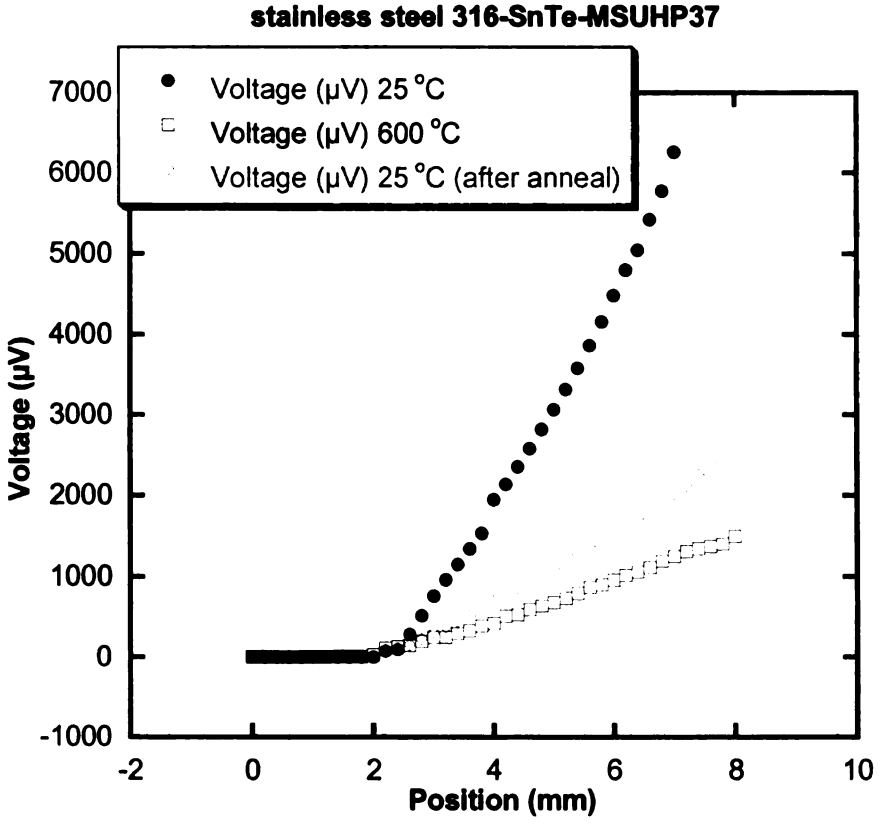

Figure 4-19. MSUHP37 bonded to stainless steel 316 using SnTe. There is permanent increase in electrical conductivity and contact resistance remains same after thermal cycle.

For hot pressed samples SnTe based results can be compared with that of diffusion bonded with molybdenum coating. For this experiment HPMSU 35 sample legs and stainless steel 316 electrodes were coated with molybdenum inside physical vapor

deposition (PVD) system. Bonding was carried out at 750 °C. As can be seen from Figure 4-20 below that as temperature is increased electrical conductivity also increases and contact resistance decreases (from 1000 $\mu\Omega$ cm^2 for 25 °C to 1750 $\mu\Omega$ cm^2 for 600 °C). This phenomenon is similar to what we observe for SnTe based modules except that initial contact resistance is very high as compared to SnTe based diffusion bonds.

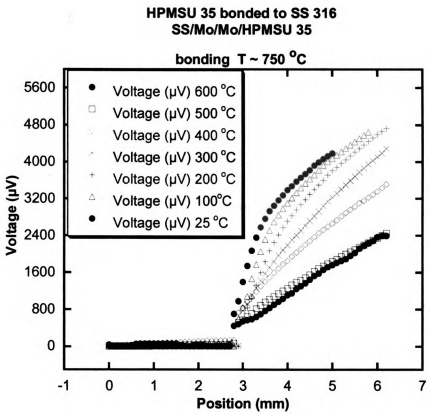

Figure 4-20. HPMSU 35 coated with Mo bonded to Mo coated stainless steel electrode. Electrical conductivity increases and contact resistance decreases with increasing measurement temperature.

In a similar experiment MSUHP 37 was directly diffusion bonded to carpenter steel without any interface coatings. The bonding temperature was ~ 800 °C and low contact

resistance bonds were obtained. Module was taken up to 450 °C for 24 hrs and no appreciable change was observed in contact resistance. Module was cooled down to room temperature and scanned and contact resistance value was same as before annealing as shown in Figure 4-21 below.

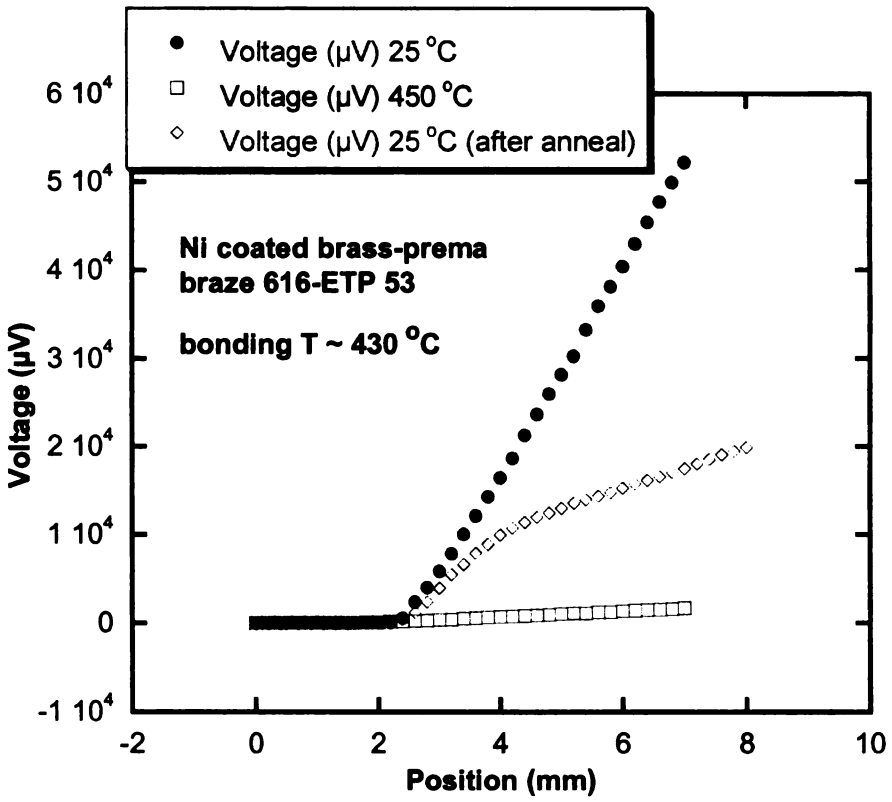

Figure 4-21. MSUHP 37 bonded to carpenter steel. Electrical conductivity improves with increasing measurement temperature. No appreciable change in contact resistance during or after annealing.

4.3.2 Prema Braze based diffusion bonded modules

A number of diffusion bonding experiments were carried out using braze as interface between hot side electrode and LAST and LASTT material. For this Premabraze 616 was purchased from Lucas Milhaupt Inc, WI. It has a nominal composition of (Ag61.5/In14.5/Cu balance) by weight with melting point of 620 °C. However bonding with LAST material is carried out at around 450 °C as Premabraze 616 makes eutectic at this temperature with LAST material (probably tellurium). First I will discuss bonding of p-type material using Premabraze 616.

4.3.2.1 Premabraze bonded modules with p-type cast TE material

Four samples prepared with Premabraze were measured inside high temperature voltage profiling system after bonding. First sample is Ni plated Cu electrode bonded to ETP 53. As it can be seen in Figure 4-22 that at room temperature there is a high resistivity region and gap of (300 μV) at the junction. The probable reason is Ag and Cu diffusion into LAST material during bonding or CTE mismatch between TE material and electrode or a combination of both. This behavior was observed for three out of four samples. As the sample is taken high in temperature this voltage gap at the junction increases about three times. This behavior is very different from bonding using SnTe where contact resistance decreases with increasing measurement temperature. After the module is cooled down to room temperature there is a permanent increase in the contact resistance as voltage gap increased from 500 μV pre-anneal to 800 μV post anneal. All Premabraze bonding were carried out under vacuum in a new system using rotary pump that can reach mTorr range.

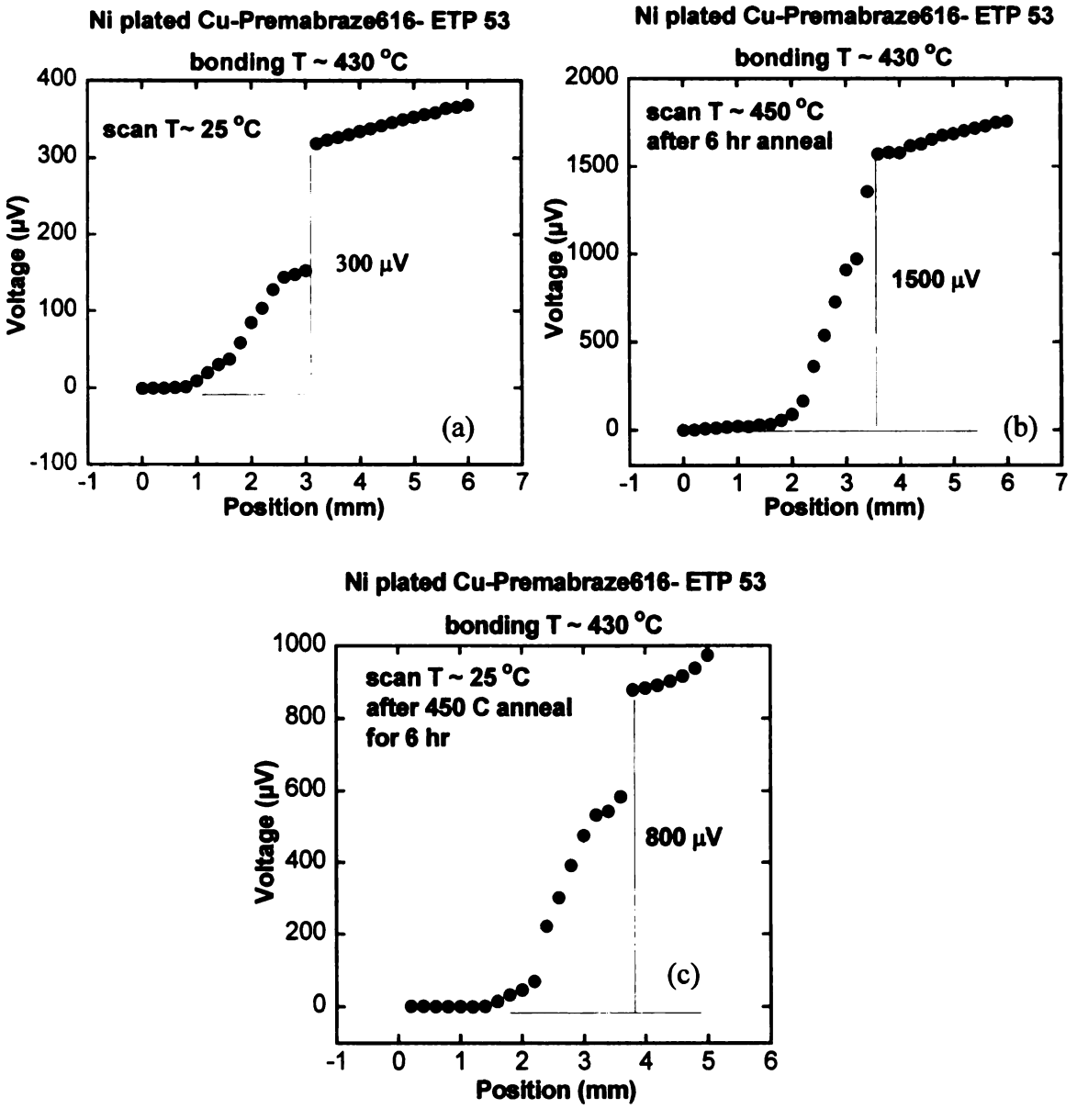

Figure 4-22. ETP53 bonded to NI plated Cu using Premabraze 616. (a) Pre anneal room temperature scan (b) Scan at 450 °C indicating increase in contact resistance (c) Post anneal room temperature scan indicating a permanent increase in contact resistance.

A similar behavior was observed for Ni electrode bonded to ETP 53 and ETP 51using Premabraze 616 as shown in Figure 4-23 and Figure 4-24. The junction resistance increases with increasing temperature and the electrical conductivity drops as can be

observed from relative conductivity slopes of Figure 4-24, Figure 4-25 and Figure 4-26. As the sample is cooled to room temperature, the junction resistance reduces as compared to high temperature but still manages a higher value than pre-anneal run value.

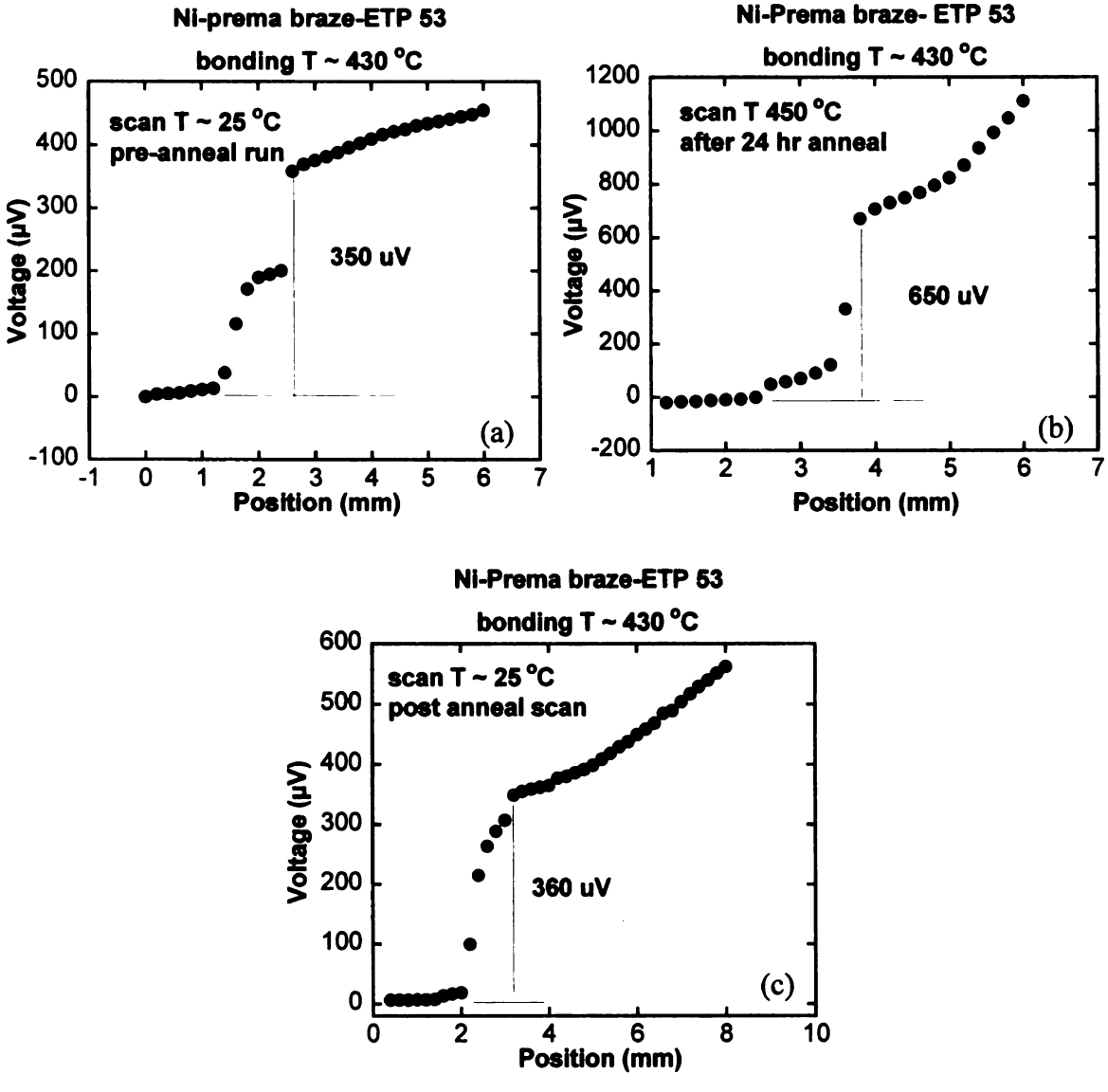

Figure 4-23. Ni electrode bonded to ETP 53 using Premabraze 616 (pre anneal scan indicating high resistance junction (b) 450 °C scan indicating increase in contact resistance (c) Post anneal scan.

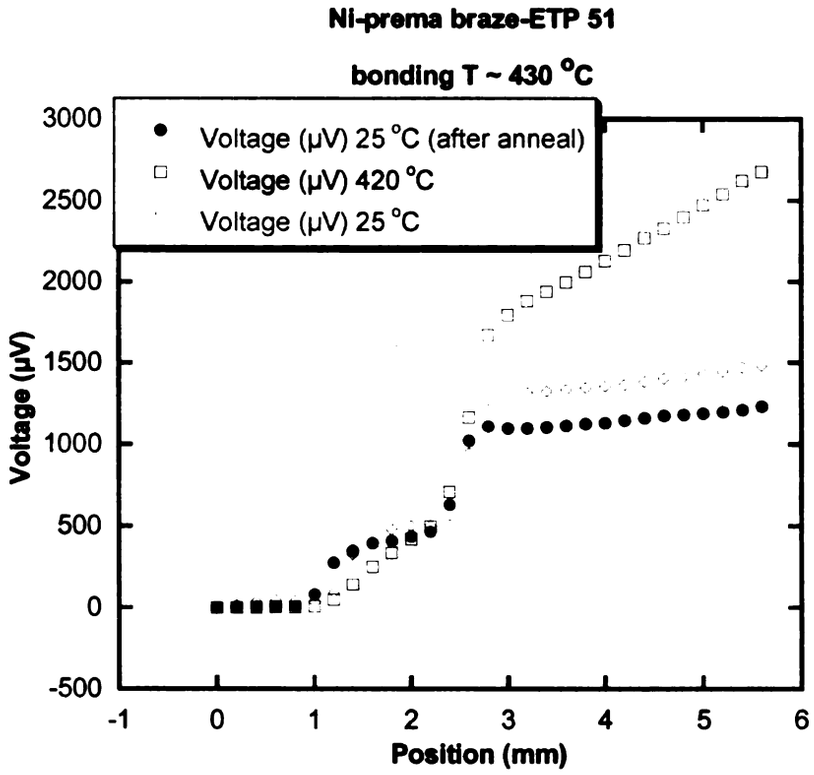

Figure 4-24. ETP 51 bonded to Ni electrode using Premabraze 616.

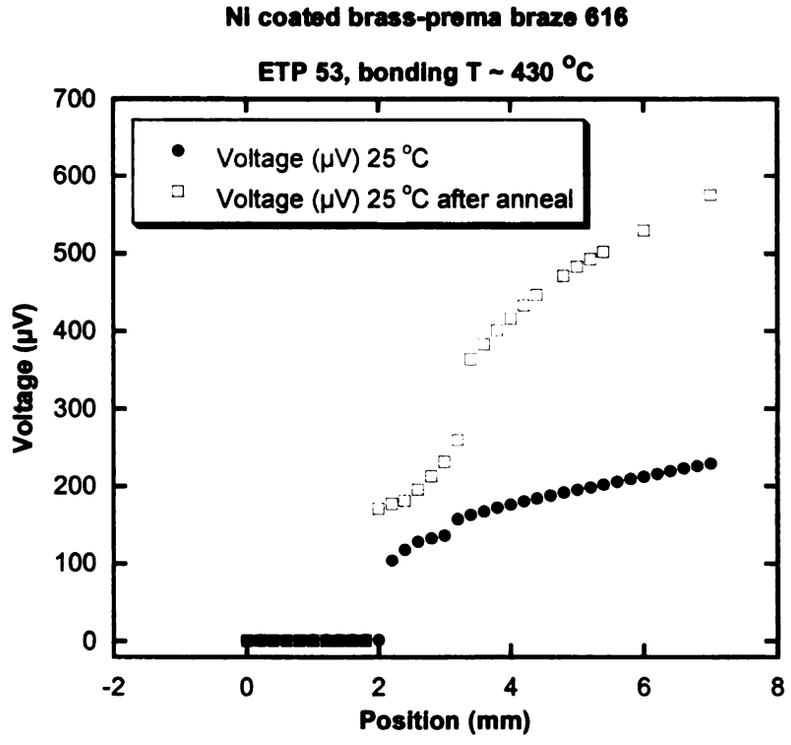

Figure 4-25. Ni coated brass bonded to ETP 53 using Premabraze 616. There is a permanent increase in junction resistance after annealing cycle.

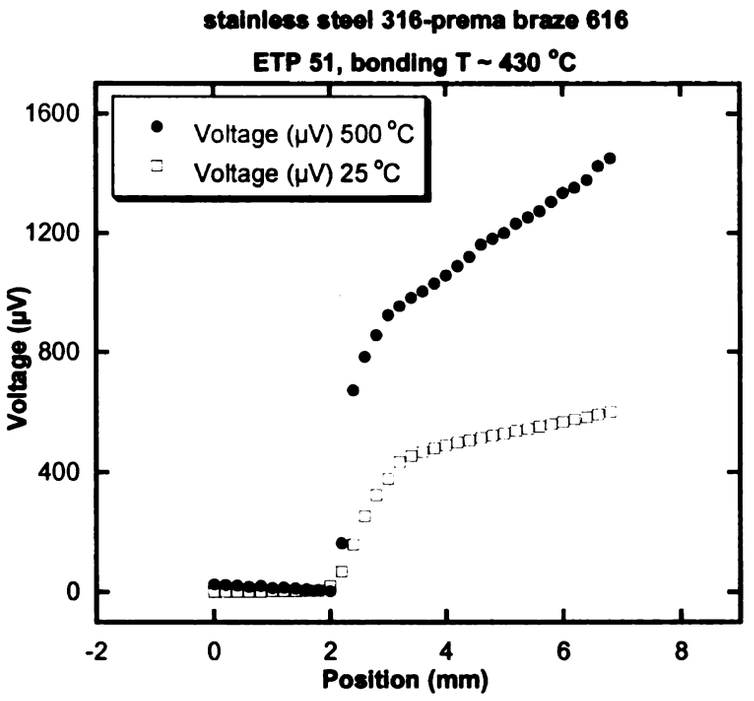

Figure 4-27. ETP 51 bonded to stainless steel 316 using Premabraze 616.

4.3.2.2 Premabraze bonded module with n-type cast TE material

Premabraze 616 seems to perform better with n-type material as compared to p-type material. Although a high resistance junction is observed but we do not see a crack in the leg 2 mm high from the junction as was the case with p-type material. It can be seen from Figure 4-28 below that as the measurement temperature is increased, junction resistance increases and then reduces back to pre anneal value after it is cooled down. For n-type bonding furnace temperature is maintained at ~ 450 °C which is about 20 °C higher than for p-type TE material with Premabraze 616. Probably Sn in p-type material helps to make eutectic at lower temperature than for n-type material.

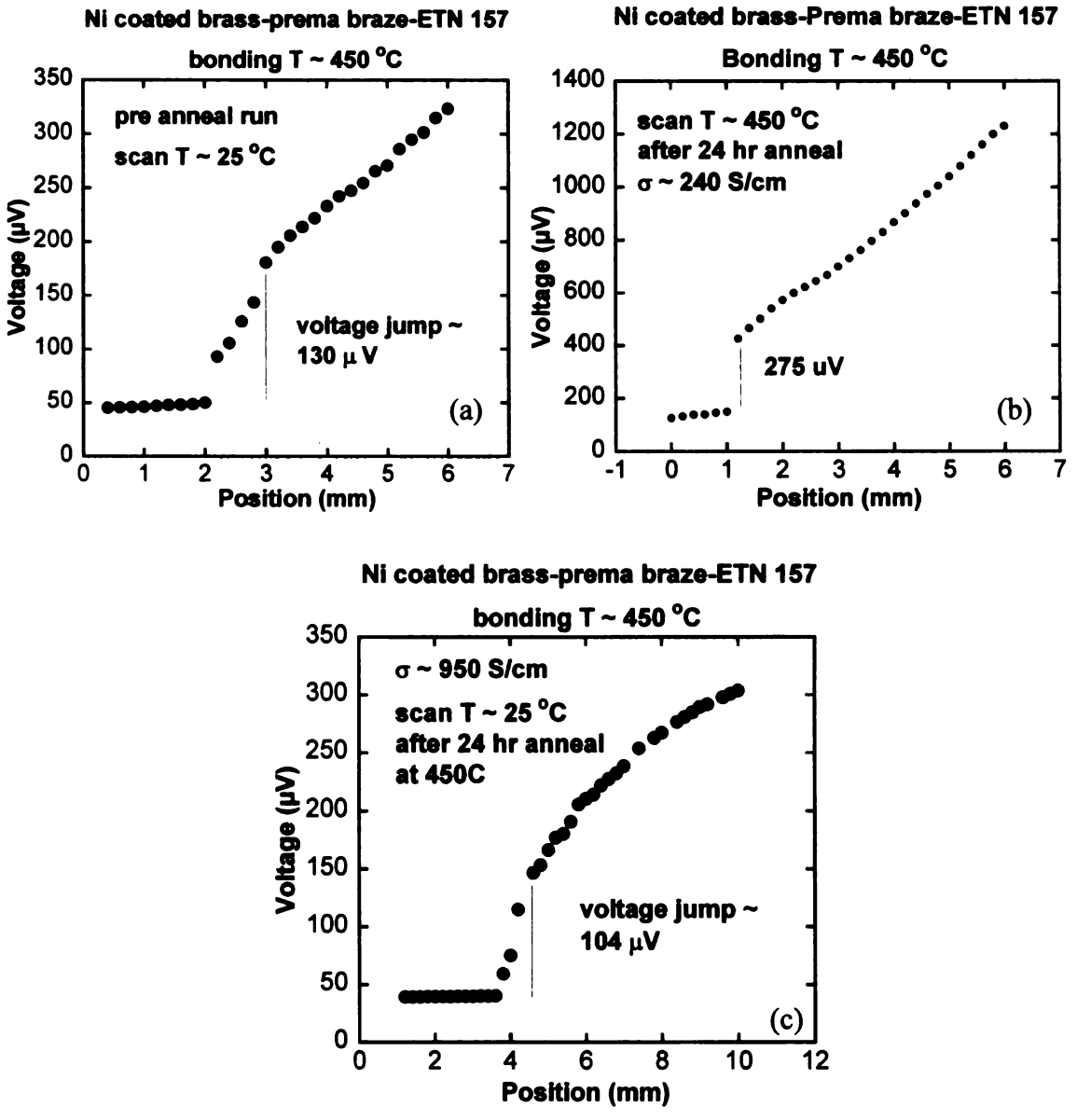

Figure 4-28. ETN 157 bonded to Ni coated brass using Premabraze616.(a) Pre anneal scan(b) 450 °C scan indicating increase in junction resistance (c) Post anneal scan indication junction resistance approaching back to pre-anneal value.

A similar behavior was observed for Ni electrode bonded to ETN 218 whereas previous module was for Ni coated brass (19×10^{-6} in/K) which has significantly different

coefficient of thermal expansion(CTE) than Ni (13 x 10^{-6} in/K). This indicates that this behavior is independent of electrode material as shown in Figure 4-29 below.

Figure 4-29. Ni electrode bonded to ETN 218 using Premabraze616. (a) Pre-anneal scan (b) 450 °C scan after 6 hr indicating increase in junction resistance (c) 450 °C scan after 24 hr indicating no appreciable change than 6 hr scan. (d) Post anneal scan indicating junction resistance reduced back to pre-anneal value.

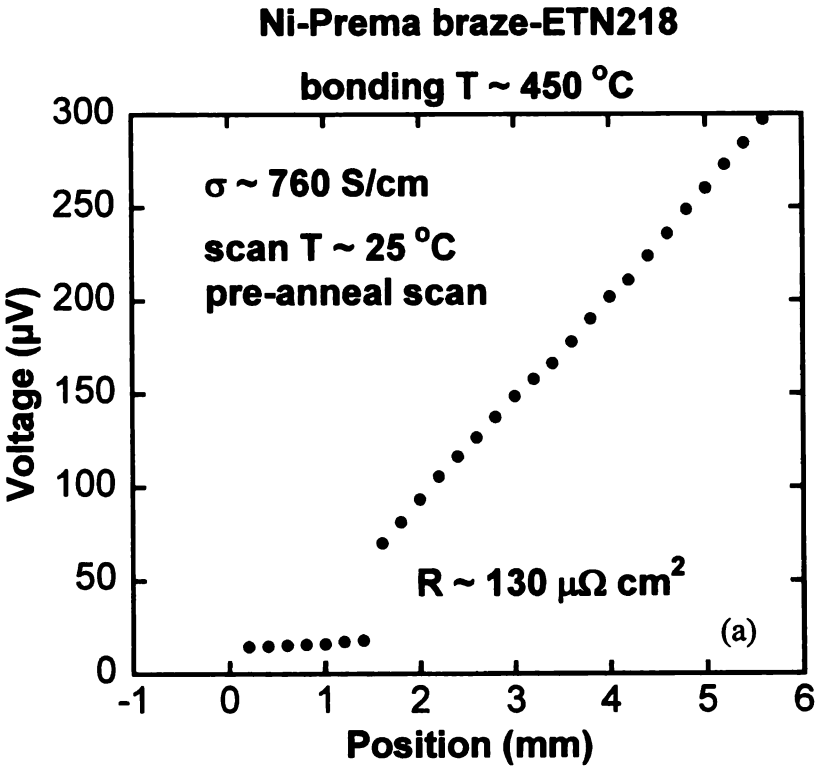
Ni-Prema braze-ETN218
bonding T ~ 450 °C
σ ~ 760 S/cm
scan T ~ 25 °C
pre-anneal scan
R ~ 130 μΩ cm²
(a)
Voltage (μV)
Position (mm)
300
250
200
150
100
50
0
-1
0
1
2
3
4
5
6

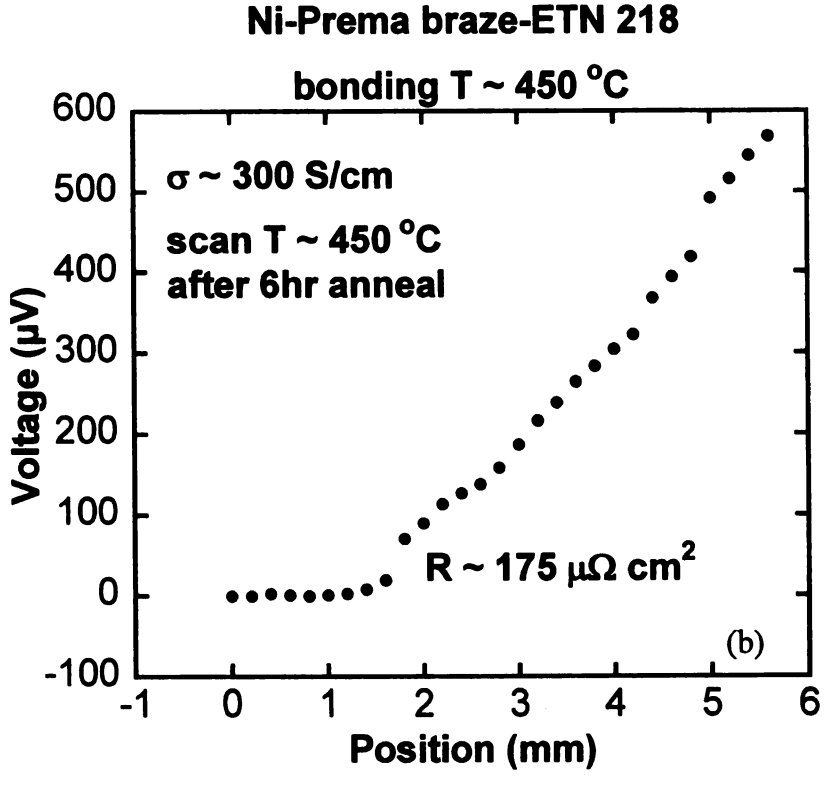
Ni-Prema braze-ETN 218
bonding T ~ 450 °C
σ ~ 300 S/cm
scan T ~ 450 °C
after 6hr anneal
R ~ 175 μΩ cm²
(b)
Voltage (μV)
Position (mm)
600
500
400
300
200
100
0
-100
-1
0
1
2
3
4
5
6

Figure 4-29. Continued.

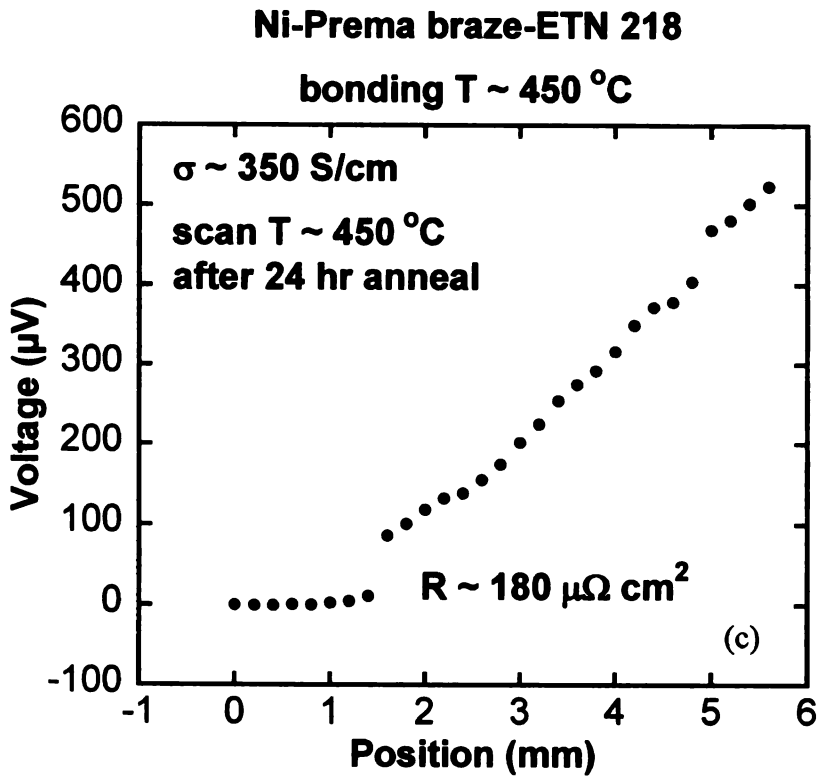

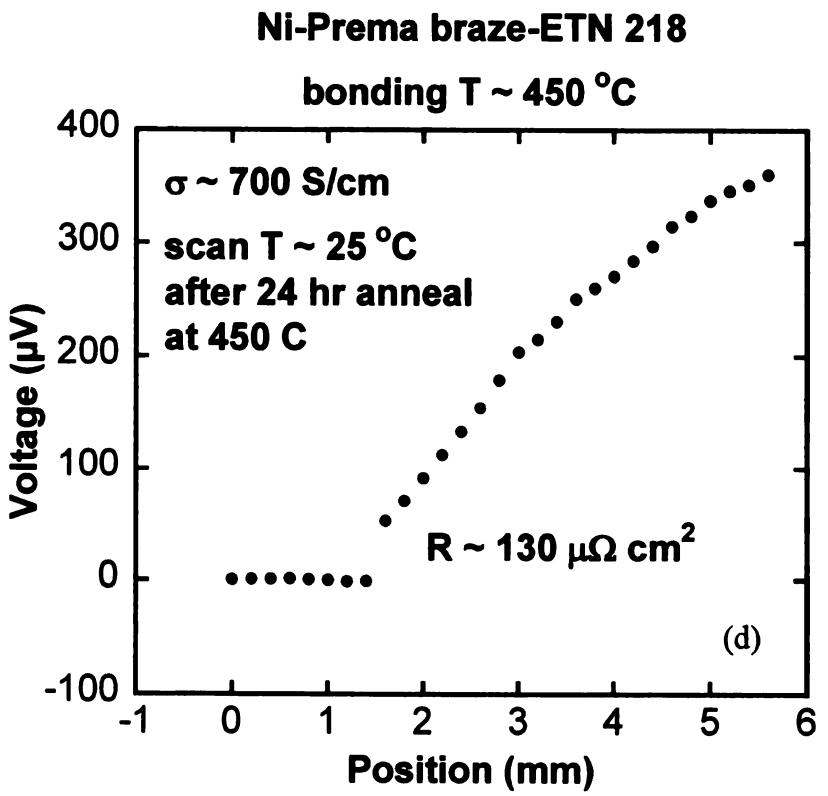

Another sample prepared with ETN 218 and Ni electrode using premabraze 616 depicted low contact resistance. However once through thermal cycle it also showed high contact resistance as shown in Figure 4-30 below.

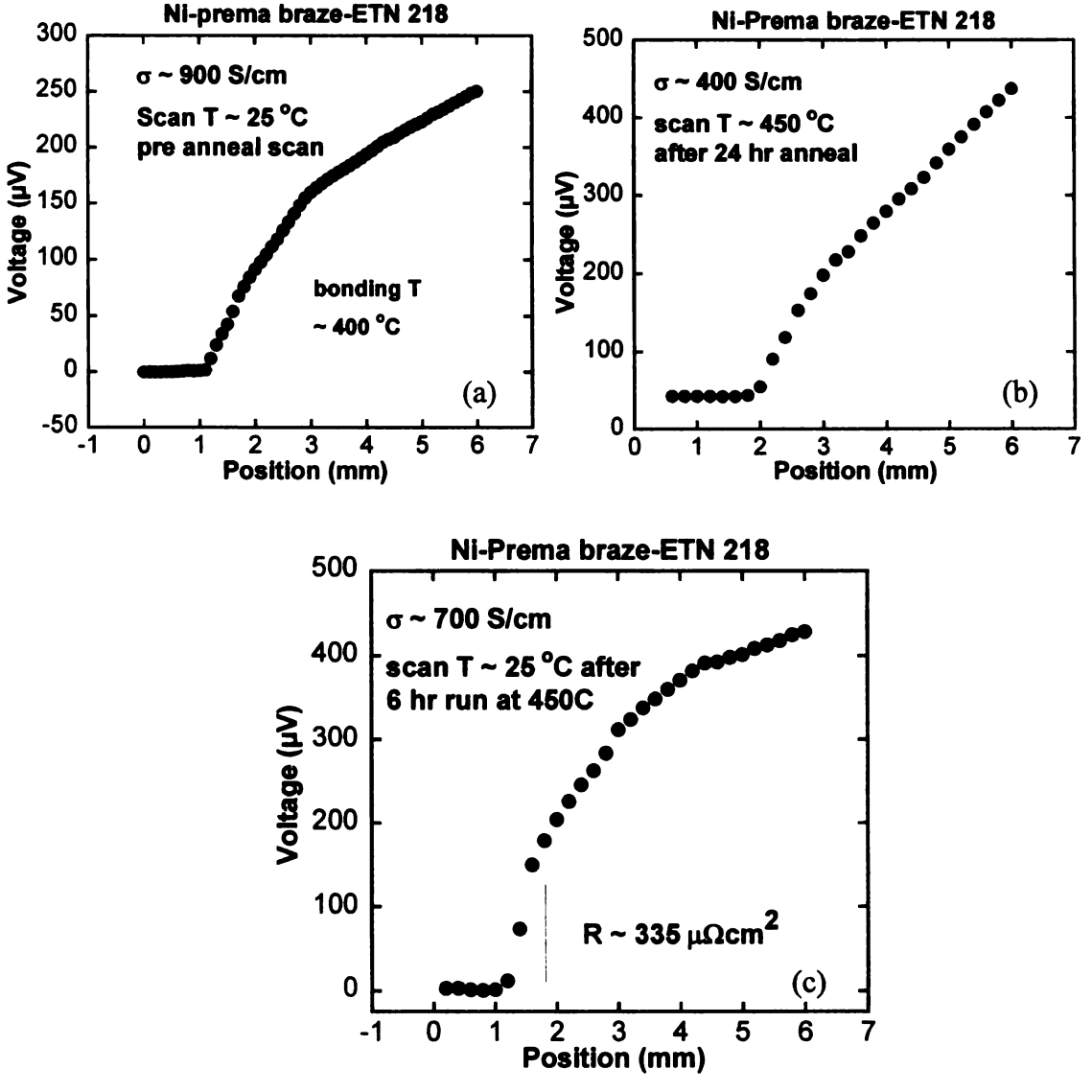

Figure 4-30. ETN 218 bonded to Ni electrode using Premabraze616. (a) Pre-anneal scan indicating a low contact resistance junction (b) 450 °C scan indicating no appreciable change in contact resistance (c) Post anneal scan indicating increase in contact resistance.

4.3.3 Low temperature solder (Cerromatrix) bonded module

The first incident of relatively high short circuit current (7 Amps) for LAST and LASTT based modules (5mm x5mm x7 mm legs) were observed for solder based hot side junctions. To ascertain its viability for long term module it was necessary to investigate high temperature contact resistance for multiple heating cycles and longer durations. For this Ni plated Cu electrode was bonded with LAST (ETN 213) using Cerromatrix solder having a composition of 48Bi/28.5Pb/14.5Sn/9Sb (by weight) and measured inside high temperature voltage profiling system (HTVPS). Melting point for this solder is 280 to 440 °F. As shown in Figure 4-31 module was first raised to 500 °C, brought back to room temperature and then again raised to 600 °C and cooled down to room temperature over a two days period of time. There is increase in contact resistance with increasing temperature and as the module is cooled down there is permanent increase in contact resistance. As the module is cycled second time we see even a further increase in contact resistance as shown in the room temperature scan after second annealing. We believe that Cerromatrix makes eutectic with the LAST material at the higher temperature and contraction during solidification of the Cerromatrix is also a possible cause of cracking in the thermoelectric material. Another contributing factor might be diffusion of Sn or Sn reacting with Te to form SnTe at the junction.

Figure 4-31. ETN 213 bonded to Ni plated Cu using Cerromatrix solder (a) Pre-anneal scan (b) 100 °C scan (c)(d) Scan indicating gradual increase in contact resistance with increasing temperature. (e) Contact resistance increasing with temperature. (f) Post anneal scan indicating a permanent increase in contact resistance as compared to pre-anneal scan (g) Second anneal 600 °C scan indicating increase in contact resistance as compared to first anneal high temperature scan (h) Post anneal scan after second run indicating after every anneal there is permanent increase in contact resistance higher than previous cycle.

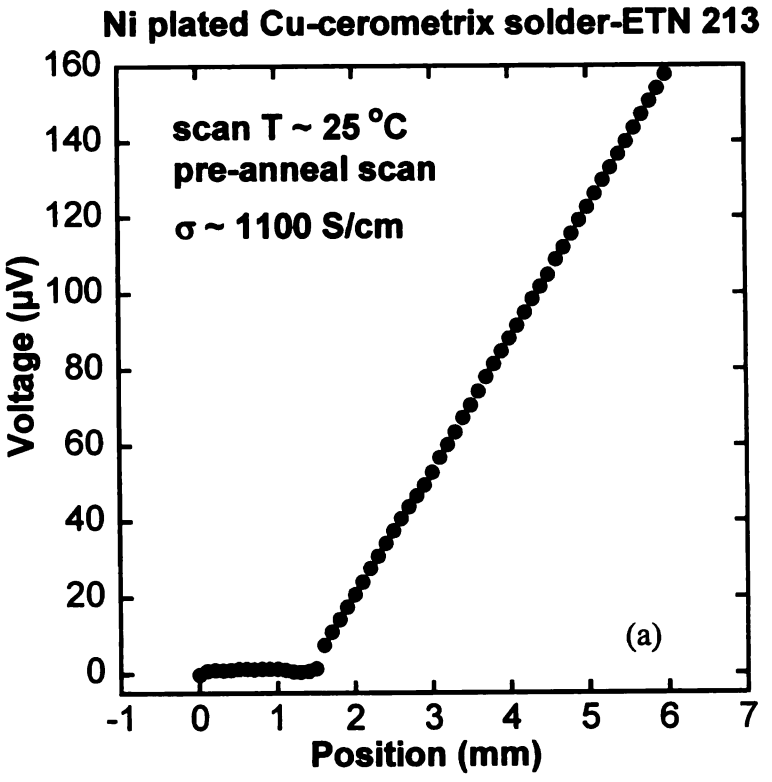
Ni plated Cu-cerometrix solder-ETN 213
scan T ~ 25 °C
pre-anneal scan
σ ~ 1100 S/cm
(a)
Voltage (μV)
Position (mm)
160
140
120
100
80
60
40
20
0
-1
0
1
2
3
4
5
6
7

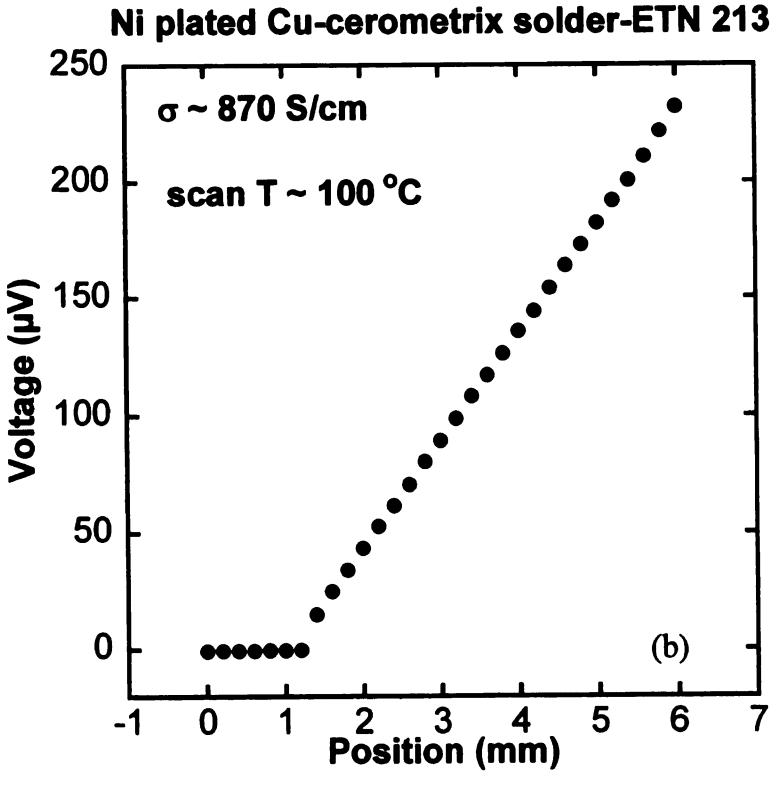
Ni plated Cu-cerometrix solder-ETN 213
σ ~ 870 S/cm
scan T ~ 100 °C
(b)
Voltage (μV)
Position (mm)
250
200
150
100
50
0
-1
0
1
2
3
4
5
6
7

Figure 4-31. Continued.

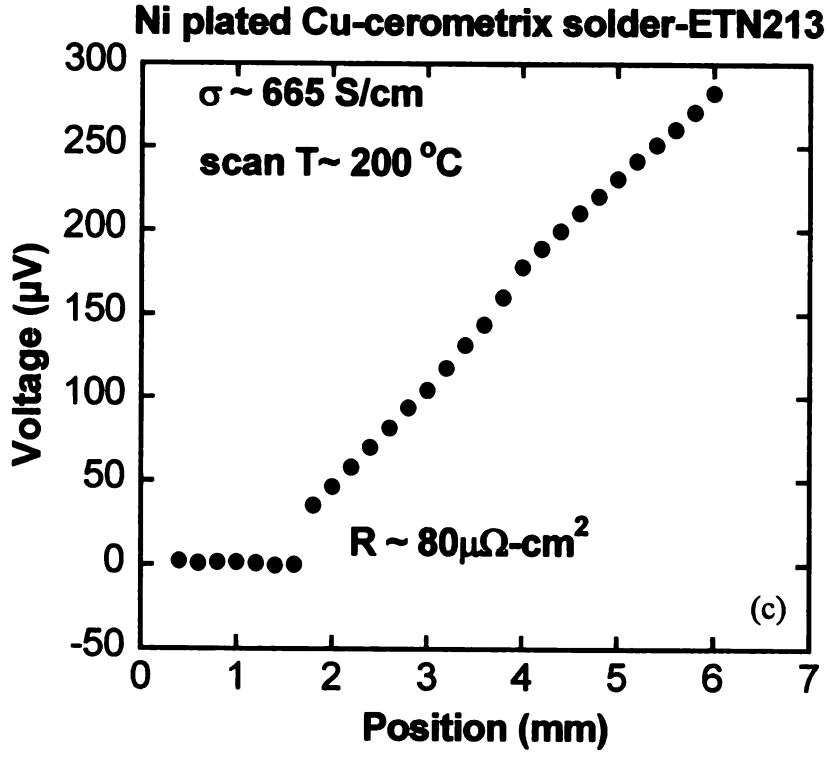

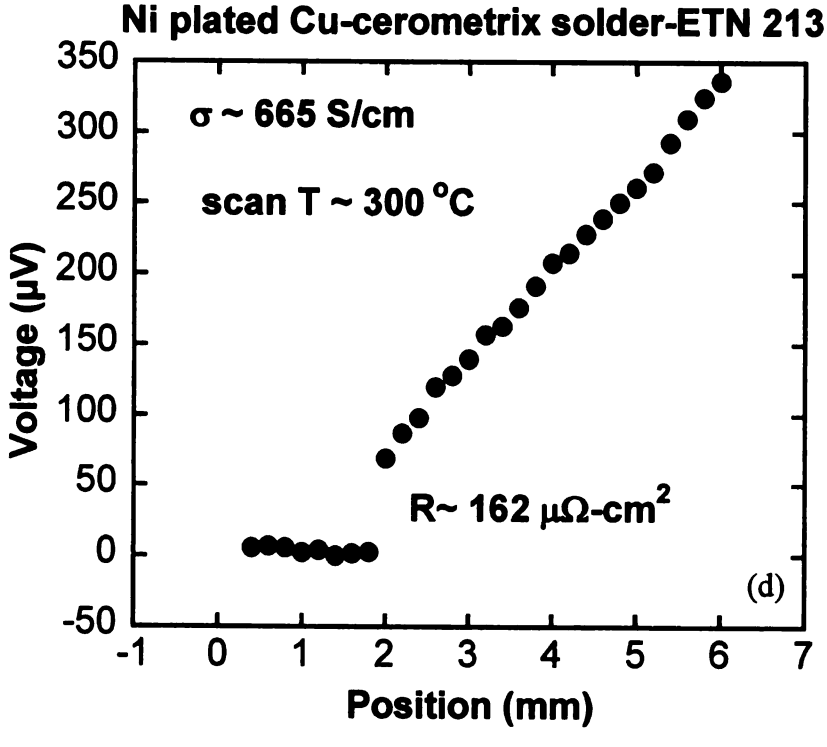

Figure 4-31. Continued.

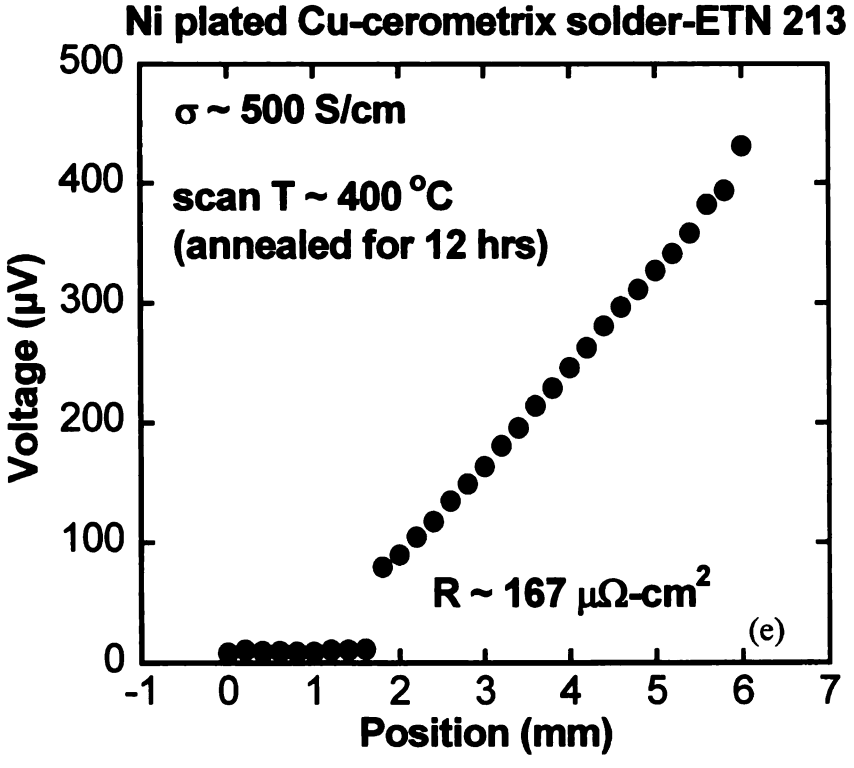

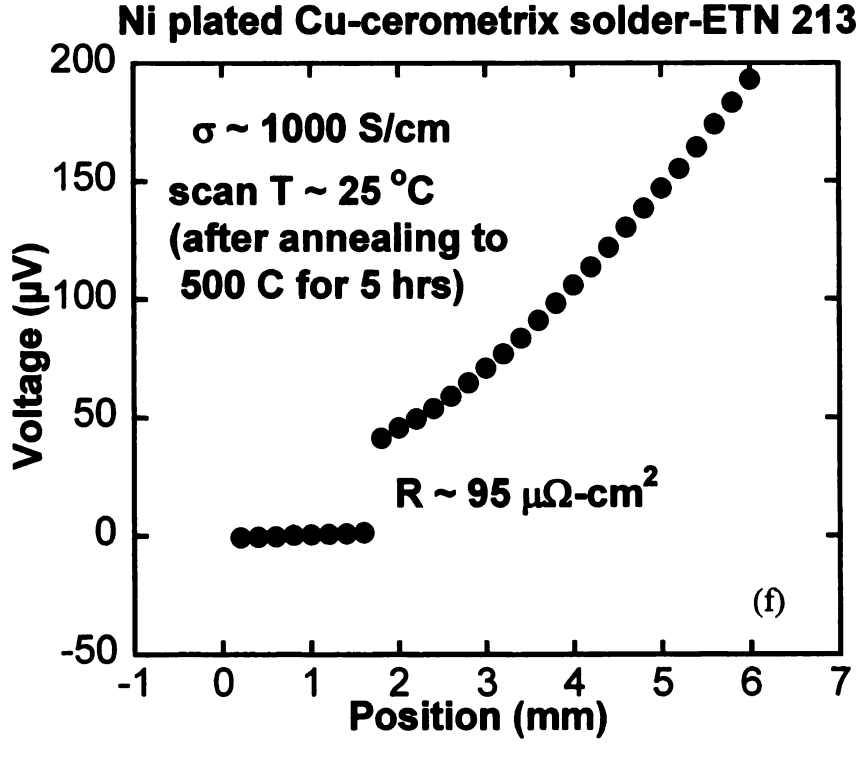

Figure 4-31. Continued.

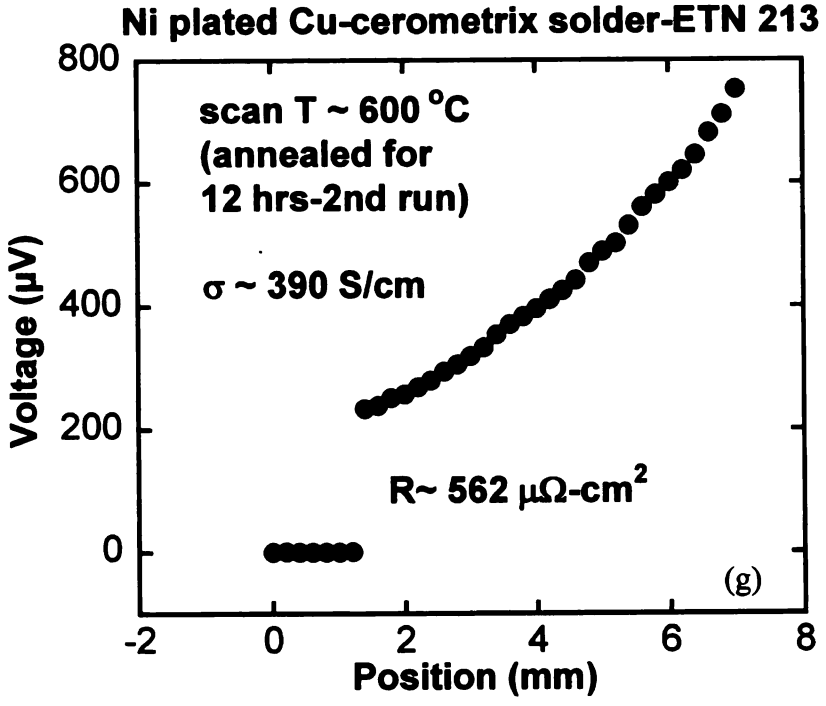

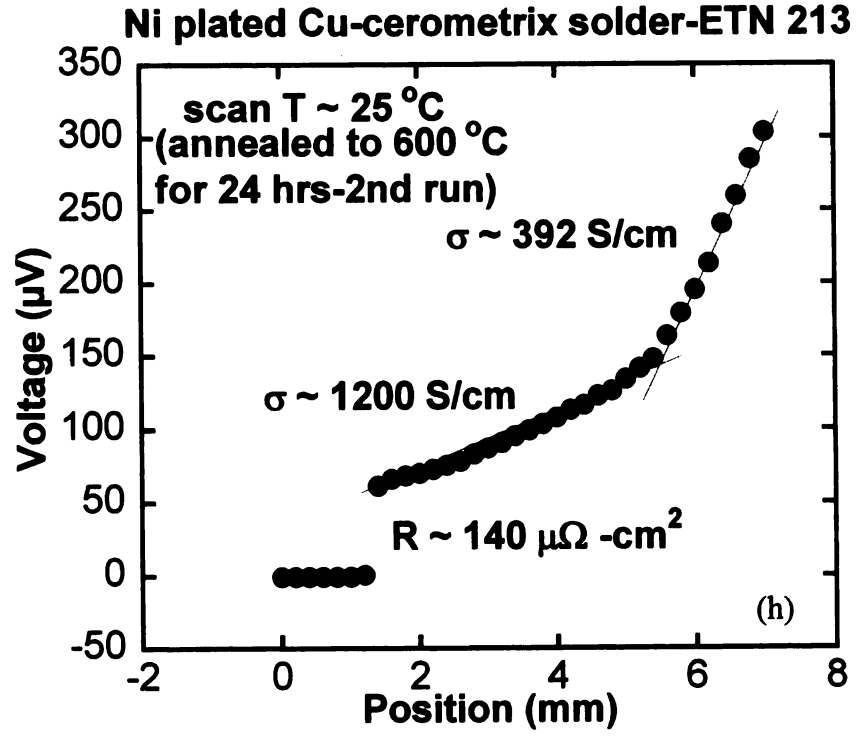

A similar behavior was observed for another Cerromatrix based module as shown in Figure 4-32 below. In this case both Cu electrode and unicouple legs were coated with Ni before bonding. However, this did not have a significant effect on the high temperature scans.

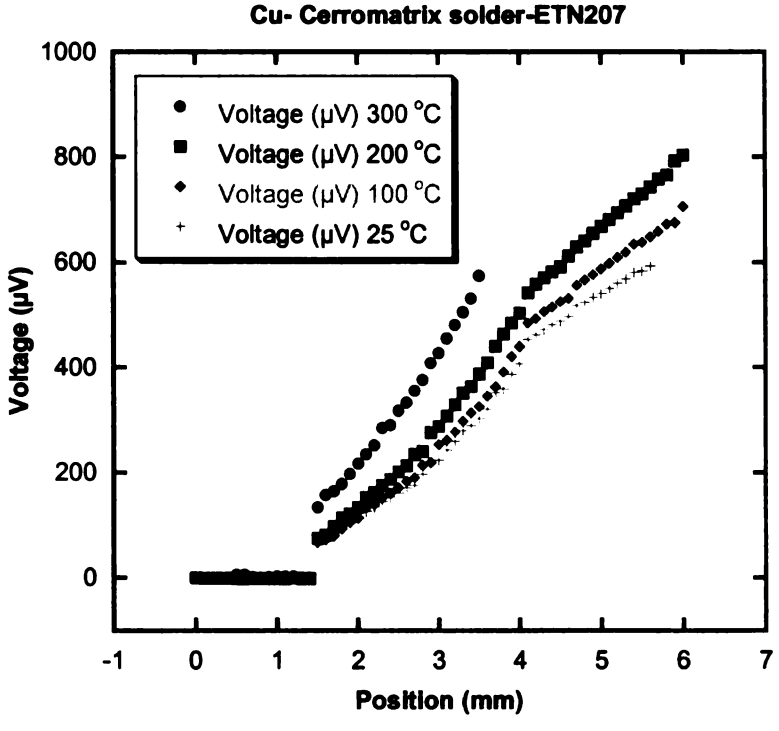

Figure 4-32. Ni plated Cu and Ni plated ETN 207 leg bonded using Cerromatrix solder. Contact resistance increases with increasing temperature.

4.3.3.1 P-type LASTT bonded using Cerromatrix solder with Cu

P-type bonding with Cerromatrix shows a different behavior than n–type and is similar to SnTe bonding in which contact resistance reduces with increasing temperature. For this experiment Cu electrode was bonded with ETP 52 using Cerromatrix solder. In the first annealing run module was taken to 600 °C under Ar for five days. It was then cooled down and again annealed to 600 °C for two days under vacuum. Successive annealing and cooling induced permanent increase in contact resistance. As can be seen from Figure 4-33 below that as the temperature increases, electrical conductivity drops and contact resistance decreases. After about 12 hrs annealing at 600 °C, electrical conductivity drops to about ~ 110 S/cm and then stays at that value for next three days. After the module was cooled to room temperature, the electrical conductivity increased to 2300 S/cm from the 1800 S/cm pre-annealed value. However, there was permanent increase in contact resistance after it was cooled down. We believe it is because during cooling LASTT material, Cerromatrix solder and electrode contract at different rates due to difference in coefficient of thermal expansion (CTE) and cause shear stresses at the surface which results in large contact resistance. In the second annealing run under vacuum electrical conductivity drops to ~ 110 S/cm equivalent to previous annealing run under Ar but unlike the first run, the contact resistance does not improve with increasing temperature. As expected, after the second annealing run the room temperature electrical conductivity increases close to 2000 S/cm and the contact resistance also increases as compared to previous run under Ar.

Figure 4-33. ETP 52 bonded to Cu electrode using Cerromatrix solder. (a) Pre anneal scan indicating high contact resistance (b) (c) (d) Contact resistance decreases with increasing temperature from 100 °C to 500 °C. (e) (f) Electrical conductivity drops from ~ 500 S/cm to 110 S/cm after 12 hr anneal at 600 °C. (g) (h) Electrical conductivity remains same for one and half days and contact resistance does not deteriorate. (i)(j)(k)(l) Electrical conductivity remains same for four days and contact resistance does not deteriorate. (m) Post anneal room temperature scan indicating permanent increase in contact resistance (n)(p) No improvement in contact resistance with increasing temperature (q) Second post anneal room temperature scan. Contact resistance increased two fold.

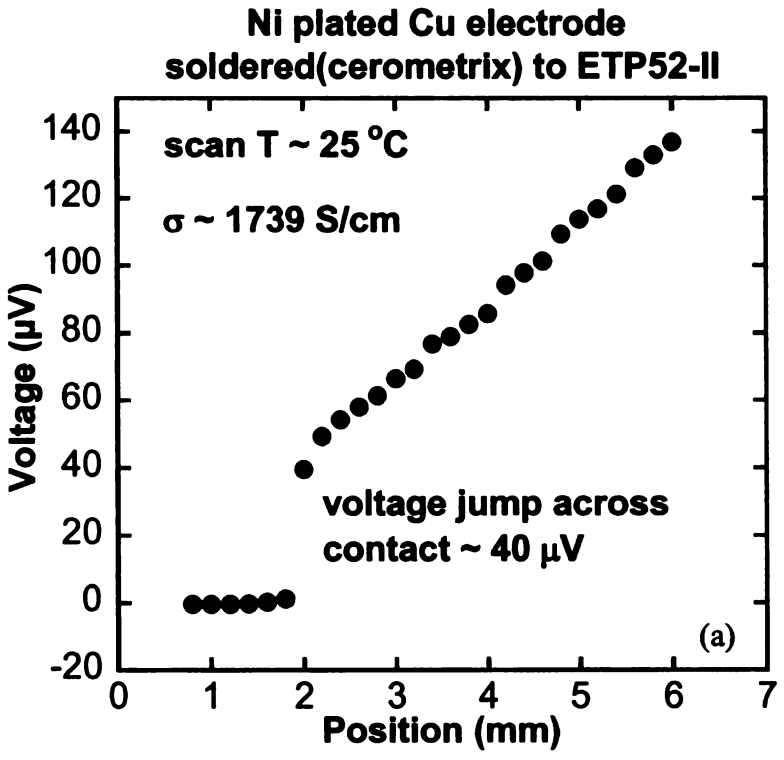
Ni plated Cu electrode
soldered(cerometrix) to ETP52-II
scan T ~ 25 °C
σ ~ 1739 S/cm
voltage jump across
contact ~ 40 μV
(a)
Voltage (μV)
Position (mm)
140
120
100
80
60
40
20
0
-20
0
1
2
3
4
5
6
7

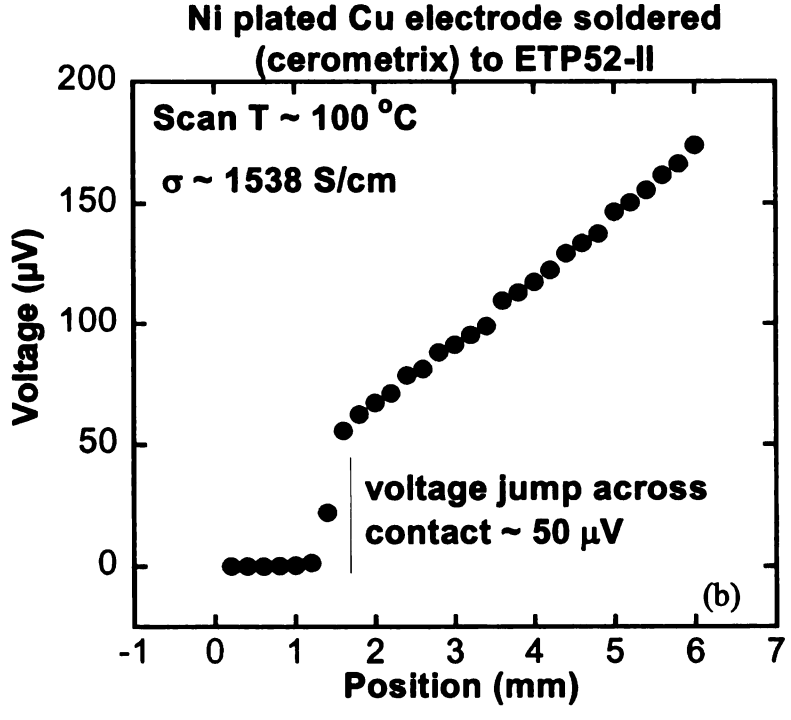
Ni plated Cu electrode soldered
(cerometrix) to ETP52-II
Scan T ~ 100 °C
σ ~ 1538 S/cm
voltage jump across
contact ~ 50 μV
(b)
Voltage (μV)
Position (mm)
200
150
100
50
0
-1
0
1
2
3
4
5
6
7

Figure 4-33. Continued.

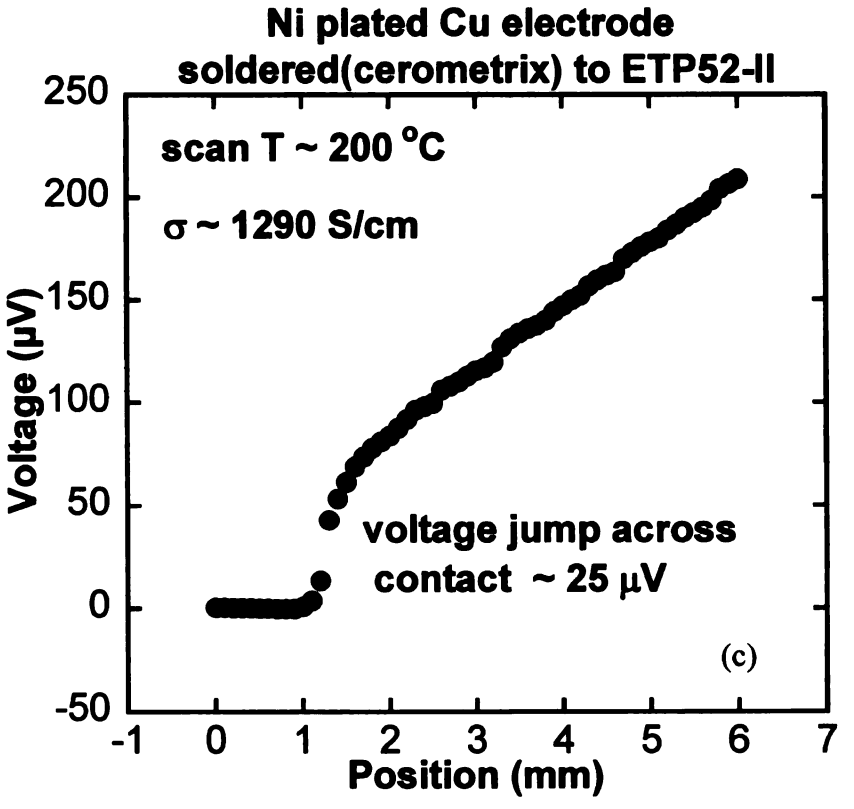

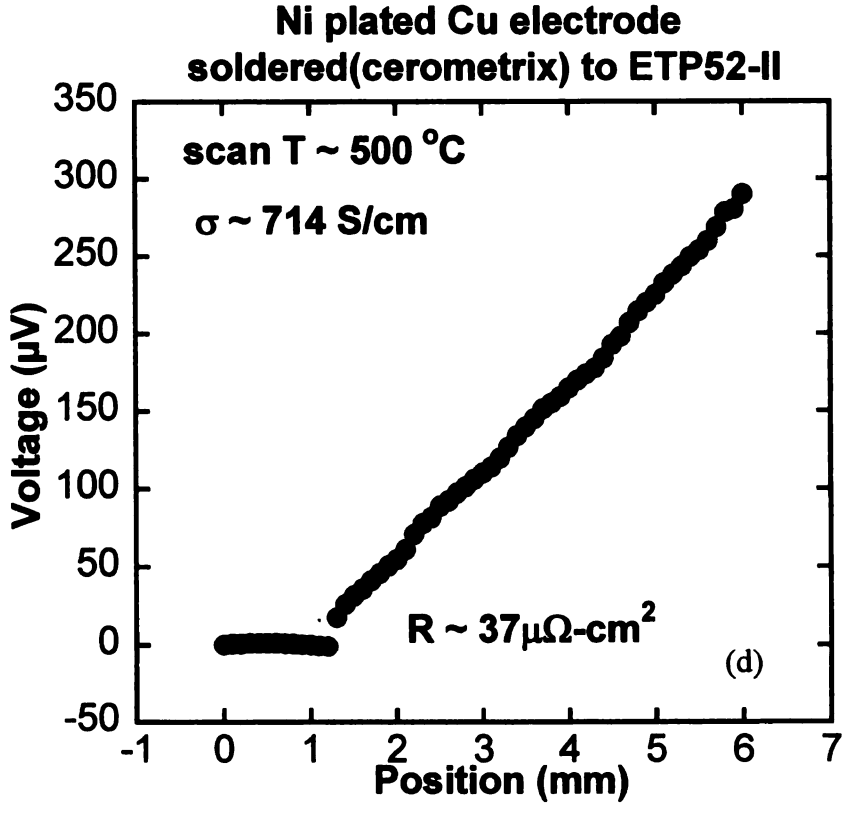

Figure 4-33. Continued.

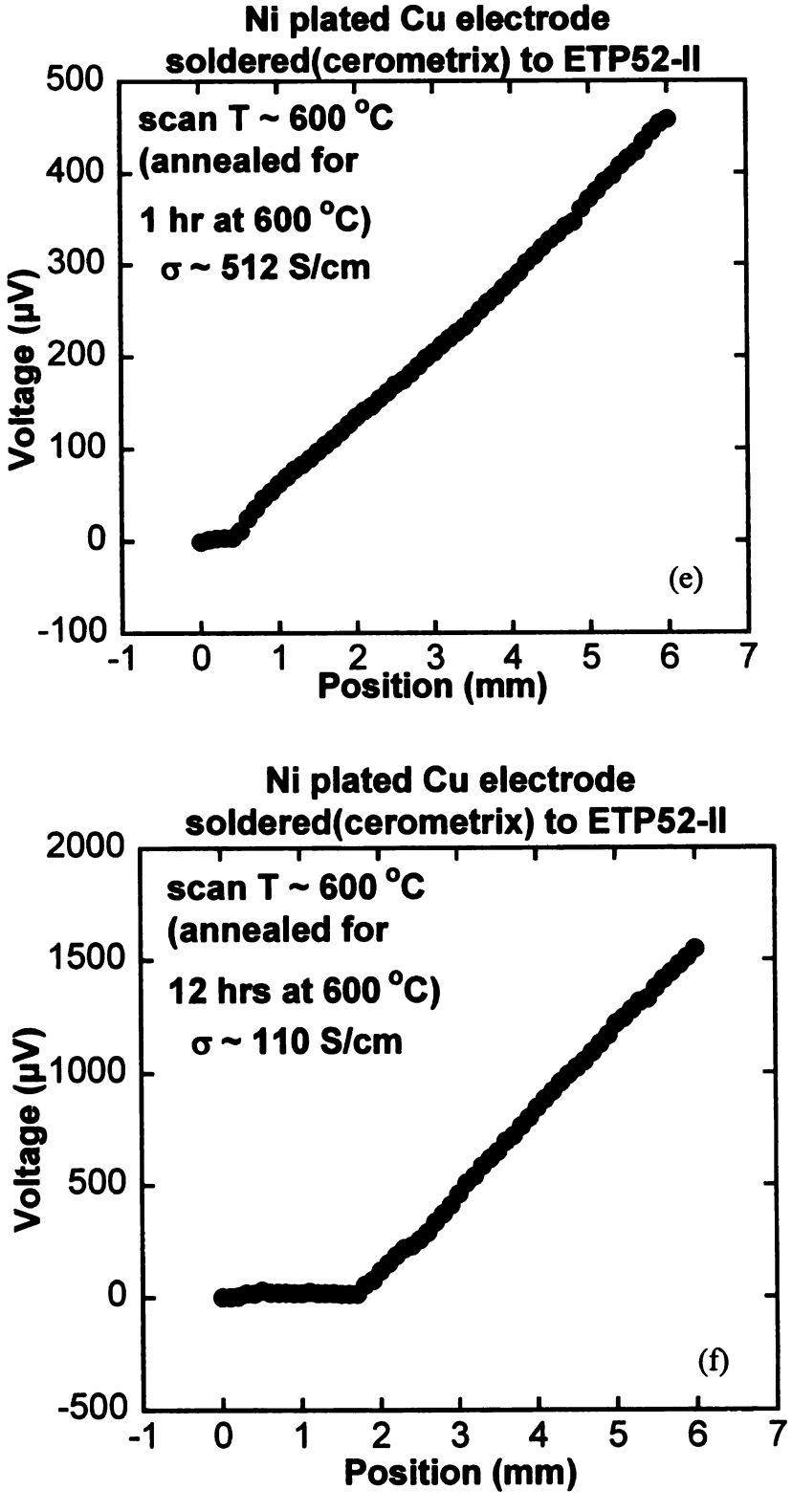

Figure 4-33. Continued.

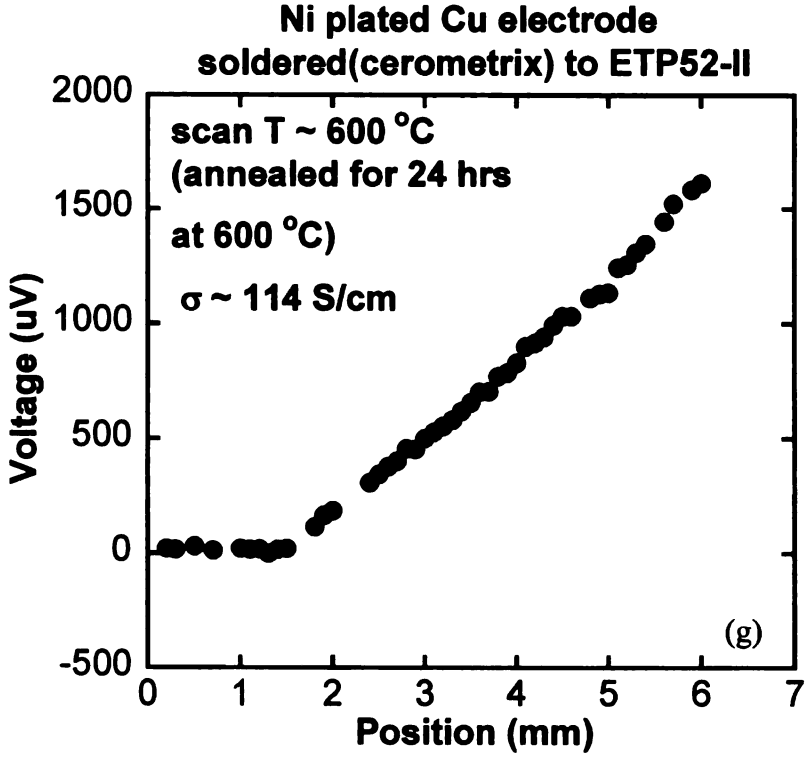

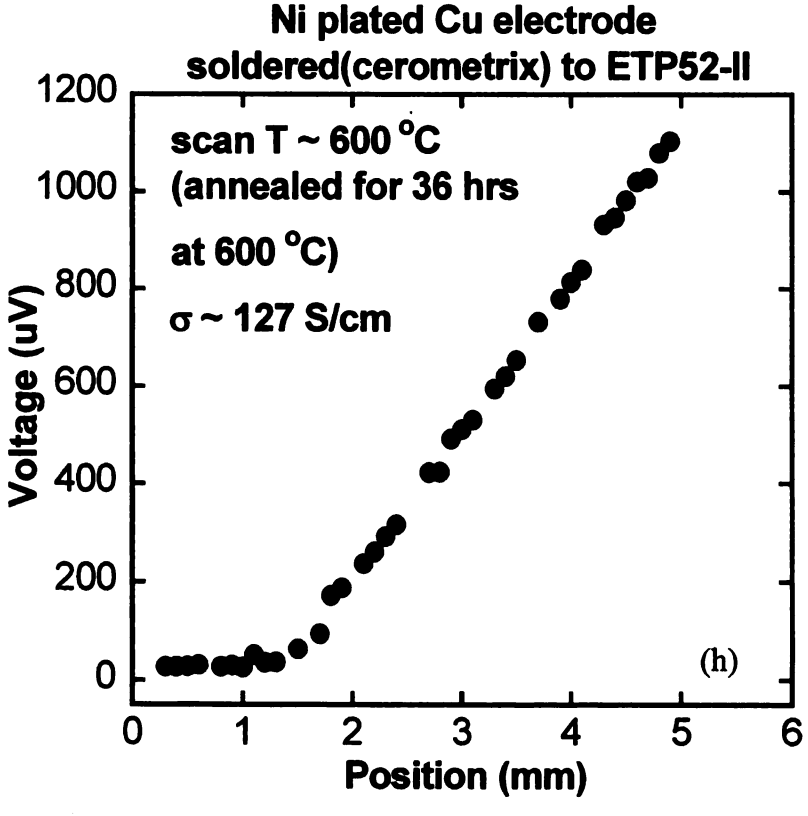

Figure 4-33. Continued.

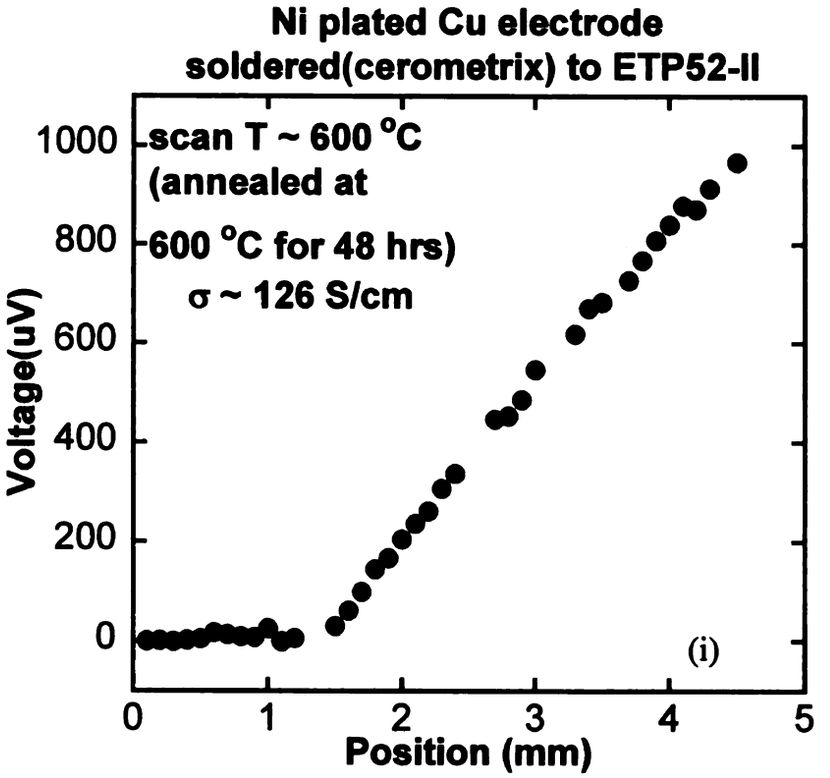

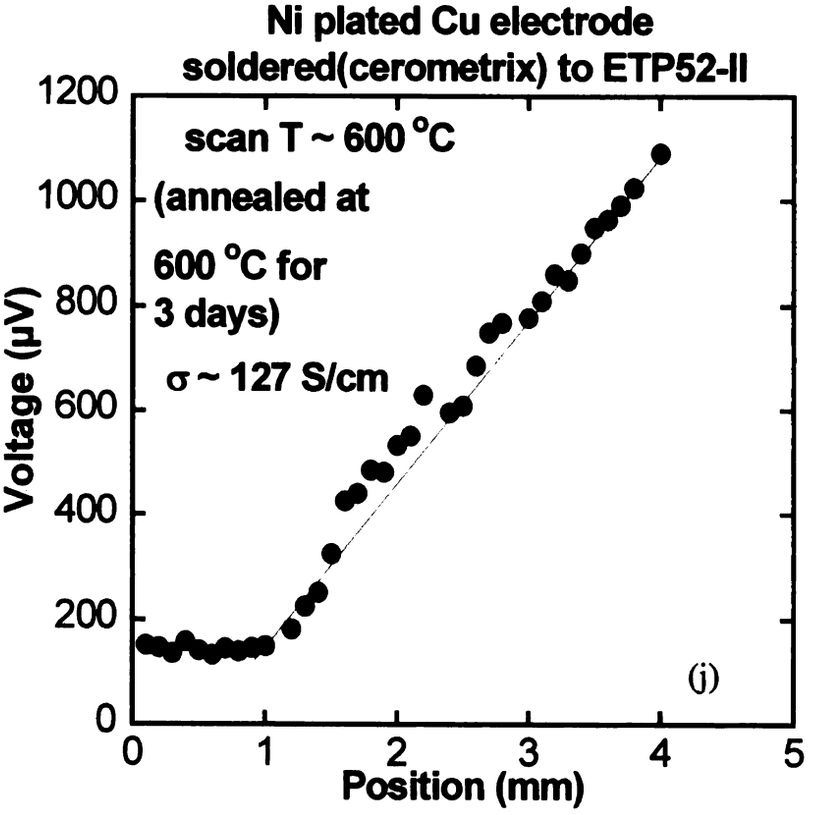

Figure 4-33. Continued.

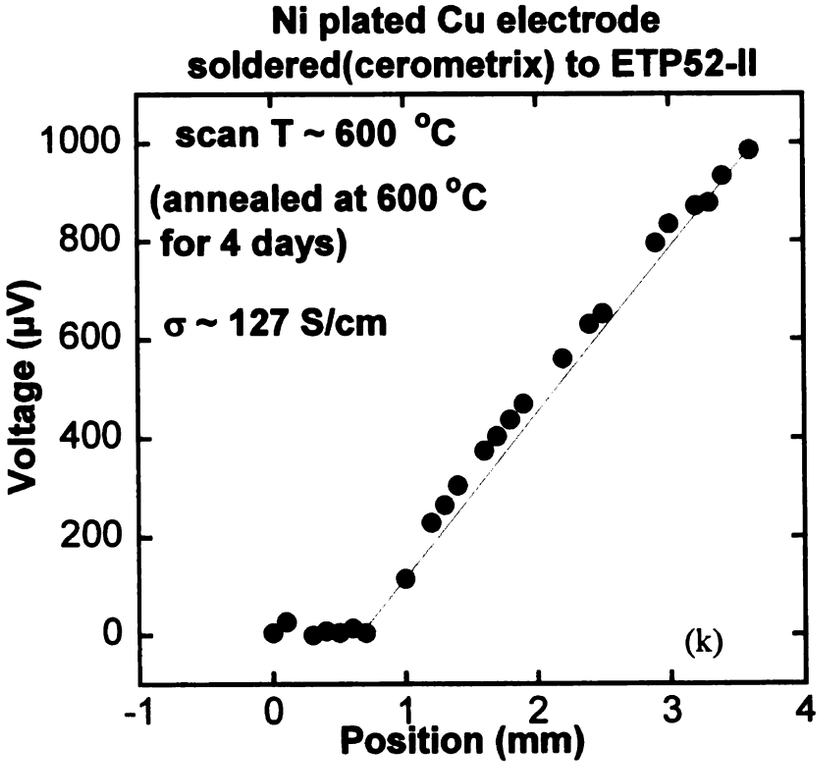

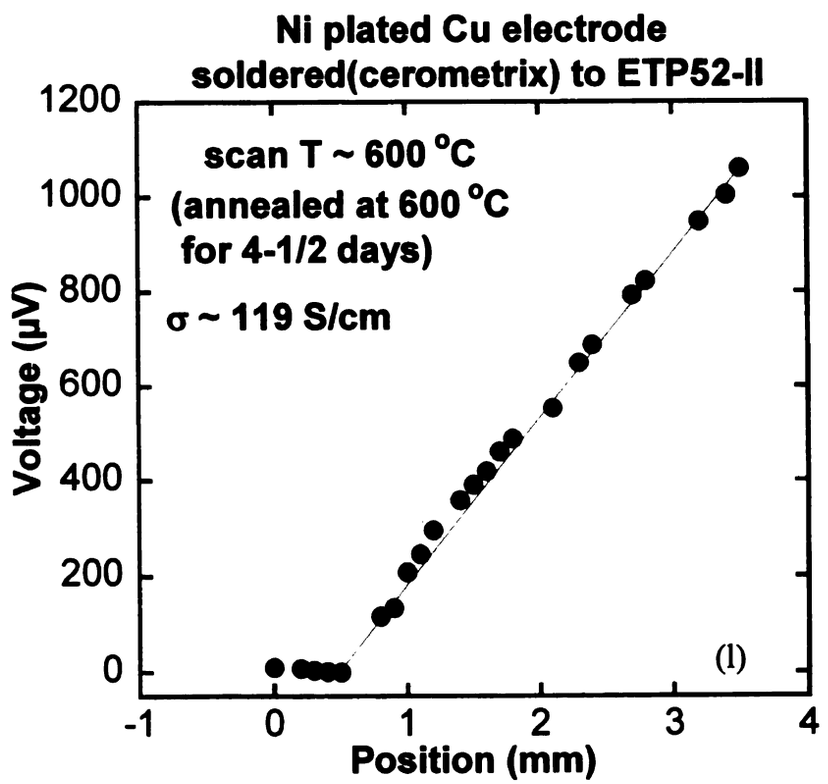

Figure 4-33. Continued.

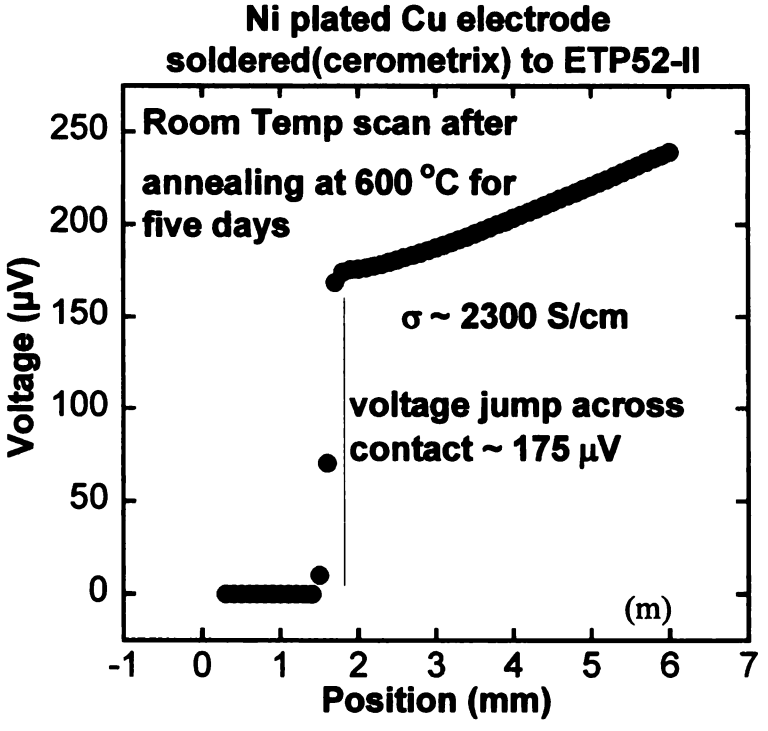

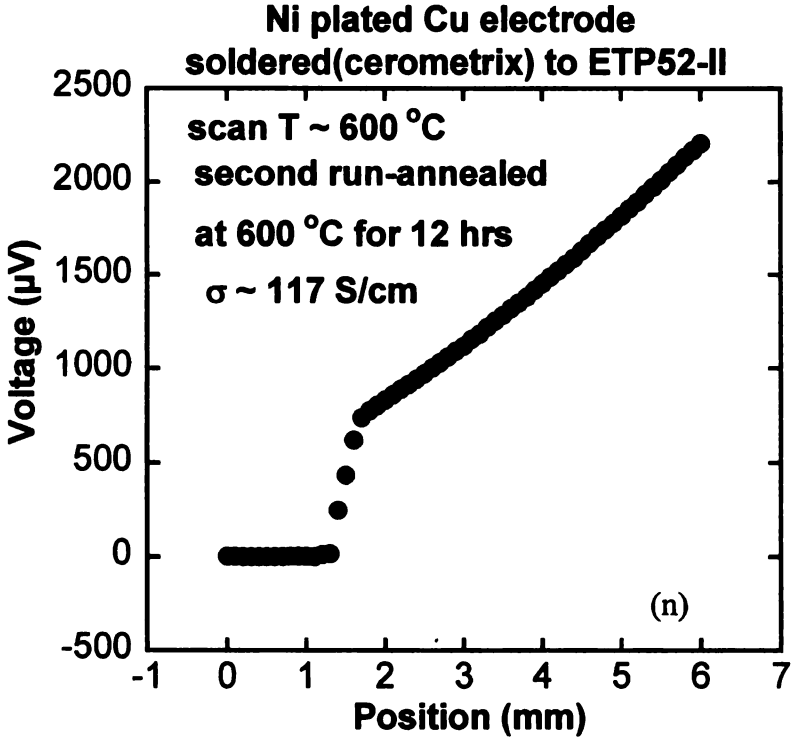

Figure 4-33. Continued.

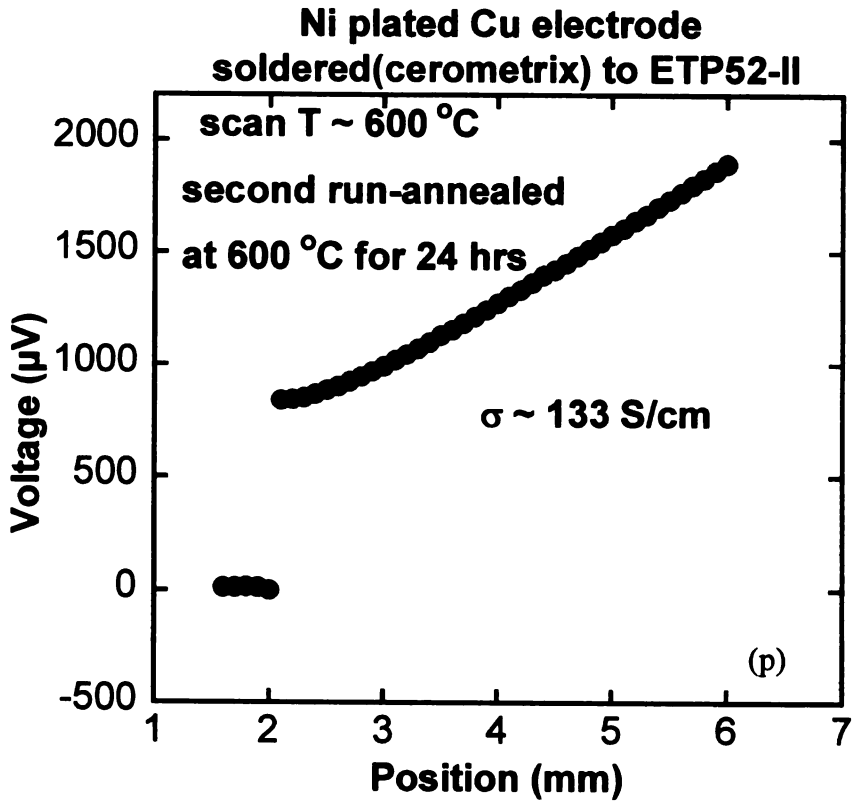

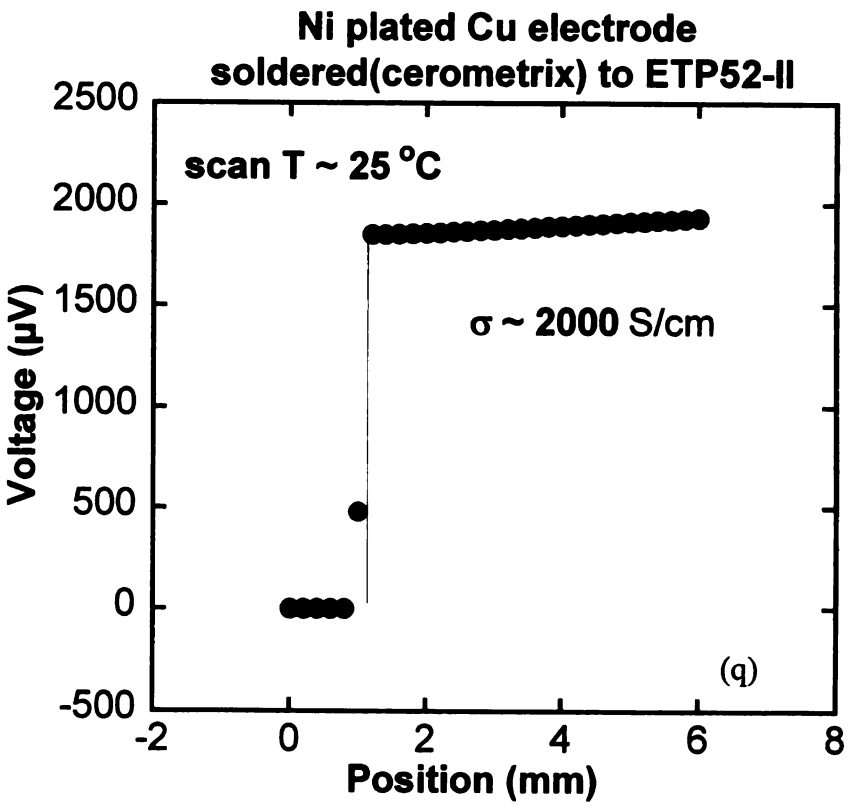

4.4 Energy Dispersive Spectroscopy (EDS) analysis of fractured surface

The sample was then fractured to investigate Cu diffusion through EDS analysis.

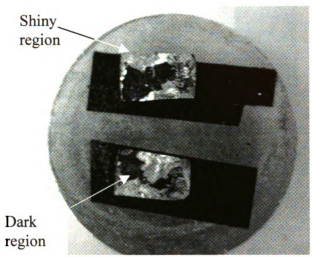

Figure 4-34. Fractured sample leg indicating dark and shiny region.

As can be seen from Figure 4-37, there are two clear regions of dark and shiny silver color on both sides of fractured leg. EDS was carried out on the sample but we were not certain about the results as it was indicating abnormal values of constituent elements. We again annealed another sample under same conditions for approximately 18 hrs. Figure 4-35 shows the broken sample part with both dark and shiny regions. EDS results for this sample are shown in Table 4-1.

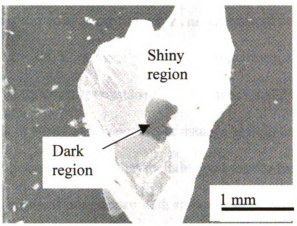

Figure 4-35. SEM picture of new p-type leg.

Table 4-1. EDS results for dark and shiny regions indicating Cu and oxygen rich regions.

Element	Dark region		Shiny region		Difference in
	Weight %	Atomic %	Weight %	Atomic %	atomic %
Cu K	8.48	17.20	3.61	7.84	9.36
Sn L	19.46	21.14	20.44	23.77	2.63
Te L	43.37	43.81	42.45	45.92	2.11
Pb M	28.69	17.85	33.17	22.10	4.25
Sb L	-	-	0.33	0.38	
Total	100.00		100.00		

Conclusion

A new high temperature voltage profiling system has been developed to investigate contact resistance at ~ 800 K. A number of SnTe, Premabraze and Cerromatrix based modules were tested for contact resistance. Among these SnTe based p-type bonds showed best results in terms of low contact resistance at high temperature. For n-type material there is variation in results that include good results for hot pressed n-type using SnTe and direct bonding of hot pressed with stainless steel. Soldered bonds initially show promising results but contact resistance increases after thermal cycling. Based on these results SnTe is better option for both type of LAST thermoelectric material.

Appendix A: Nanowire Synthesis

Introduction

My initial research efforts were focused on GeO_2 nanowire synthesis for sensor applications. Nanowires were grown using the vapor-liquid-solid (VLS) mechanism. This idea was proposed by Ellis and Wagner in 1964 [45]. In the VLS mechanism a liquid catalyst droplet sits on top of a nanowire and absorbs semiconductor material as the catalyst supersaturates, the semiconductor material drops out to form another layer of nanowire. This process continues with the supply of base material either through a gas source or from surface diffusion of atoms. The catalyst droplet also involves some amount of base material that makes a eutectic; GeO_x with melting point of 361°C. There is also evidence that nanowires grow by vapor-solid-solid (VSS) mechanism [46]. If the growth takes place below the eutectic temperature, then the catalyst (usually Au) will remain a solid. Nanowire grown through this mechanism usually have thinner diameter. Whether nanowires will grow through VLS or VSS mechanism in a particular experiment depend upon the growth temperature, vapor pressure, source element and catalyst used. [46]. I will discuss nanowire synthesis setup followed by high temperature GeO_2 and ZnO synthesis and finally low temperature synthesis of GeO_2 nanowires.

A.1 Experimental setup

In our lab the experimental arrangement consists of a quartz tube and horizontal tube furnace which is a hollow cylindrical shape with resistive heating coils covered in thermal insulation. Furnace has outside diameter of 8 inches, inside diameter of four

inches and is 12" long. A 3.35" diameter quartz tube extends through the cylindrical furnace for uniform heating of samples as shown in Figure A-1. The two ends of the quartz tube have stainless steel end caps with double 'O' rings. One end of the tube is connected to a rotary pump which can create vacuum less than 100 mTorr in the tube. The other end is connected to two gas supply lines through mass flow controllers (MFC) for control of Ar or O_2 supplies. Type 'K' thermocouple is used to measure the furnace temperature. In a typical arrangement source material is placed on a 2.5" x 6" quartz plate at the upstream end and a substrate for nanowires is placed few inches downstream inside the furnace heating zone. The arrangement has also been made to place a separate thermocouple inside the quartz tube to know more accurately the substrate temperature during growth. As a result of the low pressure environment in the tube there is always a temperature difference between furnace temperature outside the tube and actual substrate temperature inside the tube.

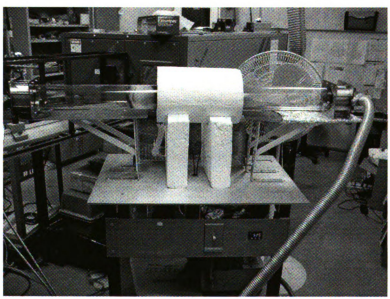

Figure A-1. Nanowire synthesis setup.

A.2 Germanium Oxide (GeO_2) nanowires

Oxide NWs have been found to have different bandgap than bulk oxides [47] e.g. bulk CuO has bandgap of 1.85 eV and CuO nanowires were measured with 2.05 eV bandgap. Nanowires are better candidates for sensors because of higher surface to volume ratio which allow larger surface activities and accumulation of charge species which can modify transport properties [48]. Germanium dioxide (GeO_2) nanowires have been reported with a photoluminescence signal an order of magnitude higher than GeO powder [49,50]. They also have higher refractive index (n=1.63) than silicates [51] which makes them attractive for optoelectronic applications and they exhibit a bandgap of 2.44 eV. This material can be used as optical waveguides [52] and our research group has investigated GeO_2 nanowires as substrate for surface enhanced Raman Spectroscopy (SERS) [53].

A.2.1 Experimental details

In this lab nanowires were grown on silicon (110) and quartz substrates. The substrate was cleaned in acetone, then methanol and DI water, all through sonication. Three different types of catalyst were tested. A gold film in the range of 2 to 15 nm was either sputtered deposited or evaporated using e-beam evaporator. Gold colloidal particles on silicon substrate have also been used as catalyst. To deposit the gold collides, the silicon substrate is first coated with *poly L lysine* which is hydrophilic for Au particles. This helps the gold particles to stick and to spread uniformly on substrate.

Platinum (Pt) wire was also used successfully as catalyst. The substrates were placed on quartz plate and inserted into the quartz tube within hot furnace zone. Source material of pure germanium was placed approximately four to five centimeters upstream. The quartz tube was evacuated to less than 100 mTorr and an argon/hydrogen gas (95/5) was introduced at 50 sccm. The pressure inside the tube was raised to about 100 to 150 Torr and the tube was then heated to 850 °C for about 30 minutes. After this a 60% Ar and 40% oxygen mixture was introduced through multi function control (MFC) unit. An alternate method is to switch off the mechanical rotary pump and open the valve to allow air to rush in the vacuum tube. The tube was then heated for about 10 to 15 minutes. The furnace was switched off and tube was allowed to cool off under Ar flow. A white wool-like growth was observed on the silicon or quartz substrate. SEM analysis showed that more dense nanowires were obtained if substrate was covered during the process. It may be because of the increased vapor pressure at the point of growth. Higher growth is observed at the edges of the substrate. This higher growth is known as edge effect where due to surface roughness of edges more source material is trapped resulting in dense growth [54]. Nanowire diameter ranges from 40 nanometers to micron size. Energy dispersive spectroscopy (EDS) analysis confirmed that atomic ratio of germanium to oxygen is close to 1:2. Some of the SEM images show gold particle at the end of nanowires which indicate that growth is taking place through VLS mechanism. The kink in nanowires as shown in Figure A-2 can be result of stacking faults and dislocations [55]. Lugstein *et al* have explained kink in Si nanowires by overall change in pressure during growth [56, 57]. We believe change in pressure is more appropriate reason in our case as we suddenly change pressure by opening valve to inlet oxygen at high

temperature. This, however, is not the case every time. Straight nanowires have been obtained by allowing mixture of oxygen/ argon gas in the chamber at high temperature.

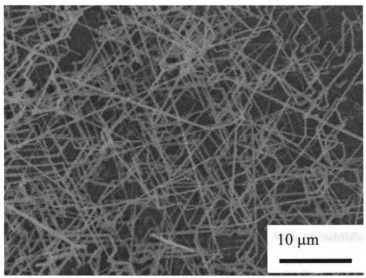

Figure A-2. GeO_2 Nanowires SEM image.

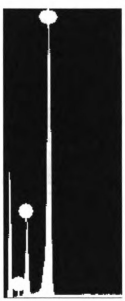

Figure A-3. EDS spectra indicating Ge and O_2 ratio.

A.3 Hotplate Synthesis of GeO_2 nanowires

Several routes of GeO_2 nanowire synthesis have been reported including physical evaporation [58], laser ablation [59], thermal oxidation [60], carbon nanotube confined reaction [61] and thermal annealing of Ge under an oxidizing environment [62]. These synthesis procedures require heating above the sublimation temperature of GeO (710 °C) to generate sufficient vapor pressure of source material. Nanowire growth can occur rapidly under these typical growth conditions and for added control, vacuum growth chamber are commonly used which might include process gas control instrumentation, vacuum pumps and furnaces (internal or external to the chamber). We have developed a low cost, low temperature, hot plate nanowire synthesis method with minimum process variables for good repeatability.

A.3.1 Experimental procedure

A hotplate capable of reaching ~ 350 °C temperature was used to grow GeO_2 nanowires on the following substrates: quartz, alumina, AlN and Si wafers each coated with 9 to 28 nm of gold. Hotplate setup is shown in Figure A-8. To fabricate the nanowires a gold (Au) coated substrate was placed on a hotplate with the Au coating facing upward and a small piece of an undoped Ge wafer was placed on top of the substrate. Aluminum foil was used to cover the sample on the hotplate taking care not to touch the samples with the aluminum. The hotplate was then heated to ~ 350 °C for about 2 hrs then switched off and allowed to cool down to room temperature before the

substrate was removed. Through an optical microscope, a white wool-like growth could be observed on the substrate.

A.3.2 Results and Discussion

The product was characterized by JEOL 6400 SEM, EDS (Oxford Instruments), JEOL 3010 TEM, Powder X ray diffraction (Rigaku), and Raman Spectroscopy (EZ Raman). Nanowires were tens of micron long and ~50 to 200 nm in diameter. For TEM analysis a Cu TEM grid (Pelco 100 mesh with lacy carbon) was placed on an AlN piece having nanowires on its surface and the TEM grid was moved several millimeters to scrape some of the nanowires onto the grid. The obtained diffraction pattern during TEM imaging is shown in Figure A-4. After two minutes of imaging, the diffraction pattern was lost which is in agreement with what has been reported elsewhere [58] and can be attributed to unstable and sensitive nature of nanowires under electron irradiation. SEM images of GeO_2 nanowires grown on aluminum nitride (AlN), alumina (Al_2O_3), quartz, and silicon (Si) wafer are shown in Figure A-5. It can be clearly seen that growth on the Si wafer and quartz are sporadic whereas on alumina and aluminum nitride there is uniform layer of nanowires. A closer look reveals that these later substrates have thin wires with more uniform morphology. We believe it is because alumina and aluminum nitride have rough surfaces providing more edges for a dense growth. EDS results in Table A-1 shows the ratio of germanium and oxygen (24:71) confirming that nanowires are GeO_2. However, EDS is susceptible to some error for oxygen concentration. Raman peak in Figure A-6 indicates that nanowires are trigonal in structure.

A.3.3 Growth Mechanism

In Addition to GeO_2 we also synthesized ZnO nanowires using a hotplate which grew only on the zinc source and any effort to grow nanowires on catalyst coated substrate was not successful. This can be explained by self catalytic nucleation and tip growth process [63] which clearly is not a VLS growth mechanism. Whereas in the case of GeO_2, nanowires could be synthesized only on a catalyst coated substrate and not on the source itself. It appears that a catalyst is necessary for low temperature growth of GeO_2 because melting point of Ge is 915 °C but melting point of Au-Ge eutectic is 356 °C (at 28 at.% Ge) [64] which is well below the sublimation point of germanium. There are previous reports of hotplate metal oxide nanowire growth. Fook *et al* [65] synthesized WO_x nanowires on a hotplate by heating a tungsten foil and collecting nanowires on a glass slide without any catalyst. They have proposed the solid-vapor-solid (SVS) growth mechanism for this synthesis process. Yanwu *et al* [63, 66] reported metal oxide NW including ZnO, CuO, α-Fe_2O_3 and CoO_x nanostructures through direct heating of the source material on a hotplate without using any catalyst. They have ascribed the solid-liquid-solid (SLS), self catalytic nucleation and tip growth mechanism for their nanowires. For the GeO_2 nanowires we have investigated we believe our synthesis mechanism is different from these reports because of the Au catalyst presence. We believe it is VLS mechanism where first GeO evaporates from Ge source. GeO then travels in vapor form to the substrate and forms eutectic with Au droplet. The captured

GeO combines with oxygen from air to form the GeO_2 nanowire. Because of close proximity of source and catalyst the GeO vapors quickly supersaturate the Au droplet which is necessary for crystalline structures [67]. No growth was observed when the substrate was placed farther from the Ge source which indicates the GeO rapidly condenses out of the gas phase. This could be caused by low vapor pressure of the GeO, and/or the time to formation of GeO_2 in the gas phase. Nanowire growth is only observed when the source is in intimate contact with catalyst coated substrate.

It may also be possible to have simultaneous oxide assisted growth. Lee and coworkers [68] proposed oxide assisted growth (OAG) for semiconducting NWs with no metal catalyst present. Under OAG, the oxides serve as catalyst and this mechanism can co-exist with the VLS mechanism in same synthesis experiment. TEM (Figure A-7) shows a metal catalyst at the tip of most nanowires; however the same metal catalyst is not visible for all the NWs observed. It is possible that the OAG mechanism coexists with VLS mechanism or that the gold catalyst is absorbed into the nanowire during growth or that the nanowires without Au tips are broken wires. Allesandro *et al* [69] heated a Ge wafer to investigate the formation of sub oxides and found that at low temperatures sub stoichiometric GeO_x is formed which is unstable and forms a poor interface with Ge. As the temperature is increased GeO_2 becomes the dominant species up to 300°C, for temperatures greater than 300°C the oxidation rate starts decreasing and beyond 400°C the amount of GeO_2 reduces and that of sub-oxide species increases. As

our experiments were for a substrate temperature near 350°C, GeO_x is expected, possibly clustering on the substrate and serving as nucleation sites for oxide assisted growth.

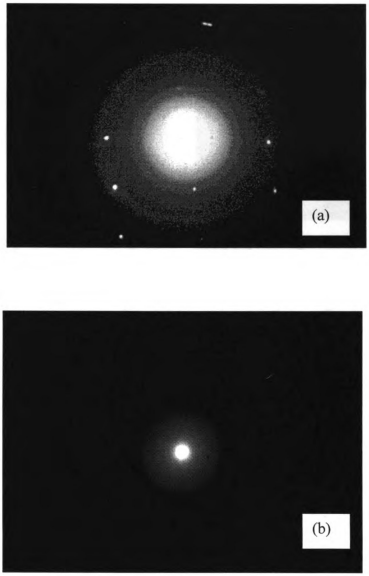

Figure A-4. (a)TEM diffraction pattern (b) after two minutes of irradiation diffraction pattern is lost and NW turns amorphous.

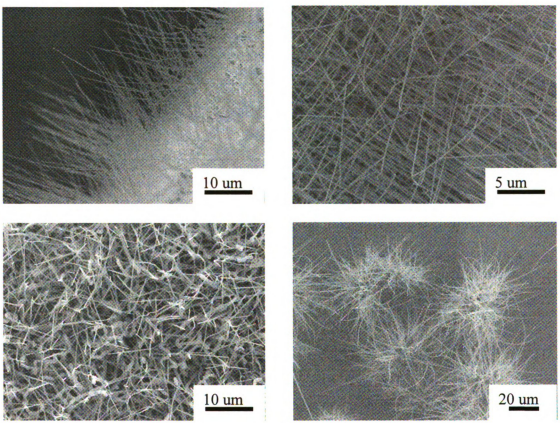

Figure A-5. SEM images of GeO_2 NWs on Au coated (a) Aluminum nitride (AlN) surface (b) Aluminum oxide(AL_2O_3) surface. Wires are straighter (needle-like) and more dense (c) quartz surface, nanowires have non uniform thickness (d) silicon (Si) substrate, nanowires are sparse and irregular.

Table A-1. EDS results indicating Ge and O ratio.

Element	App Conc.	Intensity Corrn.	Weight%	Weight% Sigma	Atomic%
O K	0.25	0.9644	31.35	4.44	71.80
Ge L	0.28	0.6883	48.42	4.58	24.44
Au M	0.11	0.6635	20.22	5.06	3.76
Totals			100.00		

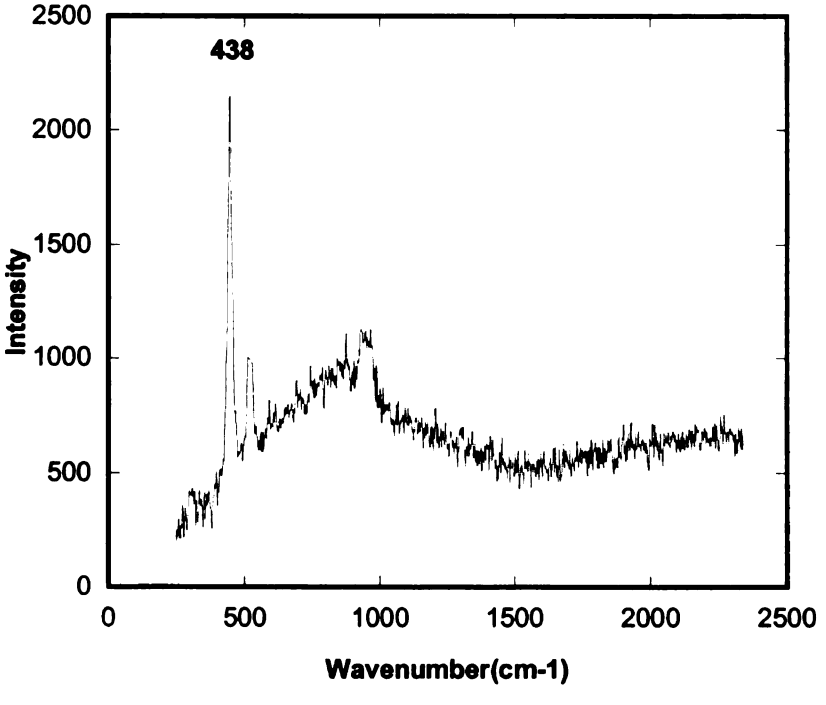

Figure A-6. Raman spectra showing GeO_2 NWs are trigonal.

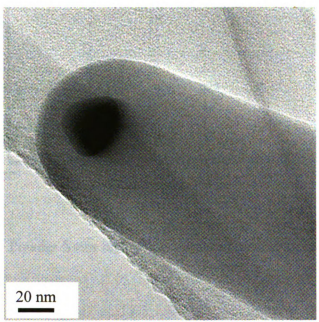

Figure A-7. TEM image showing Au eutectic.

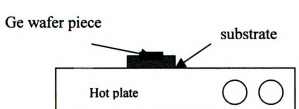

Figure A-8. Hotplate setup for nanowire synthesis.

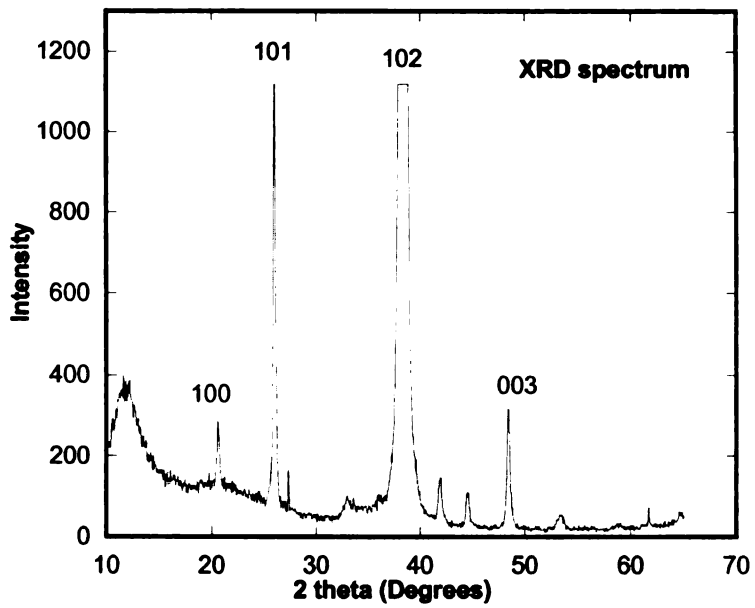

Figure A-9. Powder X-ray diffraction spectrum indicating GeO_2 peaks.

A.4 Indium Antimonide (InSb) Nanowires Synthesis

InSb is a direct bandgap semiconductor (0.18eV) with high mobility ($8x10^4$ cm^2/V-s) [70]. It is a good candidate for detector arrays operating in infrared wavelength [71]; magneto resistive sensors [72] and high speed electronic devices [73]. InSb nanowires have been studied extensively due their high mobility, direct bandgap, phase change nature and expected high figure of merit (ZT) for thermoelectric applications [74]. Figure of merit can be defined as

$$ZT=TS^2\sigma/\kappa.$$

Here S is Seebeck coefficient; T is temperature, σ is electrical conductivity and κ is thermal conductivity. For higher ZT, materials should have higher electrical conductivity

and lower thermal conductivity. Phonons are responsible for heat transfer in semiconductors at the higher temperature range and theoretically it was predicted that one-dimensional structure has higher phonon scattering with its dimensions becoming comparable to phonon mean free path [75]. This helps to reduce thermal conductivity and improve the thermoelectric efficiency of one dimensional nanowires. High mobility of electrons in InSb makes it an ideal candidate for high-speed devices.

Various synthesis methods have been reported in the literature. Electro-deposition, chemical vapor deposition (CVD), pulsed laser deposition (PLD) and physical vapor deposition (PVD) are widely used techniques. For this experiment, the vapor-liquid-solid (VLS) mechanism using a PVD technique was used to grow InSb NWs. As described in the beginning of this chapter the VLS mechanism involves a metal catalyst which serves as a seed for NW growth. We used Au thin film (10 nm) as catalyst for InSb nanowires. Pure InSb (99.99 %) source was placed in a quartz boat and thin Au coated Si (100) substrate was placed upside down on top of the quartz boat. It was placed inside a quartz tube furnace and evacuated to mTorr range. The Ar was allowed to flow into the chamber at 20 sccm. The temperature was maintained at 650 °C for about 1 hr and then allowed to cool down to room temperature. Nanowires were collected into solution by sonicating the substrate. A micropipette was used to place a drop of isopropanol on lacey carbon film coated Cu grid for TEM analysis. Selected area electron diffraction (SAED) patterns revealed that nanowires are single crystalline zincblend structure and the lattice constant is 6.7 Å which is very close to literature value of 6.48 Å. Energy dispersive spectroscopy (EDS) was carried out to determine the constituent elements. Nanowires had oxidized, but it was unknown whether, they absorbed oxygen during synthesis or

only an outer layer of atmospheric oxygen developed after taking out the sample from tube furnace. Trace oxygen in the system could also be a possible source of the nanowire oxidation. The nanowires were tens of micron long and ranged in diameter from 100 to 200 nm. The good InSb material should have In and Sb ratio of 1:1. Whereas, EDS showed that our nanowires were 49:1 ratio and could not be used for thermoelectric applications. However, they can still be used for gas sensor applications where Sb can be considered as doping to InO NWs.

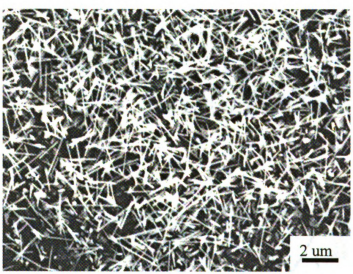

Figure A-10. InSb Nanowire SEM image.

Table A-2. EDS results indicating In and Sb ratio.

Element	Weight %	Atomic%
O K	22.84	68.00
In L	76.94	31.92
Sb L	0.22	0.08
Total	100	100

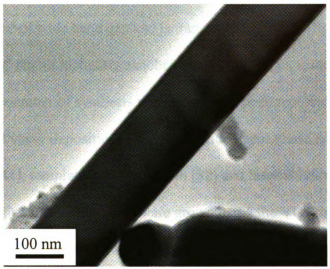

Figure A-11. InSb NW with a diameter of ~200 nm.

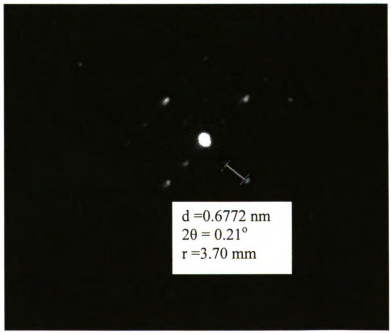

Figure A-12. InSb SAED showing zincblend structure.

A.5 Catalyst Assisted Zinc Oxide (ZnO) Nanowires Synthesis

ZnO nanowires are a primary candidate for photonic applications including UV detectors and lasing. These are wide bandgap (3.7 eV) semiconductors showing both piezoelectric [76] and thermoelectric properties [77]. It is suitable for optoelectronic applications because of wide band gap and is transparent to visible light. ZnO naowires grow in a variety of shapes including nanobelts, nanosprings, nanoshells, nanocombs and nanocages [78]. A number of synthesis techniques have been reported in literature including chemical vapor deposition [79], metal oxide vapor phase epitaxy [80], physical vapor deposition [81], template assisted growth [82] and laser ablation [83].

In this lab zinc oxide nanowires were grown using the VLS mechanism in the quartz tube furnace. Zinc powder was placed upstream at a distance of 4-5 cm from the substrate. The substrate was cleaned with acetone, methanol and DI water using sonication. A thin gold film was deposited by thermal evaporation or sputtering. The tube was evacuated to less than 100 mTorr and then Ar 99.99% was introduced in the tube to bring the pressure to ~ 10 Torr. The tube was heated up to 650 ^{o}C for about an hour. The furnace was then switched off and allowed to cool down. White wool like substance was obtained on the substrate and the source material turned from gray to whitish in color. SEM analysis showed that length is in tens of micron and diameter range is 100-200 nm.

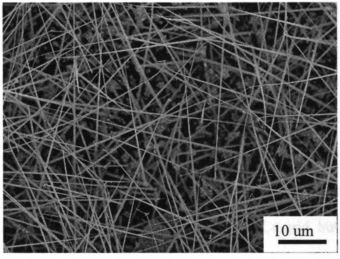

Figure A-13. ZnO nanowires grown in tube furnace.

Table A-3. EDS result indicating Zn and O ratio.

Element	App Conc	Intensity Corrn.	Weight %	Weight% Sigma	Atomic%
O K	2.36	0.7236	4.42	0.45	9.19
Si K	57.99	1.1429	68.82	0.96	81.53
Cl K	1.49	0.6652	3.03	0.19	2.85
Zn K	4.57	0.8702	7.12	0.79	3.62
Au M	6.82	0.5565	16.61	0.83	2.81
Totals			100.00		

A.6 Catalyst Free Zinc Oxide (ZnO) Nanowires Synthesis

The hot plate synthesis approach provides a low cost method compared to the quartz tube synthesis process described in the previous section. With hot plate we do not

need vacuum system or gas control for nanowire synthesis. For this particular case NWs are grown without using any catalyst which also helps to reduce cost. Pure Zn (99.99%) 30-mesh was placed in custom made quartz boat, covered from all sides but not sealed, and placed on top of a hot plate under atmospheric conditions. The material was heated at 480 °C for 2 hrs. Densely packed uniform ZnO NWs grow axially on Zn source. Wires are < 100 nm in diameter and few micron in length. First attempt was made to sonicate NWs in ispropanol and a pipette was used to place a drop on a Cu grid, but that did not prove to be successful. Then Zn source was left inside vial containing isopropanol and sonicated again. This time few wires landed on grid. Also, wires were scratched from surface directly onto a Cu grid. However, this increased the probability of adding contaminations to sample. There are other reports of such oxide nanowire growth on hotplates [84], [63] but it has been stated that due to high vapor pressure and low melting point, control of ZnO nanowires under ambient condition growth is challenging [63]. Whereas, we have been able to grow dense NWs repeatedly through hot plate process. It is assumed that nanowires grow by vapor-solid (VS) mechanism [84] and it can also be explained by self catalytic nucleation [63]. Zinc has melting point of about 420 °C. When hot plate temperature reaches this value, zinc melts and oxidizes immediately under ambient conditions. Since the melting point of zinc oxide is much higher, it solidifies and serve as nucleation site for further growth [63]. The usual VLS mechanism is ruled out because the typical indicator of VLS mechanism is a catalyst (Au) tip at the end of nanowire, whereas, no catalyst is used for hotplate nanowire growth.

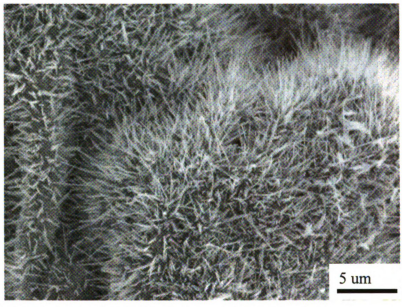

Figure A-14. ZnO NWs grown on hot plate.

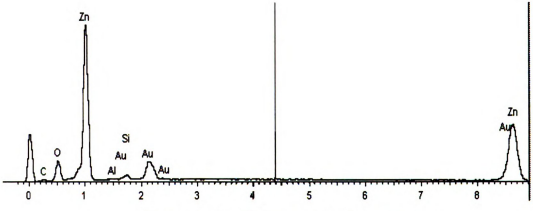

Figure A-15. EDS spectra for ZnO nanowires.

Figure A-16. TEM selected area diffraction image.

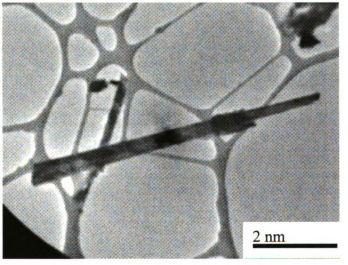

Figure A-17. ZnO NW length ~ 6 μm.

Conclusion

Oxide nanowires were synthesized using two different arrangements. GeO_2, InSb and ZnO nanowires were synthesized in tube furnace using the VLS mechanism. ZnO and GeO_2 nanowires were also synthesized using a hotplate under ambient conditions.

Hotplate ZnO nonowires follow the self-catalytic growth model and GeO_2 nanowires follow VLS growth mechanism. We suspect that oxide assisted growth mechanism may also be simultaneously present with VLS mechanism for GeO_2 nanowire hotplate synthesis. To the best of our knowledge it is the first instance of hotplate GeO_2 nanowire growth.

References

[1] Kuei Fang Hsu, Sim Loo, Fu Guo, Wei Chen, Jeffrey S. Dyck, Ctirad Uher, Tim Hogan, E. K. Polychroniadis, and Mercouri G. Kanatzidis, "Cubic $AbPb_{(m)}SbTe_{(2+m)}$ bulk Thermoelectric Materials with High Figure of Merit", *Science,* vol. 303, pp. 818-821, 2004.

[2] V.A Drebushchak, "The Peltier Effect", *Journal of Thermal Analysis and Calorimetry*, vol. 91, pp. 311-315, 2008.

[3] D.M Rowe, *CRC Handbook of Thermoelectrics*. Boca Raton: CRC Press, 1995.

[4] J. Short, Sim Loo, S Lal, K F Hsu, E Quarez, M.G Kanatzidis, T Hogan, "Hall Effect Measurement on New Thermoelectric Materials". *Mat. Res. Soc. Sym. proc*, vol. 793, pp. 323-332, 2004.

[5] Douglas T Crane, "Potential Thermoelectric applications in diesel vehicles". In *Proceeding of the Ninth Diesel Engine Emission Reduction (DEER) conference.* August 23-24, 2003. (available at http://www.bsst.com/technical_papers).

[6] HG Goldsmid and G S Nolas, "A review of the new thermoelectric materials," in *Proceedings of the IEEE 20th International Conference on Thermoelectric,* 2001, pp. 1-6.

[7] C M Bhindari, "Minimizing the thermal conductivity". in *CRC Handbook of Thermoelectrics*. Ed. D M Rowe. CRC Press: Boca Raton, FL, 1995.

[8] D. Bilc, S D Mahanti, Eric Quarez, Kuei-Fang Hsu, Robert Pcionek and M G Kanatzidis, "Resonant States in the Electronic Structure of the High Performance Thermoelectrics $AgPb_mSbTe_{2+m}$: The Role of Ag-Sb Microstructures", *Phys. Rev. Lett.* vol. 93, p. 146403, 2004.

[9] John Androulakis, Kuei Fang Hsu, Robert Pcionek, Huijun Kong, Ctirad Uher, Jonathan J. D'Angelo, Adam Downey, Tim Hogan, and Mercouri G. Kanatzidis, "Nanostructuring and High Thermoelectric Efficiency in p-Type $Ag(Pb_{1-y}Sn_y)_mSbTe_{2+m}$. ", *Adv. Mater.* vol. 18, pp. 1170–1173, 2006.

[10] Jane Y. Howe, Hsin Wang, and Jihui Yang. "Structure of Polycrystalline Thermoelectric Bulk Material $AgPb_mSbTe_{2+m}$". *Microsc Microanal,* 13(Suppl 2), 2007.

[11] E. Quarez, K F Hsu, R Pcionek, N Frangis, E K Polychroniadis, and M G Kanatzidis, "Nanostructuring, Compositional Fluctuations, and Atomic Ordering in the Thermoelectric Materials $AgPb_mSbTe_{2+m}$. The Myth of Solid Solutions" *J. of Am. Chem Soc.* vol. 127(25), pp. 9177-9190, 2005.

[12] Ono, T.; Takahama, T.; Irie, T, "The Thermoelectric Properties of $AgSbTe_2$-$AgBiTe_2$, -PbTe and -SnTe Systems", *J. Phys. Soc. Jpn.* vol. 17, p. 1070, 1962.

[13] Fei Ren, "Mechanical Characterization and Powder Processing of Lead Telluride based Thermoelectric Materials", PhD Dissertation, Deparment of Material Science and Chemical Engineering, Michigan State University, 2007.

[14] Atsuko Kosuga, Masayoshi Uno, Ken Kurosaki and Shinsuke Yamanaka, "Thermoelectric Properties of Stoichiometric $Ag_{1-x}Pb_{18}SbTe_{20}$ (x = 0, 0.1, 0.2)", *Journal of Alloys and Compounds*, vol. 391, pp. 288-291, Apr 2005.

[15] Heng Wang, Jing-Feng Li, Ce-Wen Nan, Min Zhou, Weishu Liu, Bo-Ping Zhang, and Takuji Kita. "High-performance $Ag_{0.8}Pb_{18+x}SbTe_{20}$ thermoelectric bulk materials fabricated by mechanical alloying and spark plasma sintering", *Appl. Phys. Lett.* vol. 88, p. 092104, (2006).

[16] Bradley Hall, "Powder processing, powder characterization, and mechanical properties of LAST and LASTT thermoelectric materials", Masters Thesis, Deparment of Material Science and Chemical Engineering, Michigan State University, 2008.

[17] G. Wang, W. Pan, M. N. Jiang, J. Chen, and Y. M. Luo, "Investigation of the physical and mechanical properties of hot-pressed machinable Si_3N_4/h-BN composites and FGM", *Mater. Sci. Eng. B.* vol. 90, p. 261, 2002.

[18] I A Drabkin, L B Ershova, *Energy Climate Technology (ECT) conference*, Bergen April 17-18, 2008, P1-09-1.

[19] O Yamashita, H Odahara, and S Tomiyoshi, "Effect of metal electrode on thermoelectric power in bismuth telluride compounds", *J. Materials Science,* vol. 39, pp. 5653-5658, 2004.

[20] Peter Thomas and Houldcroft, *Welding Process Technology*, Cambridge: Cambridge University Press, 1977.

[21] M G Nicholas, *Joining processes: Introduction to Brazing and Diffusion bonding,* The Netherlands: Kluwer Academic Publishers, 1998.

[22] Giles Humpston and David M Jacobson, *Principles of Soldering,* ASM International Publications, 2004.

[23] Jonathan D Angelo, "Low resistance contacts to Thermoelectric Materials", Masters Thesis, Deaprtment of Electrical and Computer Engineering, Michigan State university, 2006.

[24] N C Miller, "Method of manufacturing a bonded electrical contact for thermoelectric semiconductor element", U.S Patent 3879838, Apr 29, 1975.

[25] L F Kendall, and J H Bredt, "Diffusion barrier for semiconductive thermoelectric generator elements", U.S Patent 3650844, Mar 21, 1972.

[26] M. Weinstein and A. I. Mlavsky, "Bonding of Lead Telluride to Pure Iron Electrodes", Rev. Sci. Instrum. vol. 33, p. 1119, 1962.

[27] T R Krebs, "Stable bonded barrier leyer-Telluride thermoelectric devices", U.S Patent 3859143, Jan 7, 1975.

[28] M P Ravdel and O I Evdokimova, "Alloys With a High Coefficient of Thermal Expansion Based on the Mn-Pd System", *Metal science and heat treatment,* vol. 16, pp. 403-405, 2004.

[29] TP Hogan, *MRS Spring meeting* April 13-17, 2009, San Francisco, CA.

[30] MF Dumke, T A Tombrello, R A Weller, RH Housley, and EH Cirlin, "Sputtering of the gallium-indium eutectic alloy in the liquid phase", *Surf. Sci.* vol.124, pp. 407-422, 1983.

[31] Wade, K.; Banister, A. J. *The chemistry of aluminum, gallium, indium and thallium, vol. 12*; Pergamon texts in inorganic chemistry; Pergamon Press: New York, 1973.

[32] D Zrnic, and D S Swatik, "On the resistivity and surface tension of the eutectic alloy of gallium and indium", *J. less-common met.* vol. 18, pp. 67-68, 1969.

[33] S J French, D J Saunders, and G W Ingle, "The system gallium indium", *J Phys. Chem.* vol. 42, pp. 265-274, 1938.

[34] C. P. Rhodes, J.W. Long, M. S. Doescher, J. J. Fontanella, D. R. Rolison, "Nanoscale Polymer Electrolytes: Ultrathin Electrodeposited Poly(Phenylene Oxide) with Solid-State Ionic Conductivity", *J. Phys. Chem. B.* vol. 108, pp. 13079-13087, 2004.

[35] Ryan C. Chiechi, Emily A. Weiss, Michael D. Dickey, and George M. Whitesides, "Eutectic Gallium-Indium (EGaIn): A Moldable Liquid Metal for Electrical Characterization of Self-Assembled Monolayers", *Angew. Chem.* vol. 120, pp. 148-150, 2008.

[36] Jonathan D Angelo, "Electrical contact fabrication and electronic characterization of thermoelectric materials", PhD dissertation, Department of Electrical and Computer Engineering, Michigan State University, 2009.

[37] I.B Cadoff, and Edward Miller, *Thermoelectric Material and Devices,* New York: Reinhold Publishing Corporation, 1960.

[38] Ronald S Timsit, "Electrical contact resistance: Fundamental principles" in *Electrical Contacts: principles and applications*, Paul G Slade, Ed. New York: Marcel Dekker Inc, 1999. pp. 1-72.

[39] Kortier, William E Muller, John J Eggers, Philip E, "Thermoelectric Module", U.S Patent 4211889, Jul 8, 1997.

[40] Belson H S, and Houston B, "Thermal expansion of tin-telluride", *J Appl. Phys.* vol. 41, pp. 422-424, 1970.

[41] A Singh, S Bhattacharya, C Thinaharan, D K Aswal, S k Gupta, J V Yakhmi, K Bhanumurthi, "Development of low resistance electrical contacts for thermoelectric devices based on n-type PbTe and p-type TAGS-85 $((AgSbTe_2)_{0.15}(GeTe)_{0.85})$", *J.Phys.D: Appl. Phys.* vol. 42, p. 015502, 2009.

[42] Winston R Seeto, Roman K Weide, and Telesphore L Charland, "*Exothermic Bonding of Thermoelectric Couples*", U.S Patent 3808670, May 7, 1974.

[43] D H Hammon, "Thermal conductivity of SnTe between 100 K and 500 K", *J. Appl. Phys.* vol.37. No.8, p.3181, July 1966.

[44] H E Bates, M Weinstein, "Thermoelectric bonding study: The bonding of PbTe and PbTe-SnTe with non-magnetic electrodes", NASA-CR-290, Sep1, 1965.

[45] Wagner, R.S. and W.C. Ellis, "Vapor-liquid-solid mechanism of single crystal growth". *App. Phys. Lett.* Vol. 4, pp. 89-90, 1964.

[46] Volker Schimidt and Ulrich Gosele, "How nanowires grow", *Science,* vol. 316, pp. 698-699, May 4, 2007.

[47] M Kaur, K P Muthe, S K Despand, S Choudhury, J B Singh, N Verma, S K Gupta, J and V Yakhmi, "Growth and branching of CuO nanowires by thermal oxidation of copper", *J Crystal Growth*, vol. 289, pp. 670-675, 2006.

[48] J Q, Meng X M, Jiang Y, Lee C S and Lee S T, "Fabrication of Germanium-Filled Silica Nanotubes and Aligned Silica Nanofibers", *Adv.Mater.* vol. 15, pp. 70-73, 2003.

[49] X. C. Wu, W. H. Song, B. Zhao, Y. P. Sun and J. J. Du, "Preparation and photoluminescence properties of crystalline GeO_2 nanowires", *Chem. Phys. Lett.* vol. 349, pp. 210-214, 2001.

[50] Zacharias, and M.; Fauchet, P. M, "Light emission from GeO and GeO2 nanocrystals", *J. Non-Cryst. Solids,* vol. 227-230, pp. 1058-1062, 1998.

[51] Chun-I Wu and T P. Hogan, "Growth of GeO_2 nanowires by thermal annealing", *MRS Symp Proc*, vol 951, 2007.

[52] Z Y Lin and B.K Garside, "Low-loss GeO_2 optical waveguide fabrication using low deposition rate rf sputtering", *Appl. Opt.* vol. 21, pp. 4324-4328, 1982.

[53] M A Khan, "Substrates for surface enhanced Raman spectroscopy", PhD dissertation, Department of Electrical and Computer Engineering, Michigan State University, 2008.

[54] H Pan, S Lim, C Poh, H Sun, XWu, Y Feng and J Lin, "Growth of silicon nanowires by thermal evaporation", *Nanotechnology*, vol.16, pp. 417-421, 2005.

[55] Xuan Wang, Qingwen Li, Zhibo Liu, Jin Zhang, Zhongfan Liu, and Rongmin Wang, "Low temperature growth and properties of ZnO nanowires". *Appl. Phys. Lett.* vol. 84, No. 24, pp. 4941- 4945, 2004.

[56] A Lugstein, M Steinmair, Y J Hyun, G Hauer, P Pongratz, and E bertagnolli. "Pressure induced orientation control of the growth of epitaxial silicon nanowires". *Nano letters*. vol. 8, No. 8, pp. 2310- 2314, 2008.

[57] Youn-Joo Hyun, Alois Lungstein, Mathias Steinmair, Emmerich Bertagnolli and Peter Pongratz. "Orientation specific synthesis of kinked silicon nanowires grown by vapor-liquid-solid mechanism", *Nanotechnology*, vol. 20, p. 125606, 2009.

[58] Z G Bai, D P Yu, H Z Zhang, Y Ding, Y P Wang, X Z Gai, Q L Hang, G C Xiong, S. Q Feng, "Nano scale GeO_2 nanowires synthesized by physical evaporation", *Chem Phys Let.* vol. 303, pp. 311-314, 1999.

[59] Y H Tang, Y F Zhang, N Wang, I Bello, C S Lee, and S T Lee, "Germanium dioxide whiskers synthesized by laser ablation", *Appl Phys Lett,* vol. 74, pp. 3824-3826, 1999.

[60] H Y Dang, J Wang, and SS Fan, "the synthesis of metal oxide nanowires by directly heating metal samples in appropriate oxygen atmosphere", *Nanotechnology*, vol. 14, pp. 738-741, 2003.

[61] Y J Zhang, J Zhu, Q Zhang, Y J Yan , N L Wang, and X Z zhang, "Synthesis of GeO_2 nanorods by carbon nanotube template", *Chem Phys. Lett.* vol. 317, pp. 504-509, 2000.

[62] Y Su, X Liang, S Li, Y Chen, Q Zhou, S Yin, X Meng and M Kong, "self-catalytic VLS growth and optical properties of single crystalline GeO2 nanowire arrays", *Materials Letters* Vol.62. pp 1010-1013, 2008.

[63] Y Zhu, C H Sow, T Yu, Q Zhao, P Li, Z Shen, D Yu and J T L Thong, "Co-synthesis of ZnO-CuO Nanostructures by Directly Heating Brass in Air", *Adv Funct. Mater.* Vol. 16, pp. 2415-2422, 2006.

[64] M. Hansen and K Anderko1958 *Constitution of Binary Alloys.*, (New York: McGraw-Hill) p 206.

[65] F C Cheong, B Varghese, Y Zhu, E P S Tan, L Dai, V B C Tan, C T Lim and C H Sow, "WO 3-x nanorods synthesized on a thermal hotplate", *J Phys Chem C,* vol. 111, pp. 17193-17199, 2007.

[66] T Yu, Y Zhu, X Xu, K S Yeong, Z Shen, P Chen, C T Lim, J T L Thong and C H Sow, "Substrate-friendly synthesis of metal oxide nanostructures using a hotplate", *Small*, vol. 2, No.1, pp. 80-84, 2006.

[67] B. A. Wacaser, K. A. Dick, J. Johansson, M. T. Borgström, K. Deppert and L. Samuelson, "Preferential interface nucleation: An expansion of the VLS growth mechanism for nanowires", *Adv. Mater.* vol. 21, pp.153-165, 2009.

[68] R Q Zhang, and Y Lifshitz, S T Lee, "Oxide assited growth of semiconducting nanowires". Adv. Mater. vol. 15, No. 7-8, pp.635-640, 2003.

[69] A Molle, M N K Bhuiyan, G Tallardia, and M Fanciulli, "Formation and stability of germanium oxide induced by atomic oxygen exposure", 2006 *Mater. Sci. Semicond. Process,* vol. 9, pp. 673-678, 2006.

[70] Xueru Zhang, Yufeng Hao, Guowen Meng, and and Lide Zhang, "Fabrication of Highly Ordered InSb Nanowire Arrays by Electrodeposition in Porous Anodic Alumina Membranes", *Journal of The Electrochemical Society,* vol. 152(10), C664-C668, (2005).

[71] H. D. Su, S. Z. Chang, S. C. Lee, and T. P. Sun, "High temperature InAs infrared detector based on metal-insulator-semiconductor structure", *Electron. Lett.*, vol. 31, No.11, pp. 918-920,1995.

[72] S. A. Solin, T. Thio, D. R. Hines, and J. J. Heremans, "Enhanced Room-Temperature Geometric Magnetoresistance in Inhomogeneous Narrow-Gap Semiconductors", *Science*, vol. 289, pp. 1530-1532, 2000.

[73] T. Ashley, A. B. Dean, C. T. Elliott, G. J. Pryce, A. D. Johnson, and H. Willis, "Uncooled high speed InSb field-effect transistor", *Appl. Phys. Lett.* vol. 66, pp. 481-483, 1995.

[74] Vedernikov M.V, Uryupin O.N, Goltsman B.M, Ivanov Yu.V, and Kumzerov Yu.A, "Experimental study of thermoelectric properties of InSb nanowires", in *Proceedings of IEEE 20th International Conference on Thermoelectrics*, 2001, pp. 361-363.

[75] L D Hicks, and M. S. Dresselhaus, "Thermoelectric figure of merit of a one-dimensional conductor", *Phys Rev B*, vol. 47, pp.16631- 16634, 1993.

[76] Savarimuthu Philip Anthony, Jeong In Lee, and Jin Kon Kim. "Tuning optical bandgap of vertically aligned ZnO nanowire arrays grown by homoepitaxial electrodeposition". *Appl. Phy. Lett.* vol. 90, p. 103107, 2007.

[77] Chul-Ho Lee, Gyu-Chul Li, Yuri M Zuev and Philip Kim, "Thermoelectric Power measurement of wide bandgap semiconducting nanowires". *Appl. Phy. Lett.* vol. 94, p. 022106, 2009.

[78] Z L Wang, "Zinc oxide nanostructures: growth, properties and applications", *Journal of Physics-Condensed Matter*, vol. 16, pp. R829-R858, 2004.

[79] J J Wu, and S C Liu, "catalyst-free growth and characterizationof ZnO nanorods", *Journal of Physical ChemistryB*, vol. 106, pp. 9546-9551, 2002.

[80] W I Park, D H Kim, S W Jung and G C Yi, "Metalorganic vapor-phase epitaxial growth of well aligned ZnO nanorods", *Applied Physics Letter.* vol. 80, pp. 4232-4234, 2002.

[81] J Y Li, X L Chen, H Li, M He and Z Y Qiao," Fabrication of zincoxide nanorods", *Journal of Crystal Growth.* vol. 233, pp. 5-7, 2001.

[82] M J Zheng, L D Zheng, G H Li and W Z Shen, "Fabrication and optical properties of large scale uniform zincoxide nanowires arrays by one-step electrochemical deposition technique", *Chemical PhsicsmLetter,* vol.363, pp. 123-128, 2002.

[83] H J Son, K A Jeon, C E Kim, J H Kim, K H Yoo and S Y Lee, "Synthesis of ZnO nanowires by pulsed laser deposition in furnace", *Applied surface Science: Photon Assisted Synthesis and Processing of Functional Materials-E MRS H Symposium.* vol. 253, pp.7848-7850, 2007.

[84] Y W Zhu, T Yu, FC Cheong, X J Xu, C T Lim,V B C Tan, J T L Thong and C H Sow, "Large-scale synthesis and field emission properties of vertically oriented CuO nanowire films", Nanotechnology, vol. 16, pp. 88-92, 2004.